Towards robust design optimization of automotive turbocharger rotor-bearing systems

Eling, Rob

DOI
10.4233/uuid:fdb0da19-0ef2-4bb6-92a7-8a7acbb05dd2

Publication date
2018

Document Version
Final published version

Citation (APA)
Eling, R. (2018). *Towards robust design optimization of automotive turbocharger rotor-bearing systems*. [Dissertation (TU Delft), Delft University of Technology]. https://doi.org/10.4233/uuid:fdb0da19-0ef2-4bb6-92a7-8a7acbb05dd2

TOWARDS ROBUST DESIGN OPTIMIZATION OF AUTOMOTIVE TURBOCHARGER ROTOR-BEARING SYSTEMS

TOWARDS ROBUST DESIGN OPTIMIZATION OF AUTOMOTIVE TURBOCHARGER ROTOR-BEARING SYSTEMS

Dissertation

for the purpose of obtaining the degree of doctor
at Delft University of Technology
by the authority of the Rector Magnificus, Prof.dr.ir. T.H.J.J. van der Hagen,
chair of the Board for Doctorates,
to be defended publicly on
Tuesday 15 May 2018, 15:00 hours

by

Robert Paulus Theodorus ELING

Master of Science in Mechanical Engineering, Delft University of Technology
born in Boxmeer, the Netherlands.

This dissertation has been approved by the promotors.

Composition of the doctoral committee:

Rector Magnificus,	chairperson
Dr. ir. R.A.J. van Ostayen,	Technische Universiteit Delft, promotor
Prof. dr. ir. D.J. Rixen,	Technische Universität München, promotor
Onafhankelijke leden:	
Prof. Dr.-Ing. A. Rienäcker	Universität Kassel, Germany
Prof. dr. M. Fillon	Université de Poitiers, France
Prof. dr. ir. S.A. Klein	Technische Universiteit Delft
Prof. dr. ir. D.J. Schipper	Universiteit Twente
Prof. dr. ir. J.L. Herder	Technische Universiteit Delft

This research has been funded by Mitsubishi Turbocharger and Engine Europe.

Keywords: Turbocharger, rotordynamics, floating ring bearing, hydrodynamic, lubrication, cavitation, bearing, oil whirl, friction, robust optimization.

Printed by: Gildeprint, Enschede

Front: Turbocharger rotor, rendered image.
Back: Cross-sectional view of the fluid domain of a floating ring bearing showing the streamlines of the lubricant.

ISBN 978-94-6186-925-8

An electronic version of this dissertation is available at
http://repository.tudelft.nl/.

Work it harder, make it better
Do it faster, makes us stronger
More than ever, hour after
hour, work is never over

Daft Punk

ABSTRACT

In the competitive automotive market, the performance of turbochargers is constantly being pushed towards their theoretical optimum. In this quest for performance, the widespread availability of computing power and simulation software enables efficient virtual assessment and optimization of designs. One of the key components of the turbocharger is the rotor-bearing system, which determines the friction losses and noise output and furthermore affects the overall turbocharger efficiency, reliability and cost. The focus of this study is on developing methods to optimize the rotor-bearing system, where particular attention is paid to taking into account the product-to-product variations that are inevitable in cost-effective mass-produced parts, as well as the variations in turbocharger operating conditions.

First, a model of the rotor-bearing system was developed to predict the rotordynamic response over the operating range. This model is constructed in a step-by-step fashion, starting with a simple test case: a Laval rotor supported by plain journal bearings. As the behavior of the rotor-bearing system varies over its rotation speed range, run-up simulations were performed by a time-transient multi-physical model. In this model, several sub-models are coupled: a rotordynamic sub-model, a thermo-hydrodynamic sub-model and a thermal network model. The key to obtaining reliable predictions of the rotor-bearing dynamics was found in the thermal network model, which provides estimates of the temperatures of the walls adjacent to the bearing. The resulting simulations correspond well with measurement results and show the well-known characteristic behavior for this rotor-bearing system: a critical speed (*synchronous response*) and a half-speed oil whirl which transforms into an oil whip near twice the critical speed (*sub-synchronous response*). Also, the changes of the run-up response as a function of the rotor-bearing operating conditions were correctly predicted.

Once a satisfactory correlation was found between numerical simulation results and measurement results, the test case progressed to a Laval rotor with floating ring bearings instead of plain journal bearings. Correspondingly, the bearing model was extended to include the dynamics of the floating ring and its two oil films. The resulting run-ups showed a response consisting of a critical speed, an oil whirl and an oil whip. This time, the oil whirl had a frequency of half the speed of the ring plus the shaft, indicating the whirl occurs in the inner oil film. This oil whirl locks into an oil whip at twice the critical speed. The simulation results have been validated on a high speed Laval rotor test setup, capable of operating up to 200krpm, on which the rotor unbalance, oil supply conditions and bearing housing temperature were varied.

Analysis of a turbocharger rotor-bearing system was subsequently performed, showing a more complex response, consisting of multiple critical speeds and the co-existence

of sub-synchrononous whirling modes. The effect of the rotor-bearing operating conditions, unbalance configuration, the thrust bearing and the bearing cylindricity were investigated. Most of the trends were correctly predicted by the model, however the correlation between measurement results and simulation results is clearly inferior to the case of the Laval rotor, most likely due to the uncertainties in the actual turbocharger geometry and the actual unbalance distribution.

Lastly, an optimization of the rotor-bearing system was performed. As the turbocharger rotor-bearing model required excessive computation times for being used in an optimization study, the model describing the Laval rotor on plain journal bearings was used as a test case. Initially, a deterministic design optimization was performed, followed by a global robust optimization. The resulting robust optimum design ensures optimum rotor-bearing performance, even at the most severe operating conditions and even if all manufacturing tolerances represent the worst case scenario. Hence, the methods developed in this study are considered to form a basis for robust optimization of turbocharger rotor-bearing systems.

SAMENVATTING

De prestaties van turbo's in de automobielindustrie worden constant verder ontwikkeld richting hun optimum. Door de toenemende beschikbaarheid van computers en simulatiesoftware is het mogelijk geworden om op een snelle manier de prestaties van een ontwerp te bepalen en te optimaliseren. Een van de kritische onderdelen van een turbo is het rotor-lager systeem: het bepaalt de frictieverliezen en de geluidsemissie van een turbo alsmede beïnvloedt het de totale efficiëntie, de betrouwbaarheid en de kostprijs van een turbo. Om zo goed mogelijk aan de wensen van de markt te kunnen voldoen, is het doel van dit onderzoek methodes te ontwikkelen waarmee het turbo rotorlagersysteem geoptimaliseerd kan worden, waarbij rekening gehouden dient te worden met variaties in de bedrijfstoestand en afwijkingen in het fabricageproces van de turbo.

Een model is ontwikkeld voor het voorspellen van het rotordynamische gedrag over het toerengebied. Dit model is stap-voor-stap opgebouwd, beginnend met een Laval rotor op enkelvoudige glijlagers. Omdat het gedrag van het rotor-lager systeem verandert met het toerental, zijn simulaties van het optoeren van de rotor uitgevoerd op basis van een tijd-transient model waarin een rotordynamisch sub-model, een thermohydrodynamisch sub-model en een thermisch netwerkmodel gekoppeld zijn. De sleutel tot een goede correlatie tussen simulatieresultaten en meetresultaten is gevonden in het voorzien van voorspellingen van de wandtemperaturen van de as en het lagerhuis middels een thermisch netwerkmodel. De resulterende voorspellingen van het rotorlager gedrag kwamen goed overeen met de meetresultaten en bevatten de voor dit rotorlagersysteem typische respons: een kritische snelheid, *oil whirl* met een frequentie gelijk aan de helft van de rotatiesnelheid en *oil whip* zodra de oil whirl frequentie gelijk is aan de kritische frequentie. De veranderingen van de respons als functie van de bedrijfstoestand werden correct voorspeld door het model.

Na een goede overeenkomst tussen het model en de meetresultaten bewerkstelligd te hebben, is de casus uitgebouwd naar een Laval rotor met *floating ring* lagers in plaats van enkelvoudige glijlagers. Het model is overeenkomstig uitgebreid met de dynamica van de ring en beide vloeistoffilms. De resulterende simulaties en metingen van het optoeren van de rotor laten opnieuw een kritische snelheid, *oil whirl* en *oil whip* zien. Ditmaal lag de oil whirl frequentie op de helft van de rotatiesnelheid van de as plus de ring, wat laat zien dat de whirl in de binnenfilm plaats vindt. De whirl gaat over in een whip zodra de frequentie gelijk is aan de kritische snelheid. Validatie van de simulatieresultaten is uitgevoerd op een testopstelling, bestaande uit een Laval rotor die opgetoerd kan worden tot 200krpm, waarbij de rotor onbalans, olie toevoer condities en de lagerhuistemperatuur werden gevarieerd.

Vervolgens is een soortgelijke analyse op basis van het turbo rotor-lager systeem uit-

gevoerd. Dit systeem laat een complexere respons zien, bestaande uit meerdere kritische snelheden en meerdere sub-synchrone whirl modes. De invloed van de bedrijfscondities van het rotor-lager systeem alsmede de onbalans configuratie, het axiaallager en de onrondheid van de ring werden in kaart gebracht. De overeenkomst tussen de simulatieresultaten en de meetresultaten was minder sterk dan in de voorgaande gevallen, hoogstwaarschijnlijk door afwijkingen in de geteste turbo ten opzichte van de veronderstelde geometrie en onbalansconfiguratie.

Het initiële model van de Laval rotor met enkelvoudige glijlagers was de basis voor het ontwikkelen van een globale robuuste ontwerpoptimalisatie voor rotor-lagersystemen. Het robuuste optimum garandeert een optimale rotor-lager karakteristiek, zelfs wanneer de bedrijfscondities uitdagend zijn en zelfs wanneer de productietoleranties op de slechtst mogelijke manier uitvallen. Zodoende vormen de methodes ontwikkeld in dit onderzoek een basis voor de toekomstige optimalisatie van turbo rotor-lager systemen.

CONTENTS

NOMENCLATURE

Coordinate Systems

u,v,w	Global displacements	m
$\bar{u},\bar{v},\bar{w}$	Local displacements	m
$\bar{X},\bar{Y},\bar{Z}$	Local rotor coord.	-
θ,x,y,z	Local bearing coord.	-
$\bar{\alpha},\bar{\beta},\bar{\phi}$	Local rotations	rad
α,β,ϕ	Global rotations	rad
Θ,X,Y,Z	Global coordinates	-

Roman symbols

a	Viscosity parameter	Pa·s
A	Area	m^2
b	Viscosity coefficient	^oC
C	Clearance	m
c	(Viscosity) coefficient	-
d	Viscosity parameter	-
D	Diameter	m
e	Eccentricity	m
E	Modulus of elestacity	Pa
f	Mass fraction	-
	Function	-
F	Force	N
g	Gravitation constant	m/s^2
h	Film height	m
H	Heat transfer coefficient	$W/(m^2K)$
i	Index	-
I	Moment of inertia	$kg\,m^2$
k	Thermal conductivity	W/(m·K)
L	Length	m
m	Mass	kg
M	Torque	N·m
n	Normal vector	-
N	Order	-
p	Pressure	Pa
P	Power	W
Q	Heat	J
q	Mass flow	kg/s
r	Viscosity parameter	-
R	Radius	m
t	Time	s
T	Temperature	K
U	Unbalance	kg·m

Greek symbols

ε	Eccentricity ratio	-
γ	Shear	-
ψ	Friction loss per area	$W/(m^2)$
ω	Whirl frequency	Hz
Ω	Rotation speed	rad/s
μ	Dynamic viscosity	Pa·s
ρ	Density	kg/m^3
σ	Standard deviation	-
Θ	Rotation angle	rad
τ	Shear stress	Pa
ξ	Dimensionless pressure	-
ψ	Friction	-
Π	Surface	m^2
Λ	Boundary	m
λ	Coefficient of thermal exp.	1/K
σ	Standard deviation	-
ζ	Pressure scaling variable	Pa

Matrices and vectors

$\boldsymbol{C}$	Damping matrix	N·s/m
$\boldsymbol{F}$	Force vector	-
$\boldsymbol{g}$	Gravity vector	m/s^2
$\boldsymbol{G}$	Gyroscopic matrix	Nm·s/rad
$\boldsymbol{K}$	Stiffness matrix	N/m
$\boldsymbol{M}$	Mass matrix	kg
$\boldsymbol{q}$	Displacement vector	-
$\boldsymbol{T}$	Transformation matrix	-

Subscripts and superscripts

0	Reference conditions
acc	Acceleration
ali	Aligned
amb	Ambient
b	Bearing
bh	Bearing housing
c	Compressor
cc	Connecting channel
cent	Centrifugal
char	Characteristic
con	Continuous
coup	Coupling
cs	Cross section
d	Disk
el	Element
film	Fluid film
filt	Filter
i	Inlet
in	Inner
K	Stiffness
m	Measurement disk
mid	Midway
M	Mass
oil	Oil
out	Outer
r	Ring
rad	Radial
Ray	Rayleigh
rot	Rotor
s	Shaft
sb	Sideband
tan	Tangential
T	Transformation
unb	Unbalance
wgt	Weight
t	Turbine

Abbreviations

CFD	Computational fluid dynamics
CHT	Conjugate heat transfer
FEM	Finite element method
FRB	Floating ring bearing
Pr	Prandtl number
Re	Reynolds number
RPM	Revolutions per minute

1

INTRODUCTION

1.1. AUTOMOTIVE TURBOCHARGERS

Car manufacturers are nowadays forced to build clean, fuel-efficient vehicles in order to meet stringent global emission standards. This can be achieved by reducing the vehicle weight and the vehicle drag losses, by hybridization or complete electrification of the drive train and –most importantly on short term– by improving the internal combustion engine [1]. Turbochargers, along with direct fuel injection and variable valve timing technology, have enabled automotive manufacturers to downsize their engines significantly [2]. A downsized engine has the benefit of having less friction losses, less heat losses and less mass. Therefore, a downsized turbocharged engine has a lower fuel consumption and thus less emission of CO_2 compared to a similarly powerful non-turbocharged engine [2, 3].

A turbocharger is a mechanical device used to compress air into an internal combustion engine to increase its specific power output. The turbocharger contains a turbine which uses the residual energy in the exhaust gas of the engine to drive a compressor, as depicted in Figure 1.1. The rotation speed of the rotor increases as the exhaust gas flow increases. The compressor, in turn, uses the rotation speed to compress the air going into the combustion engine. By compressing air, its density increases. With more air available in the combustion chamber, more power can be generated during each combustion stroke. Hence, the turbocharger captures a part of the energy in the exhaust gasses, which would otherwise be expelled, in order to increase engine power.

The invention of the turbocharger is accredited to A. Büchi, who registered a patent in 1905 for compressing air into an internal combustion engine using the energy in the exhaust gases [4]. The decades after this invention, turbochargers were mostly used in aircraft applications where a high power-to-weight ratio and high-altitude performance are the dominant objectives for engines [5]. In the 1970's, mass production of turbochargers emerged for automotive applications, initially mostly for sports cars [6]. Subsequently, with the rise of fuel prizes in the 1980's, turbochargers were used in an increasing number of truck diesel engines to improve fuel efficiency and reduce exhaust emissions [5].

1

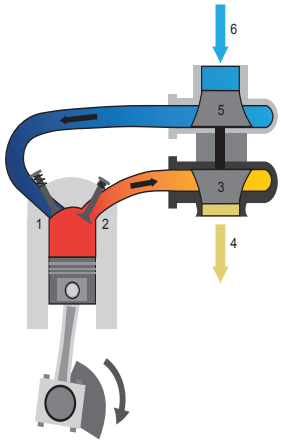

Figure 1.1: Operating principle of a turbocharger: the combustion engine draws in ambient air (1), adds fuel and ignites the mixture. The power from the combustion is sent to the crankshaft as usable shaft power. The exhaust gasses (2) still have an elevated pressure and temperature after leaving the combustion chamber. This energy is scavenged by the turbine (3). The exhaust gasses then leave the system (4) via an exhaust pipe. The scavenged energy of the turbine is used by the compressor (5) to compress fresh ambient air (6) to raise its density before going into the combustion chamber.

A turbocharger consists of four main parts, as can be seen in Figure 1.2. The turbocharger is usually directly mounted to the engine block with an exhaust manifold which is as short as possible to minimize heat losses and flow losses of the exhaust gas [5]. The compressed air from the compressor is often led through an intercooler before entering the combustion chamber so that the temperature after compression is lowered and thus the density of the air is increased.

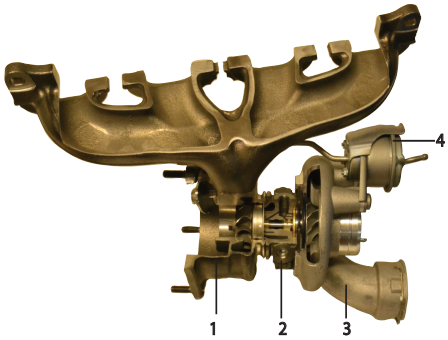

Figure 1.2: A cut-through automotive turbocharger showing (1) the turbine housing, (2) the rotor-bearing system, (3) the compressor housing and (4) the wastegate mechanism to bypass exhaust gasses over the turbine.

Commonly, radial compressor wheels and either radial or mixed radial-axial turbine wheels are used. For specific high performance applications, multiple stages of compression and expansion are applied using a combination of individual turbochargers [7].

Due to the high thermal loads, water cooling in the housings is sometimes applied to protect the bearing system [8].

1.2. TURBOCHARGER ROTOR-BEARING SYSTEMS

The rotor-bearing system lies at the heart of the turbocharger and comprises the main shaft, a compressor wheel, a turbine wheel and the bearing system. The common layout of an automotive turbocharger features a rotor suspended by bearings in the middle and wheels overhung at each side, see Figure 1.3. The turbine wheel is cast from temperature-resistant metal and welded to the shaft by means of friction welding, projection welding or electron beam welding. The compressor wheels are either cast or billet aluminum wheels connected to the shaft by a nut, either using a press fit or a close sliding fit [5]. Balancing is applied to the individual turbine rotor, the individual compressor wheel as well as to the complete rotor assembly.

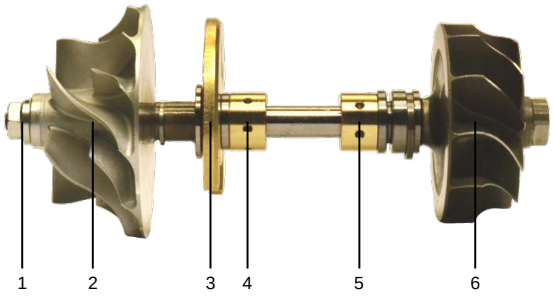

Figure 1.3: A turbocharger rotor with (1) a nut, (2) a compressor wheel, (3) a thrust bearing, (4) and (5) floating ring bearings and (6) a turbine wheel.

The bearing system is cooled and lubricated by engine oil and consists either of ball bearings or fluid film bearings. As depicted in Figure 1.4, three major types of radial bearings exist.

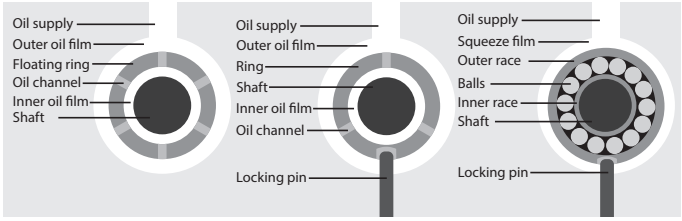

Figure 1.4: Schematic cross-sectional views of the three conventional bearing systems used in automotive turbochargers: the floating ring bearing (left), the semi-floating ring bearing (middle) and the ball bearing (right). The (semi-) floating ring bearing have a separate thrust bearing to support the axial forces coming from the compressor wheel and turbine wheel.

The radial bearings of a turbocharger can be either ball bearings or fluid film bearings. The fluid film bearings can either be semi-floating ring bearings or floating ring

bearing, see Figure 1.4. Ball bearing systems for turbochargers offer specific advantages and disadvantages compared to fluid film bearings. Friction losses are lower in ball bearing systems, leading to faster turbocharger response and higher turbocharger efficiency [9, 10]. More specifically, at normal oil operation temperature, typically a reduction of friction losses of 50% over fluid film bearings is claimed, leading to a 2% reduction of fuel consumption [9, 10]. The major drawbacks of ball bearings, however, are the higher cost price, sensitivity for oil contamination and the decreased amount of damping, which can lead to audible noise for passengers in the vehicle [11, 12]. In order to keep noise levels to an acceptable level, the balancing quality of a ball bearing turbocharger needs to be typically four times better than the balancing quality of a typical floating ring bearing turbocharger [10]. Therefore, ball bearings are nowadays mostly used for high-end and racing applications, while the more cost-effective fluid film bearings are found in the majority of passenger vehicle turbochargers.
Comparing semi-floating ring bearings and full floating ring bearings, the latter typically has lower friction losses due to the reduced shear rates in the fluid film [11, 13]. In addition, the floating ring bearing is relatively inexpensive and has a good reliability in practice [11, 14], explaining why the floating ring bearing is currently the most common type of bearing in automotive turbochargers. Contrary to ball bearings, (semi-) floating ring bearings can not carry any axial load, so a separate thrust bearing has to be included. The thrust bearing carries the loads induced by the gasses flowing through the turbocharger and is generally a tapered-land type or a groove type of thrust bearing [15].

1.3. THE QUALITY DILEMMA IN MASS PRODUCTION

Turbochargers are nowadays no longer considered to be exclusively applicable for sophisticated, high performance engines. Instead, due to the increasingly stringent emission regulations, turbochargers have become ubiquitous for any type of car [16], as reflected in the steady market growth depicted in Figure 1.5.

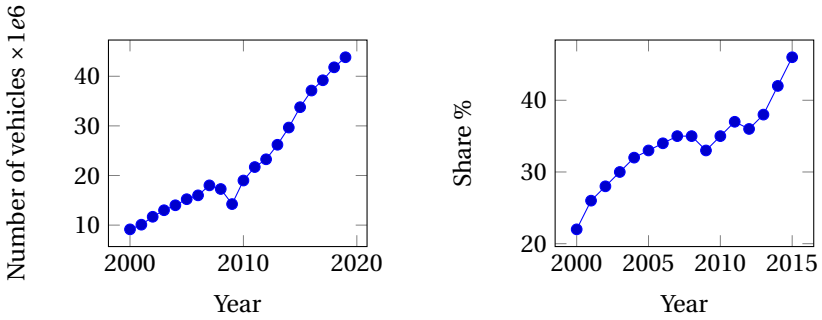

(a) Global annual sales volume of turbocharged passenger vehicles.

(b) Market share of turbocharged passenger vehicles.

Figure 1.5: Market development of automotive turbochargers showing the strong growth of the turbocharger market [16, 17].

This market growth attracted several new turbocharger manufacturers, which all try to increase their market share. Thus, there is fierce competition in developing and supplying turbochargers which fulfill customer demands –including a low price– as good as possible.

For a turbocharger to optimally fulfill the market demands, its core part –the rotor-bearing system– needs to be well-designed. The most important criteria for an automotive turbocharger rotor-bearing systems are [5, 10, 11, 14]:

- Low friction losses, leading to quick rotational transient response and high turbocharger efficiency
- Low audible noise output, preventing an unpleasant experience during driving
- Long lifetime, preventing excessive wear and failures
- Low cost price, for being competitive in offering a consumer good

Automotive turbochargers are often produced in quantities exceeding 100.000 of the same type per year [16]. For these production numbers, the automotive industry relies on controlling production processes rather than controlling the actual performance of each product [18]. In order to meet the abovementioned requirements, accurate[1] manufacturing processes are mandatory to produce turbocharger rotor-bearing systems [10]. Accurate manufacturing processes, however, are inherently expensive due to the high cost of the production equipment and its maintenance as well as due to the potentially high scrap rates in production. Hence, tight tolerances ensure constant quality but also lead to high cost, as schematically illustrated in Figure 1.6. This is the *quality dilemma* that automotive turbocharger manufacturers are facing.

Figure 1.6: The quality dilemma when producing automotive turbochargers.

1.4. RESEARCH GOAL AND RELEVANCE

An alternative method to approach the aforementioned quality dilemma is investigated in this thesis. Instead of tightening all tolerances to achieve constant quality, our goal is to create a rotor-bearing design which can accept imperfections without unacceptable consequences to its quality. Creating a design which is less sensitive to variations, both caused by the production as well as by the operating conditions of the turbocharger in

[1] The term *accurate* implies here that the allowed variations from the nominally specified geometries of the product are small.

use, implies that the *robustness* of the product is increased.

The goal of this research is stated as:

To develop a method for optimizing the mass-produced automotive turbocharger rotor-bearing system, based on a validated model and resulting in a realistic optimal design which takes into account production and environmental variations.

As the method will be based on a validated numerical model, testing cost and time-to-market can be reduced. The resulting new designs should comply optimally with the market demand, while taking into account realistic variations in the manufacturing processes. In addition, manufacturing cost savings can be achieved by relaxing specific tolerances so that less accurate production processes can be allowed and that less parts need to be scrapped during production.

1.5. RESEARCH SCOPE

This study comprises a step-by-step construction of a validated rotor-bearing model, focussing on the radial dynamics of the rotor-bearing system, which can generally be assumed to be independent of the axial and torsional dynamics of the turbocharger rotor [19]. We will investigate the influence of the design of the rotor and the bearings as well as its operating conditions –such as oil supply conditions and unbalance loads– on the rotordynamic response and on the bearing friction losses.
We concentrate our study on plain journal bearings and floating ring bearings; ball bearings and semi-floating ring bearings are not studied here. Furthermore, topics not addressed in this research are the influence of aerodynamic loads on the wheels of the rotor as well as the influence of external vibration from the bearing housing on the system. The rotor layout will be either a Laval rotor or a turbocharger rotor, as depicted in Figure 1.7.
A method for robust optimization of a high-speed rotor-bearing system will be proposed and applied to a Laval rotor-bearing system. Within the timeframe of this study, it was however not feasible to apply robust optimization to a turbocharger rotor-bearing system. Nevertheless, the robust optimzation method developed is generic and can thus be applied to any rotor-bearing system, including turbocharger rotor-bearing systems.

1.6. STRUCTURE OF THE THESIS

The literature review in **Chapter 2** first introduces a selection of fundamental concepts of rotordynamics and hydrodynamics relevant for this study. We will discuss what is already known on the dynamics of turbocharger rotor-bearing systems and identify the open challenges.
The first rotor-bearing modeling effort is presented in **Chapter 3**. In order to exclude many uncertainties in the complex geometry of an automotive turbocharger, simplifications to the rotor-bearing system will be made here: the rotor geometry is simplified and a plain journal bearing is considered instead of floating ring bearings, as depicted in the overview in Figure 1.7. The purpose of this study is to develop a model which can pre-

dict the rotordynamic and friction response of a high-speed rotor on fluid film bearings accurately and computationally efficiently. We will particularly investigate what level of modeling comprehensiveness is needed for the different physical phenomena to obtain acceptable correlation with experimental results.

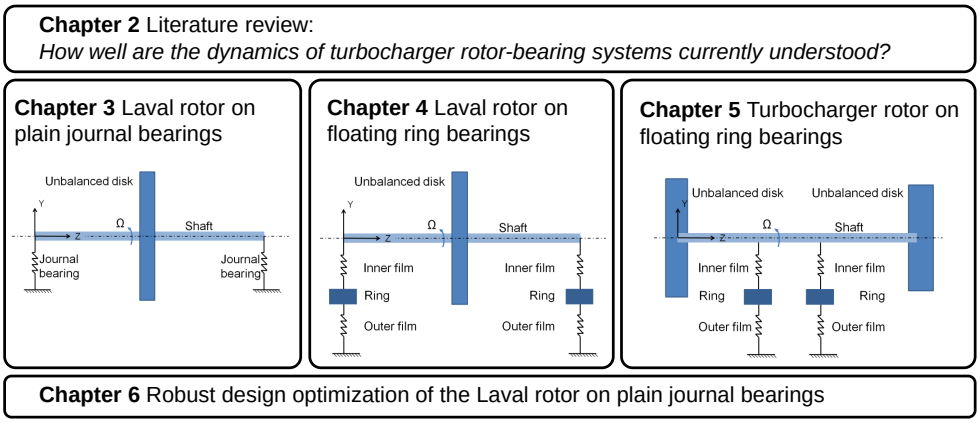

Figure 1.7: Structure of this thesis.

After having gained insight into the relevance of various physical phenomena, the next step is to extend the model of Chapter 3 from plain journal bearings to floating ring bearings, which is done in **Chapter 4**. Furthermore, a high speed Laval rotor test setup is presented and used to evaluate the influence of various operating conditions on the rotordynamic response. The measurement results are compared with simulation results to validate the rotor-bearing model over a range of operating conditions.
The extension from a Laval rotor to a real turbocharger is made in **Chapter 5**. In this Chapter, run-up simulations of a turbocharger rotor-bearing system are compared with measurements. Furthermore, the influence of the unbalance configuration, the oil supply conditions and the thrust bearing on the rotor-bearing dynamics are evaluated.
Once we have presented the well-validated rotor-bearing models, the next step is to perform robust optimization. This will be done in **Chapter 6**, where the Laval rotor with plain journal bearings will be optimized. First, the optimization problem is introduced, followed by a sensitivity study, a deterministic optimization and finally the robust optimization.
Lastly, the concluding **Chapter 7** gives an overview of the developed insights and recommendations for follow-up research.

2

LITERATURE REVIEW: TOWARDS ACCURATE PREDICTION OF THE DYNAMICS OF TURBOCHARGER ROTOR-BEARING SYSTEMS

How well are the dynamics of turbocharger rotor-bearing systems currently understood?

The answer to this question is to be provided by this literature review. First, some background information on rotordynamics and hydrodynamic bearings is provided in Sections 2.1 and 2.2 to get acquainted with the relevant concepts and terminology. Section 2.3 elaborates on the dynamic response of turbocharger rotor-bearing systems, followed by the identification of open research opportunities in Section 2.4.

2.1. DYNAMICS OF ROTATING MACHINERY

The dynamic behavior of rotating machines concentrates on the interaction of the *rotor*, its *bearings* and possibly the *support structure* of the bearings [20, 21]. In scientific studies as well as in engineering practice, mathematical models of rotor-bearing systems are developed to analyze the behavior of existing systems and to improve the behavior of new designs. The analysis of a rotor-bearing system can focus on motion in axial, lateral and torsional direction with respect to the rotor. In most common rotor-bearing systems, these types of motion can be analyzed independently [20]. Only in special cases these motions are coupled, such as under severe shaft rubbing [22] or misaligned gear coupling between rotors [23].

There are some important differences between structural dynamics of non-rotating structures and dynamics of rotating structures. Like any elastic structure, a rotor-bearing

system has natural frequencies of vibration. Unbalance on the rotor exerts a harmonic force on the rotor-bearing system, synchronous to the rotation frequency. When this excitation frequency equals one of the natural frequencies of the rotor-bearing system, a resonance occurs which is termed *critical speed* and is associated with an increased response and a phase shift. The natural frequencies of the rotor-bearing system itself, however, are a function of rotation speed due to the fact that gyroscopic couples act on the rotor. Moreover, the stiffness and damping of many types of bearings change as a function of rotation speed. Hence, in rotordynamics, both the excitation frequency as well as the eigenfrequencies are a function of rotation speed[20].

For a symmetric non-rotating rotor, lateral vibration modes appear in pairs with the same natural frequency. Once rotation is imposed, the pair of natural frequencies splits into two separate values. When vibrating at one of the natural frequencies, the corresponding mode shape follows a *whirl orbit*: an orbital motion of the center of the shaft superposed on the main rotation around the shaft axis, as depicted in Figure 2.1. If the whirl orbit is traversed in the same direction as the rotation of the rotor, it is called a *forward whirl* whereas a *backward whirl* is in opposite direction to the rotation of the rotor, see Figure 2.1.

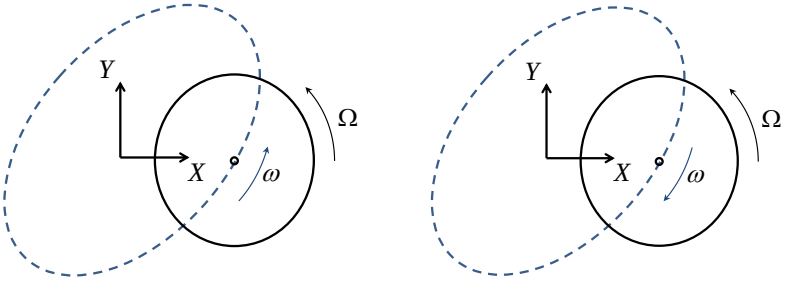

(a) Forward whirl. (b) Backward whirl

Figure 2.1: Whirling of the rotor: the center of the shaft follows the blue orbit at whirl speed ω while rotating around its own center at rotation speed Ω.

Usually, the pair of eigenfrequencies consists of a forward whirling mode which tends to increase in frequency as the rotation speed increases and a backward whirling mode which decreases in frequency with increasing rotation speed. The splitting in forward and backward whirling of a rotor originates from the non-symmetric coupling in the transverse plane induced by gyroscopic effects and by rotationally induced bearing forces. Considering the gyroscopic effects, the way the pair of eigenfrequencies split depends on how much the rotor tilts in a particular mode: the more tilting, particularly tilting of the disks, the more distinct the two eigenfrequencies become [20, 24, 25]. For rotor-bearing systems with isotropic bearing properties, unbalance can only excite forward whirling modes, and so critical speeds will only occur when the rotation speed equals one of the frequencies of the forward whirl modes. However, in case the bearings are anisotropic, unbalance can also excite backward whirling modes [26].

In case the whirl speed equals the rotation speed, $\omega = \Omega$, the whirl is called *synchronous*: the shaft traverses one whirl orbit within the time of one full rotation. Unbalance excitation commonly results in synchronous whirl orbits. When $\omega > \Omega$, the whirl is *supersynchronous* whereas if $\omega < \Omega$ it is *subsynchronous*. The first type of whirl commonly occurs if the rotor is excited multiple times per rotation, for example by gears, electromagnets or compressor blades. The latter type of whirl is often triggered by fluid film bearings.

When the lateral stiffness of the rotor is several orders larger than the bearing stiffness, the rotor may be considered to be *rigid*. In case the lateral stiffness of the rotor is several orders of magnitude smaller than the bearing stiffness, the rotor-bearing system can be assumed to be *rigidly supported* on its bearings. In practice, the lateral stiffness of a turbocharger rotor is often of a similar order of magnitude as the bearing stiffness and hence the rotor-bearing system needs to be treated as a *coupled system* [24], which will now be discussed.

2.1.1. COUPLED ROTOR-BEARING DYNAMICS

The simplest way of including the bearing influence is by representing each bearing as a linear spring-damper element which acts on the rotor. The eigenfrequencies as a function of rotation speed can be calculated and plotted in a *Campbell diagram*, which is a general way to represent the dynamic behavior of the rotor, as shown in Figure 2.2.

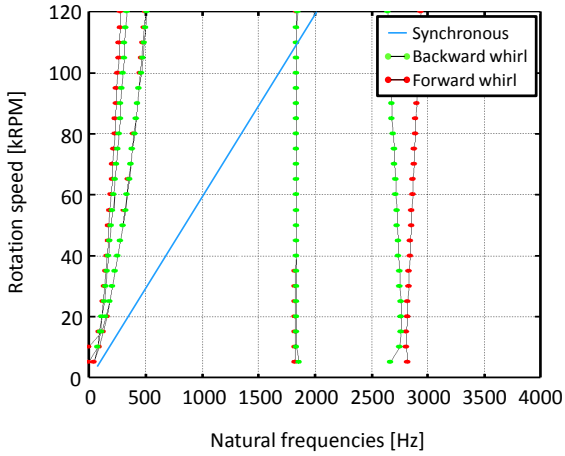

(a) Campbell diagram.

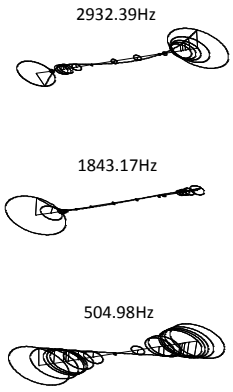

(b) Whirl modes evaluated at 100.000rpm.

Figure 2.2: Example of a Campbell diagram. When the synchronous frequency equals a (forward) whirling mode, resonance occurs, which is termed critical speed. In this case, a critical speed is predicted near Ω = 110kRPM, ω = 1843Hz. Figure 2.2b represents the mode shapes evaluated at a particular speed, in this case 100.000rpm.

Commonly, these calculations are performed on a finite element basis as it accommodates the coupled analysis of flexible rotors and bearing forces [20, 21, 25, 27]. Simple rotors can be modeled using beam elements and rigid disk elements. More complex rotors, for example when the blades of a wheel are flexible, need more detailed finite element models, for example based on volume elements. Model order reduction methods and substructuring techniques are often applied to reduce the computational effort of these geometrically complex rotors [28, 29].

2.1.2. FLUID-STRUCTURE INTERACTION OF ROTORS SUPPORTED BY HYDRODYNAMIC BEARINGS

Hydrodynamic bearings (also called *fluid film bearings*) are applied in high load and high rotation speed applications because of their high load capacity, low cost and low wear rates [20]. Hydrodynamic bearings can carry a load by the *hydrodynamic lift* principle: pressure builds up when a viscous fluid is being dragged into a converging section, as shown in Figure 2.3a. For a journal bearing, the dimensionless ratio of the instantaneous shaft displacement to the total bearing clearance is called the *eccentricity ratio*. In case the load on the rotor is static, the rotor will generally find an equilibrium position. The position of this equilibrium depends on the load: for light loads, the rotor operates near the center of the bearing, whereas for heavy loads, it operates near the walls of the bearings so that the eccentricity ratio approaches one [30].

Early fluid film bearings have been designed to carry static loads. However, with the increase of rotation speed of machines in the 20th century, dynamic loading of journal bearings increased [31, 32]. When a rotating unbalance force acts on the rotor, the rotor follows a circular orbit synchronous to the speed of rotation, as shown in Figure 2.3b.

Particularly for bearings which carry a relatively light static load, once the rotation speed exceeds a threshold speed, the system may become unstable: the rotor no longer finds a stable equilibrium but will instead start orbiting in a *limit cycle*. This phenomenon is called *oil whirl* [30, 33, 34]. For a plain journal bearing, the oil whirl typically starts at a rotation speed between one to two times the critical speed and is a forward whirl. The frequency of this whirl is approximately half the rotation speed, which can be explained on the basis of conservation of mass in the bearing where the average oil velocity is slightly lower than half the rotation speed [24, 35], as shown in Figure 2.3c.

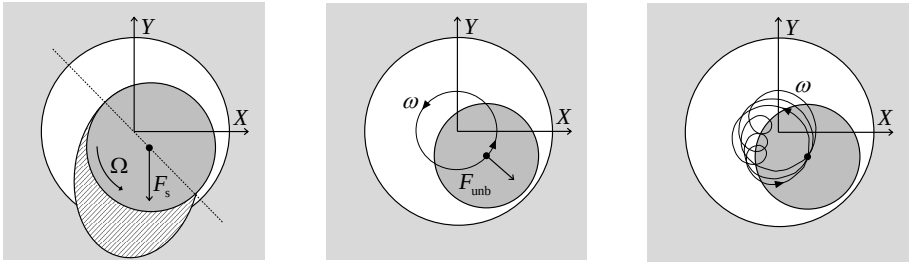

(a) Principle of hydrodynamic lubrication of a shaft in an oil film carrying a static load while rotating at speed Ω. The marked area represents a pressure buildup.

(b) Synchronous response of a shaft with unbalance load: whirling speed $\omega = \Omega$.

(c) Combined synchronous and subsynchronous response under oil whirl conditions: ω is composed of harmonics Ω and ~0.5Ω.

Figure 2.3: Schematic depiction of a hydrodynamic bearing under static load, under a rotating unbalance load and in oil whirl condition.

As the oil whirl has a frequency of approximately half the rotation speed, it can be understood that when the rotation speed approaches twice the first critical speed, transfer of energy from the oil whirl to the first rotor-bearing mode can occur: the frequency of oil whirl coincides with the frequency of the first rotor-bearing mode. This phenomenon is termed *oil whip* and can result in large amplitude oscillations which can be catastrophic for machines using hydrodynamic bearings [36, 37]. Contrary to oil whirl, oil whip oscillations will typically occur at a constant frequency: the oil whip *locks* into the eigenfrequency of the rotor-bearing system and do no longer increase in frequency by an increase in rotation speed. Figure 2.4a shows these phenomena in a *waterfall plot*.

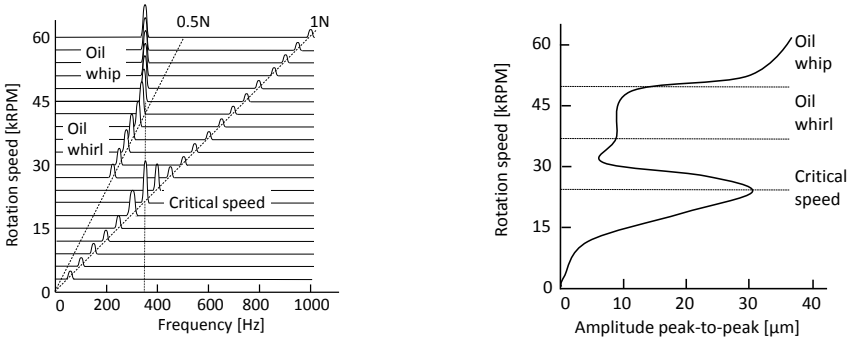

(a) Waterfall plot showing critical speed, oil whirl and oil whip. 1N represents the first order (synchronous response). Image based on [38]

(b) Data of figure 2.4a as a 2D plot. Note that 60krpm equals 1000Hz.

Figure 2.4: Illustration of the response of a typical symmetric Laval rotor supported by hydrodynamic bearings, as will be treated in Section 3. A critical speed, oil whirl and oil whip can be distinguished.

2.1.3. STABILITY EVALUATION OF ROTORS ON HYDRODYNAMIC BEARINGS

Oil whirl and oil whip are a risk for the safe and reliable operation of a machine and therefore extensive research has been performed on the stability of rotors suspended by hydrodynamic bearings. Newkirk and Taylor [39] are regarded to be the first researchers to report on fluid-induced vibrations in a rotor-bearing system in 1925. The first studies concentrated solely on the fluid film instability; hence the transition from oil whirl to oil whip, which involves interaction between the bearing forces and the rotor flexibility, was not yet recognized [36]. It later became clear that the bearing and the rotor needed to be analyzed simultaneously [36, 40].

Rotor-bearing modeling presented in literature consider either *linear* or *non-linear* models. For the linear approach, the bearing stiffness and damping terms are obtained by assuming a static equilibrium position and applying small perturbations in displacement and velocity, respectively. This concept was introduced by Stodola [41] and Hummel [42] already in the 1920's. Initially, this method was considered to be inappropriate as the bearing stiffness and damping of a fluid film bearing are highly non-linear [43]. It was not until 1962 that Lund [43, 44] showed that linearization can actually yield reasonably accurate predictions. Lund evaluated the stability of the system by calculating the eigenvalues of the system, which gives the onset speed of instability from which oil whirl might be expected.

Besides the modal approach, other methods have been used as well to study the dynamic behavior of the linearized rotor-bearing system. Lund and Saibel [45] presented an early study in using path-following methods in a technique called method of averaging. This technique determines instability by means of the linearized bearing dynamic coefficients. From the unstable point, the method assumes an elliptical orbit and searches numerically for an orbit with zero average velocity. Other techniques, such as the method of multiple scales [46, 47] and Hopf bifurcation theory [48, 49] have been applied to predict the stability limits of a rotor-bearing system. Gardner [50] compared these three methods with numerical time integration and found that their predictions are only valid for small amplitudes and for small deviations from the stable equilibrium. The use of linearized bearing coefficients can nowadays still be acceptable under the condition of small displacements from an equilibrium position. The resulting predictions, however, are often quite under-predicting the onset speed of instability [51]. Non-linear models are therefore more suitable for evaluation of the dynamics of rotors on hydrodynamic bearings in the regime far from static equilibrium [24, 33].

Mainly two types of analysis of *non-linear models* are used to evaluate the stability of a rotor on hydrodynamic bearings: *periodic solution techniques* and *numerical time integration methods* [34, 52]. Periodic solution techniques determine the oscillations of the rotor-bearing system as a function of rotation speed assuming a periodic solution. Different types of techniques are employed to this end: the harmonic balance method [53], the collocation method [54] or the shooting method [55, 56]. After having determined an equilibrium solution, its stability is subsequently evaluated, which can be stable, unstable or describing a limit cycle oscillation. As such, these methods can determine the

nature of the dynamics of the system in terms of stability. Stability evaluations of the non-linear model are done by evaluating the Floquet multipliers [57] or the Lyapunov exponents [58]. Furthermore, these analyses can demonstrate that the rotor can *jump* from a stable equilibrium position to a (large) whirl orbit once the onset speed of instability is exceeded [34].

The onset speed of oil whirl and the subsequent sub-synchronous whirl orbit depend on many factors. First of all, the rotor-bearing design plays an important role [34]. Furthermore, the bearing operating conditions play an important role. The influence of these operating conditions can be different from one rotor-bearing design to another, which could explain many contradictory findings in literature:

- *Unbalance* can increase the onset speed of instability and can reduce the whirl orbit amplitudes [24, 57]. Experiments of Deepak and Noah [59], on the other hand, show that unbalance can reduce the onset speed of instability.
- Another contradiction relates to the role of the *oil temperature*. Newkirk [32, 60] found that warmer oil results in a greater range of stable operation whereas Pinkus [61] reported that cooler oil increases the stable range.
- Also the role of *cavitation* on the stability of the rotor-bearing system is ambiguous. Someya [62] reports that the formation of air bubbles by cavitation can reduce the stability of a bearing, although it is generally acknowledged that cavitation is essential for the stable operation of hydrodynamic bearings [46, 63].
- One more inconsistency relates to the influence of the *oil feed pressure* on the onset speed of instability: Capone [64] observed a reduction in onset speed of instability at an increase of oil supply pressure while in the study of Guo [65] and also in our experiments (see Section 3.4.7), an increase of supply pressure increased the onset speed of instability.

These inconsistencies illustrate that the response of a rotor supported by hydrodynamic bearings differs from one design to another. Therefore, models need to be comprehensive to include all relevant physical aspects and their mutual influence. The examples of rotor-bearing systems studied in literature by periodic solution techniques [58, 66–68] are all restricted to simple rotor-bearing geometries, due to the fact that analytical descriptions were used to describe the rotor-bearing system. These descriptions do not capture the multiphysical character of the rotor-bearing system including detailed geometrical features. Thus, the examples of periodic solution techniques shown in literature are computationally efficient and provide a fundamental understanding of the dynamic response which can be expected, they are not useful to accurately predict the rotor-bearing behavior of more complex systems. Alternatively, the use of periodic solution techniques combined with a more detailed system description may be an interesting alternative, which will not be evaluated in this study though.

When the aim is to accurately model the dynamic response of the rotor-bearing system including all relevant physical aspects, the current trend is to use *multiphysical time-transient models* [69]. Such models simultaneously evaluate the rotordynamics

and the fluid film dynamics in a coupled fashion for each time step. The increase of computational power in the last decades has enabled researchers to include more and more details in their models [40]. Industrial applications for these multiphysical time-transient models of rotor systems suspended by hydrodynamic bearings include combustion engine crankshaft bearings [70], camshafts [71], compressors [72], turbines [73] and turbochargers [11].

2.2. HYDRODYNAMIC LUBRICATION

The previous section has illustrated the role of hydrodynamic bearings: as a machine element, it supports the rotor by providing stiffness and damping but it can also cause self-excited oscillations. This section will elaborate on the hydrodynamic pressure buildup in the bearing.

2.2.1. FLOW AND PRESSURE DESCRIPTIONS FOR HYDRODYNAMIC BEARINGS

The first to report on the pressure buildup in hydrodynamic bearings was Towers in 1883 [35]. During his research on friction in lubricated bearings used for railway applications, he incidentally found that pressure is generated in fluid film bearings [40]. These experimental observations motivated Reynolds to derive a theoretical description for the fluid flow in a thin film. Reynolds' differential equation, commonly referred to as *the Reynolds equation*, may be regarded as a simplification of the Navier-Stokes equations [74] and is to date the basis of most hydrodynamic lubrication models due to its fair balance between accuracy and computational efficiency and robustness.

The Reynolds equation in its base form is a non-homogeneous partial differential equation with variable coefficients describing fluid flow in two directions. In case of a journal bearing, these are the axial and circumferential directions. Exact analytical solutions for the Reynolds equation describing the fluid flow in a journal bearing in both directions are unknown. Instead, four alternative approaches exist in solving the Reynolds equation:

1. Under the assumption that the bearing is infinitely long, the flow in axial direction may be neglected. This leads to the *long bearing solution* first published by Sommerfeld in 1904 [75]. The long bearing solution is regarded to be valid for bearing designs where the bearing length-to-diameter ratio L/D>2 [76], which are rarely used in practice due to the high risk of misalignment problems and sealing difficulties [77].

2. Under the assumption that the bearing is infinitely short, the pressure-driven component of the flow in circumferential direction may be neglected. This leads to the *short bearing solution*, of which the idea was proposed by Michell in 1929 and finally solved by Ocvirk in 1952 [78]. The short bearing solution is regarded to be valid for bearing designs with L/D<0.5 and eccentricities up to 0.75 times the nominal clearance [76].

3. An *approximate analytical solution* can be derived to describe the flow in the bearing in both directions, as first proposed by Cameron in 1949 [79] and more recently

by other researchers [80–83].

4. A *numerical approximate* can be found by solving the Reynolds equation over the fluid domain by a discretization scheme like the finite element method, finite volume method or finite difference method [27].

The first three approaches assume the oil film to be isoviscous and are unable to include details like the presence of the feed channel, shaft tilting, elastic deformations and local cavitation. Therefore, the accuracy of the first three approaches is limited and hence the fourth option has become the most popular method in lubrication problems the last four decades, facilitated by the widespread availabiltiy of computing power [40].

Alternatively, *CFD-methods* which solve the more elaborate Navier-Stokes equations in three directions may be used to predict the pressure distribution in a hydrodynamic bearing, as shown for example by Guo [65] and Gertzos [84]. This method is generally computationally inefficient for fluid bearing problems as it requires a large number of elements in order to keep a reasonable element aspect ratio over the relatively thin film domain. Therefore, numerically solving the Reynolds equation is currently the preferred approach for many lubrication problems [27], especially for time-transient calculations where the pressure distribution needs to be predicted for numerous time steps.

2.2.2. CAVITATION IN HYDRODYNAMIC BEARINGS

Hydrodynamic bearings work on the principle of creating hydrodynamic pressure by forcing fluid into a converging section, as shown in Figure 2.3. Conversely, when the fluid traverses a diverging section, a hydrodynamic pressure decrease will occur. Fluids, however, can only withstand a very limited amount of tensile stress and therefore *cavitation* will occur if the pressure decays to the cavitation pressure [85].

Cavitation may occur as *vapour cavitation* as well as *gaseous cavitation* [86]. Vapour cavitation occurs when the pressure in the fluid is under the vapour pressure, resulting in a thermodynamic phase transformation. The sudden implosion of vapour cavitation at the trailing edge of the cavitation zone typically causes pitting erosion in fluid film bearings [87]. Gaseous cavitation involves the release of gas which is dissolved in the fluid if the pressure is below the saturation pressure and is more gradual and stable than vaporous cavitation [85].

In Sommerfeld's long bearing solution from 1904, the effect of cavitation was not considered and hence the predicted pressure distribution contained a positive and a negative peak, equal in magnitude. In 1914, Gümbel was the first to take cavitation in a journal bearing into account and proposed to set the pressure at the diverging section of the bearing to zero instead, which is called the *Half-Sommerfeld solution*, see Figure 2.5. Swift and Stieber later proposed to impose continuity of pressure near the rupture boundaries, which is a physically more realistic approach. This boundary condition was already considered by Reynolds, hence it is often referred to as the *Reynolds condition* [86, 88].

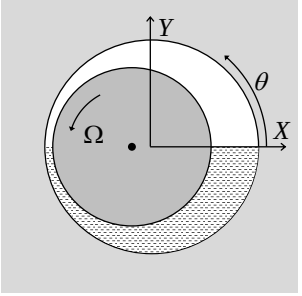

(a) A shaft running in eccentric position. The dotted area represents the cavitated area.

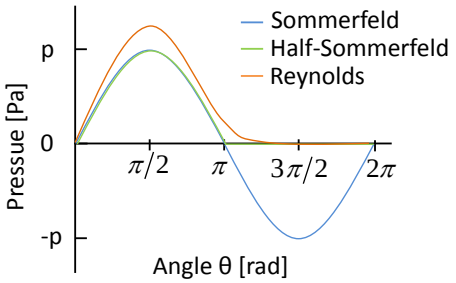

(b) Solutions of the Reynolds equation for Figure 2.5a depending on the cavitation conditions.

Figure 2.5: Pressure fields for the Sommerfeld, half-Sommerfeld and Reynolds boundary conditions.

Although being convenient for analytical methods, none of the abovementioned approaches yields *conservation of mass* through the cavitated volume [89]. Especially in conjunction with thermal analysis of the fluid film, conservation of mass is required for accurate predictions [88, 90]. Therefore, complementary cavitation descriptions have been developed. One of the first mass-conservative cavitation conditions was proposed by Jacobson and Floberg in 1957 [91], commonly referred to as the *JFO conditions* [86, 88]. In this method, the flow through the cavitated zone is assumed to be purely driven by Couette flow in the form of streamers over a fraction of the bearing length. The remaining fraction of the cavitated area is assumed to be filled with gas. These conditions can be applied in iterative numerical solvers, such as the early models based on Christopherson [92]. More recently, Bayada [93] compared several finite element formulations based on the JFO conditions. Most of the formulations herein constitute a complimentary condition: in the cavitated regions, the mass fraction distribution is unknown, and the pressure distribution is known, whereas in the full film region, the pressure distribution is unknown, and the mass fraction distribution is known.

The assumption of *streamer cavitation* was questioned by Heshmat in 1991 [94] who observed in his experiments that a part of the lubricant traverses the cavitated zone as a layer of liquid adhered to the rotating shaft. Mistry [91] later showed that the contribution of this adhered layer to the pressure distribution can be neglected for high-speed journal bearings and high eccentricties.

Although the use of JFO cavitation conditions yield more realistic results than Half-Sommerfeld or Reynolds conditions [77], several difficulties have been reported in its implementation in numerical methods, especially under transient conditions [95, 96]. Therefore, Elrod [95] proposed a variable substitution in the Reynolds equation, which was easier to implement in numerical methods. The cavitation model influences the output of rotor-bearing models. Brewe [96] applied Elrod's methods and found good agreement between his predictions and experimental results of Jakobson of a dynamically loaded hydrodynamic bearing. Nitzschke [97] also studied Elrod's cavitation model

on a flexible rotor running on fluid film bearings. He applied both Elrod's cavitation conditions as well as Gümbel cavitation conditions and found significant differences. The bearing stiffness was considered to be underestimated by the Gümbel-based model which resulted in lower critical speed predictions. Hence, mass-conservative cavitation algorithms, such as the method proposed by Elrod, seem to give more realistic predictions. Improvements on Elrod's method have recently been suggested by several authors [88, 98].

2.2.3. FLUID RHEOLOGY

Already in 1883, Petrov discovered that the *viscosity* of a fluid, and not its density as was previously considered, was the physical property responsible for drag and hydrodynamic lift. For many lubricants, viscosity depends on temperature, pressure and shear rate. Therefore, appropriate rheological relations are crucial to describe the viscosity as a function of the aforementioned fluid properties [51, 99].

Reynolds was one of the first to propose a *temperature-viscosity* relation in 1886 [100]. Although being relatively simple, it is considered to be accurate only for a very limited temperature range [51]. Vogel stated another temperature-viscosity relation in 1921 which is considered to be a simple, yet accurate, description for oil on a moderate temperature range [100]. A different relation was later proposed by Walther, which also forms the basis of the current American Society for Testing and Materials (ASTM) charts which are often used in engineering.

For applications where the pressures become extreme, for example in case of lubricated gear contacts, the *pressure-dependency* of the viscosity is often more important than its temperature-dependency [101]. At extreme contact pressures, the lubricant might even behave as a solid [51]. Many different empirical pressure-viscosity relations exist [102]. An often used description for the pressure-viscosity relation is formulated by Barus, which is considered to be accurate for pressures up to 0.5GPa [103].

In case high shear rates are encountered in the fluid, the viscosity might become *non-Newtonian*. Particularly in multigrade engine oils, polymer additive chains align at shear rates typically over $10^3 s^{-1}$, causing the viscosity to decrease [51]. This can result in a significant decrease of bearing carrying capacity and friction losses [104]. Cross developed a shear rate-viscosity relation, which was considered by Wright [105] to be an accurate description for hydrodynamic bearings using multigrade oil. Taylor [106] combined the Cross equation with the short bearing formulation and to analyze the film thickness of automotive crankshaft bearings. Many other shear rate-viscosity relations have been proposed [107], which mostly claim to be more accurate than the Cross equation. The difficulty in applying most of these novel descriptions is that the specific parameters for an oil type are not commonly available in literature and vary from manufacturer to manufacturer [108].

All of the previous descriptions focused on the viscosity as a function of one of the

fluid properties. In practical lubrication problems, the temperature, shear rate and pressure will all vary. Therefore, *combined viscosity descriptions* have been developed. For example, Sander [99, 109], proposed a practical fluid rheology model for engine oil and validated his viscosity model by journal bearing friction measurements. His rheology model conveniently combines the Vogel equation, the Barus equation and the Cross equation.

2.2.4. THERMAL ASPECTS OF HYDRODYNAMIC BEARINGS

Accurate bearing performance predictions require an accurate *thermal model*: the viscosity of oil can change by more than 80% by a temperature change of 25 degrees [51]. Moreover, bearing clearances can change due to thermal expansion and most bearing materials such as babbitts can only withstand a limited temperature increase. In his lubricant experiments in 1886, Reynolds already noted that as the load on the bearing was increased, the lubricant temperature also increased. In 1933, Kingsbury found significant discrepancies between his theoretical predictions and his measurements of bearing load capacity, which he could trace back to thermal effects [77].

The temperature of the lubricant changes under the influence of viscous dissipation, heat input from and to the adjacent surfaces, as well as due to mixing of lubricant at the inlet [40]. It is therefore a complex problem for which initially isoviscous *adiabatic approaches* have been developed, where the temperature field in the bearing is assumed to be uniform. The isoviscous method was pioneered by Swift in 1937 [110] and is based on a global energy balance over the bearing fluid domain. This approach yields reasonable results and is computationally efficient. It is therefore often used for engineering approximations [77]. For high bearing loads or high bearing speeds, the isoviscous approach may become inaccurate, however, as the local temperature gradients become significant [111].

Models which include the temperature variation in circumferential direction [112] resulted in improved bearing performance predictions. Dowson [113] proposed the use of the generalized Reynolds equation where the local variation of viscosity and density are considered both in plane of the film and over the thickness of the film. The generalized Reynolds equation and a distributed energy differential equation are simultaneously solved to predict the distributed thermal distribution, which nowadays is generally referred to as *thermo-hydrodynamic analysis*.

Dowson [114] and Ferron [77] experimentally observed that the temperature distribution in axial direction can often be neglected. Therefore, many thermodynamic analyses have been evaluated on the midplane of the bearing [115–118]. In case shaft tilting is involved, however, the temperature distribution in axial direction may not simply be allowed to be homogeneous [111, 119].

Another simplification which has also often been adopted is the assumption of negligible temperature gradients across the film thickness, which might yield inaccurate predictions [120]. Therefore, various approaches exist for taking into account the tempera-

ture distribution across the film temperature. Typically, they can be regarded as averaging methods and polynomial approximation methods [121]. Averaging methods, as used by Lee and Kim [122], use the averaged viscosity and density from the energy equation in the Generalized Reynolds equation. Polynomial approximations [123] assume the fluid temperature, density and viscosity distribution to follow a polynomial form for which the coefficients need to be determined.

Lubricant feed channels have a significant influence on the temperature distribution in a hydrodynamic bearing [77]. The pressure in the oil feed is usually maintained at a fixed supply pressure, preventing cavitation to occur near the inlet region. In the feed channel, fresh oil flows into the bearing and some backflow occurs: oil leaves the bearing and re-enters the feed channel. This latter phenomenon causes *mixing*: (usually hot) oil from the bearing mixes with (usually cold) oil in the feed channel. Gethin and El Deihi [124] managed to get a good correspondence between their temperature predictions and their measurements by using a heat balance over the inlet channel. Their flow predicitions, however, did not correspond with their measurements due to the lack of a proper treatment of conservation of mass near the inlet region [77]. Later studies on the effect of the lubricant feed channels, such as those of Dowson [125], Vijayaraghavan [126] and de Brito [77] feature mass-conservative cavitation conditions, which are proven to give more accurate predictions regarding the performance of hydrodynamic bearings.

As the oil film is in direct contact with the shaft and the bearing housing, it is important to obtain accurate *temperature estimates of these walls*. The interest of researchers in the field of lubrication, however, is often limited to the fluid film domain. Therefore, it appears that often overly simplified models have been used to predict the temperature of the walls adjacent to the fluid film bearing. Early models used adiabatic boundary conditions on the bearing surfaces [127], which commonly leads to an overestimation of the film temperature as the heat transfer to the bearing housing and the shaft is assumed to be zero. Another, more common approach uses the assumption of an adiabatic bearing housing and an isothermal shaft [116, 128] which is claimed to give a conservative upper value of bearing liner temperatures for selecting the design of plain journal bearings. Dowson [114] carried out measurements on the shaft and bearing housing temperatures and concluded that the radial heat fluxes in his setup could not be neglected. The same conclusion was also drawn by Fitzgerald [129]: the assumption of adiabatic walls can lead to significant errors in the thermal predictions. Therefore, the transport of heat to both the shaft and the bearing housing have been included in many subsequent studies [130].

2.3. TURBOCHARGER ROTOR-BEARING SYSTEMS

The previous sections presented background information on *rotordynamics* and *hydrodynamics*. In this section, an overview of the history of research on *turbocharger rotor-bearing systems* is presented, followed by an evaluation of recent studies on this topic. Two periods of research are described separately. First, the period 1900-2000 is discussed, where the floating ring bearing was initially conceived as a means of *reducing friction and increasing the threshold speed of instability*. Later, researchers recognized

that floating ring bearings can safely operate in a speed range far beyond the onset speed of oil whirl. In the period 2000-present, the focus has turned to *accurate modeling the dynamics of turbocharger rotor-bearing systems*, where specifically the thermal modeling plays an important role.

2.3.1. EARLY MODELING AND ANALYSIS OF FLOATING RING BEARINGS: 1900-2000

As mentioned in Section 1.2, many automotive turbochargers nowadays use floating ring bearings to support the rotor. Figure 2.6 presents a schematic cross-sectional view of a floating ring bearing. The origin of floating ring bearings can be traced back to the beginning of the 20th century, when floating ring bearings were used in steam turbines to enable stable operation at high rotation speeds [131, 132]. Another application of the FRB was reported in 1922, when Bristol Aeroplane Company adopted the FRB concept for crankshaft bearings to overcome thermal issues which occurred due to increasing bearing loads in aero piston engines [131]. The exact date of invention of the FRB is unknown, but probably dates early in the 20th century. One of the first patents for a floating ring bearing was filed in 1941 in Germany [133]. However, earlier patents already mention floating ring bearings [134].

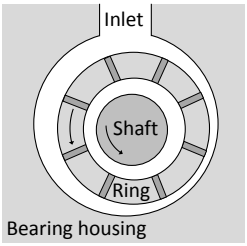

Figure 2.6: Schematic representation of a floating ring bearing. Oil flows from the inlet to the inner and outer oil films and can exit the bearing in axial direction. The ring can freely translate and rotate within its clearance.

One of the first studies dedicated to floating ring bearings was published in 1947 by Shaw and Nusdorfer [132]. They motivated the use of floating ring bearings as an enabler for stable operation of turbines and compressors at high rotation speeds. They reasoned that the flow through two film clearances can be larger than through a single one -within the limits of stability- and consequently the FRB can withstand a higher load without overheating. A model of a FRB under constant unidirectional load was created based on the long bearing theory and steady state isoviscous conditions. The model was used to derive analytical functions for the ring speed ratio, the oil flow, oil temperature and the friction losses. The analytical results were then compared with experimental results and calculated values of a plain journal bearing which had a clearance equal to the inner FRB clearance. As the model was isoviscous, the predicted ring speed ratio was assumed to be invariant of shaft rotation speed. Measurements showed this assumption to be invalid: the ring speed ratio was overpredicted. The attitude angle was assumed to be constantly

90°, which approximately holds for small eccentricties only. The bush was observed to whirl during the measurements, especially at light bearing loads, but the model assumed static equilibrium conditions.

Most importantly, it was found that FRBs offer reduced friction losses when compared to similar plain journal bearings. This observation was already published in 1935 by Orloff [135], who reasoned that if the velocity for each oil film is only half the shaft velocity, then the friction loss per oil film would be only one fourth of the friction losses of a plain journal bearing. As a result, the friction losses of the floating ring bearing would be half that of a plain journal bearing: two times one fourth. Orloff noted that this comes at the cost of a reduced carrying capacity, so floating ring bearings would be particularly interesting in high speed, low load applications.

The lower friction of the floating ring bearing compared to a plain journal bearing was later confirmed by Kettleborough [136] and Tatara [137]. Moreover, Tatara and later also Tanaka [138] found that the FRB could operate in a stable manner above the threshold speed of linear stability and claimed that the increased stability of a FRB is an even greater advantage over a plain journal bearing than the advantage of friction reduction. Tondl [139] compared experimental results of various types of hydrodynamic bearings and observed that floating ring bearings have the highest onset speed of instability. The good stability properties of floating ring bearings for high-speed rotors were also confirmed by Dworski [140].

An early attempt to describe the dynamic operation of the FRB was made by Orcutt and Ng [141]. Their steady state FRB modeling results corresponded reasonably well with their measurement results in terms of Sommerfeld number, attitude angle, oil flow and friction losses. For the dynamic analysis, Orcutt and Ng used local linearization to find the bearing stiffness and damping terms. The effective dynamic coefficients, however, were calculated based on synchronous vibration, which is generally invalid for oil whirl [142]. In their experiments, Orcutt and Ng [141] found that the FRB shows stable whirling operation above the predicted threshold value of stability and found that it is more meaningful to control the amplitude of the whirl instead of only predicting its onset rotation speed. Hence, Orcutt and Ng doubted the relevance of linear stability analysis for FRBs.

Tanaka [138] studied the stability of a flexible Laval rotor supported by FRBs. Using a linearized stability analysis based on an isoviscous model, he failed to produce accurate predictions for the threshold speed of stability for lightly loaded bearings. Moreover, the time integration used to predict the whirling behavior only showed part of the start of a whirl, and not a stable limit cycle. Eventually, Li and Rohde [142] in 1981 proved the existence of stable limit cycles by numerical time integration of the floating ring bearing dynamics, which explained the ability of the floating ring bearing to operate at high rotation speeds. Subsequent research, for example [143–146], has consequently shown that the subsynchronous whirl reaches a limit cycle that allows continuous operation.

All floating ring bearing models up to 1983 assumed isothermal conditions. Trippett and Li [147] noted that the isoviscous models of their predecessors [132, 140] yielded an overprediction of the ring speed ratio, and therefore developed a simple thermal model using adiabatic boundary conditions for the shaft and the bearing housing and based on a half-Sommerfeld assumption. Although the adiabatic assumptions were considered to be a crude assumption, the ring speed ratio predictions showed reasonable correspondence with the measurement results. Clarke [148] extended his thermal model to include heat transfer to the shaft and the bearing housing by conduction. Clarke solved the Reynolds equation and the energy equation using the finite element method and considered conservation of mass over the floating ring bearing in his model but limited his analysis to steady state conditions.

2.3.2. OVERVIEW OF ROTOR-BEARING MODELS: 2000-PRESENT

To summarize the previous section: at the beginning of the 21st century, it was clear that rotors using floating ring bearings have relatively low friction losses and can traverse multiple critical speeds and can have several forms of sub-synchronous limit cycle oscillations without becoming fatally unstable. Typically, these sub-synchronous whirl orbits have a frequency of either approximately half the ring speed or half the shaft speed plus the ring speed[143], and they can even co-exist simultaneously, see Figure 2.7 [144].

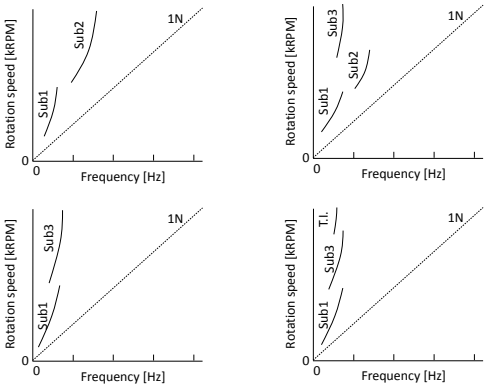

Figure 2.7: Waterfall plots showing several typical responses (shaft displacement) of turbocharger rotor-bearing systems. *1N* is the synchronous response, *sub* denotes a sub-synchronous response and *T.I.* is a potentially catastrophic *total instability*. Image based on Schweizer [144].

This behavior was understood from experiments and could be *qualitatively* well predicted using non-linear rotor-bearing models [143, 149]. Since the beginning of this century, most of the models have been focused on improving the *quantitative* correlation between measurement data and numerical predictions.

Most modeling efforts since the year 2000 aim to replace costly experimental tests by numerical evaluation of new rotor-bearing designs and are therefore performed with financial support of turbocharger manufacturers. Improper designs can lead to turbocharger noise [150, 151], and possibly even to catastrophic damage due to oil coking

deposit buildup [152] and due to large shaft oscillations caused by whip [153].

A major effort in modeling the dynamic response of a turbocharger rotor-bearing system was delivered by the research group of San Andres [143, 146, 154–156]. Holt [143] published the initial study which included a flexible turbocharger rotor model based on Timoshenko beams and disks, a finite length bearing model and a lumped thermal model, based on the model of San Andres [154]. A non-Newtonian viscosity function was incorporated and the change of clearances as a function of temperature was included. A description of the cavitation model is not given; most likely Gümbel boundary conditions have been used. The effect of the oil inlet channel was modeled as a constant force on the rotor and the presence of oil connecting channels has been ignored: both the inner and outer oil films were always assumed to be supplied with sufficient oil by a circumferential oil groove midway the length of the bearing.

The simplification of the oil supply channel and the absence of coupling between the inner and the outer channel have probably caused some discrepancies observed in the response of the rotor-bearing system to changes in the oil feed pressure [157]. Subsequently, an attempt was made by San Andres [146] to improve predictions by imposing the experimentally determined ring speeds and an unbalance estimation based on the work of Rivadeneira [155] in his run-up simulations. Another improvement in their FRB model was that the difference in inner and outer supply pressures due to a centrifugal pressure difference was taken into account. However, during their experiments, the rings failed to rotate at speeds over 50krpm, causing large amplitude half-speed whirl. The most recent update of the rotor-bearing model of the group of San Andres involves a distributed thermal description [152] to replace the previous lumped thermal model [154]. The new thermal model takes the oil connecting channels in the FRB into account as a pressure constraint. Results under steady state conditions have been presented. However, it remains unclear whether the thermal model was operated in conjunction with the previously presented time-transient model [146]. Furthermore, only results of a semi-floating ring bearing are presented and there is no experimental validation of the results. In a later publication [12], the distributed thermal model seems not to be employed.

Since the year 2000, several other research groups have also developed turbocharger rotor-bearing models. These models are all based on coupling a Reynolds-based finite bearing model to a discretized beam model which is solved in time [144, 153, 158–164]. These models are validated by measurements on a turbocharger which is driven by hot air. It is surprising to see that almost all of these authors claim a good correlation between their predictions and their measurement results, as the modeling comprehensiveness between these studies vary greatly. Moreover, the unbalance distribution of the test turbocharger is not known beforehand. Tian [164] shows that the rotordynamic response of a turbocharger depends not only on the amount of unbalance; it depends also on the phase of the unbalance vector on the compressor side with respect to the unbalance vector on the turbine side. Depending on the unbalance configuration, the subsynchronous response can change significantly, as can be observed in Figure 2.8.

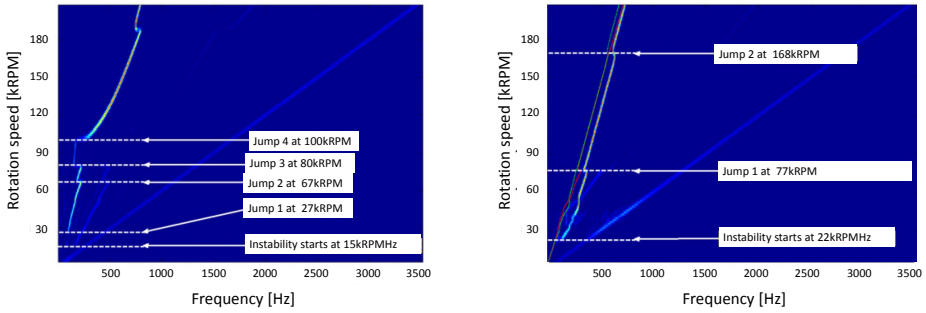

(a) Unbalance vectors in counterphase.

(b) Unbalance vectors in phase.

Figure 2.8: Waterfall plots showing the different responses for a turbocharger rotor with unbalance vectors on the compressor wheel and the turbine wheel in counterphase and in phase. Images based on Tian [164].

Tian [164] furthermore makes note of the term *Critical Limit Cycle*, which he describes as a synchronization of the inner and the outer fluid film which excites the rotor natural frequency. Schweizer [153] also makes note of this phenomenon, which he dubs as *Total instability*, as also displayed in Figure 2.7. The amplitudes of the rotor while oscillating in this mode can become large; Schweizer therefore considers them to be potentially catastrophic for the operation of the turbocharger.

2.3.3. FRICTION LOSSES AND THERMAL MODELING OF TURBOCHARGERS

The power losses in the bearing system can subtract a significant part of the power delivered from the turbine to the compressor, especially at conditions where the combustion engine is running at low speeds [165]. Friction losses not only reduce the efficiency of the turbocharger but also -more importantly- have a negative effect on the transient response of the turbocharger. For these reasons, it is important to evaluate the friction losses of the turbocharger.

The temperature of the shaft and the bearing housing play a major role in the friction losses of the bearings. An important finding from the aforementioned model of San Andres [152] is that the heat input from the hot turbine shaft accounts for 97% of the total heat input at low speed conditions and 65% of the heat input at high speed conditions, see Figure 2.9. Therefore, it is important to take this heat input into account when modeling the turbocharger rotor-bearing dynamics [152] and thus a thermal model of the complete turbocharger can contribute in providing friction loss predictions in real-life conditions. Thermal modeling a complete turbocharger, however, is a complicated task as the amount of heat flowing through the many heat flow paths in a turbocharger depends on the shape and the operating conditions of the turbocharger at hand [166]. Particularly for an automotive turbocharger, these operating conditions are constantly varying in time due to constantly changing engine operating points and due to the pulsating exhaust gas flow.

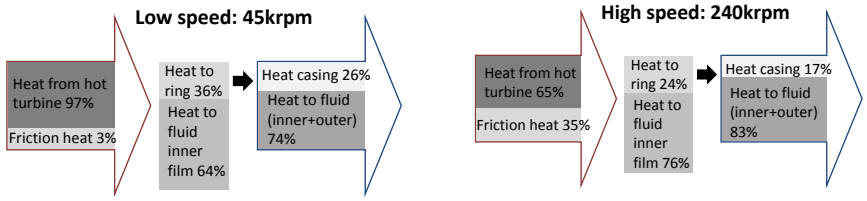

(a) Energy flow at 45krpm.

(b) Energy flow at 240krpm.

Figure 2.9: Thermal flows through a turbocharger rotor-bearing system. Data from San Andres [152].

An effort to model the temperature distribution of a complete turbocharger has been made by Baines [166], who constructed a 1D heat transfer model to investigate the turbine efficiency and the role of heat transfer within the turbocharger. In order to get a reasonable correlation between predictions and measurements, Baines fitted the forced convection coefficients based on measurement data. Serrano [165] presented a simple isoviscous model to estimate the friction losses of a turbocharger based on steady state shear losses of the journal bearings and the thrust bearing, but used correction coefficients for each individual component - sometimes as small as $^1/_3$ of the original friction prediction - to obtain reasonable correlation with measurement values. Furthermore, the heating from the shaft, as described by San Andres [152] to be of major importance, was not included in the model. Based on a 3D conjugate heat transfer analysis, Bohn [167] demonstrated that at low speed, heat is transferred from the turbine to the compressor. At high speed, the compressor temperature increases and heat is transferred mostly from the compressor to the lubricating oil. Bohn, however, did not couple his CHT-model to the analysis of friction losses in the bearing system. More recently, Porzig [168] coupled a 3D conjugate heat transfer model (CHT) of a turbocharger to the rotor-bearing model of Vetter [169] and concluded that the assumption of adiabatic boundary conditions yields considerable discrepancies, whereas his CHT-corrected predictions showed a reasonable correlation with measurements in terms of ring speed ratio. Porzig, however, did not manage to provide accurate predictions for the shaft temperature.

These recent studies [165–168, 170] show that the temperature in the bearing housing and the shaft strongly rely on the specific geometry of the turbocharger and its operating condition. The friction losses of the bearing system depend on its geometry, on the oil inlet pressure and the oil inlet temperature [171]. Furthermore, large amplitude oscillations –for example due to self-excited sub-synchronous whirl– can also cause an increase of friction losses [172]. Without knowing the temperatures of the shaft and the turbine, predicting the friction losses of a real turbocharger is therefore a challenging task.

Three methods have primarily been used to experimentally determine the friction losses of a turbocharger:

- measurement of the enthalpy change of the lubricant,

- measurement of the difference of enthalpy change of the gasses flowing over the turbine minus those over the compressor,
- or the direct measurement of the torque and rotation speed of the rotor [171].

The first two methods seem inaccurate, as there is considerable heat transfer within the turbocharger which is not directly related to friction heat, as previously explained and also observed in the measurements of Sjöberg [173].

The approach based on the third option as demonstrated by Deligant [171] seems more accurate. Deligant used an experimental setup with a torquemeter between the turbine and the compressor to measure the friction losses of the bearing system. He determined that typically $^1/_3$ of the friction losses originate from the journal bearings whereas $^2/_3$ of the friction losses originate from the thrust bearing, which can be even more in case there is an axial load present on the shaft. Hoepke [174] used a similar approach as Deligant [171], however, he concluded the exact opposite: $^2/_3$ of the friction losses originate from the journal bearings whereas $^1/_3$ of the friction losses originate from the thrust bearing. This shows that the friction losses of the turbocharger rotor-bearing system clearly depend on its design and operating conditions and therefore sufficently detailed models are required for accurate friction predictions.

2.3.4. AERODYNAMIC AND EXTERNAL EXCITATION

Kerth [157] investigated the influence of the aerodynamic load from the compressor wheel and the turbine wheel. He concluded that only a static displacement is caused by the external aerodynamic load, without further effects on the dynamic response. Maruyama [175, 176] investigated the influence of external vibrations, caused for example by an oscillating combustion engine. He observed that the oscillations of the rotor can be 20%-30% larger when mounted on a combustion engine which causes external excitation by engine vibrations and pulsations [176]. The extra vibrations were mostly sub-synchronous oscillations occuring at various frequencies. Both the aerodynamic load and the external excitation seem to influence the dynamic response of a turbocharger mounted to a combustion engine and should therefore be taken into consideration. Alternatively, when a turbocharger is measured on a cold gas stand with vibration isolation from the bearing housing and no significant pressures at the compressor and turbine wheel [12], these two effects might be small enough to ignore.

2.3.5. OIL CONNECTING CHANNELS

As mentioned in Section 2.3.2, many studies have recently been performed to study the dynamic behavior of a rotor supported by floating ring bearings, see for example [144, 153, 158–164]. These models involve simultaneous solving of the fluid flow in the oil films and the rotordynamic equations for the rotor.

Due to the highly non-linear dynamic characteristics of the FRB, these models are often based on time-transient calculations. In order to keep calculation times within reasonable limits, the fluid flow can be described by the Reynolds equation. The necessary assumptions for this equation are generally valid for the thin film sections of the

FRB fluid domain, however, they do not hold for the oil connecting channels, where inertia terms can not simply be neglected, see Figure 2.10.

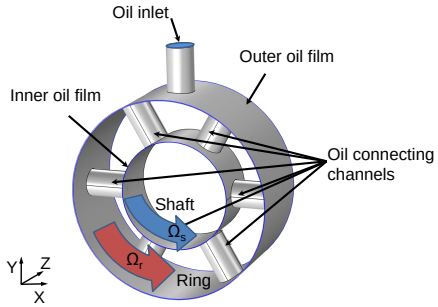

Figure 2.10: Fluid domain of a floating ring bearing.

Some of these studies on FRB dynamics [144, 161, 176, 177] have completely ignored the presence of the oil connecting channels. As the area of the oil connecting channels in some turbocharger applications accounts for over a quarter of the thin film area, it seems inappropriate to neglect their influence on the pressure distribution of the FRB. Alternatively, other studies [162, 168] have modeled these channels as a 'passive' pressure coupling, where the inner film pressure is equalized with the outer film pressure, but the influence of the fluid dynamics in the connecting channels were excluded. This approach also seems inappropriate, as the oil connecting channels can be seen as two-sided lid-driven cavities, which are known to exhibit complex vortices in the fluid which influence the pressure distribution [178]. Moreover, it is known that a sudden pressure decrease/increase may occur at the transition between a thin film section and an open fluid section[179], caused by inertial and viscous effects, sometimes referred to as *ram pressure*.

In the study in Appendix D, the behavior of the flow throught the oil connecting channels of a FRB was analyzed in detail using a 3D CFD model [180]. The results were linearized to serve as a basis for a connecting channel metamodel which can mimic the behavior of the connecting channel in a Reynolds-based flow model. The following two conclusions were drawn:

- the flow through the connecting channels adds rotating momentum to the ring, increasing the ring speed by 4% – 10% compared to predictions where only the thin film traction torque on the ring would have been included.
- the flow through the connecting channels cause local pressure changes in the oil films near the channel inlets and outlets, but in general do not significantly change the bearing reaction forces to the shaft, compared to a model using a 'passive' pressure coupling. Particularly at eccentricities over 0.3 times the bearing clearance, the pressure distribution in the oil films is dominated by hydrodynamic pressure buildup and the contribution of the internal flow effects in the oil connecting

channels become negligibly small.

2.3.6. THE THRUST BEARING

Most turbocharger rotors are supported by two radial bearings and one thrust bearing, as depicted in Figure 1.3. The thrust bearing carries the force resulting from the static pressure distribution as well as the impulse balance of the air on both the compressor and the turbine wheel. This force acts in direction of the turbine or in direction of the compressor as a function of the operating conditions and therefore the bearing is two-sided. Thrust bearings in turbochargers are usually taper-land type, of which an example is shown in Figure 2.11a.

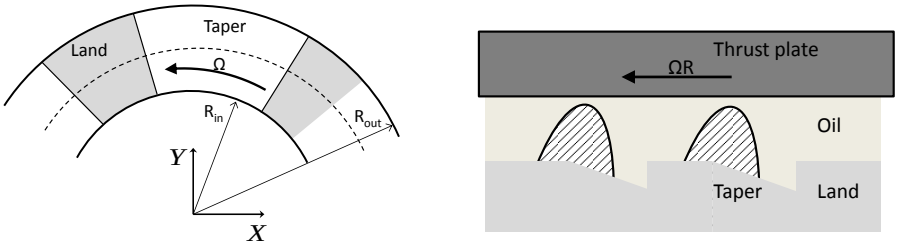

(a) Top view of a taper-land type thrust bearing.

(b) Cross-sectional view of a thrust bearing section. The marked areas indicate hydrodynamic pressure buildup.

Figure 2.11: Taper-land type thrust bearing.

A thrust bearing can add stiffness and damping to tilting displacements of the shaft [181], which may either originate from bending of the shaft or due to opposing rigid body displacement at each shaft end within the compliance of the radial bearings. The thrust bearing, however, has been excluded from analysis in almost all studies on the lateral dynamics of turbocharger rotor-bearing systems. Recently, Vetter [169] compared modeling results with and without the presence of a thrust bearing, and found that a model without the presence of a thrust bearing showed more sub-synchronous modes than a model which did incorporate the thrust bearing. The difference was mostly observable at rotation speeds below 50krpm. A comparison with experimental data, however, was not presented. Li [182] also performed an analysis using several short bearing descriptions. Li showed in his predicitions that the thrust bearing reduces the sub-synchronous oscillations at low rotation speeds, but his computation model showed rather weak correlation with measurement results. Hoepke [174] performed experiments with a turbocharger, externally driven by an electric motor, with and without a thrust bearing. Runs with the thrust bearing were operated at speeds up to 130krpm, whereas the turbocharger without the thrust bearing showed large amplitude oscillations and therefore the runs were limited to 90krpm. Chatzisavvas [183] compared a runup prediction with and without a thrust bearing model and found that the prediction without a thrust bearing showed significantly more sub-synchronous vibrations.

It may be concluded that the thrust bearing has influence on the lateral rotordynamic behavior of turbochargers, especially at low rotation speeds. However, to date, a detailed, experimentally validated model to explain the influence of the thrust bearing on the lateral dynamics is still lacking.

2.3.7. ALTERNATIVE BEARING DESIGNS FOR TURBOCHARGERS

Although many turbocharger rotor-bearing models have been developed to predict the non-linear response of the rotor-bearing system, actually very few alternative bearing designs have been studied to reduce self-excited vibrations. Tamunodukobipi [184] studied the influence of placing the oil connecting channels between the inner and the outer fluid film under an angle with respect to pure radial direction, as depicted in Figure 2.12a. Tamunodukobipi reasoned that directing the oil which flows into the inner oil film against the main flow direction would reduce the fluid velocity in the inner fluid film, which would reduce the whirl frequency ratio of the system and make it more stable. By experimental identification of his measurement results, Tamunodukobipi showed that angled fluid injection reduces the cross-coupling stiffness and damping. Although the results are promising, it is not clear if the positive effect on reducing the sub-synchronous response is due to momentum exchange in the inner film or due to the fact that there is a phase shift in the transfer of pressure from the inner film to the outer film and vice versa.

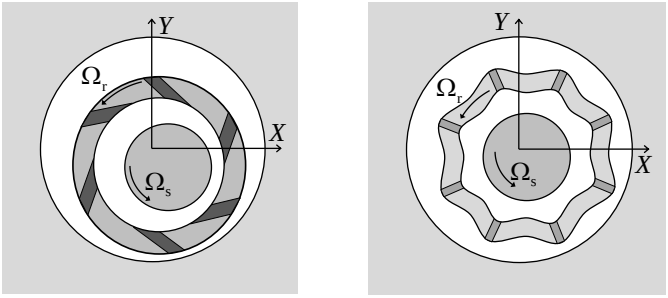

(a) Angled injection [184].

(b) Multilobe floating ring bearing [185].

Figure 2.12: Alternative bearing geometries.

Nowald [186] presented a research where *axial grooves* in the inner film of the FRB were applied. The sub-synchronous vibration behavior was changed, but overall was not reduced. Experimental validation of results was also lacking. Eling [185] presented the concept of *multilobe floating ring bearings*, see Figure 2.12b, and used a simple iso-viscous rotor-bearing model to perform predictions. Based on measurements and predictions, a reduction of sub-synchronous vibration over the full operating range was demonstrated at the cost of an increase in friction losses.

The effect of a *circumferential groove* in the outer oil film was investigated by Woschke

[187], who observed in his model and measurements that the sub-synchronous vibrations increases when a radial groove is present. In our measurements, such a groove actually reduced the amount of sub-synchronous vibration. *Surface texture* was investigated analytically by Pei [177], who constructed a steady state thermo-hydrodynamic floating ring bearing model. Pei concluded that surface texture, especially when applied to the inner fluid film, can increase the oil flow through the bearing and therefore reduce the local temperatures of the inner fluid film. The friction losses, however, were expected to increase. Experimental validation of these predictions were lacking and hence the effect of surface texture on the performance of floating ring bearings is still not well evaluated.

2.4. STATUS QUO AND IDENTIFICATION OF OPEN CHALLENGES

Research on the dynamic behavior of turbocharger rotor-bearing systems rests on a solid foundation of rotordynamics and (thermo-) hydrodynamics. At the beginning of this century, the dynamic behavior of turbocharger rotor-bearing systems was already qualitatively well understood. Each of the two oil films of the floating ring bearing can become unstable and jump into several different oil whirl modes, typically with a whirl frequency of either half the ring speed or half the shaft speed plus ring speed. Depending on the rotor-bearing design and its operating conditions, the jump speeds for each mode are different. When the inner and outer fluid film both become unstable and synchronize, total instability might occur which can lead to failure of the rotor-bearing system.

Time-transient multiphysical models can capture highly non-linear dynamic behavior typical for rotor-bearing systems with hydrodynamic bearings. Most recent turbocharger rotor-bearing models solve the Reynolds equation for each of the two fluid films of the two floating ring bearings for each time step while simultaneously determining the (lumped) temperatures of the oil films and the rotordynamic motion. The latest versions of these models claim to be able to predict the amplitudes of vibration within 35% of the measured amplitudes and frequencies [163].

In the current status of research, many researchers have claimed to have found a good correlation between turbocharger measurements and numerical predictions. A common approach is to use rotordynamic measurements of a turbocharger running on a hot gas test stand as a base for validation of models. In this approach, the relevance of some influence factors on the rotor-bearing dynamics is unclear, in particular:

- the aerodynamic load on the compressor wheel and the turbine wheel
- the thrust bearing
- the various seals in a turbocharger
- the influence of the bearing support structure
- the oil connecting channels between the inner fluid film and the outer fluid film.

Particularly when a hot gas stand is used to run the turbocharger, the temperatures vary greatly over the rotor-bearing system and hence its dynamics are greatly affected [170]. Moreover, the exact unbalance amount of a turbocharger test sample is difficult to define accurately. All these uncertainties diminish the validity of test results of a turbocharger, particularly on a hot gas test stand, as a reliable basis for validation.

Instead, it makes sense to perform a step-by-step validation of models by starting with a rotor-bearing system which is not affected by these uncertainties. That is why we will first analyze the dynamics of a Laval rotor supported by plain journal bearings in the next Chapter, Chapter 3. This will be followed by an analysis of the Laval rotor supported by floating ring bearings in Chapter 4. Once the rotor-bearing model is validated on these two applications, the rotor-bearing model will be used to analyze the dynamics of the turbocharger rotor-bearing system in Chapter 5.

3

DYNAMIC BEHAVIOR OF A FLEXIBLE LAVAL ROTOR SUPPORTED BY PLAIN JOURNAL BEARINGS

Rotors supported by fluid film bearings exhibit interesting dynamic behavior caused by the interaction of the fluid film bearings with the structural dynamics of the rotor. In this chapter, we will construct a rotor model, a fluid film bearing model and a thermal model of a Laval rotor supported by plain journal bearings. These three models are coupled and used to perform run-up simulations. The results are validated by experiments. Furthermore, the influence of oil supply conditions and rotor unbalance are investigated. Ultimately, the goal of this chapter is to evaluate how accurate the modeling is and which physical effects are determining the behavior of the rotor-bearing system during a run-up.

This Chapter is based on the following publications:

- Eling, R.; te Wierik, M.; van Ostayen, R.; Rixen, D. Towards Accurate Prediction of Unbalance Response, Oil Whirl and Oil Whip of Flexible Rotors Supported by Hydrodynamic Bearings. *Lubricants* **2016**, 4, 33.
- Eling, R.; te Wierik, M.; van Ostayen, R.A.J. Multiphysical modeling comprehensiveness to model a high speed Laval rotor on journal bearings. *Proceedings of the 14th EDF - Pprime Workshop*, **2015**; pp. 1–14.

3.1. DESCRIPTION OF THE ROTOR-BEARING SYSTEM

A Laval rotor —also referred to as *Jeffcott rotor*— is a symmetric rotor containing one rigid disk on a flexible shaft, supported by a bearing at each rotor end, as depicted in Figure 3.1. Due to its simplicity, this type of rotor is often used to demonstrate basic characteristics of rotordynamics such as *critical speed* and *whirl orbits* [20].

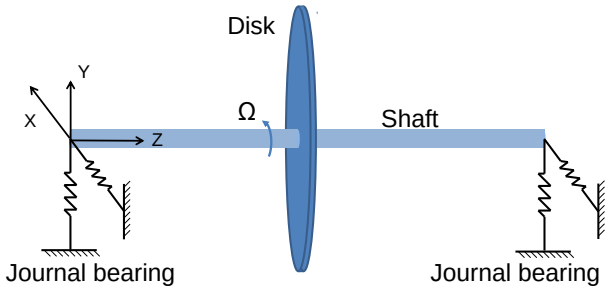

Figure 3.1: Schematic representation of a Laval rotor supported by journal bearings.

3.2. MODELING THE LAVAL ROTOR ON PLAIN JOURNAL BEARINGS

The Laval rotor is often modeled as a massless, elastic shaft supported by two rigid bearings. However, in the light of our application —turbocharger rotor-bearing systems which are known to encounter supercritical rotor speeds and are supported by hydrodynamic bearings— we need to take into account shaft inertia and bearing compliance. Particularly due to the hydrodynamic bearings, the interaction between rotordynamics and bearing dynamics results in complex dynamic behavior which requires the rotor and the bearings to be analyzed as a coupled system [40]. Moreover, as the viscosity of the lubricant (typically oil) may depend strongly on the film temperature, which in turn depends on the thermal boundary conditions, a thermal model including the bearing housing and the shaft needs to be incorporated. A schematic depiction of the coupled rotor-bearing model is given in Figure 3.2.

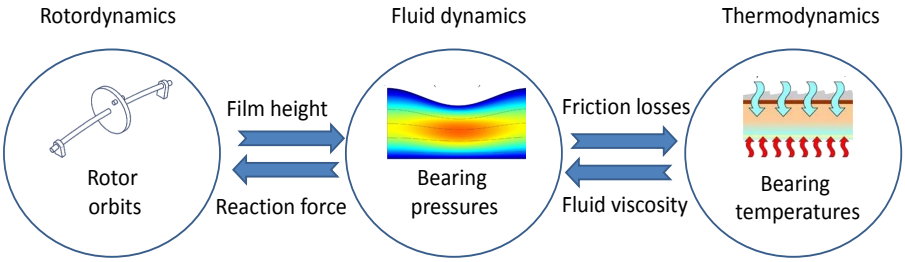

Figure 3.2: Schematic depiction of the coupled model of the rotor-bearing system. The rotor model is explained in Section 3.2.1-3.2.3, details of the bearing model can be found in Section 3.2.4 and the thermal model is described in 3.2.5.

For reasons of generality, a Finite Element rotor formulation is used, where the rotor is described by a number of shaft elements and a disk element. The bearing model can be considered as a non-linear spring-damper system, which gives a reaction force to the rotor as a function of displacement $\mathbf{q}$, velocity $\dot{\mathbf{q}}$ and rotation speed Ω_s. The third component in Figure 3.2 is the thermal model of the rotor-bearing system, which influences the characteristics of the bearing by the temperature-dependent viscosity of the fluid.

3.2.1. ROTOR MODEL: SHAFT ELEMENTS

The rotor model is a shaft-line model, where the rotor is divided into a number of shaft elements with a node at each end of every shaft element. The rotor model essentially describes the equations of motion for all rotor elements as a result of external loads, bearing forces and the internal forces as a result of elastic deformations.

Figure 3.3a depicts a single shaft element. The shaft elements have local coordinates $\mathbf{q}^{\text{el}}$ to describe radial and axial translation as well as rotor bending and torsion:

$$\mathbf{q}^{\text{el}} = \begin{bmatrix} \bar{u}_1 & \bar{v}_1 & \bar{w}_1 & \bar{\alpha}_1 & \bar{\beta}_1 & \bar{\phi}_1 & \bar{u}_2 & \bar{v}_2 & \bar{w}_2 & \bar{\alpha}_2 & \bar{\beta}_2 & \bar{\phi}_2 \end{bmatrix}^T \tag{3.1}$$

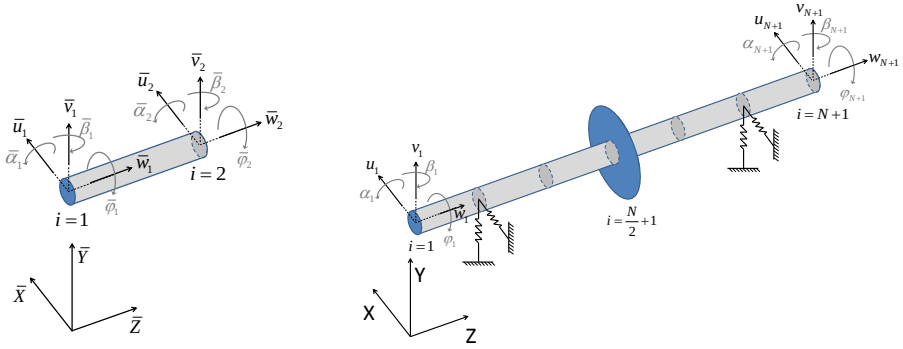

(a) Local coordinates of a single shaft element

(b) Rotor assembly in global coordinate frame XYZ

Figure 3.3: Coordinates to describe the kinematics of the rotor. The overline notation denotes the local frame of an element. Index i represents the node number and N represents the number of beam elements.

The shafts are assumed to be slender and hence shear effects and rotary inertia effects are ignored while setting up the equations describing the dynamic behavior of the shaft: Euler-Bernoulli assumptions. Furthermore, we assume each shaft element to have a constant cross-section and constant isotropic material properties. Each shaft element has a mass matrix $\boldsymbol{M}^{\text{el}}$, a gyroscopic matrix $\boldsymbol{G}^{\text{el}}$, and a stiffness matrix $\boldsymbol{K}^{\text{el}}$ with the following structure:

$$\boldsymbol{M}^{\text{el}} = \begin{bmatrix} \boldsymbol{M}^{\text{el}}_{11} & \boldsymbol{M}^{\text{el}}_{12} \\ \boldsymbol{M}^{\text{el}}_{21} & \boldsymbol{M}^{\text{el}}_{22} \end{bmatrix}, \qquad \boldsymbol{G}^{\text{el}} = \begin{bmatrix} \boldsymbol{G}^{\text{el}}_{11} & \boldsymbol{G}^{\text{el}}_{12} \\ \boldsymbol{G}^{\text{el}}_{21} & \boldsymbol{G}^{\text{el}}_{22} \end{bmatrix} \qquad \boldsymbol{K}^{\text{el}} = \begin{bmatrix} \boldsymbol{K}^{\text{el}}_{11} & \boldsymbol{K}^{\text{el}}_{12} \\ \boldsymbol{K}^{\text{el}}_{21} & \boldsymbol{K}^{\text{el}}_{22} \end{bmatrix} \tag{3.2}$$

where the sub-matrices with the subscripts $_{11}$ and $_{22}$ describe the coefficients at each node. The sub-matrices with subscripts $_{12}$ and $_{21}$ describe the interconnection between the nodes within each element. The local elementary matrices $\boldsymbol{M}^{\mathrm{el}}$, $\boldsymbol{G}^{\mathrm{el}}$ and $\boldsymbol{K}^{\mathrm{el}}$ can be found in Appendix C.

The shaft elements $i = 1...N$ are assembled within a global reference frame using global coordinates $\boldsymbol{q}$ to construct the rotor, as depicted in Figure 3.3b:

$$\mathbf{q} = \begin{bmatrix} u_1 & v_1 & w_1 & \alpha_1 & \beta_1 & \phi_1 & \dots & u_{N+1} & v_{N+1} & w_{N+1} & \alpha_{N+1} & \beta_{N+1} & \phi_{N+1} \end{bmatrix}^T \tag{3.3}$$

The rotor model is assembled from the individual elemental matrices as follows:

$$\boldsymbol{M} = \sum_{\mathrm{el}=1}^{N} \boldsymbol{T}^T \boldsymbol{M}^{\mathrm{el}} \boldsymbol{T} \tag{3.4}$$

$$\boldsymbol{G} = \sum_{\mathrm{el}=1}^{N} \boldsymbol{T}^T \boldsymbol{G}^{\mathrm{el}} \boldsymbol{T} \tag{3.5}$$

$$\boldsymbol{K} = \sum_{\mathrm{el}=1}^{N} \boldsymbol{T}^T \boldsymbol{K}^{\mathrm{el}} \boldsymbol{T} \tag{3.6}$$

where $\boldsymbol{T}$ are the transformation matrices which convert the local element descriptions to the stationary global reference frame and assemble the elements 1...N to a global matrix.

3.2.2. ROTOR MODEL: DISK ELEMENT

The disk is assumed to be rigid and its inertia properties can therefore be lumped on a single node on the shaft. The presence of a disk on a node — for example shown in Figure 3.3b on node index $i = \frac{N}{2} + 1$ — has the following contribution to the local mass matrix $\mathbf{M}^{\mathrm{el}}$:

$$\mathbf{M}_d = \begin{bmatrix} m_{\mathrm{d}} & 0 & 0 & 0 & 0 & 0 \\ 0 & m_{\mathrm{d}} & 0 & 0 & 0 & 0 \\ 0 & 0 & m_{\mathrm{d}} & 0 & 0 & 0 \\ 0 & 0 & 0 & \frac{m_{\mathrm{d}}(3R_{\mathrm{d}}^2+L_{\mathrm{d}}^2)}{12} & 0 & 0 \\ 0 & 0 & 0 & 0 & \frac{m_{\mathrm{d}}(3R_{\mathrm{d}}^2+L_{\mathrm{d}}^2)}{12} & 0 \\ 0 & 0 & 0 & 0 & 0 & \frac{m_{\mathrm{d}}R_{\mathrm{d}}^2}{2} \end{bmatrix} \tag{3.7}$$

where R_{d} and L_{d} are the length and the radius of the disk and the mass is calculated by:

$$m_{\mathrm{d}} = \rho_{\mathrm{d}} \pi R_{\mathrm{d}}^2 L_{\mathrm{d}} \tag{3.8}$$

where ρ_d is the material density of the disk. The disk has the following contribution to the local gyroscopic matrix $\mathbf{G}^{el}$:

$$\mathbf{G}_d = \begin{bmatrix} 0 & 0 & 0 & 0 & 0 & 0 \\ 0 & 0 & 0 & 0 & 0 & 0 \\ 0 & 0 & 0 & 0 & 0 & 0 \\ 0 & 0 & 0 & 0 & \frac{m_d R_d^2}{2}\Omega_s & 0 \\ 0 & 0 & 0 & -\frac{m_d R_d^2}{2}\Omega_s & 0 & 0 \\ 0 & 0 & 0 & 0 & 0 & 0 \end{bmatrix} \tag{3.9}$$

As can be observed, the gyroscopic terms depend on rotation speed Ω_s. As a result, the eigenfrequencies of the rotor are a function of rotation speed [20].

3.2.3. ROTOR MODEL: FORCES

Several forces act on the rotor. Firstly, the rotating unbalance force caused by the amount of unbalance $m_{unb} r_{unb}$, which is lumped as a single vector on the disk and increases quadratically with rotation speed Ω_s:

$$F_{unb} = m_{unb} R_{unb} \Omega_s^2 \quad , \tag{3.10}$$

The rotating unbalance force can be transferred to the stationary global reference frame by:

$$\begin{Bmatrix} F_{X_{unb}} \\ F_{Y_{unb}} \end{Bmatrix} = F_{unb} \begin{Bmatrix} \cos\Theta_s \\ \sin\Theta_s \end{Bmatrix} \quad , \tag{3.11}$$

where the rotation angle Θ_s in the XY-plane is 0 at $t = 0$ along the X axis, but rotates in time with the rotor at rotation speed Ω_s:

$$\Theta_s = \int_0^t \Omega_s dt \tag{3.12}$$

Furthermore, gravitational acceleration applies a distributed weight load on the rotor:

$$\mathbf{F}_{wgt} = \mathbf{Mg} \tag{3.13}$$

The rotor is supported by bearings, which apply a force to the rotor as will be explained in Section 3.2.4:

$$\mathbf{F}_b = f(\mathbf{q}, \dot{\mathbf{q}}, \Omega_s) \tag{3.14}$$

The resulting equations of motion are thus formed by transforming all local equations to the stationary global reference frame X, Y, Z and collecting all mass, stiffness, (gyroscopic) damping and (external) load terms:

$$\mathbf{M}\ddot{\mathbf{q}} + \mathbf{G}\dot{\mathbf{q}} + \mathbf{K}\mathbf{q} = \mathbf{F} \tag{3.15}$$

In order to account for material damping (and for example damping in the interfaces between the shaft and the disk), we assume Rayleigh damping, which is considered to be

a simple-yet-appropriate approximation for the lightly damped rotor. Rayleigh damping can be incorporated in the equations of motion:

$$\mathbf{M}\ddot{\mathbf{q}} + \left(\mathbf{G} + \mathbf{C}_{\text{Ray}}\right)\dot{\mathbf{q}} + \mathbf{K}\mathbf{q} = \mathbf{F} \tag{3.16}$$

where $\mathbf{C}_{\text{Ray}}$ is proportional to the mass and stiffness of the rotor [188]:

$$\mathbf{C}_{\text{Ray}} = c_{\text{M}}\mathbf{M} + c_{\text{K}}\mathbf{K} \tag{3.17}$$

As only two modes are expected to be active in the operating range, the coefficients of $\mathbf{C}_{\text{Ray}}$ can conveniently be tuned so that the numerical model matches the experimentally observed damping ratios.

At this point, the number of degrees of freedom of the rotor can be reduced by techniques such as Guyan reduction or SEREP [20]. In this study, reduction in the number of degrees of freedom of the rotor did not lead to a considerable reduction in computation time during time transient simulations of the coupled rotor-bearing system, hence these techniques are not included in this study.

3.2.4. BEARING MODEL

The rotor is supported by plain journal bearings, which is a simple type of hydrodynamic bearing where the shaft —sometimes referred to as the *journal*— is separated from the stationary bearing housing by a lubricant film. The lubricant, in this case oil, is supplied to the bearing via the inlet at an elevated pressure and flows out in axial direction via the sides of the bearing at ambient pressure, see Figure 3.4a.

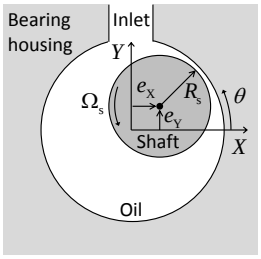

(a) Cross-sectional view of the plain journal bearing. The shaft operates at eccentricity (e_X, e_Y). The oil film thickness is exaggerated here for visualization.

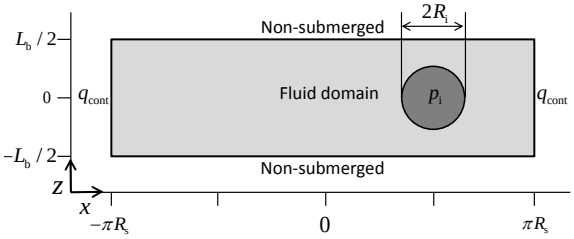

(b) Fluid domain and boundary conditions for the unwrapped 2D bearing model: ambient pressure $p = 0$ is imposed at the sides of the fluid domain $z = -L_b/2$, $z = L_b/2$ and inlet pressure $p = p_i$ is imposed on the inlet channel domain, marked in dark grey. A periodic boundary condition connects the flow between sides $x = -\pi R_s$ and $x = \pi R_s$.

Figure 3.4: Schematic depiction of the plain journal bearing and its unwrapped 2D fluid domain.

The rotation speed of the shaft Ω_s induces a shear flow of viscous oil which creates the carrying capacity of the oil film, as already shown in Figure 2.3a. The film thickness is very small compared to the bearing radius, so the film curvature is small which means we can unwrap the cylindrical fluid domain to a 2D fluid domain by setting $x = \theta R_s$ as

depicted in Figure 3.4b.
The fluid flow may be predicted by solving the Navier-Stokes equation in three directions over the fluid domain. This, however, is a computationally expensive task [189, 190], especially in time-transient simulations where the fluid flow needs to be predicted for a large number of time steps. A common method for obtaining the pressure distribution in a fluid film bearing is to simplify the 3D Navier-Stokes equations to the 2D Reynolds equation. The Reynolds equation assumes that the fluid inertia forces are negligible compared to viscous forces. This is based on the ratio of fluid inertia forces to viscous forces, expressed as the *Reynolds number*. For journal bearings, the shear flow Reynolds number can be calculated by [191]:

$$\mathrm{Re}_* = \frac{\rho_{\mathrm{oil}} \Omega_{\mathrm{s}} R_{\mathrm{s}} h}{\mu_{\mathrm{oil}}} \frac{C}{R_{\mathrm{s}}} \tag{3.18}$$

where ρ_{oil} and μ_{oil} are the density and the viscosity of the oil. h is the local thickness of the fluid film and C denotes the nominal radial bearing clearance. In most fluid film lubrication applications where oil is used as a lubricant $\mathrm{Re}_* < 1$ and hence the fluid inertia forces can be neglected [192]. Furthermore, Reynolds equation assumes that the fluid has no slip on the solid-fluid interfaces and external body forces on the fluid are neglected. For a fluid film with thickness h supporting a shaft with radius R_{s} rotating at rotation speed Ω_{s}, Reynolds equation can be written as [51]:

$$\frac{\partial}{\partial x}\left(-\frac{h^3 \rho_{\mathrm{oil}}}{12\mu_{\mathrm{oil}}}\frac{\partial p}{\partial x} + \frac{\Omega_{\mathrm{s}} R_{\mathrm{s}} h \rho_{\mathrm{oil}}}{2}\right) + \frac{\partial}{\partial z}\left(-\frac{h^3 \rho_{\mathrm{oil}}}{12\mu_{\mathrm{oil}}}\frac{\partial p}{\partial z}\right) + \frac{\partial h \rho_{\mathrm{oil}}}{\partial t} = 0 \tag{3.19}$$

The first term in brackets represents the circumferential fluid flow, both pressure-driven and shear driven. The second term between brackets represents the pressure-driven axial flow and the third term is the flow due to squeeze motion of the shaft towards the bearing housing. Solving this partial differential equation over the fluid domain, which is depicted in Figure 3.4b, gives the pressure distribution $p(x,z)$. The pressure in y direction (over the thickness of the film) is assumed to be constant, based on the ratio of bearing clearance to shaft radius $\frac{C}{R_s} \ll 1$ [192].
As can be seen in Figure 3.4a, the film thickness h depends on the rotor displacements e_{X} and e_{Y}. In our analyses, we assume that the shaft and bearing housing surfaces are smooth (i.e. no surface roughness) and undeformable. The flow regime is assumed to be fully hydrodynamic: mechanical contact between surfaces is assumed not to occur.

An often used assumption in the analysis of rotors supported by fluid film bearings is *perfect alignment*: the center axis of the rotor is assumed to be always parallel to the center axis of the bearing bore. The film thickness h would then be:

$$h_{\mathrm{ali}} = C - e_X \cos(\theta) - e_Y \sin(\theta) \tag{3.20}$$

In case the shaft tilting over angles α and β (see Figure 3.3b) is taken into account, the film thickness function for the bearing becomes [193]:

$$h = C - \left(z \sin\beta + e_X\right)\cos(\theta) - \left(z \sin\alpha + e_Y\right)\sin(\theta) \tag{3.21}$$

where the local axial coordinate z is defined such that:

$$\{z| - L_{b/2} \leq z \leq L_{b/2}\} \tag{3.22}$$

In the analyses in this Section, we make use of the film height description including shaft tilting, Equation 3.21.

The pressure distribution over the bearing fluid domain depicted in Figure 3.4b can be predicted by solving the Reynolds equation, Equation 3.19, while taking into account the boundary conditions at the edges of the domain as depicted in Figure 3.4a. The pressure distribution predicted by the Reynolds equation may contain sub-ambient pressure regions where the film thickness is increasing along x direction (*a diverging film section*) or in case $\frac{\partial h}{\partial t}$ is positive (*negative squeeze motion*). In reality, liquids can only sustain a limited amount of tensile stress and hence *cavitation* occurs [51]. Therefore, a cavitation description needs to be added to the model.
Cavitation in dynamically loaded journal bearings has been described in detail, for example in references [90, 96, 98, 194]. In our model, we choose a cavitation description which assumes *fluid streamers*: the cavitation zone is filled with gas through which multiple liquid streamers are formed in which the transport of fluid through the cavitated region occurs. The streamers are assumed to be attached to both the shaft and the bearing housing surfaces.

For our model, the cavitation description of Alakhramsing [108] is selected as it was proven to be a stable and mass-conservative approach for finite element-based simulation of lubrication problems [88]. For this particular cavitation description, we first start with the observation that the flow in a cavitated fluid film is described by two variables: pressure p and the lubricant mass fraction f which is the local ratio of liquid volume to total volume. The mass fraction is between zero and one in the cavitation zone and is by definition one in the full film zone. The pressure in the cavitation zone is equal to the cavitation pressure, which is set to ambient pressure in our studies. Although it has been reported that sub-ambient pressures can occur [98], the assumption of constant ambient pressure in the cavitation zone is a commonly accepted assumption [96, 108]. Hence, the pressure is constant in the cavitated area whereas the mass fraction is constant elsewhere. This observation allows us to describe both variables fully deterministically using only one new variable ξ:

$$\begin{aligned} f(x,z) &= 1 + \xi(\xi < 0)c_T \\ p(x,z) &= \xi(\xi \geq 0)\zeta \end{aligned} \tag{3.23}$$

In words, this means that in the full film domain, the Boolean function $(\xi < 0) = 0$, which means that the mass fraction f is one here. Furthermore, in the full film domain, the Boolean $(\xi \geq 0) = 1$, so that the pressure distribution in the full film domain is prescribed by $p(x,z) = \xi\zeta$, where the pressure scaling factor ζ is defined as [88]:

$$\zeta = \frac{\mu_0 \Omega_s R_s^2}{C} \tag{3.24}$$

ensuring a smooth transition from the cavitated domain to the full film domain.

In the cavitated domain, the Boolean function $(\xi \geq 0) = 0$ and hence the pressure is zero by definition. The mass fraction in the cavitation zone is given by: $f(x,z) = 1 + \xi c_T$, in which c_T is a transformation coefficient that arises from a flow balance in circumferential direction under the assumption of streamer cavitation, so that the transition of ξ can be described at the reformation boundaries in FEM descriptions, see Alakhramsing [88].
Hence, ξ determines the mass fraction in the cavitation zone and determines the pressure distribution elsewhere. The Reynolds equation can now be stated for the new variable ξ instead of p:

$$\frac{\partial}{\partial x}\left(-\frac{fh^3\rho_{\mathrm{oil}}}{12\mu_{\mathrm{oil}}}\frac{\partial \xi}{\partial x}\zeta + \frac{f\Omega_\mathrm{s}R_\mathrm{s}h\rho_{\mathrm{oil}}}{2}\right) + \frac{\partial}{\partial z}\left(-\frac{fh^3\rho_{\mathrm{oil}}}{12\mu_{\mathrm{oil}}}\frac{\partial \xi}{\partial z}\zeta\right) + \frac{\partial f h\rho_{\mathrm{oil}}}{\partial t} = 0 \tag{3.25}$$

Equation 3.25 is solved on the fluid domain depicted in Figure 3.4b under the following boundary conditions:

- Inlet pressure p_i is imposed as a Dirichlet boundary condition on the inlet domain
- Periodic boundary conditions are imposed on the edges $x = \pm\pi R_\mathrm{s}$
- Non-submerged boundary conditions are imposed on the edges $z = \pm\frac{L_b}{2}$

The non-submerged boundary condition allows flow to exit the bearing at the edges under ambient pressure condition. There is, however, no inflow of oil from the edges at the sides of the bearing in case the oil film is locally cavitated. This boundary condition is imposed on the edges as:

$$(\xi \geq 0)\left(q_\mathrm{z}n_\mathrm{z} > 0\right)\xi = 0 \tag{3.26}$$

so in the cavitation zone, $(\xi \geq 0) = 0$ and hence there is no flow through this boundary whereas in the full film zone $(\xi \geq 0) = 1$, the flow can only be outwards and will do so under ambient pressure, which is zero (relative pressure): $\left(q_\mathrm{z}n_\mathrm{z} > 0\right)\xi = 0$.

The bearing reaction forces to the rotor can be calculated by integrating the resulting pressure distribution from Equation 3.25 and the shear forces of the fluid over the rotating bearing surface:

$$\mathbf{F}_\mathrm{b} = \begin{bmatrix} F_\mathrm{X} \\ F_\mathrm{Y} \end{bmatrix} = -\int_{-L_b/2}^{L_b/2}\int_{-\pi R_\mathrm{s}}^{\pi R_\mathrm{s}} \begin{Bmatrix} p\cos\left(\frac{x}{R_\mathrm{s}}\right) + \tau\sin\left(\frac{x}{R_\mathrm{s}}\right) \\ p\sin\left(\frac{x}{R_\mathrm{s}}\right) - \tau\cos\left(\frac{x}{R_\mathrm{s}}\right) \end{Bmatrix} dxdz \tag{3.27}$$

where:

$$\tau = \frac{\mu_{\mathrm{oil}}\Omega_\mathrm{s}R_\mathrm{s}}{h} - \frac{h}{2}\frac{\partial p}{\partial x} \tag{3.28}$$

While performing the simulations for the Results Section, Section 3.4, we observed that the bearing forces originating from fluid shear stresses are negligibly small compared to

the forces arising from the hydrodynamic pressure, hence Equation 3.27 can be simplified by removing the terms related with τ.

Shaft tilting leads to an asymmetric pressure distribution in axial direction [193]. Therefore, the bearings also apply a torque to the shaft, which is calculated by:

$$M_X = \int_{-L_b/2}^{L_b/2} \int_{-\pi R_s}^{\pi R_s} p \cos\left(\frac{x}{R_s}\right) z \, dx \, dz \qquad M_Y = \int_{-L_b/2}^{L_b/2} \int_{-\pi R_s}^{\pi R_s} p \sin\left(\frac{x}{R_s}\right) z \, dx \, dz \tag{3.29}$$

3.2.5. THERMAL MODEL

As explained in the previous Section, the rotation speed of the shaft Ω_s induces a shear flow of oil which creates the hydrodynamic bearing forces $\mathbf{F}_b$. The rotation speed also induces velocity gradients along the height of the fluid film, which together with the viscous property of oil results in friction losses. These viscous friction losses cause an increase in temperature of the fluid film and its direct surroundings: the bearing housing and the shaft.

An analysis where the heat transfer in solids and fluids is treated as a coupled system, a *conjugate heat transfer analysis*, provides a first impression of the thermal behavior of the rotor-bearing system. Such an analysis can be found in Appendix B. Figure 3.5 presents an example of the temperature distribution predicted by the conjugate heat transfer model, based on the geometry specified in Table 3.1.

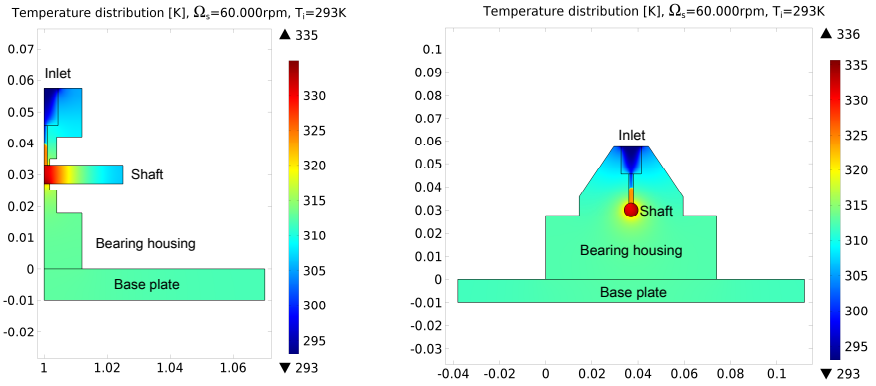

(a) Cross-sectional view in the YZ-plane at $X = 0$.

(b) Cross-sectional view in the XY-plane at $Z = 0$.

Figure 3.5: Temperature distribution based on a steady state conjugate heat transfer analysis at Ω_s=60.000rpm, T_i=293K. X, Y and Z coordinates in [m].

Furthermore, in the analysis described in Appendix B we observed that:

- the majority of temperature increase of the oil occurs in the inlet channel upstream of the oil film instead of in the thin film domain itself. This is caused by

mixing of recirculating hot oil from the bearing film with the cooler supplied oil in the inlet channel as well as by heat transfer from the bearing housing to the inlet channel. As a result, the oil which enters the oil film has a temperature similar to the bearing housing and not similar to to externally imposed oil feed temperature.

- the temperature distribution in the bearing housing is close to uniform.
- the temperature distribution in the shaft sections outside of the bearings has a significant thermal gradient in axial direction.
- only a small part of the friction heat is carried away by the oil. Most of the heat is dissipated by convection to ambient air from the shaft and the bearing housing. Therefore, we can not assume that the oil film is thermally isolated from the shaft and the bearing housing: adiabatic conditions can not be assumed.

Due to its high computational cost, the 3D conjugate heat transfer model is not suitable for time-transient analysis where thousands of time steps need to be analyzed. Instead, based on the results of the full 3D conjugate heat transfer model, a simplified *lumped thermal model* is constructed to predict the temperatures of the bearing housing and the shaft. In this model, the continuous temperature distribution is reduced to a discrete number of temperatures at key locations: the *thermal nodes* [195]. This reduction requires that the ratio of internal conduction resistance to external convection resistance is low, so that the temperature of a body can be assumed to be uniform over its volume [196]. This assumption can be shown to be correct using the results of the full 3D calculations.

Figure 3.6 gives a schematic representation of the rotor-bearing system and the thermal nodes selected in the lumped thermal model. The following assumptions are made in the thermal network model:

- heat transfer by radiation is neglected as the temperatures are expected to be moderate.
- the friction losses in the fluid film are regarded to be the only heat source: friction losses due to air friction are neglected.
- thermal interaction between the two bearings is neglected for simplicity, but can be included by simply coupling multiple individual thermal networks at node $T_{\text{s\_out}}$.
- the temperatures are considered to be in steady state conditions.

The last assumption is based on the thermal time constant of the rotor-bearing system, which is determined to be in the order of five seconds, see Appendix B. Thus, the themodynamics are much slower than the high frequencies which characterize the rotor-bearing structural and fluid dynamics [90]. Therefore, the thermal network model only features steady-state components.

Figure 3.7 presents the thermal network: friction heat Q_ψ is generated in the fluid film and is transported via three paths. The upper path represents transport of heat by

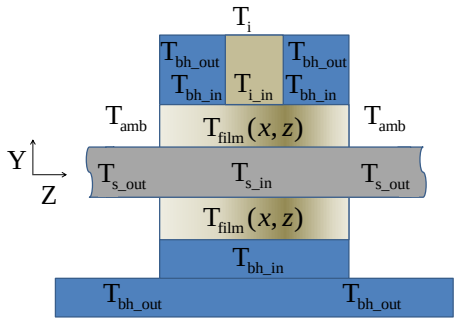

Figure 3.6: Cross-sectional schematic view of the rotor-bearing system indicating the nodes used in the thermal network model. $T_{film}(x, z)$ is the temperature distribution as described by Equation 3.31. All other thermal nodes are lumped scalar values.

the oil flow, which enters the bearing at temperature T_i. The middle path represents the transport of heat via the bearing housing and the lower path represents transport of heat via the shaft. The coefficients of heat transfer of the thermal network model and a comparison between the thermal network model and the conjugate heat transfer model can be found in Appendix B. The thermal network method presented here can be extended to include —for example— the heat input from a hot turbine or from losses in a generator [197]. For each bearing, an individual thermal network model is created.

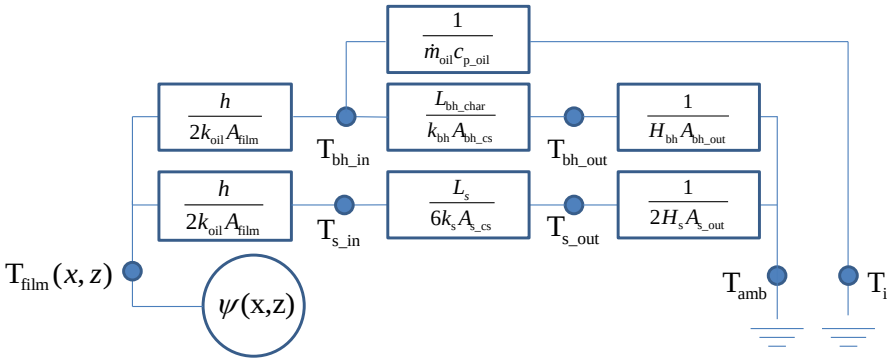

Figure 3.7: The thermal network model of the rotor-bearing system including the bearing housings. The friction heat ψ partly exits the bearing by heating the lubricant whichs flows through the bearing $\dot{m}_{oil}$ and partly by heat conduction and convection from the lubricant to the rotor and the bearing housing to the ambient air. Details on the heat transfer coefficients can be found in Appendix B.

The thermal network model describes how the heat is transported from the fluid film. The temperature distribution in the fluid film itself is evaluated at the plane halfway the film thickness, at $y = h/2$, and is described by the energy equation [101], where c_{p_oil} represents the specific heat capacity, q_x represents the flow in circumferential direction and k_{oil} is the thermal conductance:

$$\begin{aligned}&\frac{\partial}{\partial x}\left(-k_{\text{oil}}h\frac{\partial T_{\text{film}}}{\partial x}+c_{\text{p\_oil}}q_{\text{x}}T_{\text{film}}\right)+\frac{\partial}{\partial z}\left(-k_{\text{oil}}h\frac{\partial T_{\text{film}}}{\partial z}+c_{\text{p\_oil}}q_{\text{z}}T_{\text{film}}\right)+....\\&\rho_{\text{oil}}c_{\text{p\_oil}}h\frac{\partial T_{\text{film}}}{\partial t}=\psi-\frac{2fk_{\text{oil}}}{h}\left(2T_{\text{film}}-T_{\text{s\_in}}-T_{\text{bh\_in}}\right)\end{aligned}\tag{3.30}$$

In words, this means: *convective heat transer within the fluid film + conduction within the fluid film + thermal storage = viscous dissipation − heat transfer to the surrounding walls.*

Due to cavitation, conduction can only take place in x-direction at fraction f of the fluid film. In addition, as we have assumed streamer type cavitation, conduction in z-direction is zero in the cavitated area. Hence, the energy equation is written as:

$$\begin{aligned}&\frac{\partial}{\partial x}\left(-fk_{\text{oil}}h\frac{\partial T_{\text{film}}}{\partial x}+c_{\text{p\_oil}}q_{\text{x}}T_{\text{film}}\right)+\frac{\partial}{\partial z}\left(-(\xi>0)k_{\text{oil}}h\frac{\partial T_{\text{film}}}{\partial z}+c_{\text{p\_oil}}q_{\text{z}}T_{\text{film}}\right)+...\\&f\rho_{\text{oil}}c_{\text{p\_oil}}h\frac{\partial T_{\text{film}}}{\partial t}=\psi-\frac{2fk_{\text{oil}}}{h}\left(2T_{\text{film}}-T_{\text{s\_in}}-T_{\text{bh\_in}}\right)\end{aligned}\tag{3.31}$$

where the friction loss of the bearing ψ over the bearing surface per unit area arises from both pressure work and shear losses:

$$\psi=\frac{(\xi>0)\,h^3{P_0}^2}{12\mu_{\text{oil}}}\left(\left(\frac{\partial\xi}{\partial x}\right)^2+\left(\frac{\partial\xi}{\partial z}\right)^2\right)+\frac{f\mu_{\text{oil}}{\Omega_{\text{s}}}^2{R_{\text{s}}}^2}{h}\tag{3.32}$$

The distributed temperature field in the film is coupled to the lumped thermal network nodes by Equation 3.31. The total friction losses of the bearing can be calculated by:

$$\dot{Q}_{\psi}=\int_{-L_{\text{b}}/2}^{L_{\text{b}}/2}\int_{-\pi R_{\text{s}}}^{\pi R_{\text{s}}}\psi\,dx\,dz\tag{3.33}$$

As the film temperature T_{film} increases, its viscosity decreases. In addition, the viscosity decreases with increasing shear rate. In order to account for these effects, we make use of the relation between oil viscosity, shear rate and temperature by combining the Vogel equation with the Cross equation [198]:

$$\mu_{\text{oil}}(T_{\text{film}},\dot{\gamma})=ae^{\frac{b}{(T_{\text{film}}+c)}}\left(r+\frac{1-r}{1+(K\dot{\gamma})^d}\right)\tag{3.34}$$

using the constants a, b, c, d and r corresponding to the specific type of oil, see Appendix A and the shear rate $\dot{\gamma}$ is defined as the local fluid velocity divided by the local film thickness. The viscosity of the oil is assumed to be independent of pressure, as the peak pressures under dynamic load are expected to be moderate [51]. Furthermore, at moderate temperature and pressure conditions, all other lubricant properties, such as density ρ_{oil} and specific heat $c_{\text{p\_oil}}$, can be assumed to be constant as well [77]. The thermal boundary conditions for the fluid domain depicted in Figure 3.4b are as follows:

- The oil enters the bearing via the inlet domain at lumped temperature T_{film}.
- The oil leaves the bearing via the sides at $z=\pm\frac{L_b}{2}$ under condition $\frac{dT_{\text{film}}}{dz}=0$.
- Periodic boundary conditions are imposed on the edges $x=\pm\pi R_s$.

3.2.6. COUPLED RUN-UP NUMERICAL PROCEDURE

The Reynolds equation (Equation 3.25) is solved together with the energy equation (3.31) and the structural dynamic equation, Equation 3.16, using a Galerkin finite element method [199]. The Reynolds equation requires numerical stabilization in crosswind and streamline direction, for which artificial diffusion is applied, as developed by Alakhramsing [108]. Furthermore, the energy equation is stabilized using SUPG. A second order backward differentiation scheme is used for time integration.
A mesh convergence study was performed by comparing the time-transient response at several operating conditions based on gradually refining the mesh until no significant differences in response were observed.
The simulation of a run-up experiment of 250rpm to 60.000rpm in 20s requires a computation time in the order of 100 hours to 200 hours on four 3.6GHz processors, depending on the chosen operating conditions of the rotor-bearing system. In general: the higher the eccentricity ratio during a run-up (such as during oil whirl), the higher the computation time. A reduction of these calculation times is possible by further tuning the discretization and solver settings as the current solver settings are tuned for numerical robustness instead of speed.

3.3. TEST SETUP

3.3.1. DESCRIPTION OF THE TEST SETUP

For the validation of our rotor-bearing model, a test setup has been constructed. The setup comprises a Laval rotor supported by two journal bearings and is driven by a 250W permanent magnet DC motor, see Figure 3.8.

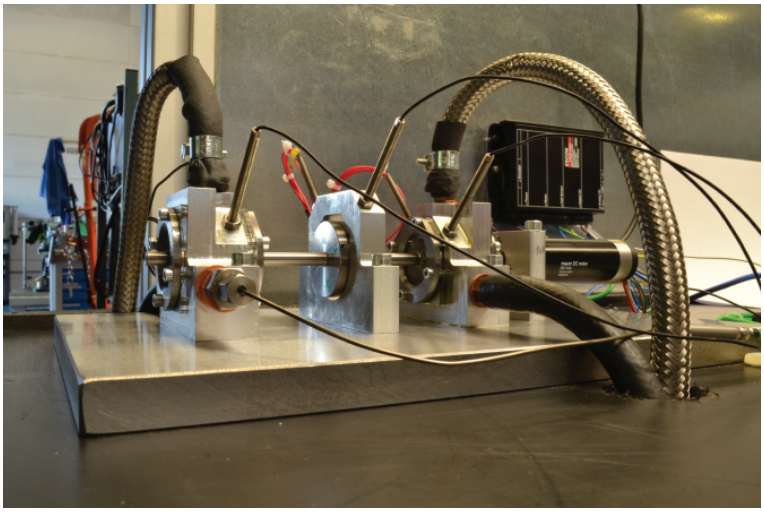

Figure 3.8: Test setup used for the experiments in this Section. The rotor is driven by an electric motor, shown at the right hand side of the setup. Oil is supplied to the bearings by the braided hoses at conditioned pressure and temperature. Dimensions and material properties are listed in Table 3.1.

The motor is coupled to the rotor by a compliant silicone rubber coupling element which should minimize the influence of motor vibrations on the rotor vibrations and vice versa. Furthermore, it limits the effect of misalignment of the rotor with respect to the motor. The rotor itself was manufactured to be concentric within 2 μm to minimize the influence of manufacturing imperfections on the dynamic behavior. Technical drawings of the components of the test setup can be found in Reference [200].

The radial displacements of the rotor are measured by eddy current displacement transducers, see Figure 3.9: two orthogonally mounted sensors per location are used to measure the shaft position at each location.

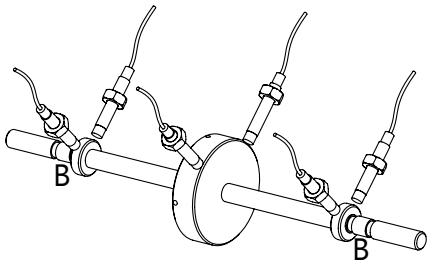

Figure 3.9: Rotor with orthogonally placed displacement sensors. Three locations are measured: adjacent to each journal bearing and on the central disk. The amount of unbalance on the rotor can be changed by turning grub screws in radial direction into the central disk. Bearing locations are marked by B. Illustration by Te Wierik, [200].

Figure 3.10 gives a labeled overview of the most important parts of the test setup.

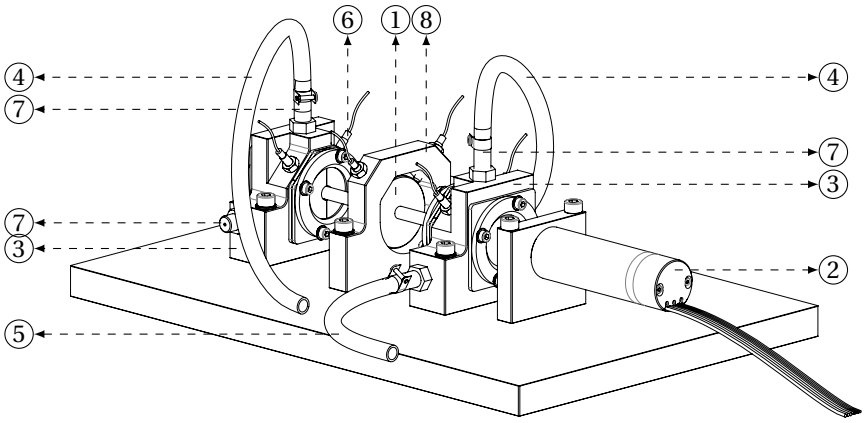

Figure 3.10: Schematic overview of the test setup. The rotor (1) is driven by the electric motor (2). The bearing housings (3) have an oil inlet (4) and outlet (5) and contain shaft displacement sensors (6) and thermocouples (7). The displacement of the central disk is measured by displacement sensors mounted in the central bracket (8). Drawing edited from [200].

Not shown in Figure 3.10 though noteworthy: the mass flow of oil is measured at the oil outlet by a digital weighing scale. Furthermore, the bearing friction losses are measured by substracting the no-load electric motor power (i.e. from a run without the Laval rotor attached to the motor) from the actually consumed motor power.

Table 3.1. Parameters for the Laval rotor supported by plain journal bearings .

	Variables			
	Name	Value	Unit	Description
Rotor	R_s	3	mm	Radius of shaft
	R_d	17.5	mm	Radius of center disk
	R_m	6	mm	Radius of measurement disk
	L_s	166.6	mm	Rotor length, excl. coupling length
	L_d	9	mm	Length of center disk
	L_m	4	mm	Length of measurement disk
	L_{s1}	120	mm	Length of bearing span
	L_{s2}	105.4	mm	Length of measurement disk span
	I_{rot}	$10.4{\cdot}10^{-6}$	kg·m^2	Rotor inertia in rotating direction
	m_{rot}	105.8	g	Rotor mass
Bearing	L_b	3.6	mm	Length of bearing
	C	11	um	Clearance of bearing
	R_i	1	mm	Radius of bearing inlet
Oil (Mobil1 5W30)	ρ	855	$^{kg}/_{m^3}$	Density
	κ_{oil}	0.145	$^{W}/_{m\cdot K}$	Thermal conductance
	C_p	2.1	kJ/kg·K	Thermal capacity
	A_{oil}	$0.44{\cdot}10^{-3}$	Pa·s	Viscosity temperature dependence
	B_{oil}	633	^oC	Viscosity temperature dependence
	C_{oil}	88.6	^oC	Viscosity temperature dependence
	r_{oil}	0.5	-	Viscosity shear dependence
	m_{oil}	0.8	-	Viscosity shear dependence
	K_{oil}	$7.2{\cdot}10^{-7}$	s^{-1}	Viscosity shear dependence

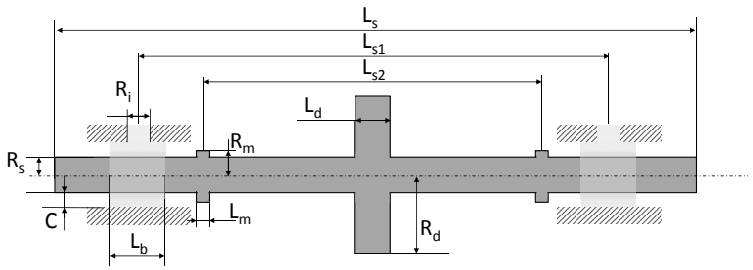

Figure 3.11: Dimensions of the Laval rotor on plain journal bearings.

3.3.2. EXPERIMENTAL PROCEDURE

Before any tests were conducted, the rotor was balanced in-situ by one-plane balancing to minimize the amount of residual unbalance. All run-ups are performed at a rotation speed from 250 rpm to 52.000 rpm with an angular acceleration of $1000^{\text{rpm}}/_{\text{s}}$ while sampling the displacement sensors at a frequency of 51.2kHz. The repeatability was investigated by performing multiple runs throughout the test session at reference input conditions. Five runs at reference conditions were made, where the deviations between these five runs were less than one percent.

3.4. RESULTS

Having presented the numerical model in Section 3.2 and the test setup in Section 3.3, the results of both will now be compared to see if we can predict the dynamic behavior of the flexible Laval rotor supported by plain journal bearings. First, the eigenfrequencies of the uncoupled rotor are evaluated, followed by a modal analysis of the linearized rotor-bearing system. The rest of this Section will present simulation results versus measurement results of the time-transient response of our Laval rotor during a runup.

3.4.1. MODAL ANALYSIS OF THE UNCOUPLED ROTOR

Modal analysis is performed on the rotor model [20], where the rotor is in free-free conditions without the presence of bearings and under non-rotating conditions $\Omega_s = 0$ rpm. As can be seen in Table 3.2, the results from the rotor model corresponds well with experimental results obtained by hammer impact testing:

Table 3.2: Result of modal analysis of the rotor under non-rotating, free-free conditions.

	Numerical model	Hammer impact measurement
Eigenfrequency [Hz]	761	764

The first eigenfrequency at 761Hz is a bending mode with the shaft ends moving in phase. All other eigenfrequencies, including the torsional and axial modes, have an eigenfrequency over 2kHz and are therefore out of the excitation range of the synchronous unbalance excitation of the rotor.

3.4.2. MODAL ANALYSIS OF THE LINEARIZED ROTOR-BEARING SYSTEM

The bearing system is known to be highly non-linear in terms of stiffness and damping terms. However, when we linearize the bearing forces around a static equilibrium condition, we can perform a linear modal analysis. The equilibrium point that we use is the equilibrium of the rotor under gravity load. The assumption of finding a static equilibrium is not valid in case the rotor experiences (severe) whirl. However, the results from this linear analysis are often a good indication of the actual behavior of the rotor-bearing system in reality [69].

We now make the following assumptions to find an analytical expression as a base for our simplified linearized bearing coefficients:

- the flow in circumferential direction is negligible compared to the flow in axial direction (*short bearing assumption*) [201],
- the influence of the oil supply channel is ignored,
- the oil is isoviscous,
- Gümbel cavitation conditions are applied, which means that only the positive part of the pressure distribution predictted by the Reynolds equation is taken into account,
- the shaft is always aligned with the bearing bore.

These assumptions are only used for the modal analysis in this Section. For the remainder of this study, these assumptions do not hold: instead the assumptions described in the previous sections of this Chapter are applied.

Under static equilibrium, the bearing forces in radial and tangential directions can then be expressed as [201]:

$$F_{\text{rad}} = \frac{\mu_{\text{oil}} R_{\text{s}} {L_{\text{b}}}^3 \Omega_{\text{s}} \varepsilon^2}{C^2 \left(1-\varepsilon^2\right)^2} \qquad F_{\text{tan}} = -\frac{\mu_{\text{oil}} R_{\text{s}} {L_{\text{b}}}^3 \pi \Omega_{\text{s}} \varepsilon}{4C^2 \left(1-\varepsilon^2\right)^{3/2}} \tag{3.35}$$

Figure 3.12 schematically depicts these forces:

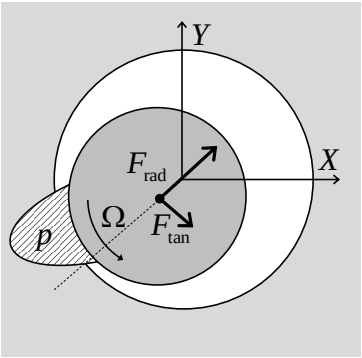

Figure 3.12: Visualization of radial and tangential forces from the oil film to the bearing.

Based on these expressions, the 2×2 linearized stiffness and damping matrices of each bearing can be calculated, as described by Hamrock [201]. Typically, these matrices are not symmetric and the cross-coupling stiffness terms are often larger than the principal stiffness terms. Moreover, depending on the instantaneous eccentricity, one of the cross-coupling stiffness terms can even be negative, causing a (linearly) unstable system [20].
Based on the linearized stiffness and damping matrices, an eigenvalue analysis of the linearized rotor-bearing system is performed, which results in the Campbell plot of Figure 3.13a and the associated mode shapes in Figure 3.13b. The stability of the solution is judged by the sign of the real part of the calculated eigenvalues.

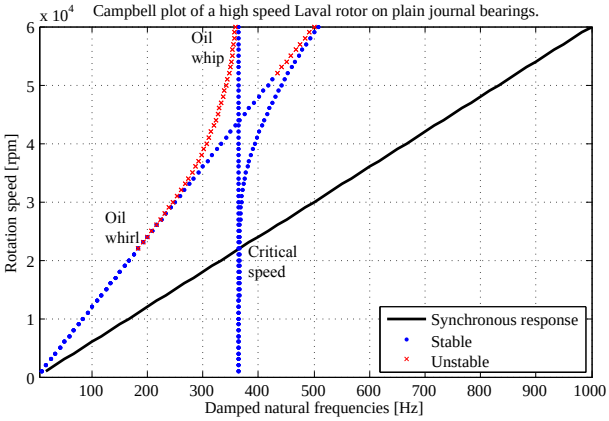

(a) Campbell plot predicting a critical speed traversal at 22.000rpm, the onset of oil whirl at 21.800rpm and the transition to oil whip above 40.000rpm.

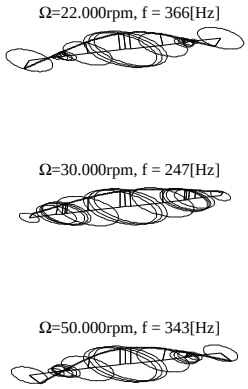

(b) Mode shapes. Upper: near the critical speed. Middle: in oil whirl condition. Lower: in oil whip condition.

Figure 3.13: Results of the eigenvalue analysis of the linearized rotor-bearing system.

The Campbell plot shows a typical response of a flexible Laval rotor on plain journal bearings:

- traversal of a critical speed caused by the first shaft bending mode at $\Omega_{\text{critical}} = 366\text{Hz} = 21960\text{rpm}$.
- above this critical speed, the first rigid body mode (a cylindrical mode, see Figure 3.13b) becomes linearly unstable at $\omega_{\text{whirl}} = \Omega_{\text{critical}}/2 = 183\text{Hz}$.
- at rotation speeds above 40.000rpm, the whirl locks into the first shaft bending mode, resulting in a whip mode which combines rigid body motion and bending motion.

Furthermore, a second whirling mode is predicted to become unstable around 52.000rpm. This is the conical mode of the shaft, a pure rigid body whirl.

As further detailed in [69], it can be concluded that predictions based on this relatively simple linearized short bearing model are capable of predicting the important frequencies of the rotor-bearing system relatively well. However, it generally underestimates the onset speed of whirl and can not be used to predict the amplitudes when whirl occurs, because the non-linearities become dominant then.

3.4.3. RESULTS AT REFERENCE OPERATING CONDITIONS

Having performed the linear rotordynamic analysis, we now have an understanding of the rotor eigenfrequencies and their corresponding mode shapes. The next step is to perform a run-up analysis. To that end, we perform a run-up from 1000rpm to 52.000rpm in 60 seconds. Although not included in this thesis, some run-ups up to 60.000 rpm have

also been performed, but did not show any additional interesting behavior over runs up to 52.000 rpm.

The *reference operating conditions* are as follows:

- The bearings are supplied with oil at a supply pressure of 2.8 bar and a temperature of 298K.
- The ambient temperature is 298K.
- An unbalance amount of 250mg·mm is applied on the central disk.

Figure 3.14 presents the measurement data of all six shaft displacement sensors during a run-up.

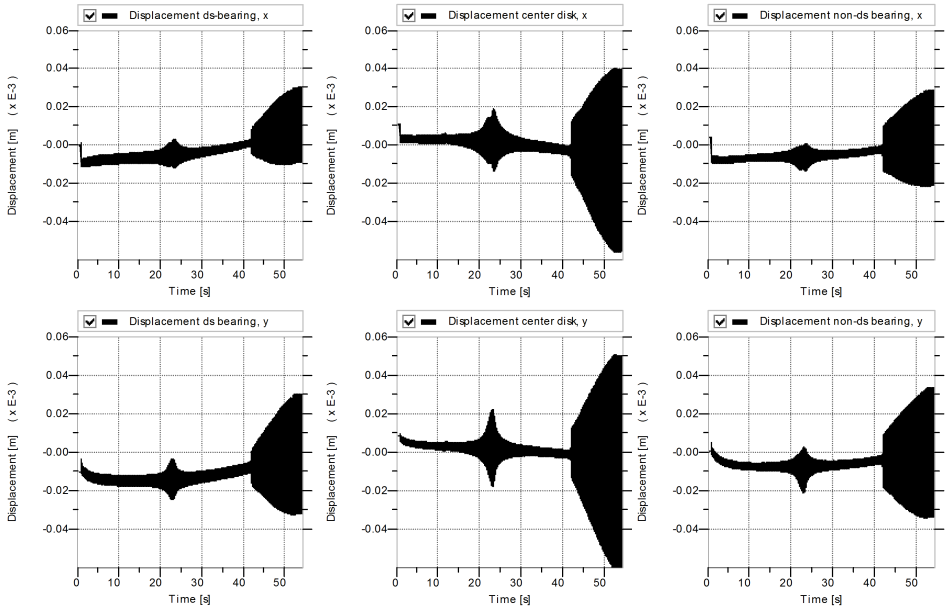

Figure 3.14: Raw measurement data of shaft displacement measured on three locations in X- and Y-direction under reference operating conditions. The response between 20s and 30s is the traversal of the critical speed. The increase from 42s onwards is the onset of oil whirl followed by oil whip. The gradual change of the mean value of the shaft displacements is caused by the interaction of hydrostatic feed pressure, gravity forces and hydrodynamic pressure: the shaft moves towards the center as the rotation speed increases.

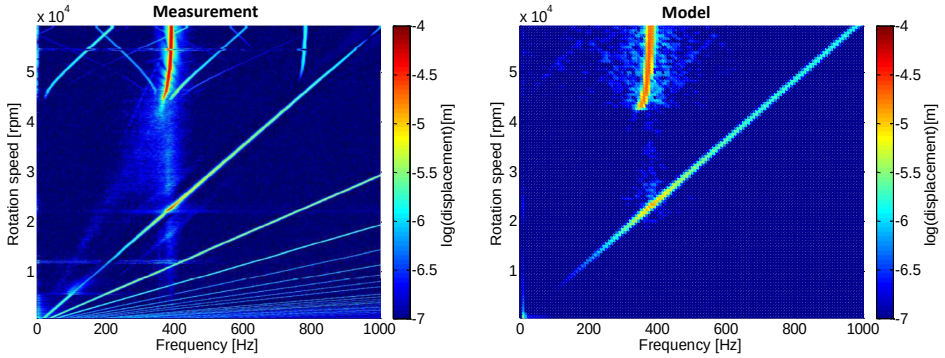

Figure 3.15: Waterfall plots of the rotor response based on measurement data (left) and the model output (right). These waterfall plots display the frequency content of the displacement of the measurement disk as a function of the rotation speed, at reference operating conditions. Clearly noticeable is the synchronous response: the diagonal line $\omega = \Omega_s$ which traverses a critical speed at 23krpm. Furthermore, the region for which $\omega < \Omega_s$ contains the sub-synchronous response, where the occurence of an oil whirl at speeds above 40krpm can be observed.

The same data is also displayed in Figure 3.15: *waterfall plots* of the response of the rotor, measured on the small disk adjacent to the bearing, see Figure 3.9. The data shows the occurrence of a critical speed traversal around $\Omega_{\text{critical}} = 22.800\text{rpm}$. A sub-synchronous oil whirl starts at a rotation speed of approximately 44.000rpm at a frequency of $\omega_{\text{whirl}} = 360\text{Hz}$. At rotation speeds over 50.000rpm, the oil whirl locks into the first shaft bending mode to form a whip at $\omega_{\text{whip}} = 380\text{Hz}$.

The measurement shows some super-synchronous response, probably caused by the unroundness of the measurement surface, which is not included in the model. Furthermore, the measurement shows *modulation sideband frequencies* in the sub-synchronous regime. These modulation sidebands are responses composed of linear combinations of the dominant responses (for example: $\omega_{\text{sb1}} = \Omega_s - \omega_{\text{whirl}}$, $\omega_{\text{sb2}} = 2\omega_{\text{whirl}} - \Omega_s$) and are a result of non-linear bearing characteristics [11]. The sidebands are also observed in the simulation output, although being less pronounced. Overall, based on Figure 3.15, the correspondence between the measurement and the model is good.

The results from this runup are also in good agreement with the prediction from the linearized model presented in Figure 3.13a: the critical speed is correctly predicted and the oil whirl frequency corresponds well. The main discrepancy between the prediction of the linearized model and the measurement results is the onset speed of the oil whirl: the linearized model predicts 22krpm whereas the measurement result and the non-linear model both show that the oil whirl only starts at 44krpm. It is expected that the external feed pressure, which is not included in the linearized model, increases the stability of the rotor-bearing system by forcing the rotor to run at a high eccentricity. This influences the onset speed of oil whirl, as will be shown in Section 3.4.7.

Figure 3.16 depicts the intensity of the synchronous and sub-synchronous whirl orbits. Over a run-up, the displacement of the locations near the bearing as well as on the center disk (see Figure 3.9) are filtered using bandpass filters for the synchronous component $0.9\Omega_s < \omega < 1.1\Omega_s$ and the sub-synchronous component $0.1\Omega_s < \omega < 0.9\Omega_s$. The data of the non-driveside bearing is used here, to minimize the influence of the rotor-motor coupling element.
The response measured near the bearing is actually larger than the bearing clearance. This is due to bending of the rotor: as the rotor displacement is measured on a disk adjacent to the bearing (see Figure 3.9), the shaft bending causes the measured amplitudes to be magnified. The values predicted by the model were based on the same location adjacent to the bearing.

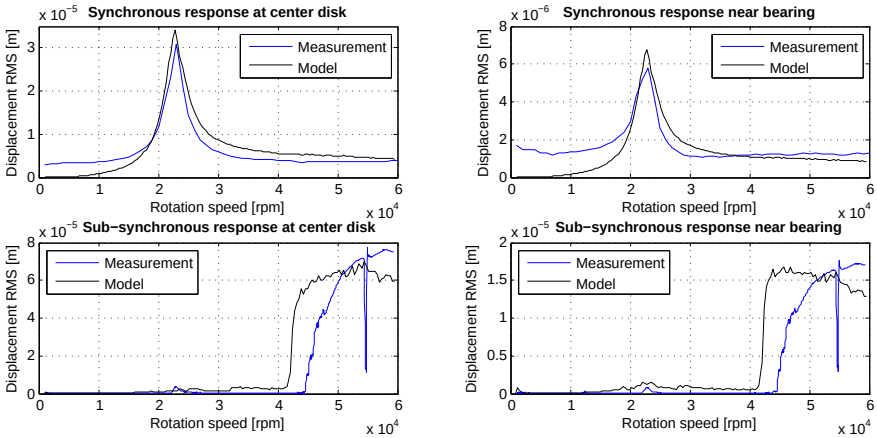

Figure 3.16: Synchronous and sub-synchronous rotordynamic response at reference operating conditions.

The critical speed and its amplitude are well predicted by the model. At low rotation speeds, the experiment shows some synchronous response which most likely comes from residual out-of-plane unbalance or slight shaft bow. The amplitude of the sub-synchronous prediction is in good agreement with the measurement result. However, the model underpredicts the onset speed of oil whirl by some 2000rpm.

Figure 3.17 shows the friction losses in a bearing, the average film temperature, the average viscosity and the oil flow rate of a single bearing as a function of rotation speed. The measured bearing friction losses are typically 20% lower than the predicted friction losses. A possible explanation is that the shear rate-viscosity coefficients of the oil is incorrectly modeled: we make use of shear rate coefficients based on values found in literature [198]. Possibly, the oil which was used during the experiments showed more shear thinning than expected, which results in a decrease in friction losses.
The measured temperatures are typically 2K-5K higher than the predicted temperatures. It should be mentioned that the temperatures were measured at the exit of the bearing, where the oil might be slightly warmer than the average film temperature, which could explain some of the difference. Another cause for the deviation might be in the thermal

network model, which can underpredict the temperature of the boundaries of the fluid domain by 2K, as shown in Figure B.8. This difference in temperature is reflected in the average viscosity, which is inversely proportional to the temperature.
The increased oil flow near the critical speed and during oil whirl is observed in the measurements and the simulation results. The model, however, predicts the oil flow rate generally to be slightly lower. This could be related to the oil film temperature. We believe the oil film temperature during the experiments was slightly higher than predicted, which resulted in a higher oil flow rate as the lubricant viscosity dropped.

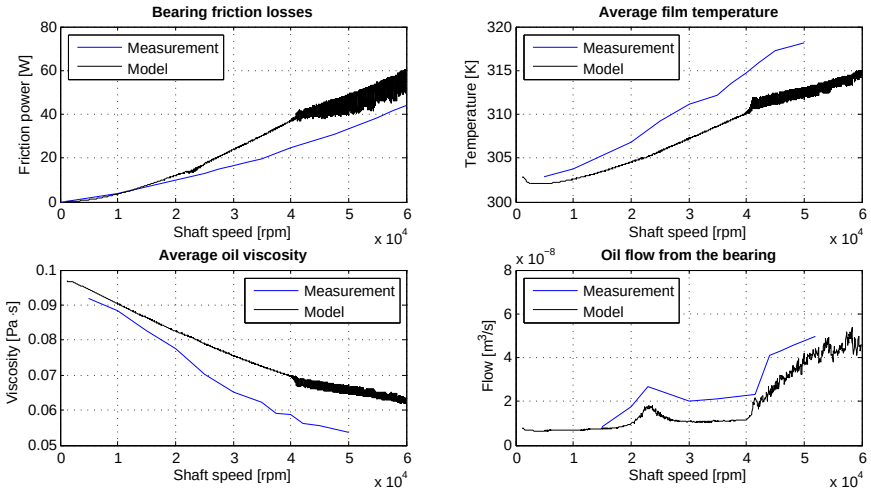

Figure 3.17: Friction losses, film temperature, average viscosity and oil flow rate of the non-driveside bearing.

Figure 3.18 gives insight in the state of the bearing obtained at rotation speed Ω_s = 40.000rpm. At the particular moment the data was captured for these figures, the shaft operated at an eccentricity ratio of $\epsilon = 0.4$. Shaft tilting as per Equation 3.21 is taken into account, which explains why there is asymmetry over the axis $z = 0$.
The bearing creates a peak pressure near the minimum film thickness point. At this point, the friction losses and temperature are at their maxima. The bearing is partly cavitated, as can be seen in the mass fraction being smaller than one on two locations: next to the maximum pressure point and at the zone where the film thickness is diverging in circumferential direction, at $x = 3 \cdot 10^{-3}$m.
The effect of the supply channel on the film state can also be seen in these figures: the pressure at the inlet is equal to p_i. The inflow of oil at pressure p_i prevents the film from cavitation around the inlet. Furthermore, the oil which flows in at the inlet is relatively cold compared to the film temperatures.
The maximum pressure in the fluid film is generally in the order of $1 \cdot 10^6$Pa, and hence we can safely neglect the elasticity of the shaft and the bearing housing. The shear rates are typically in the order of $10^6 s^{-1}$ and therefore the oil operates in the non-Newtonain regime. The Reynolds numbers indicate that the flow in the bearing is always laminar and hence we can neglect the fluid inertia terms and use Reynolds equation.

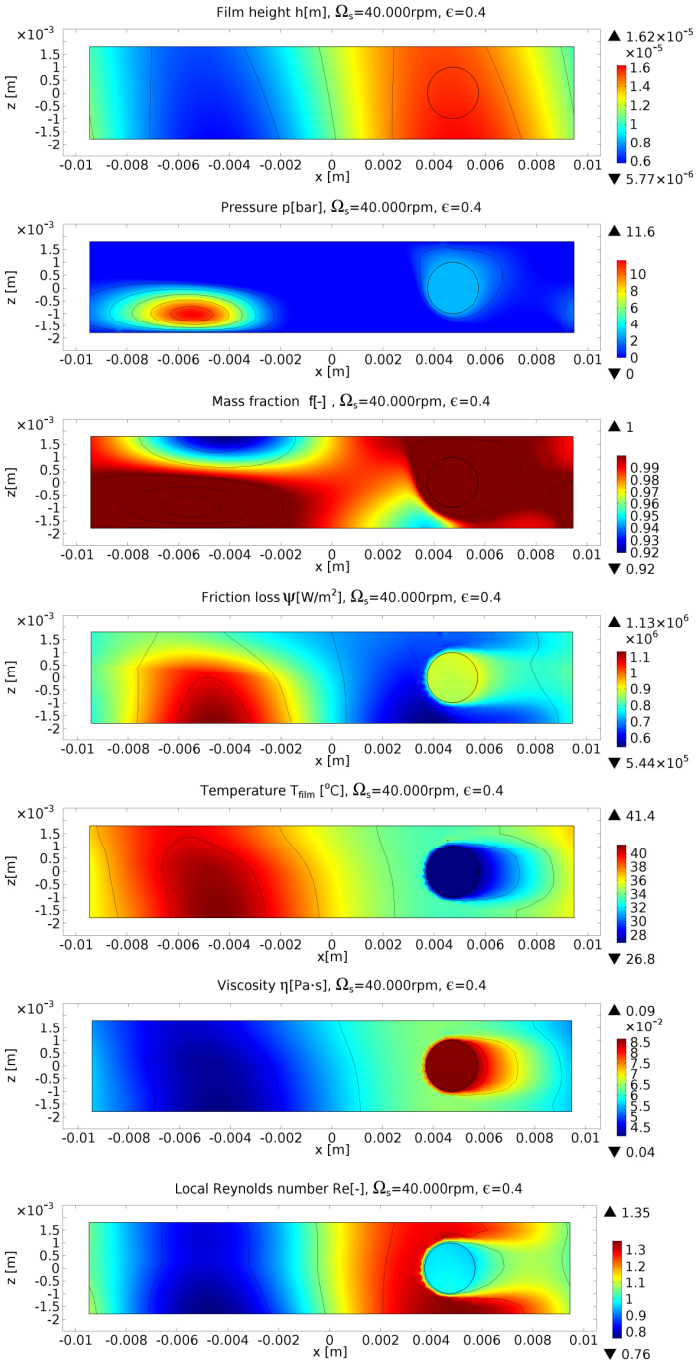

Figure 3.18: Contour plots of the bearing fluid domain representing its state at a rotation speed of Ω_s = 40.000rpm and an eccentricity ratio of 0.4. The data is taken from a run-up simulation of the coupled rotor-bearing system. The absence of symmetry over the axis z=0 is due to shaft tilting.

3.4.4. RESULTS AT VARIOUS OPERATING CONDITIONS

The influence of unbalance, oil feed temperature, oil feed pressure and bearing clearance on the rotordynamic response and the friction losses were studied using the following experimental scheme:

Table 3.3: Experimental scheme used for testing

	Lower value	Reference condition	Upper value
Rotor unbalance [mg·mm]	50	175	350
Oil feed temperature [K]	298	310	348
Oil feed pressure [Pa]	1e5	3e5	5e5

All variations of these conditions were measured on the test setup and simulated with the rotor-bearing model. Additionally, some runs with a bearing clearance of 15µm instead of the reference 11µm were also performed, but these where prematurely ended when the oil whirling amplitudes became excessive. All results will now be presented: the influence of each variable is displayed and it is investigated if the model is able to follow the same trends as observed during the measurements.

3.4.5. INFLUENCE OF ROTOR UNBALANCE

The influence of unbalance on the rotor is most noticeable at the critical speed, as can be seen in the measurement results in Figure 3.23.

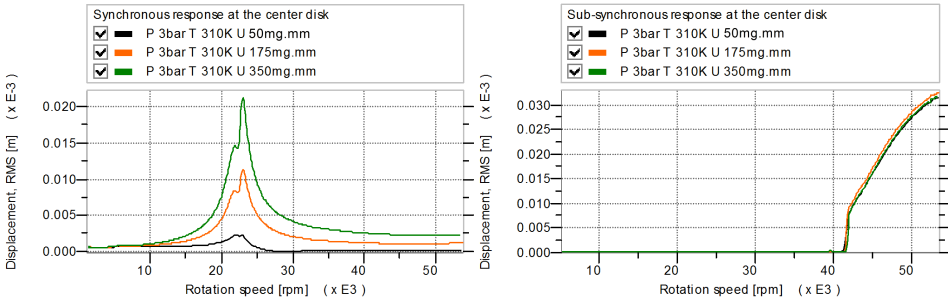

(a) Measurement result

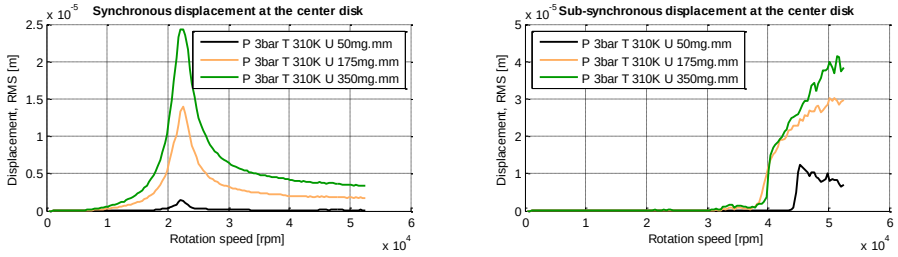

(b) Simulation result

Figure 3.19: Influence of rotor unbalance on the rotordynamic response of the rotor-bearing system.

The amplitude of vibration increases linearly with unbalance, as can also be seen in Figure 3.23. The onset speed of whirl, the whirl frequency and the whirl amplitude did not change significantly over the tested unbalance range.

The simulation results show a similar trend, as can be seen in Figure 3.19b. One clear discrepancy is observed between the simulation results and the experimental results: the model predicts a very late onset of oil whirl for the 50mg·mm condition, which is currently not fully understood. Possibly, the measurement setup contained some additional out-of-plane unbalance or misalignment error which was not included in the model which may interfere with accurate prediction of the onset speed of whirl at minimum unbalance conditions.

3.4.6. INFLUENCE OF OIL FEED TEMPERATURE

An increase of oil supply temperature from 298K to 348K results in a decrease of the onset speed of oil whirl from 43krpm to 30krpm. The amplitude at the critical speed decreased with increasing temperatures as did the the amplitude of oil whirl. The friction losses decreased with an increase of temperature, as can be seen in Figure 3.24a.

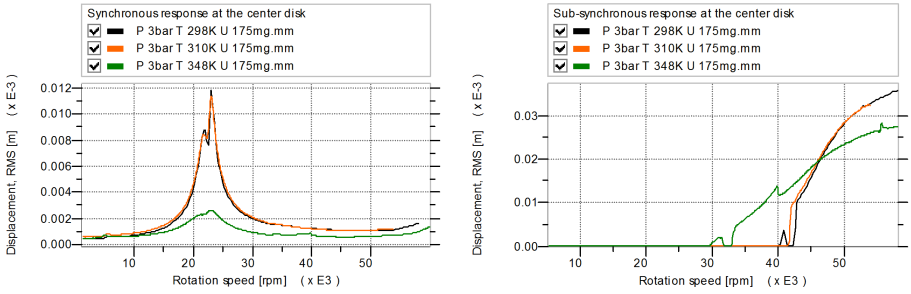

(a) Measurement result

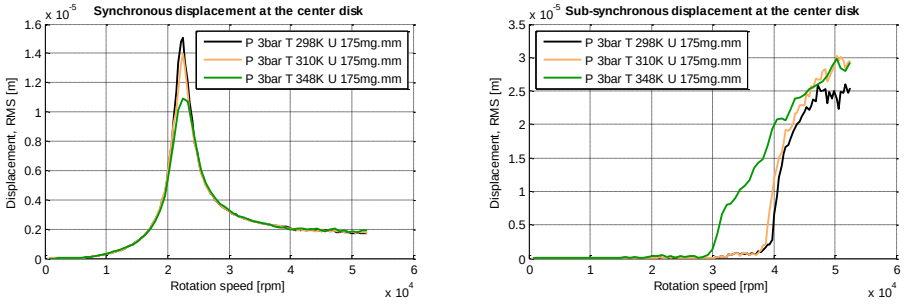

(b) Simulation result

Figure 3.20: Influence of oil feed temperature on the rotordynamic response of the rotor-bearing system.

The model results in Figure 3.20b show a similar trend in the synchronous response and in the onset speed of oil whirl. The influence of temperature on the whirl amplitude

seems to be less distinguished in the model.
As can be seen in Figure 3.21: at hot oil conditions, a half-speed oil whirl precedes the whirl/whip transition. The half-speed oil whirl makes a jump to the whirl/whip trace at a rotation speed of 40krpm.

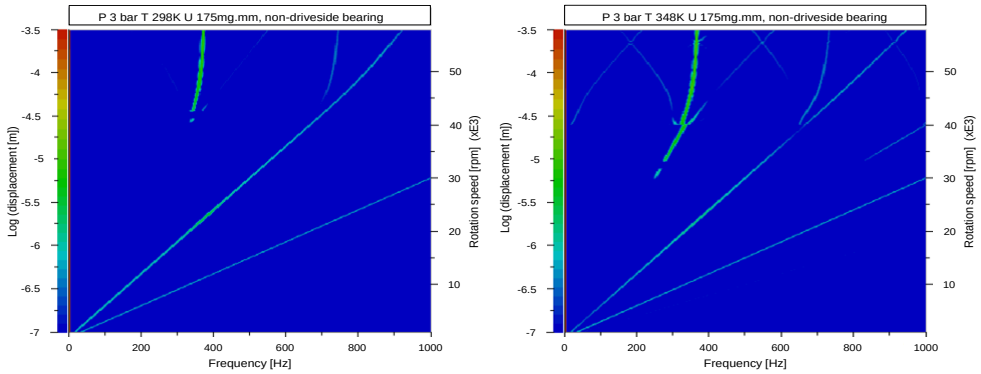

Figure 3.21: Measurement results: waterfall plots of the rotor displacement under cold (left) and warm oil conditions (right). Under warm oil conditions, a half-speed whirl precedes the whip transition.

3.4.7. INFLUENCE OF OIL FEED PRESSURE

The influence of the supply pressure can be seen in Figure 3.22.

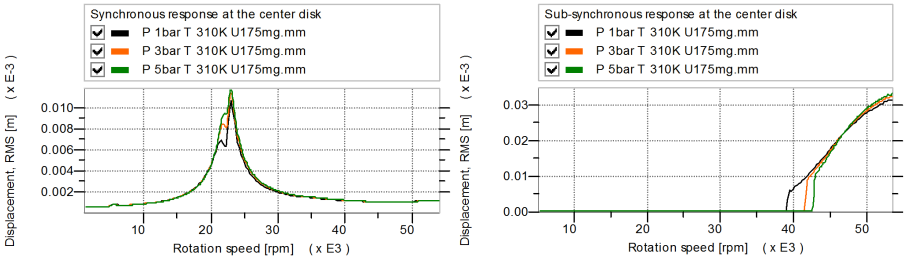

(a) Measurement result

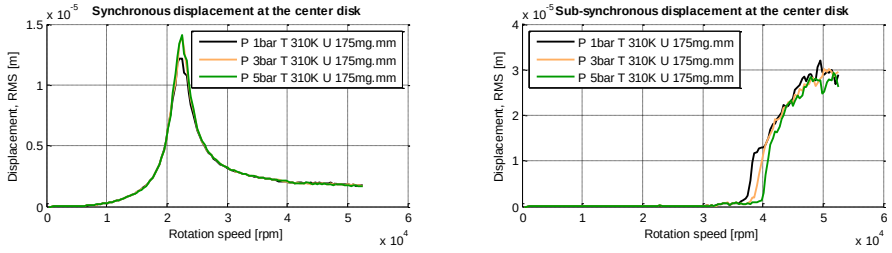

(b) Simulation result

Figure 3.22: Influence of oil feed pressure on the rotordynamic response of the rotor-bearing system.

A higher oil feed pressure delays the onset speed of oil whirl. It is considered that the hydrostatic pressure of the supply channel pushes the rotor to an eccentric position. Hence, the rotor stability is increased and the onset of instability is delayed.

The peak amplitude at the critical speed increases with increasing supply pressure: the peak amplitude at 5 bar is 10% higher than at a feed pressure of 1 bar. The whirl amplitudes did not change significantly with increasing oil feed pressure. A very similar response was observed by simulations, as can be seen in Figure 3.22b.

3.4.8. INFLUENCE OF BEARING CLEARANCE

The influence of changing the bearing clearance is most pronounced in the unbalance response at the critical speed, as can be seen in Figure 3.23. The model predicts a similar trend, albeit less pronounced in difference between 11µm and 15µm. Furthermore, the oil whirl amplitudes with the 15µm clearance bearing were also larger, however, the runups with 15µm clearance bearings were stopped at 45.000rpm as a safety precaution.

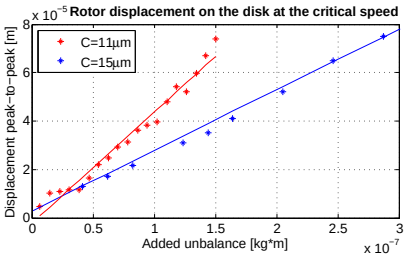

(a) Measurement result

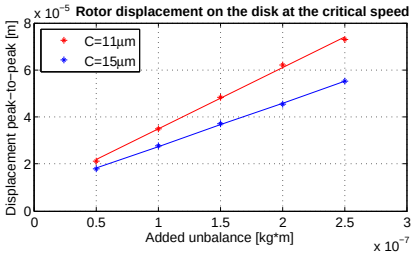

(b) Simulation result

Figure 3.23: Influence of changing the clearance of the bearing on the unbalance response of the rotor, measured on the central disk. Oil supply conditions: p_i=2bar T_i=298K.

3.4.9. FRICTION LOSSES

The bearing friction losses were found to be independent of the amount of unbalance. A minor dependence on feed pressure was observed, as well as a clear influence on oil feed temperature, as depicted in figure 3.24. Unfortunatly the friction losses were not measured during the test runs according to the complete experimental scheme of Table 3.3; instead, only a limited range of variations was used to measure the variation of the friction losses.

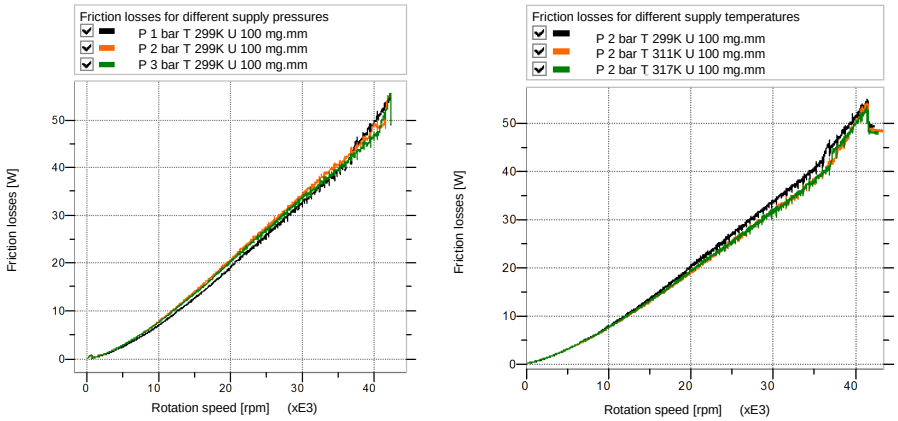

(a) Measurement result

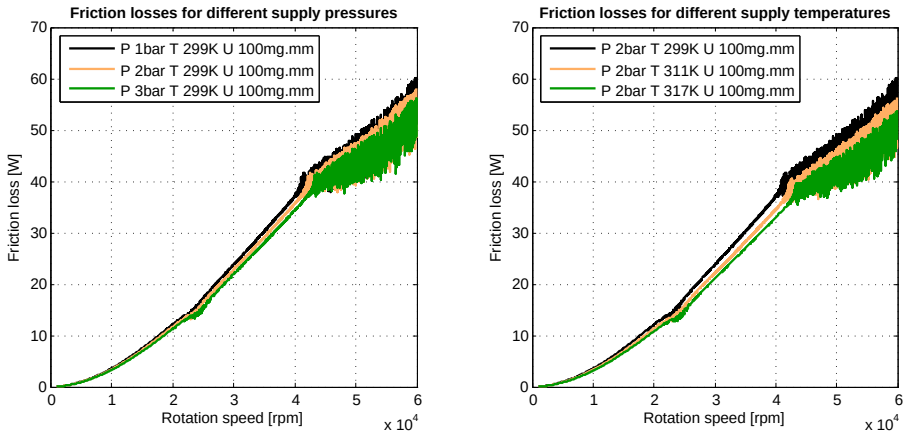

(b) Simulation result

Figure 3.24: Friction losses as a function of oil supply pressure (left) and oil supply temperature (right)

It is noteworthy that an increase of inlet temperature from 299K to 317K only leads to a reduction of friction losses of 8%, although the viscosity drops by approximately 50%. In case the friction losses were entirely dependent on shear losses and if the film temperature would have been identical to the supply temperature, a reduction of approximately 50% would be expected. This shows that the bearing housing plays an important role in the film temperature: at low supply temperatures, it pre-heats the oil before it enters the oil film, as was also observed in the conjugate heat transfer analysis in Appendix B.

Figure 3.24b presents the numerical friction loss predictions. It follows the trends observed during the measurements.

3.4.10. SUMMARY INFLUENCE FACTORS

Table 3.4 summarizes the results obtained by varying the input parameters on the plain journal bearing test setup.

Table 3.4: Summary of influence factors: + denotes the effect increases with an increase in the specific value, – denotes the effect decreases with an increase in the specific value, 0 denotes the effect does not change by more than 5% with an increase in the specific value.

	Effect				
Variable	Critical speed amplitude	Onset speed of whirl	Whirl ampl.	Whirl freq.	Friction losses
Rotor unbalance	+	0	0	0	0
Oil feed temp.	-	0	-	0	-
Oil feed pressure	+	+	0	0	0
Bearing clearance	-	-	+	0	-

3.5. CONCLUSION

The goal of this Chapter is to present a validated model for predicting the dynamic response of a flexible rotor supported by plain journal bearings. The details of the rotor model, fluid bearing model and thermal model have been presented. The main challenge of setting up the model was the thermal model: the temperatures of the shaft, bearing housing and –most importantly– the oil inlet channel were found to vary significantly with rotation speed. Therefore, a thermal network model of the complete rotor-bearing system has been included in the model. In addition, a test setup was developed to validate the rotor-bearing model.

In general, the simulation results correspond well with the measurement results. The critical speed predictions correspond with the measurement results within two percent. The maximum disk displacement amplitude while traversing the critical speed is typically similar to within ten to twenty percent. The prediction of the onset speed of oil whirl showed a similar correspondence. More importantly, the model has shown to be able to correctly predict most of the trends in variation of oil feed temperature, oil feed pressure, unbalance amount and clearance.

What has also been observed, is that a relatively simple analysis using linearized bearing coefficient based on an isoviscous short bearing model can yield fairly accurate results in terms of critical speed and whirling frequency, but is unable to accurately predict the onset speed of whirl and whirling amplitudes due to the non-linear character of the system at high eccentricity ratios.

Although our detailed model is considered to be sufficiently accurate for our purpose, the following improvements can be studied in future research:

- considering different cavitation models such as a gas bubble cavitation model [202].
- considering variation of viscosity over the film thickness [126].
- studying the outflow conditions at the edges of the bearing, which probably does not fully satisfy our non-submerged boundary conditions. Instead, a bubbly mixture is more likely to be present at the edges of the bearing [203]. Nowald [204] recently showed that the type of boundary condition at the side of the bearing can significantly affect the sub-synchronous response.

Improvements in the test setup may be considered in the following directions:

- experimental identification of the shear rate dependent viscosity parameters of the oil.
- active temperature control of the bearing housing and the oil inlet channel.

From the results in this chapter, it may be concluded that the different components selected to build the model are sufficiently accurate, and may be used to build a model for more complex bearing types such as the floating ring bearing which will be treated in the next chapter.

4

DYNAMIC BEHAVIOR OF A FLEXIBLE LAVAL ROTOR ON FLOATING RING BEARINGS

Floating ring bearings are commonly used in turbochargers due to their low wear rate, relatively inexpensive construction and because they can safely run at rotation speeds far beyond the onset speed of oil whirl. Floating ring bearings have two oil films, which can both exhibit oil whirl. The interaction between the two oil films and the rotor results in various sub-synchronous whirl modes. In this section, a model will be presented to predict the dynamic behavior of such a rotor-bearing system. A test setup is constructed to validate the model, followed by a description of the influence parameters on the dynamic behavior.

The experimental part of this Chapter has been published in: Eling, R.; te Wierik, M.; van Ostayen, R.; Rixen, D. Rotordynamic and Friction Loss Measurements on a High Speed Laval Rotor Supported by Floating Ring Bearings. *Lubricants* **2017**, 5, 7.

4.1. DESCRIPTION OF THE ROTOR-BEARING SYSTEM

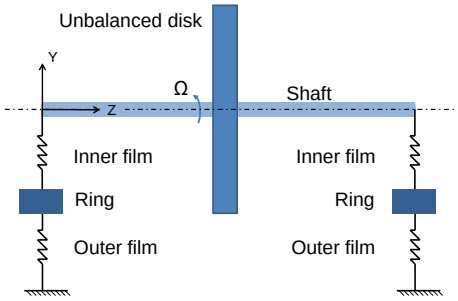

(a) Schematic depiction of the rotor-bearing system.

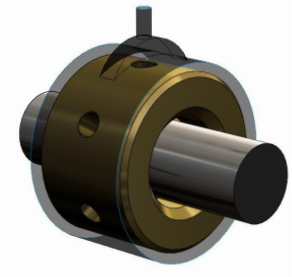

(b) A floating ring bearing with a shaft section [200].

Figure 4.1: Laval rotor on floating ring bearings. Dimensions and material properties can be found in Section 4.3.

Figure 4.1 gives a schematic representation of the rotor-bearing system which will be studied in this Chapter. The most important differences with respect to the one studied in the previous Chapter are:

- The plain journal bearings are replaced by floating ring bearings
- The bearing housing temperature is now controlled by liquid cooling/heating.

4.2. MODELING THE LAVAL ROTOR ON FLOATING RING BEARINGS

Analogous to Chapter 3, a finite element based model is constructed to predict the response of the rotor-bearing system during a run-up. As depicted in Figure 4.2, the model consists of twelve coupled modules:

- The structural dynamic model of the rotor, where the rotor position and rotor deformation are predicted.
- The dynamics of the two rings, where the ring position as well as the ring rotation speed are determined.
- The four fluid film modules, where the pressure distribution of the inner and outer fluid films of the two bearings are determined.
- The four thermal models, where the temperature distribution in each fluid film is determined.
- The thermal network model, which determines the temperatures of the walls adjacent to the fluid films.

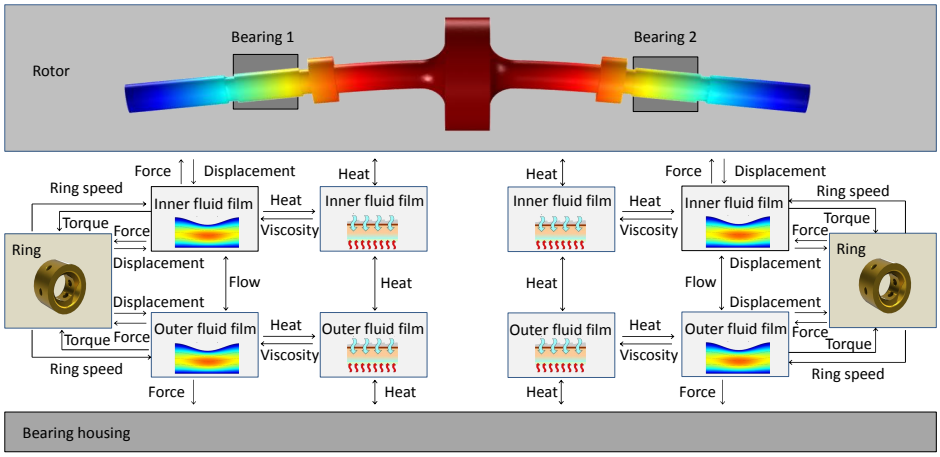

Figure 4.2: Schematic representation of the coupled modules within the rotor-bearing model.

Note that all of these modules are distributed models except for the thermal network model, which is a lumped model. The model is used to perform time-transient analysis: for each time step the (dynamic) equilibrium is calculated. In the following Section, each of the submodels will be detailed.

4.2.1. FLUID FILM MODEL

The kinematic description of a floating ring bearing in a stationary reference frame and the unfolded fluid domain are depicted in Figure 4.3. The floating ring bearing contains a ring which can freely translate and rotate. The forces and torques of the inner and outer oil film act on the ring and determine its position and rotation speed.

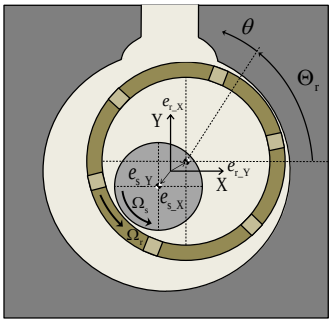

(a) Floating Ring Bearing kinematic description. Clearances are magnified for visualization.

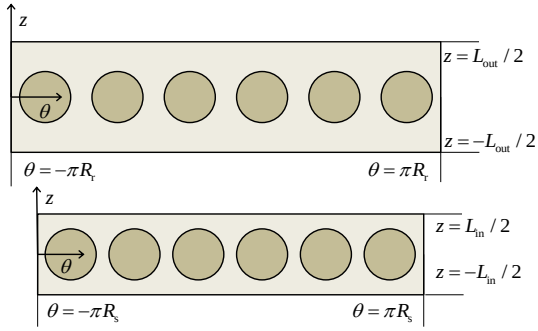

(b) Film domain of the floating ring bearing in the co-rotating reference frame $\{\theta, z\}$. The dark circles represent the oil connecting channels between the inner and outer oil films.

Figure 4.3: Floating ring bearings. The fluid domain consists of the outer oil film and the inner oil film.

An external oil feed pump delivers oil to the bearing via an oil groove on top of the

bearing housing. Six radial holes in the ring connect the inner and the outer oil film, enabling oil to flow to the inner oil film. The oil flows out of the bearing in axial direction at the sides of the fluid films, at ambient pressure.

As can be observed in Figure 4.3a, the film thickness of the outer film depends on the displacement of the ring and can be described in the global reference frame as:

$$h_{\text{out}} = C_{\text{out}} - e_{\text{r\_X}} \cos(\Theta) - e_{\text{r\_Y}} \sin(\Theta) \tag{4.1}$$

where C_{out} represents the nominal outer clearance, $e_{\text{r\_X}}$ and $e_{\text{r\_Y}}$ are the ring displacements in global X and Y direction and Θ is the global angle:

$$\Theta = \tan^{-1}\left(\frac{Y}{X}\right) \tag{4.2}$$

The instantaneous rotation angle of the ring Θ_{r} in the global reference frame at time t can be found by integrating its rotation speed over time, taking the X-axis as 0 at $t = 0$s:

$$\Theta_{\text{r}} = \int_0^t \Omega_r(t)\,dt \tag{4.3}$$

The film thickness of the inner film depends on the displacements of the ring $e_{\text{r\_X}}$ and $e_{\text{r\_Y}}$ and of the shaft $e_{\text{s\_X}}$ and $e_{\text{s\_Y}}$:

$$h_{\text{in}} = C_{\text{in}} - \left(e_{\text{s\_X}} - e_{\text{r\_X}}\right)\cos(\Theta) - \left(e_{\text{s\_Y}} - e_{\text{r\_Y}}\right)\sin(\Theta) \tag{4.4}$$

As the ring rotates, the six fluid connecting channels move along. In case a stationary reference frame would have been used, this would have caused numerical difficulties: the connecting channels would move through the fluid domain and for every time step a new mesh would need to be created. As this would be a numerical burden, a co-rotating reference frame $\{\theta, z\}$ is used, which is co-rotating with the ring, as depicted in Figure 4.3b. As a consequence, the oil feed channel –which is stationary in the inertial reference frame– now moves over the fluid domain of the outer fluid film.

The bearing is thus modeled in a co-rotating reference frame, whereas the rotordynamic model uses an inertial reference frame. Rotation matrices are used to transform local kinematics to global kinematics. The eccentricities for the film thickness in the co-rotating reference frame are:

$$\begin{bmatrix} e_{\text{s\_x}} \\ e_{\text{s\_y}} \\ e_{\text{r\_x}} \\ e_{\text{r\_y}} \end{bmatrix} = \begin{bmatrix} \cos(\Theta_{\text{r}}) & \sin(\Theta_{\text{r}}) & 0 & 0 \\ -\sin(\Theta_{\text{r}}) & \cos(\Theta_{\text{r}}) & 0 & 0 \\ 0 & 0 & \cos(\Theta_{\text{r}}) & \sin(\Theta_{\text{r}}) \\ 0 & 0 & -\sin(\Theta_{\text{r}}) & \cos(\Theta_{\text{r}}) \end{bmatrix} \begin{bmatrix} e_{\text{s\_X}} \\ e_{\text{s\_Y}} \\ e_{\text{r\_X}} \\ e_{\text{r\_Y}} \end{bmatrix} \tag{4.5}$$

Thus, we can write the film thickness functions in the co-rotating reference frame as:

$$\begin{aligned} h_{\text{out}} &= C_{\text{out}} - e_{\text{r\_x}} \cos\left(\frac{\theta}{R_{\text{r}}}\right) - e_{\text{r\_y}} \sin\left(\frac{\theta}{R_{\text{r}}}\right) \\ h_{\text{in}} &= C_{\text{in}} - \left(e_{\text{s\_x}} - e_{\text{r\_x}}\right)\cos\left(\frac{\theta}{R_{\text{s}}}\right) - \left(e_{\text{s\_y}} - e_{\text{r\_y}}\right)\sin\left(\frac{\theta}{R_{\text{s}}}\right) \end{aligned} \tag{4.6}$$

The flow in the fluid films can now be described by the Reynolds equation [51]:

$$\frac{\partial q_\theta}{\partial \theta} + \frac{\partial q_z}{\partial z} = \frac{\partial f h \rho_{\text{oil}}}{\partial t} \tag{4.7}$$

In the rotating reference frame, the flows through the outer film in circumferential direction q_{θ_out} and axial direction q_{z_out} are defined as:

$$\begin{aligned} q_{\theta\_\text{out}} &= \frac{-f {h_\text{out}}^3 \rho_\text{oil}}{12\mu_\text{oil}} \frac{\partial \xi}{\partial \theta}\zeta + \frac{f\Omega_\text{r} R_\text{r} h_\text{out}\rho_\text{oil}}{2} \\ q_{z\_\text{out}} &= \frac{-f {h_\text{out}}^3 \rho_\text{oil}}{12\mu_\text{oil}} \frac{\partial \xi}{\partial z}\zeta \end{aligned} \tag{4.8}$$

where the variable ξ is a switching variable describing the pressure p in the full film area and the mass fraction f in the cavitated area as defined by Equation 3.23. The mass-conservative cavitation description as introduced in Section 3.2.4 is also applied here. Furthermore, notice the plus sign of the second term of q_{θ_out} which originates from the rotating reference frame, rotating at speed Ω_r. The scaling pressure ζ is defined as:

$$\zeta = \frac{\mu_0 \Omega_\text{s} R_\text{s}}{C_\text{in}} \tag{4.9}$$

so that the physical pressure p in the fluid film can be calculated as expressed by Equation 3.23. Lastly, the derivation of the squeeze term, $\frac{\partial h}{\partial t}$ in Equation 4.7 can be found in Appendix E. Similar to the flow description of the outer film, the flow in the inner film can be described by:

$$\begin{aligned} q_{\theta\_\text{in}} &= \frac{-f {h_\text{in}}^3 \rho_\text{oil}}{12\mu_\text{oil}} \frac{\partial \xi}{\partial \theta}\zeta - \frac{f(\Omega_\text{s}-\Omega_\text{r}) R_\text{s} h_\text{in}\rho_\text{oil}}{2} \\ q_{z\_\text{in}} &= \frac{-f {h_\text{in}}^3 \rho_\text{oil}}{12\mu_\text{oil}} \frac{\partial \xi}{\partial z}\zeta \end{aligned} \tag{4.10}$$

Note that due to the rotating reference frame, the flow depends on $(\Omega_\text{s} - \Omega_\text{r})$ instead of $(\Omega_\text{s} + \Omega_\text{r})$ which would have been the case in an inertial reference frame.

The following boundary conditions have been imposed on the edges of the fluid domains depicted in Figure 4.4:

- continuity of flow is imposed in circumferential direction:

$$\begin{aligned} \xi_\text{out}|_{-\pi R_\text{r}} &= \xi_\text{out}|_{\pi R_\text{r}} \\ \xi_\text{in}|_{-\pi R_\text{s}} &= \xi_\text{in}|_{\pi R_\text{s}} \end{aligned} \tag{4.11}$$

- non-submerged boundary conditions are imposed in axial direction, which means that oil can flow out at the sides at ambient pressure, but can not flow in:

$$\begin{aligned} \left((\xi_\text{in} \geq 0)\left(q_\text{z} n_\text{z} > 0\right)\xi_\text{in}\right)\Big|_{-L_\text{in}/2}^{L_\text{in}/2} &= 0 \\ \left((\xi_\text{out} \geq 0)\left(q_\text{z} n_\text{z} > 0\right)\xi_\text{out}\right)\Big|_{-L_\text{out}/2}^{L_\text{out}/2} &= 0 \end{aligned} \tag{4.12}$$

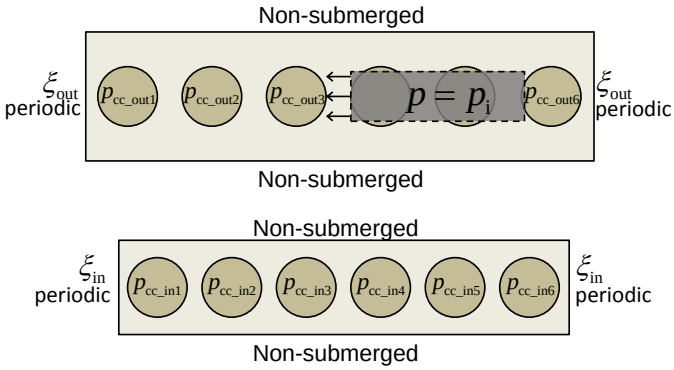

Figure 4.4: Boundary conditions for the flow model.

The oil supply channel is a rectangular area defined in the inertial reference frame as:

$$\Pi_i \left(Z \left\{ -L_{i/2}, L_{i/2} \right\}, \Theta \left\{ \pi/2 - \Theta_{i/2}, \pi/2 + \Theta_{i/2} \right\} \right) \tag{4.13}$$

which is converted to a rectangle moving along with rotation speed $-R_r\Omega_r$ in the co-rotating reference frame, as depicted in Figure 4.4:

$$\Pi_i \left(z \left\{ -L_{i/2}, L_{i/2} \right\}, \theta \left\{ \pi/2 - \Theta_{i/2}, \pi/2 + \Theta_{i/2} \right\} - \Omega_r \right) \tag{4.14}$$

Within this supply channel domain, the pressure is set to $p = p_i$.

The oil connecting channels are assumed to be passive coupling elements. This means that the channel is modeled as a direct pressure communication channel which is assumed not to have any internal fluid dynamics. The effect of the exchange of momentum between the ring and the fluid in the connecting channel can result in a significantly higher ring speed, as demonstrated in Appendix D. This effect is excluded here, as the model of the oil connecting channels as presented in Appendix D resulted in numerical convergence issues. Instead, we write a simple flow balance between the flow entering and exiting each channel i = {1...6}:

$$\int_{\Lambda_{cc\_in,i}} q d\Lambda_{cc_{in,i}} + \int_{\Lambda_{cc\_out,i}} q d\Lambda_{cc_{out,i}} = 0 \tag{4.15}$$

where $\Lambda_{cc,i}$ represents the circumference of a connecting channel with index i = {1...6}. The pressures on the circumference on the inside and the outside of each connecting channel are calculated by iteration so that Equation 4.15 holds, taking into account the centrifugal pressure difference between the inner and outer oil films:

$$p\big|_{\Lambda_{cc\_in,i}} = p\big|_{\Lambda_{cc\_out,i}} - p_{cent} \tag{4.16}$$

where:

$$p_{cent} = \frac{\rho_{oil}{\Omega_r}^2}{2} \left({R_s}^2 - {R_r}^2 \right) \tag{4.17}$$

These pressures $p_{\Lambda_{\text{cc\_in,i}}}$, $p_{\Lambda_{\text{cc\_out,i}}}$ are then imposed to the surfaces which represent the fluid connecting channels in the thin film domain marked by $p_{\text{cc\_in,i}}$, $p_{\text{cc\_out,i}}$ in Figure 4.4.

Once the pressure distribution in both oil films is found, the bearing forces in the rotating reference frame can be calculated. For calculating the bearing forces, the shear forces can be neglected, as described in Section 3.2.4, resulting in:

$$\begin{aligned}
\begin{bmatrix} F_{\text{x_in}} \\ F_{\text{y_in}} \end{bmatrix} &= -\int_{-L_{\text{in}}/2}^{L_{\text{in}}/2}\int_{-\pi R_{\text{s}}}^{\pi R_{\text{s}}} \begin{Bmatrix} p\cos\left(\frac{\theta}{R_{\text{s}}}\right) \\ p\sin\left(\frac{\theta}{R_{\text{s}}}\right) \end{Bmatrix} d\theta\, dz \\
\begin{bmatrix} F_{\text{x_out}} \\ F_{\text{y_out}} \end{bmatrix} &= -\int_{-L_{\text{out}}/2}^{L_{\text{out}}/2}\int_{-\pi R_{\text{r}}}^{\pi R_{\text{r}}} \begin{Bmatrix} p\cos\left(\frac{\theta}{R_{\text{r}}}\right) \\ p\sin\left(\frac{\theta}{R_{\text{r}}}\right) \end{Bmatrix} d\theta\, dz
\end{aligned} \tag{4.18}$$

and transformed to forces in the stationary reference frame:

$$\begin{bmatrix} F_X \\ F_Y \end{bmatrix} = \begin{bmatrix} \cos(\Theta_{\text{r}}) & -\sin(\Theta_{\text{r}}) \\ \sin(\Theta_{\text{r}}) & \cos(\Theta_{\text{r}}) \end{bmatrix} \begin{bmatrix} F_x \\ F_y \end{bmatrix} \tag{4.19}$$

The ring is driven by shear forces from the inner fluid film and in turn drives the oil flow in the outer film. Hence, the shear forces from the inner and outer films determine the ring rotation speed. The following momentum balance determines the equilibrium ring rotation speed at every time step:

$$I_{\text{ring}}\dot{\Omega}_r = M_{\text{in}} - M_{\text{out}} \tag{4.20}$$

where:

$$\begin{aligned}
M_{\text{in}} &= R_{\text{s}}\int_{-L_{\text{in}}/2}^{L_{\text{in}}/2}\int_{-\pi R_{\text{s}}}^{\pi R_{\text{s}}} \frac{\mu_{\text{oil}} f(\Omega_{\text{s}}-\Omega_{\text{r}})R_{\text{s}}}{h_{\text{in}}} - \frac{h_{\text{in}}}{2}\frac{\partial p}{\partial \theta}\, d\theta\, dz \\
M_{\text{out}} &= R_{\text{r}}\int_{-L_{\text{out}}/2}^{L_{\text{out}}/2}\int_{-\pi R_{\text{r}}}^{\pi R_{\text{r}}} \frac{\mu_{\text{oil}} f(\Omega_{\text{r}})R_{\text{r}}}{h_{\text{in}}} - \frac{h_{\text{out}}}{2}\frac{\partial p}{\partial \theta}\, d\theta\, dz
\end{aligned} \tag{4.21}$$

and I_{ring} represents the moment of inertia of the ring.

4.2.2. THERMAL MODEL

As can be seen in Figure 4.5, there are many heat flow paths. In this Section, these heat flow paths will be described.

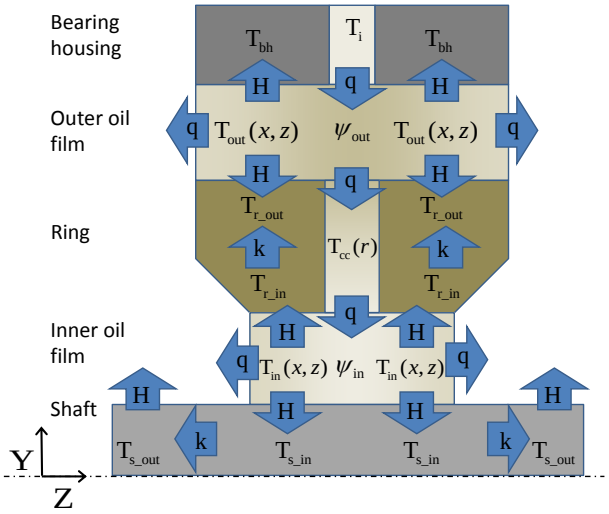

Figure 4.5: Schematic cross-section of the rotor-bearing system with the thermal nodes T and the friction losses ψ. Heat transfer paths are indicated by arrows, where q represents heat flow by oil flow, k represents conduction and H represents convection to ambient temperature.

The temperature of the bearing housings in the experimental test setup is actively controlled. By doing so, the temperature of the oil at the inlet T_i and the temperature of the bearing housing walls T_bh become prescribed values. Therefore, the thermal model can be restricted to the fluid domain, the ring and the shaft.

First, the friction ψ generated in the inner and the outer oil films is calculated by [101, 152]:

$$\begin{aligned}\psi_\mathrm{in} &= \frac{(\xi>0)h_\mathrm{in}^3}{12\mu_\mathrm{oil}}\left(\left(\frac{\partial \xi P_0}{\partial \theta}\right)^2+\left(\frac{\partial \xi P_0}{\partial z}\right)^2\right)+\frac{(\xi>0)\mu_\mathrm{oil}(\Omega_\mathrm{s}-\Omega_\mathrm{r})^2 R_\mathrm{s}^2}{h_\mathrm{in}}\\ \psi_\mathrm{out} &= \frac{(\xi>0)h_\mathrm{out}^3}{12\mu_\mathrm{oil}}\left(\left(\frac{\partial \xi P_0}{\partial \theta}\right)^2+\left(\frac{\partial \xi P_0}{\partial z}\right)^2\right)+\frac{(\xi>0)\mu_\mathrm{oil}\Omega_\mathrm{r}^2 R_\mathrm{r}^2}{h_\mathrm{out}}\end{aligned} \tag{4.22}$$

In these equations, the first terms originate from the friction from pressure extrusion flow and the second term from the shear-driven flow. These flows are obtained by solving the Reynolds equation, Equation 4.7 for each film, meaning the fluid flow and thermal equations are coupled.

Heat from the fluid films is transferred to the bearing housing, the ring and the shaft. In this analysis, heat transfer by convection is assumed, which for such laminar flow can be described by [152]:

$$H = 3\mathrm{Pr}^{1/3}\frac{k_\mathrm{oil}}{h} \tag{4.23}$$

where H is the convective heat transfer coefficient, k_oil is the thermal conductance of oil and h is the film thickness. The local Prandtl number Pr is given by:

$$\mathrm{Pr} = \frac{c_\mathrm{p\_oil}\mu_\mathrm{oil}}{k_\mathrm{oil}} \tag{4.24}$$

where $c_{\mathrm{p\_oil}}$ is the specific heat capacity of oil.

Heat transfer to the ring causes the ring temperature to rise. Analogue to the analysis of San Andres [152], the temperature of the ring is assumed to be constant in circumferential direction. Assuming the thermal storage terms for the ring can be ignored, the radial temperature profile of the ring is governed by:

$$\frac{d}{dr}\left(-r k_{\mathrm{r}} \frac{dT_{\mathrm{r}}}{dr}\right) = 0 \tag{4.25}$$

Integration of this equation yields expressions for the temperature of the ring at the inner and outer surfaces:

$$\begin{aligned} T_{\mathrm{r\_in}} &= \frac{\dot{Q}_{\mathrm{r}}}{k_{\mathrm{r}} 2\pi L_{\mathrm{in}}} \ln\left(\frac{R_{\mathrm{s}}}{R_{\mathrm{r\_mid}}}\right) + T_{\mathrm{r\_mid}} \\ T_{\mathrm{r\_out}} &= \frac{\dot{Q}_{\mathrm{r}}}{k_{\mathrm{r}} 2\pi L_{\mathrm{out}}} \ln\left(\frac{R_{\mathrm{r}}}{R_{\mathrm{r\_mid}}}\right) + T_{\mathrm{r\_mid}} \end{aligned} \tag{4.26}$$

where $T_{\mathrm{r\_mid}}$ is the temperature midway the ring at radius $R_{\mathrm{r\_mid}} = (R_{\mathrm{s}} + R_{\mathrm{r}})/2$. The heat flow through the ring $\dot{Q}_{\mathrm{r}}$ is furthermore given by:

$$\begin{aligned} \dot{Q}_{\mathrm{r\_in}} &= H\left(T_{\mathrm{in}} - T_{\mathrm{r\_in}}\right) \\ \dot{Q}_{\mathrm{r\_out}} &= H\left(T_{\mathrm{r\_out}} - T_{\mathrm{out}}\right) \end{aligned} \tag{4.27}$$

as there is no thermal storage in the ring, $\dot{Q}_{\mathrm{r\_in}} = \dot{Q}_{\mathrm{r}} = \dot{Q}_{\mathrm{r\_out}}$ and hence $T_{\mathrm{r\_mid}}$ and the corresponding $T_{\mathrm{r\_in}}$ and $T_{\mathrm{r\_out}}$ can be found.

The heat going into the shaft is dissipated by forced convection to the ambient air, as described in Appendix B, Equation B.2.

The fluid film temperature distribution can now be described by the following energy equation for the inner and outer fluid film respectively:

$$\begin{aligned} &\frac{\partial}{\partial\theta}\left(-f k_{\mathrm{oil}} h_{\mathrm{in}} \frac{\partial T_{\mathrm{in}}}{\partial\theta} + c_{\mathrm{p\_oil}} q_\theta T_{\mathrm{in}}\right) + \frac{\partial}{\partial z}\left(-(\xi_i > 0) k_{\mathrm{oil}} h_{\mathrm{in}} \frac{\partial T_{\mathrm{in}}}{\partial z} + c_{\mathrm{p\_oil}} q_z T_{\mathrm{in}}\right) + \ldots \\ &\rho_{\mathrm{oil}} c_{\mathrm{p\_oil}} f h_{\mathrm{in}} \frac{\partial T_{\mathrm{in}}}{\partial t} = \psi_{\mathrm{in}} - f H(T_{\mathrm{in}} - T_{\mathrm{s}}) - f H(T_{\mathrm{in}} - T_{\mathrm{r\_in}}) \end{aligned} \tag{4.28}$$

$$\begin{aligned} &\frac{\partial}{\partial\theta}\left(-f k_{\mathrm{oil}} h_{\mathrm{out}} \frac{\partial T_{\mathrm{out}}}{\partial\theta} + c_{\mathrm{p\_oil}} q_\theta T_{\mathrm{out}}\right) + \frac{\partial}{\partial z}\left(-(\xi_i > 0) k_{\mathrm{oil}} h_{\mathrm{out}} \frac{\partial T_{\mathrm{out}}}{\partial z} + c_{\mathrm{p\_oil}} q_z T_{\mathrm{out}}\right) + \ldots \\ &\rho_{\mathrm{oil}} c_{\mathrm{p\_oil}} f h_{\mathrm{out}} \frac{\partial T_{\mathrm{out}}}{\partial t} = \psi_{\mathrm{out}} - f H(T_{\mathrm{out}} - T_{\mathrm{r\_out}}) - f H(T_{\mathrm{out}} - T_{\mathrm{bh}}) \end{aligned} \tag{4.29}$$

In these equations k_{oil} and $c_{\mathrm{p\_oil}}$ represent the thermal conductance and specific heat capacity of the oil. These equations are solved over the domain depicted in Figure 4.6 with the following boundary conditions:

- Oil enters the fluid domain via the inlet at a temperature of T_{i}. The stationary inlet domain travels through the co-rotating fluid domain as described by Equation 4.14. Within the oil inlet domain, perfect mixing is assumed.

- Heat transport from and to the six oil connecting channels is determined by a heat balance, which assumes perfect mixing of the flow from the inner and outer films within the channel. For each of the 6 channels $i = \{1...6\}$, the average channel temperature $T_{\text{cc\_i}}$ is determined by solving:

$$\left(T_{\text{in}} - T_{\text{cc\_i}}\right) \int_{\Lambda_{\text{cc\_in,i}}} q c_{\text{p\_oil}} d\Lambda_{cc_{\text{in\_i}}} = \left(T_{\text{out}} - T_{\text{cc\_i}}\right) \int_{\Lambda_{\text{cc\_out,i}}} q c_{\text{p\_oil}} d\Lambda_{cc_{\text{out\_i}}} \tag{4.30}$$

- Periodic boundary conditions are imposed on the edges $x = \pm\pi R_{\text{in}}$ and $x = \pm\pi R_{\text{out}}$.
- Non-submerged boundary conditions are imposed on the edges $z = \pm\frac{L_{\text{in}}}{2}$ and $z = \pm\frac{L_{\text{out}}}{2}$.

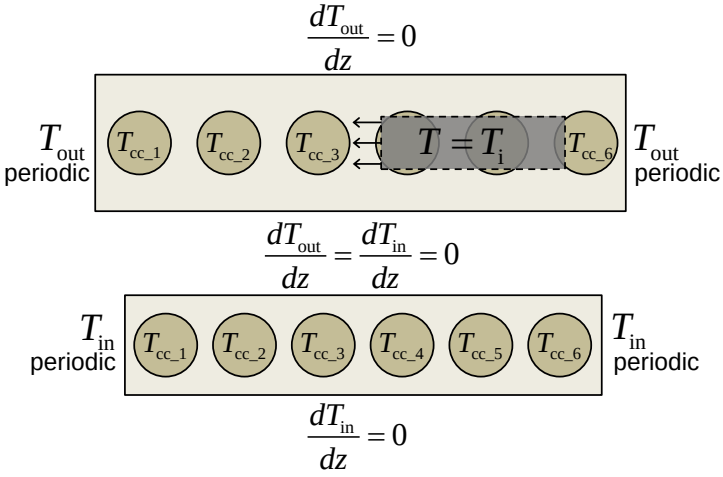

Figure 4.6: Boundary conditions for the thermal model.

As the fluid films generate considerable heat and the bearing clearances are relatively small, thermal expansion could have a significant effect on the bearing clearances. Therefore, the effective clearances were calculated after performing a time-transient run-up showing a negligible clearance change, as can be seen in Figure 4.19.

4.2.3. ROTOR MODEL

Analogous to the rotor of Chapter 3, the rotor contains one disk in the center and two small disks near the bearings which are added to prevent cross-talk between the displacement sensors in the lateral directions X and Y, see Figure 4.7.

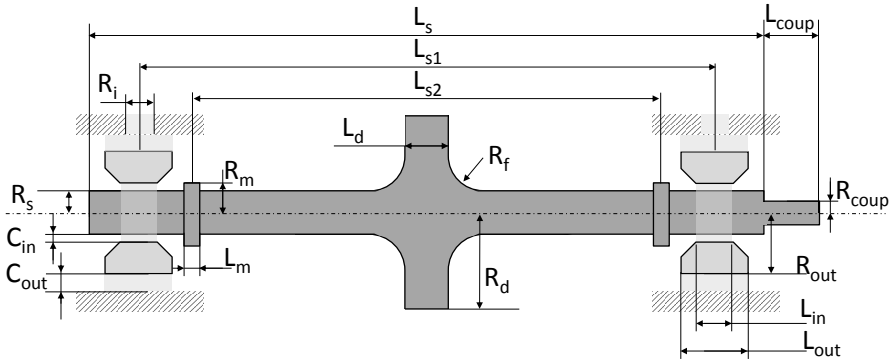

Figure 4.7: Laval rotor. Dimensions can be found in Table 4.2. The rotor is coupled at the right hand side to an electric motor controlling the rotation speed.

The main differences with the rotor geometry of Chapter 3 are that the shaft diameter was increased and the bearing span was decreased. A fillet has been added in the transition from shaft to disk, to minimize peak stresses. Details of the geometry can be found in Table 4.2.

The shaft is described by 22 Euler-Bernoulli beam elements, following the methods presented in Chapter 3. For both the shaft and the disks, the gyroscopic coupling terms have been included. Furthermore, an unbalance vector is assumed to act on the center of the disk, as described by Equation 3.10 and 3.11.

4.3. TEST SETUP

The test setup consists of a Laval rotor driven by an electric motor and supported by floating ring bearings. The Laval rotor is coupled to the motor by a compliant coupling, which minimizes the transfer of energy between both parts and minimizes the influence of misalignment. The coupling is made from a polyurethane tube section, so that its contribution of mass and stiffness to the rotor can conveniently be neglected. An overview of the test setup is displayed in Figure 4.8. A picture is displayed in Figure 4.9.

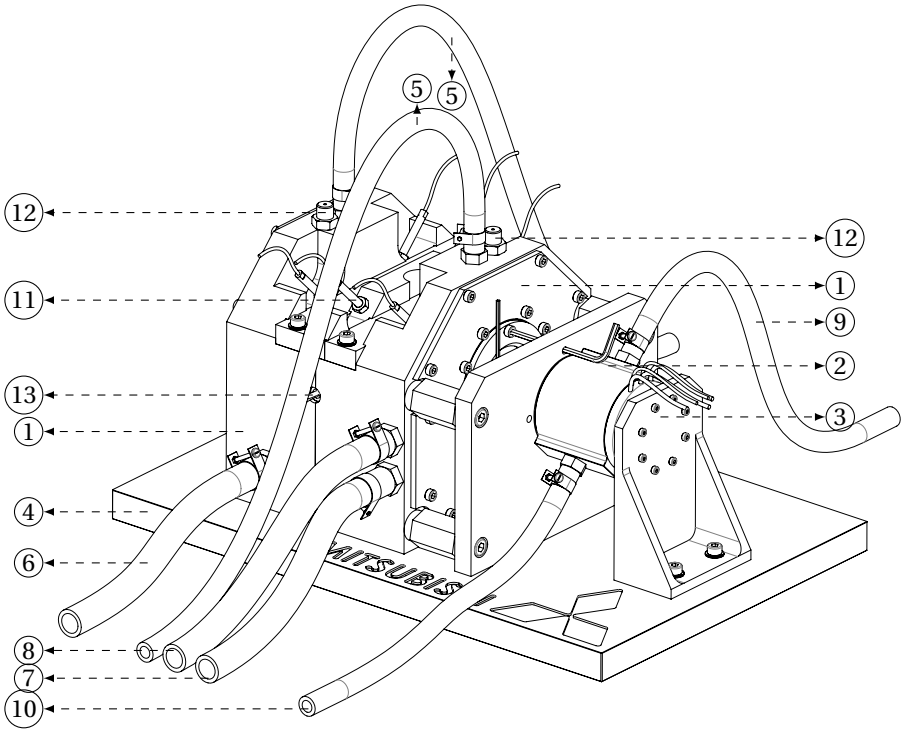

Figure 4.8: Overview of the experimental setup. Image based on [200].

Table 4.1: Descriptions for the parts labeled with encircled numbers in Figure 4.8

Number	Description
1	Bearing housing
2	Motor
3	Motor support bracket
4	Baseplate
5	Oil supply line
6	Oil drain line
7	Liquid cooling/heating supply

Number	Description
8	Liquid cooling/heating drain
9	Motor cooling supply
10	Motor cooling drain
11	Shaft displacement sensor
12	Thermocouple
13	Optical sensor

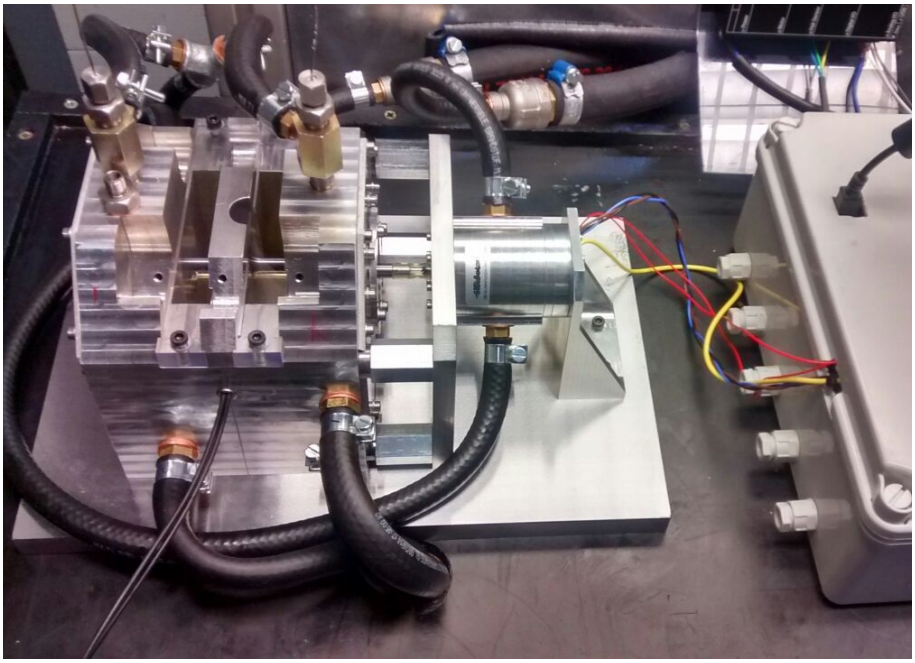

Figure 4.9: Floating ring bearing test setup.

The physical properties of the rotor, the ring and the lubricant are summarized in Table 4.2.

Table 4.2: Parameters for the Laval rotor supported by floating ring bearings.

Rotor parameters				Ring parameters			
Name	Value	Unit	Description	Name	Value	Unit	Description
R_s	3.75	mm	Radius of shaft	C_{in}	8.5	μm	Inner clearance
R_d	15	mm	Radius of center disk	C_{out}	30	μm	Outer clearance
R_m	6	mm	Radius measurement disk	L_{in}	5	mm	Length inner film
R_f	5	mm	Radius of fillet	L_{out}	8	mm	Length outer film
L_s	137	mm	Shaft length	R_{out}	6.465	mm	Outer ring radius
L_d	9	mm	Length of center disk	I_r	$1.5{\cdot}10^{-7}$	kg·m^2	Ring rotation inertia
L_m	5	mm	Length measurement disk	m_r	5.39	g	Ring mass
λ_s	$1.2{\cdot}10^{-5}$	K^{-1}	Coeff. th. expansion shaft	λ_r	$1.4{\cdot}10^{-5}$	K^{-1}	Coeff. th. exp. ring
L_{s1}	80	mm	Length of bearing span	Oil parameters			
L_{s2}	58	mm	Measurement disk span	ρ_{oil}	855	kg m^{-3}	Oil density
L_{coup}	8	mm	Length of coupling section	c_{poil}	2.1	kJ/kg·K	Heat capacity
R_{coup}	2.25	mm	Radius of coupling section	k_{oil}	0.145	W/m·K	Thermal conductance
ρ_s	7700	kg m^{-3}	Material density	A_{oil}	0.44	mPa·s	Temperature coeff.
E_s	210	GPa	Material Young's modulus	B_{oil}	633	^{o}C	Temperature coeff.
I_{rot}	$9.2{\cdot}10^{-6}$	kg m^2	Rotor rotation inertia	C_{oil}	88.6	^{o}C	Temperature coeff.
m_{rot}	101	g	Rotor mass	r_{oil}	0.5	-	Shear rate coefficient
				m_{oil}	0.8	-	Shear rate coefficient
				K_{oil}	$7.2{\cdot}10^{-7}$	s^{-1}	Shear rate coefficient

4.3.1. ROTOR

The Laval rotor is constructed from a solid piece of tool steel (1.2379) and is produced by precision-grinding, resulting in a rotor with a concentricity error smaller than one micrometer over the entire rotor length. The center disk features four radial holes at 90 degrees circumferential spacing where grub screws can be inserted to set the amount of unbalance on the rotor, see Figure 4.10. Adjacent to each bearing surface, small disk features are present, which were necessary to minimize the cross-talk between the eddy current sensors for shaft orbit measurements, as shown in Figure 4.10. By hammer impact measurements, we determined the first two bending frequencies of the rotor –when suspended in compliant rubber bands– to be at 1601Hz and 3925Hz.

4.3.2. SENSOR CONFIGURATION

The test setup is equipped with sensors for measuring the rotor displacements, friction losses and oil temperatures. The temperatures of the oil in the inlet channel, of the bearing housing and of the oil just downstream the bearings were measured by thermocouples. The dissipated friction losses in the bearings were found by substracting the internal losses of the motor from the total motor power, where the internal losses were measured by running the motor without the Laval rotor. The power necessary to accelerate the rotor, $P_{\text{acc}} = \Omega_{\text{s}} I_{\text{rot}} \dot{\Omega}_{\text{s}}$, was also substracted from the total motor power.
The rotation speed of the shaft and the rings were measured by optical sensors, which are triggered by surfaces coated with black marking stripes. The displacements of the rotor were measured by eddy current displacement sensors with a resolution smaller than 0.1 micrometer and were sampled at a frequency of 51.2kHz. Figure 4.10 shows the rotor with the displacement sensors and the shaft rotation speed sensor.

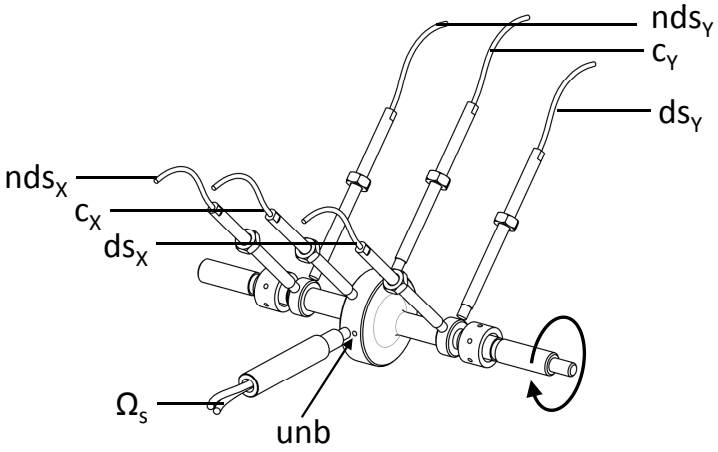

Figure 4.10: Rotor with a rotation speed sensor (Ω_s) and six orthogonally placed displacement sensors. *ds* marks drive side, *nds* marks non-drive side and *c* represents center disk. Unbalance can be configured by inserting grub screws in the threaded hole indicated by *unb*. Image based on [200]

4.3.3. LUBRICATION SYSTEM AND TEMPERATURE CONTROL

Oil was fed to the floating ring bearings at a controlled temperature and pressure. Since there is only a relatively small flow of oil through the bearings, bypass channels were included just upstream the bearing housing to ensure that the oil is circulating thoroughly from the temperature-controlled oil sump to control the oil inlet temperature as good as possible. Temperature control was also applied to the bearing housing: it is constructed from aluminium and features strategically positioned chambers to allow temperature-controlled liquid to flow through. The bearing oil and the bearing housing liquids were kept in two separate circuits, so that combinations of warm oil in a cold housing can be studied and vice versa. In this study, the temperatures of the bearing housing and the oil which is supplied to the bearings were always equal.

4.3.4. OIL

For all measurements in this study, multigrade automotive engine oil SAE 5W30 was used. The friction losses due to the shearing of oil causes an increase of temperature in the bearings, so the viscosity will change. Furthermore, the shear rates in the bearing at high rotation speeds are considerable, so the engine oil behaves as a non-Newtonian, shear thinning fluid. Therefore, the viscosity is also a function of shear rate $\dot{\gamma}$. The following combination of the Vogel and the Cross equation is a suitable description of the oil viscosity function in this case [198]:

$$\mu_{\text{oil}}(T,\dot{\gamma}) = A_{\text{oil}} e^{\frac{B_{\text{oil}}}{(T_{\text{film}}+C_{\text{oil}})}} \left(r_{\text{oil}} + \frac{1-r_{\text{oil}}}{1+(K_{\text{oil}}\dot{\gamma})^{m_{\text{oil}}}} \right) \tag{4.31}$$

The viscosity coefficients for the oil, as can be found in Table 4.2, were obtained by measurements of oil samples on a cone-on-plate viscometer. As the pressures in floating ring bearings are typically moderate [185], the pressure dependency of the viscosity can be neglected.

4.3.5. MEASUREMENT SEQUENCE

For all run-ups, the rotor was accelerated from 20.000rpm to 180.000rpm in 100 seconds at a constant acceleration rate. We ascertained that the rotordynamic response and thermal distribution during a 100 seconds run is identical to the response in a 1000 seconds run, demonstrating that quasi-steady conditions can be assumed. The same holds for the temperatures.

It was observed that a run-up differs from a run-down: hysteresis occurs in the sub-synchronous response. This means that in a run-up, the onset speed of a certain whirl is higher than the speed at which this whirl vanishes again during a run-down. This was also observed in the simulations of Tian [145] and the measurements of San Andres [205]. In this study, we present only run-up measurements.

Prior to the measurements, the rotor was balanced in-situ to minimize the unbalance caused by mounting the coupling between the motor and the Laval rotor. The balancing was done in one plane, on the center disk of the rotor. In this study, the balanced condition is referred to as *0mg·mm*, although strictly speaking, some residual out-of-plane unbalance is present. The *0mg·mm* balanced condition was achieved by adjusting the grub screws by iteration until a minimum response over the operating range was ob-

served.
The repeatability of the test setup was checked by repetitive measurements using the standard operating conditions. This was done throughout the measurement campaign, i.e., after performing various run-ups with different oil supply temperatures, rotor unbalance and oil supply pressures, the test setup was operated again at the standard operating condtions. For all measured values, these repetitive runs showed maximum deviations of less than 2 percent between runs, demonstrating the repeatability of the measurement results.
The temperature of the bearing housing was monitored during the measurements, showing fluctuations of maximum 3K during a run-up. This relatively stable temperature is a result of the liquid cooling/heating channels in the aluminium bearing housing.

4.4. RESULTS

In this Section, the results of a run-up at standard operating conditions are extensively analyzed: measurement results are compared to simulation results. Subsequently, the effects of varying the oil feed pressure, oil feed temperature and rotor unbalance are analyzed. Lastly, the effect of changing the bearing clearances is evaluated.

4.4.1. ROTORDYNAMIC RESPONSE AT STANDARD OPERATING CONDITIONS

The standard operating conditions are as follows:

- The oil inlet pressure p_i is set at 2 bar.
- The oil inlet temperature T_i is set at 310K.
- The bearing housing temperature T_{bh} is set at 310K .
- The rotor unbalance is set at 100mg·mm.

Under these conditions, the response depicted in Figure 4.11 has been measured.

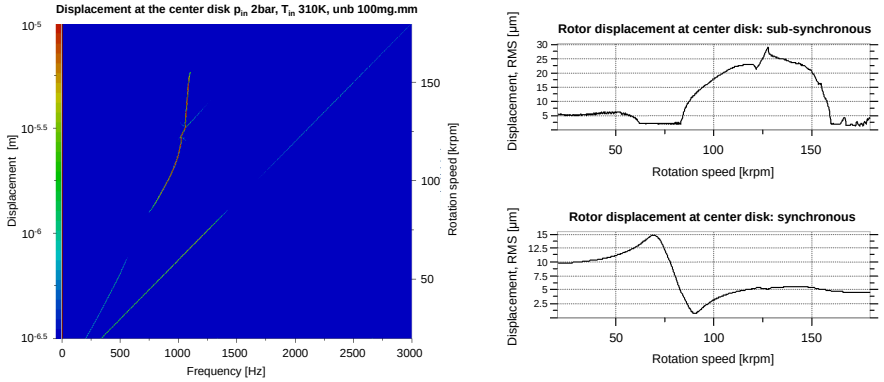

(a) (b)

Figure 4.11: Measurement results: displacement of the center disk under standard operating conditions: Waterfall plot (**a**), sub-synchronous and synchronous displacement intensities (**b**).

The waterfall plot, Figure 4.11a, shows the displacement of the center disk as a function of the rotation speed. When bandpass filters $0.10\Omega_s < \omega_{filt} < 0.90\Omega_s$ and $0.95\Omega_s < \omega_{filt} < 1.05\Omega_s$ are applied to this data, the sub-synchronous and synchronous content of the shaft displacement is found. Figure 4.11b gives the RMS value of the sub-synchronous and synchronous displacement of the disk as a function of the rotation speed.
During the run-up, the following phenomena have been observed:

- from 20krpm to 62krpm, some mild sub-synchronous oil whirl occured at a frequency of half the sum of the shaft speed and the ring speed: $\omega = \frac{(\Omega_s+\Omega_r)}{2}\frac{1}{2\pi}$. The ring speed can be found in Figure 4.17.
- the synchronous response peaked at 68krpm: the critical speed of this rotor-bearing system. After passing this critical speed, the synchronous response decayed again. Before the critical speed, even at the lowest measured speeds, there is significant synchronous response caused by misalignment or (out-of-plane) unbalance.
- at 83krpm an oil whirl starts, this time at a frequency somewhat below $\omega = \frac{(\Omega_s+\Omega_r)}{2}\frac{1}{2\pi}$.
- at 115krpm the oil whirl interfered with half the shaft rotation speed and jumped to a frequency of $\omega = \frac{\Omega_s}{2}\frac{1}{2\pi}$.
- at 130krpm the oil whirl locked into the first bending mode of the rotor-bearing system (which is the same mode that is triggered at 83krpm by the synchronous excitation) and formed a whip.
- at 158krpm the oil whip vanished.

These findings correspond with Woschke [206], who observed that sub-synchronous whirling is initially excited at a frequency corresponding to the fluid velocity in one of the films. These whirls may eventually lock into a non-linear eigenmode of the rotor-bearing system.
By combining the data of all six displacement sensors, it is observed that the rotor always whirls in a forward, cylindrical mode: the whirl is in the same direction as the shaft rotation speed and the orbits of the three locations along the shaft are all in phase, see Figure 4.12. No conical modes were observed during the measurements, which would commonly occur in case of a turbocharger rotor [159] which has two overhung disks instead of one center disk.

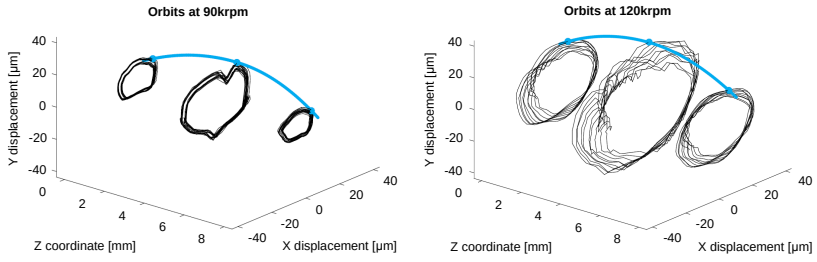

(a) (b)

Figure 4.12: Rotor orbits at (**a**) 90krpm and (**b**) 120krpm. Image based on [200].

The simulations show a very similar response, as can be observed in Figure 4.13 .

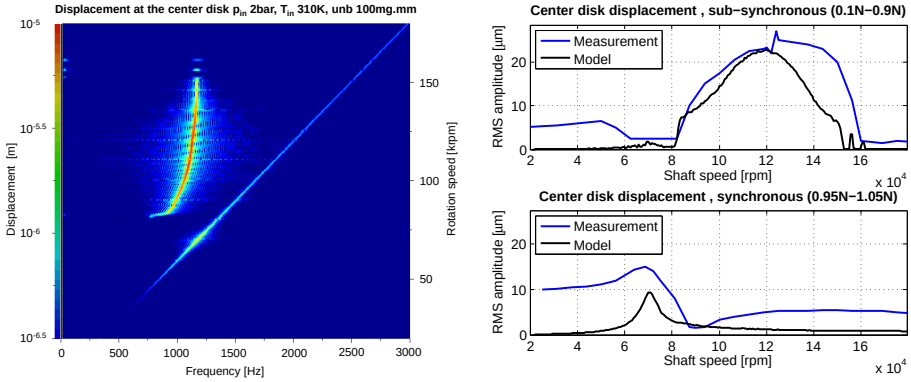

(a) (b)

Figure 4.13: Simulation results: **(a)** waterfall plot and **(b)** sub-synchronous and synchronous components of the displacement of the center disk during a run-up.

The waterfall plot based on the simulation output is very similar to the waterfall plot of the measurement, Figure 4.11a. Particularly, the following details are similar:

- the synchronous response shows the critical speed traversal at 68krpm.
- the onset speed of oil whirl at 83krpm is correctly predicted.
- the oil whirl frequency running from 900Hz to 1100Hz is similar to the measurement results.
- the vanishing of the oil whirl at 155krpm was also observed in the measurements.

The two main discrepancies between the measurement and the simulation results are:

- the sub-synchronous response between 115krpm and 125krpm. During the measurements, the oil whirl temporarily jumped to $\omega = \Omega_s/2$ which was not observed in the simulation results. We have no clear understanding of this discrepancy.
- the measured synchronous response before passing the critical speed is higher than predicted. This is very likely due to misalignment and residual unbalance: in the model, the rotor is assumed to be perfectly aligned and only have an unbalance vector acting on the center disk whereas on the test setup the motor and the rotor might have been misaligned and might have had an unbalance vector which was not exactly on the midplane of the disk. Although care is taken to accurately design, manufacture and assemble the test setup, imperfections in the micrometer range are likely to be present in the test setup.

Figure 4.14 shows the maximum eccentricities of the bearing over the operating range as predicted by the model, where the inner and outer eccentricities are defined as:

$$\begin{aligned} \varepsilon_{\text{in}} &= \frac{\sqrt{(e_{\text{s\_X}} - e_{\text{r\_X}})^2 + (e_{\text{r\_Y}} - e_{\text{r\_Y}})^2}}{C_{\text{in}}} \\ \varepsilon_{\text{out}} &= \frac{\sqrt{e_{\text{r\_X}}{}^2 + e_{\text{r\_Y}}{}^2}}{C_{\text{out}}} \end{aligned} \tag{4.32}$$

As can be seen, the oil whirl seems to occur mostly in the inner oil film, reaching eccentricities over 0.8. As can be seen, the model predicts another oil whirl above 150krpm which is not observed in the displacement on the center disk depicted in Figure 4.13. This secondary oil whirl is also reflected in the ring speed, as presented in Figure 4.17.

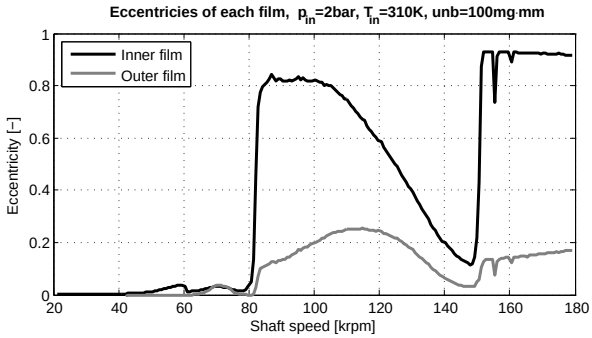

Figure 4.14: Simulation result: maximum eccentricity of one of the two bearings during a run-up.

Another aspect of interest of this study pertains to the bearing friction loss, which can be a significant part of the power losses in a turbocharger, particularly in low engine load conditions [165]. Figure 4.15 presents the friction losses of one bearing as a function of rotation speed, at standard operating conditions. In case the friction losses would be simply related to Couette flow, Petroff's equation of the friction losses would be stated in the form of $P_{\text{friction}} \sim \Omega^2 \mu_{oil}$ [51]. Clearly, the response in Figure 4.15 does not increase quadratically with rotation speed, so the viscosities of the oil films appear to decrease significantly as the rotation speed increases.
The friction losses, however, are not only a function of the Couette shear losses. As can be observed in Figure 4.15, the friction losses of the floating ring bearing also strongly depend on squeeze motion as reflected by the increase of friction losses once oil whirl occurs at 83krpm. The same conclusion was also drawn by Tian [172], who discovered by simulations that oil whirl significantly contributes to the friction losses of a floating ring bearing. Our model predicts a similar trend, and as shown in Figure 4.16 predicts that the friction losses mostly originate from the inner oil film, but overestimates the increase of friction losses at the onset speed of oil whirl.

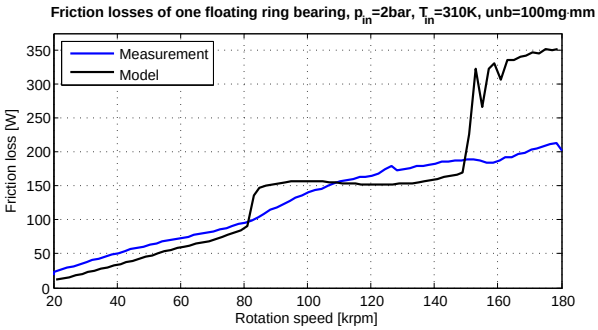

Figure 4.15: Friction losses of a floating ring bearing as a function of the shaft rotation speed under standard operating conditions.

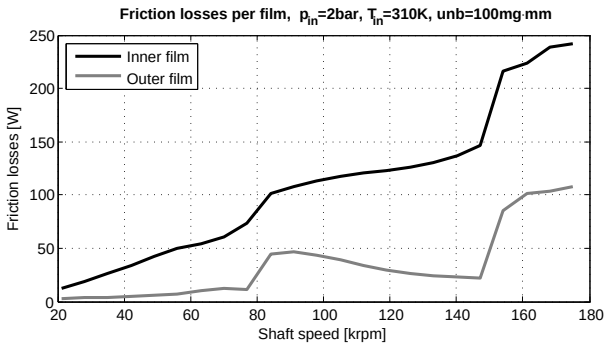

Figure 4.16: Simulation result: friction losses of a floating ring bearing as a function of the shaft rotation speed under standard operating conditions.

As can be seen in Figure 4.17, this seems to be related to an overestimation of the ring speed during oil whirl. The same goes for the sudden increase of friction losses at speeds above 150krpm, which is caused by an overprediction of the ring speed in this range.

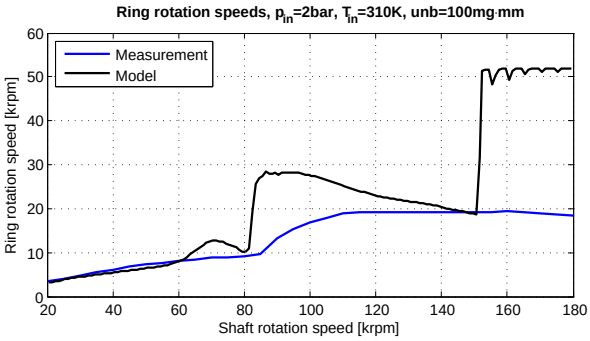

Figure 4.17: Ring speed under standard operating conditions.

From the start at 20krpm, the ring speed gradually increases as the shaft speed increases. At 83krpm, the oil whirl starts (see Figure 4.11a) and the ring speed suddenly increases. At speeds above 115krpm, the ring speed becomes constant. Trippett and Li [147] also observed this and reasoned that this is due to the greater increase of the temperature in the inner oil film, which has a smaller clearance and therefore greater friction losses than the outer fluid film [174]. This, however, seems only part of the explanation. As the ring speed ratio quite abruptly becomes constant at the same moment that oil whirl occurs, it seems that the constant ring speed is imposed by the oil whip conditions. At speeds above 160krpm, the oil whirl vanishes and subsequently the ring speed even decreases with increasing shaft speed. The ring speed profile of Figure 4.17 is similar to the profile measured by Köhl [203].
Figure 4.18 presents the predicted temperatures of the oil films at standard operating conditions. The increase of oil film temperature at the onset speed of whirl at 83krpm can be recognized.

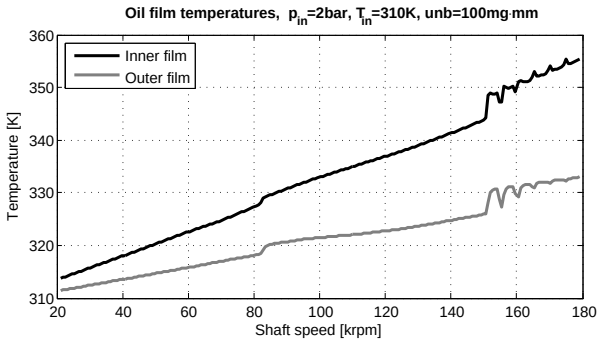

Figure 4.18: Simulation result: average oil film temperatures under standard operating conditions.

As a consequence of the increased film temperature the film clearances vary only slightly, as depicted in figure 4.19.

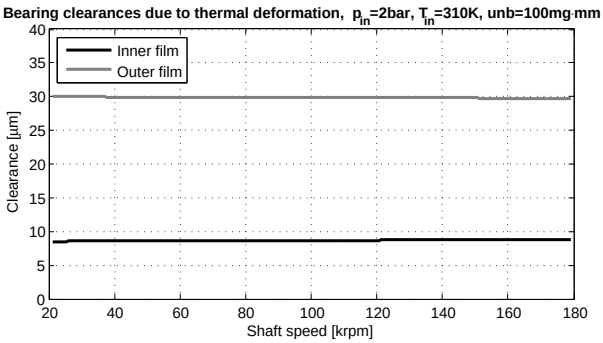

Figure 4.19: Simulation result: bearing clearances due to thermal deformation under standard operating conditions.

Unfortunately, no measurement data is available to validate the predictions of the inner and outer oil film temperatures: we decided not to disturb the circular shape of the bearing bore of the test setup by including thermocouples, as it is known that non-circular features strongly influence the sub-synchronous response [185].

Figure 4.20 presents the distribution of pressure, temperature, viscosity and mass fraction in the oil films at 145.000 rpm. The following details can be observed:

- as can be seen in the *Film height* plot, the eccentricity of both films are in phase and are both relatively small, i.e. less than 0.1, at the moment of plotting the data.

- in the *Pressure* distribution plot, two pressure peaks are observed in the outer fluid film, corresponding to the hydrostatic oil feed pressure ($x = [0.005, 0.015]$) and a hydrodynamic oil pressure peak ($x = [-0.01, 0]$). The effect of the oil connecting channels can clearly be recognized in the pressure distribution of the inner oil film, where the oil connecting channels clearly restrict the area of the hydrodynamic pressure buildup.

- the *Mass fraction* plot shows that the outer fluid film is almost entirely non-cavitated due to the presence of the oil feed channel. The inner film is partly cavitated at the diverging section. The oil connecting channels locally limit the extent of the cavitation.

- in the *Temperature* distribution over the film areas, the inflow of relatively cold oil at the oil feed channel in the outer oil film ($x = [0.005, 0.015]$) can clearly be observed. Furthermore, the inner oil film is considerably warmer than the outer oil film, so also the oil which flows through the oil connecting channels supplies relatively cold oil to the inner oil film.

- the *Viscosity* distribution is inversely similar to the *Temperature* distribution as the viscosity is strongly dependent on the temperature.

- lastly, the *Friction losses* in the inner oil film are typically one order of magnitude larger than in the outer oil film as the velocity difference over the inner oil film is larger and the film clearance is smaller than in the outer oil film. Furthermore, the friction losses are higher at locations where the viscosity is locally higher.

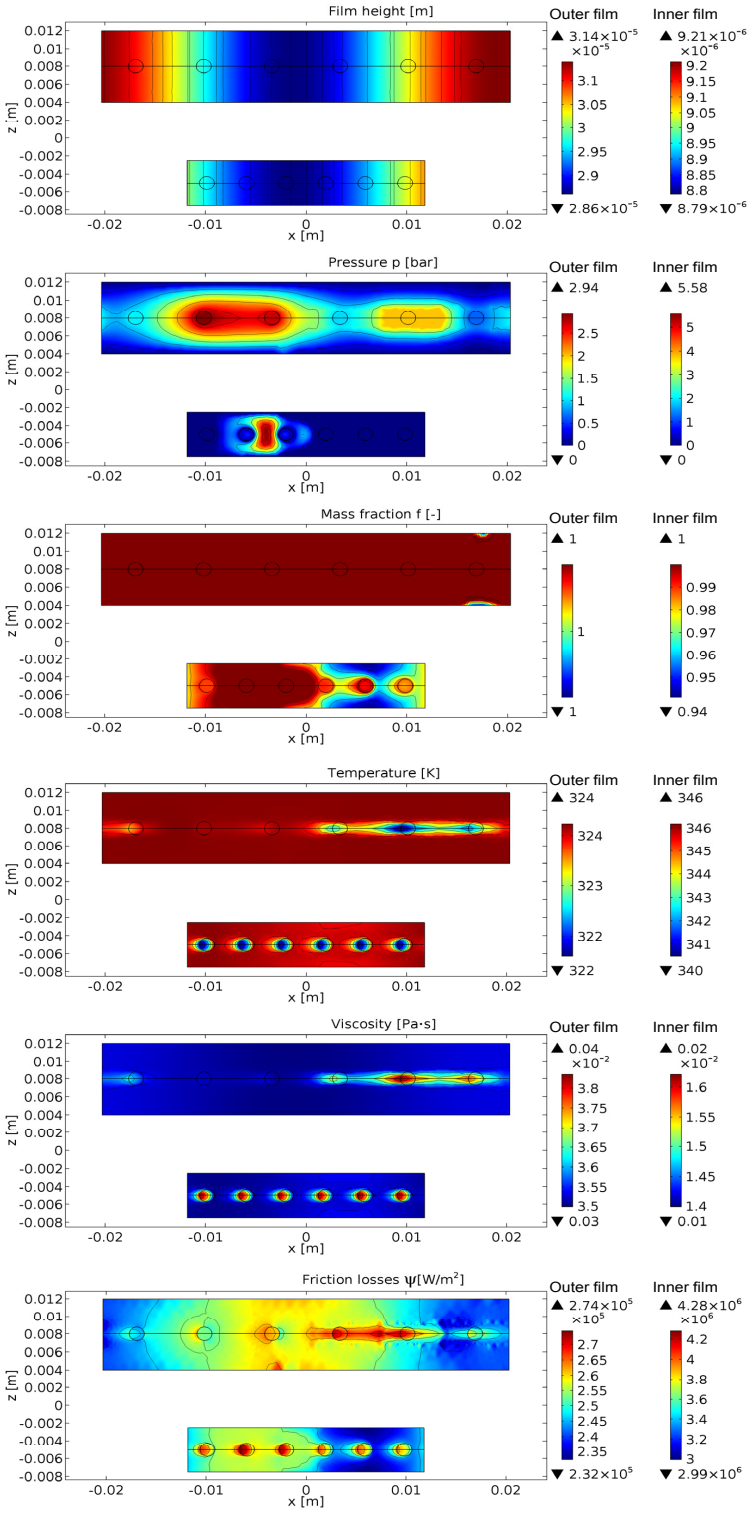

Figure 4.20: Simulation result: contour plots of the bearing fluid domains representing its state at a rotation speed of Ω_s = 145.000 rpm. The data is taken from a run-up simulation of the coupled rotor-bearing system.

4.4.2. RESPONSE AS A FUNCTION OF OIL FEED PRESSURE

Having studied the response of the rotor-bearing system at standard operating conditions, we subsequently investigate its response under different operating conditions. First, the influence of the oil feed pressure is investigated. During the experiments, the feed pressure was varied between 1 bar and 3 bar, see Figure 4.21 and Figure 4.22. During the measurements, we observed that at feed pressures above 3 bar, the ring is pushed into contact with the bearing housing surface and causes a static friction which is not overcome by hydrodynamic forces at speed below 50krpm, resulting in the ring to stick to the bearing housing at rotation speeds below 50krpm. This phenomenon is not observed in our predictions in Figure 4.22 as there is no mechanical contact description in the model.

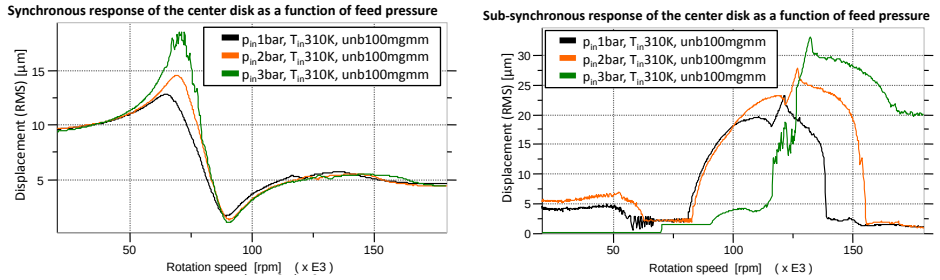

(a) (b)

Figure 4.21: Measurement results: influence of oil feed pressure on the rotordynamic response.

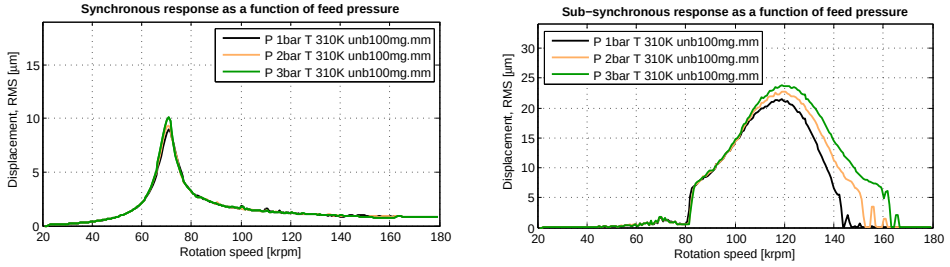

(a) (b)

Figure 4.22: Simulation results: influence of oil feed pressure on the rotordynamic response.

The synchronous response at the center disk and at the bearings increases with feed pressure. This is counter-intuitive, as an increase in feed pressure is expected to result in a higher bearing stiffness and therefore also a smaller response at the bearings. We currently have no plausible explanation for this interesting phenomenon. Brouwer [207] performed shaft motion measurements on a turbocharger rotor supported by floating ring bearings and also found that the shaft orbit amplitudes increase with increasing oil feed pressure.

Schweizer [159] observed that an increase of pressure can delay the onset speed of oil whirl, which is also found in our measurements but not in our simulations. A possible explanation for this is the lack of a mixed lubrication description in our model, which may be necessary in case the higher oil feed pressure pushes the ring in downward direction, so partial mechanical contact may occur here.

The maximum oil whirl amplitudes are higher at increased feed pressures and the oil whirl remains over a longer rotation speed range, as can also be observed in the waterfall plots in Figure 4.23.

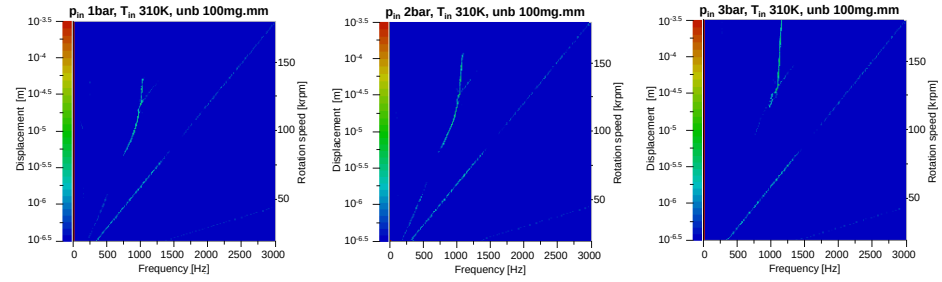

(a) (b) (c)

Figure 4.23: Measurement results: influence of oil feed pressure on the rotordynamic response.

The friction losses of the floating ring bearing increase with an increase of oil feed pressure, see Figures 4.24 and 4.25.

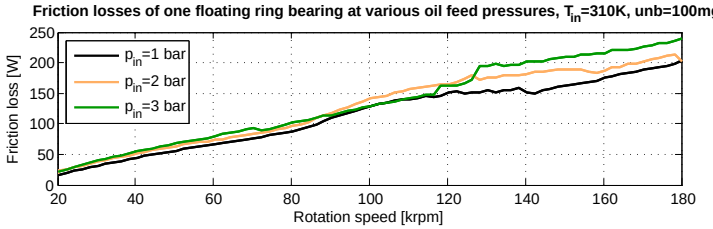

Figure 4.24: Measurement results: friction losses of a floating ring bearing as a function of oil feed pressure.

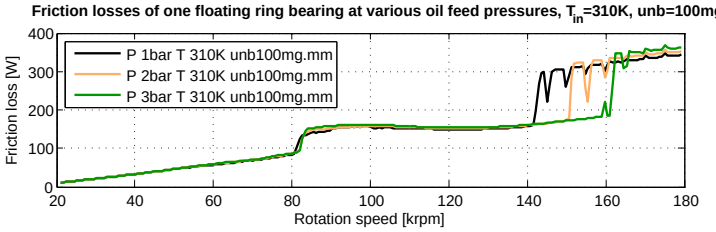

Figure 4.25: Simulation results: friction losses of a floating ring bearing as a function of oil feed pressure.

As can be observed in the waterfall plots in Figure 4.23, this increase is partly due to oil whirl: at high oil feed pressure, oil whirl occurs more severely over a wide operating range, resulting in an increase of friction losses as more energy is dissipated due to the oil whirl motion. A higher oil feed pressure results in less cavitation and hence less stability in the bearing, so oil whirl is more severe.

Furthermore, the higher fill rate of the bearing results in an increase of oil volume where shear losses occur. Lastly, an increase in oil feed pressure also increases the oil flow rate through the bearing and therefore more heat is carried away from the bearing which in turn results in a higher average viscosity in the bearing and thus more friction losses [171].

Deligant [171] obtained similar results in his measurements: a 10% increase of friction losses over a 2 bar pressure increase. Deligant, however, did not relate this explicitly to the oil whirl but instead related it to cooler oil films due to the increased oil flow at higher feed pressures.

The simulation results are obscured by the overprediction of the ring speed at speeds above 140krpm, as depicted in Figure 4.17. Eventually, higher feed pressures are indeed predicted to cause larger friction losses.

4.4.3. RESPONSE AS A FUNCTION OF OIL FEED TEMPERATURE

An increase of oil feed temperature generally leads to a decrease of rotor displacement amplitude, as can be observed in Figures 4.26 and 4.27. This is in contradiction to the measurements of Brouwer [207], who observed that the displacement amplitudes of the rotor are generally largest at high oil feed temperatures. This shows that different rotor-bearing geometries will react differently to an increase of oil feed temperature.
The onset speed of oil whirl is slightly increased by increasing the temperature. We observed that the ring speeds are generally higher in case the oil feed temperature increases, as was also measured by Porzig [168]. From the simulation data, we observed that an increase of oil feed temperature causes the temperature and thus the viscosity of the outer oil film to be closer to the temperature of the inner oil film. The temperature of the bearing housing is the same as the temperature of the oil feed channel so increasing this temperature directly affects the outer fluid film viscosity.

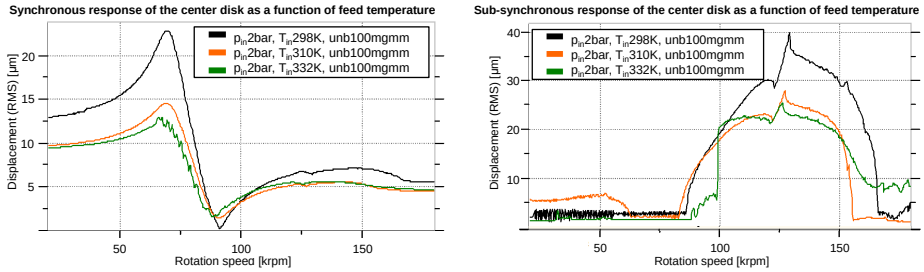

(a) (b)

Figure 4.26: Measurement results: influence of oil feed temperature on the rotordynamic response.

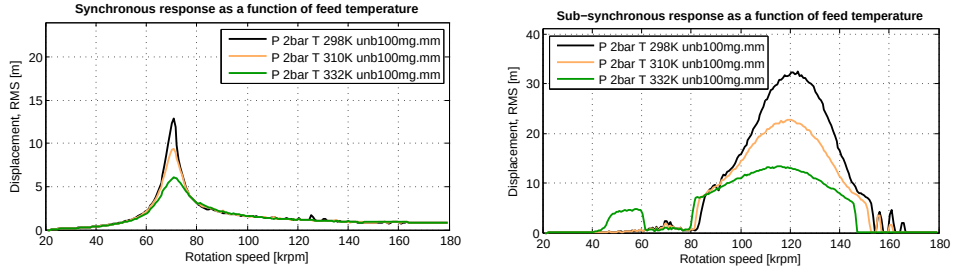

(a) (b)

Figure 4.27: Simulation results: influence of oil feed temperature on the rotordynamic response.

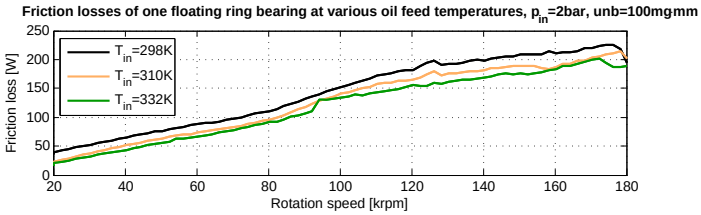

Figure 4.28: Measurement results: friction losses of a floating ring bearing as a function of oil feed temperature.

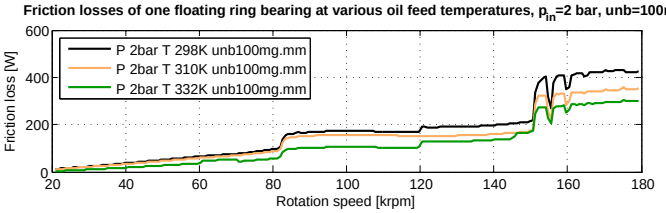

Figure 4.29: Simulation results: friction losses of a floating ring bearing as a function of oil feed temperature.

As can be expected, the friction losses decrease by increasing the oil feed temperature, see Figure 4.28 and 4.29. However, the reduction, typically 10% to 20%, is considerably less than the reduction of the oil feed viscosity, which is more than 50% in case of increasing the oil temperature from 298K to 332K. Similar results were also measured by Deligant [171], who observed a 10% to 20% decrease in friction losses at an oil feed temperature increase of 20K. Friction heating causes the temperature of the inner film to be considerably higher than the oil feed temperature at low oil feed temperatures, which reduces the difference between friction losses at low and high oil feed temperatures.

4.4.4. RESPONSE AS A FUNCTION OF ROTOR UNBALANCE

As can be expected, adding unbalance to the rotor will increase the synchronous amplitude at the critical speed, as can be seen in Figure 4.30. Moreover, we observed that rotor unbalance can suppress the onset speed of whirl, but can also cause it to remain in an oil whirl over a larger speed range.

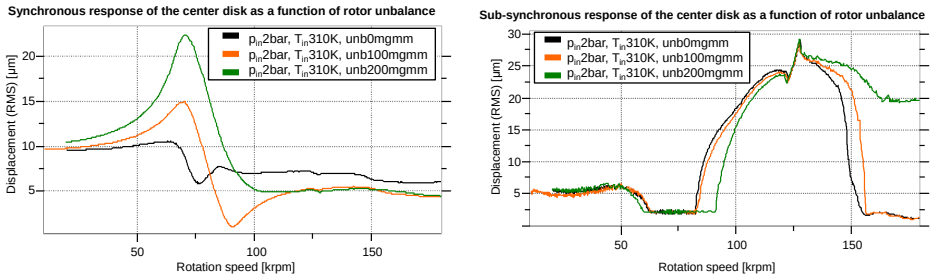

(a) (b)

Figure 4.30: Measurement results: Influence of rotor unbalance on the rotordynamic response.

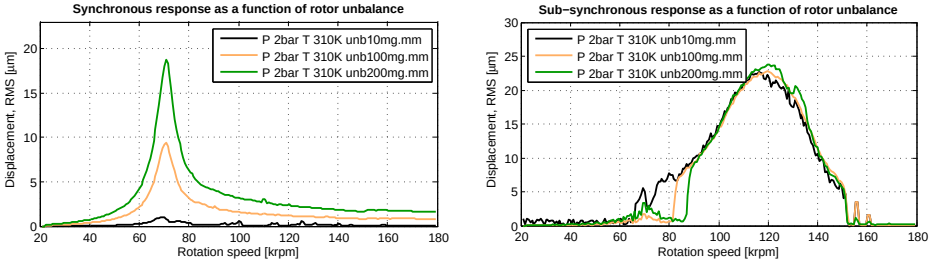

(a) (b)

Figure 4.31: Simulation results: Influence of rotor unbalance on the rotordynamic response.

The simulation results in Figure 4.31 show a similar increase in synchronous response with increasing unbalance. It should be noted that simulations with an unbalance of 0mg·mm did not converge, hence an unbalance value of 10mg·mm was chosen

instead. The increase of the onset speed of oil whirl was also found in the simulations; the simulations however did not predict the persistent oil whirl above 140krpm for the experiment with the maximum unbalance.

As the rotor with a high unbalance level remains in oil whirl at speeds above 140krpm, its friction losses are also larger in this range, as can be seen in Figure 4.32. For the rest of the speed range, the unbalance amount does not significantly affect the friction losses.

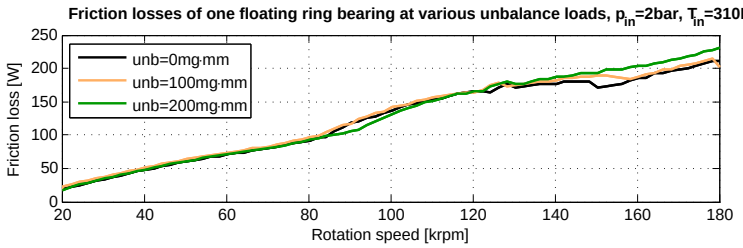

Figure 4.32: Measurement results: friction losses of a floating ring bearing as a function of rotor unbalance.

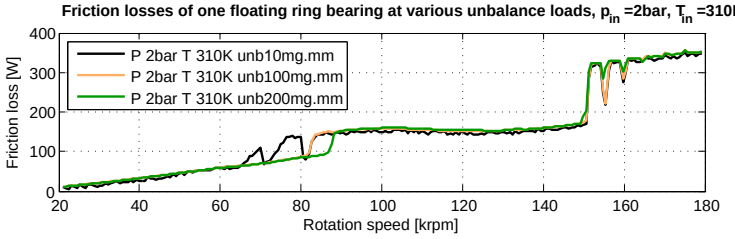

Figure 4.33: Simulation results: Friction losses of a floating ring bearing as a function of rotor unbalance.

4.4.5. RESPONSE AS A FUNCTION OF BEARING CLEARANCES

Three sets of bearing clearances have been evaluated, as can be seen in Table 4.3. It should be noted that these bearings have clearances which were especially chosen for this study and as such, are not strictly representative for bearings found in commercially available turbochargers. The bearing clearances were measured before and after testing to ensure they conform to the values stated in Table 4.3.

Table 4.3: Bearing clearances evaluated in this study.

	Inner clearance [μm]	Outer clearance [μm]
Bearing 1	8.5	30
Bearing 2	13	35
Bearing 3	16.5	41

All of these bearings were tested with a relatively high unbalance load, 250mg·mm, to make the influence of rotor imperfections small compared to the influence of the added

unbalance.

Figures 4.34, 4.35 and 4.36 demonstrate that the sub-synchronous response generally increases with increasing clearances. The opposite is observed for the synchronous response, which decreases with increasing bearing clearances.

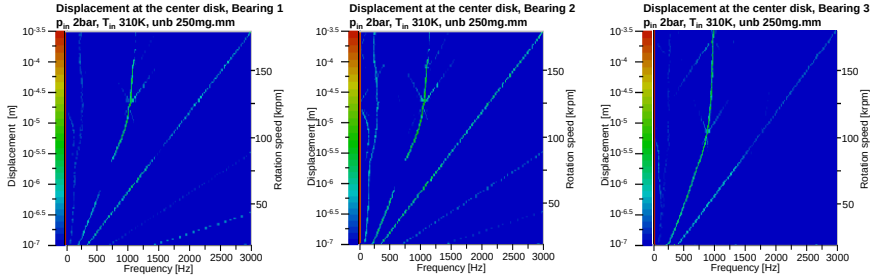

(a) (b) (c)

Figure 4.34: Measurement results: influence of bearing clearance on the rotordynamic response.

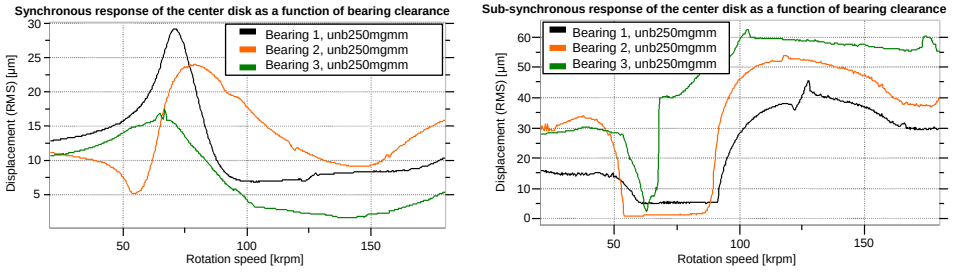

(a) (b)

Figure 4.35: Measurement results: influence of bearing clearance on the rotordynamic response.

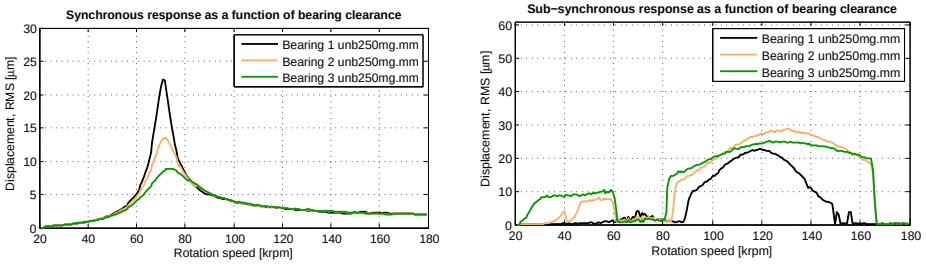

(a) (b)

Figure 4.36: Simulation results: influence of bearing clearance on the rotordynamic response.

The critical speed of Bearing 2 seems to be higher than the two other bearings, as depicted in Figure 4.35a. It is expected that this was caused by out-of-plane unbalance, as the response also shows an anti-resonance around 55krpm. Measurements of Bearing 2 with a further increased unbalance of 400mg·mm (not included here) confirmed that the critical speed was similar to the measurements with Bearing 1 and Bearing 3.
Figures 4.37 and 4.38 present the friction losses for the various bearing clearances.

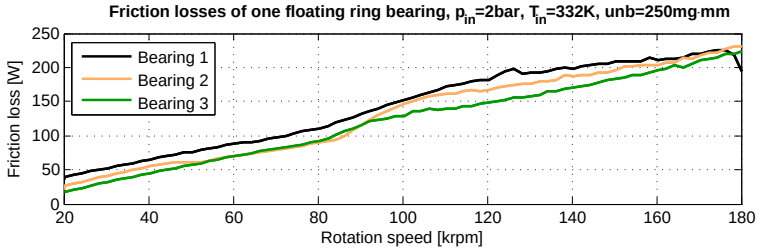

Figure 4.37: Measurement results: friction losses of floating ring bearing with various clearance combinations, as indicated in Table 4.3.

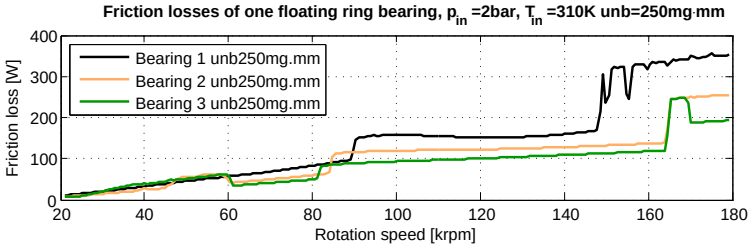

Figure 4.38: Simulation results: friction losses of floating ring bearing with various clearance combinations, as indicated in Table 4.3.

Remarkably, almost no difference has been observed between the friction losses of the three different bearing configurations. Although Bearing 1 has clearances which are 1.5 to 2 times smaller than those of Bearing 3, the differences in friction losses are typically no more than 10%, as can be seen in Figure 4.37. According to the simple Petroff equation, the friction power should be inversely proportional to the clearance C: $P_{\text{friction}} \sim \Omega^2 \mu_{\text{oil}} / C$.
The reason why the friction losses seem to be independent of the bearing clearances is depicted in Figure 4.39. As can be observed, the minimum film thickness occuring during a run-up is similar between the different bearing clearances. As the minimum film thickness depends on the rotor (unbalance) load, which is constant for the different bearings, the minimum film height is independent of the bearing clearance. And as at high eccentricities, the minimum film height largely determines the friction losses [51], the friction losses are similar for different bearing clearances. Moreover, the heat generated by friction is mostly dissipated through the rotor and the bearing housing, so

an increase of oil flow doesn't necessarily result in lower film temperatures and so more friction losses here.

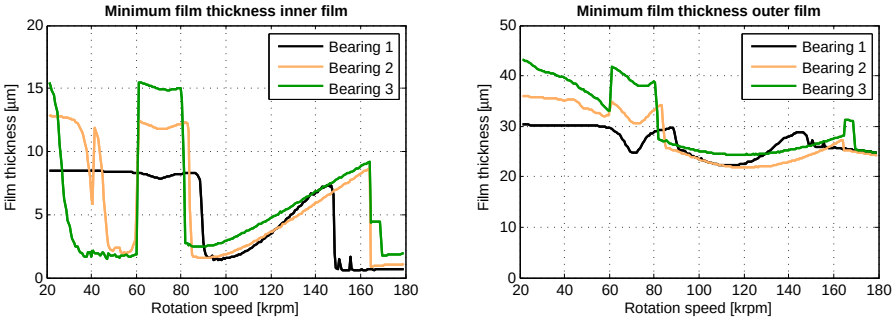

Figure 4.39: Simulation results: minimum film thickness of the various bearing clearance combinations, as indicated in Table 4.3.

4.4.6. SUMMARY INFLUENCE FACTORS

Table 4.4 summarizes the results obtained by varying the input parameters on the floating ring bearing test setup.

Table 4.4: Summary of influence factors: + denotes the effect increases with an increase in the specific value, − denotes the effect decreases with an increase in the specific value, 0 denotes the effect does not change by more than 5% with an increase in the specific value.

	Effect				
Variable	Critical speed amplitude	Onset speed of whirl	Whirl ampl.	Whirl freq.	Friction losses
Rotor unbalance	+	+	0	0	0
Oil feed temp.	-	0	-	0	-
Oil feed pressure	+	0	+	+	+
Bearing clearance	-	-	+	-	-

Comparing the results of the floating ring bearing, Table 4.4 with the results of the plain journal bearing, Table 3.4, we see that both systems behave very similar to changes in oil supply temperature, pressure and rotor unbalance. The oil whirling behavior of the floating ring bearing seems to be more sensitive to variations in oil feed conditions: particularly the oil whirl amplitude shows a stronger tendency to vary with the input parameters.

4.5. CONCLUSIONS

This Chapter describes the dynamic behavior and the friction losses of a Laval rotor supported by floating ring bearings. The model from Chapter 3 was extended and a test setup was developed to validate the model. This test setup can be seen as a simplified turbocharger rotor-bearing system, which is not affected by the influence of seals, external vibrations, heat from a turbine and aerodynamic forces on wheels. Moreover, the test setup enabled a more precise control of unbalance compared to a turbocharger rotor-bearing system.

The model generally shows good correlation with the measurement results. The model is able to correctly predict the amplitude and rotation speed of the critical speed and how these change as a function of oil pressure, oil temperature, rotor unbalance and bearing clearance. Some residual unbalance or misalignment error on the test setup causes an offset in the measurement results, though. Regarding the sub-synchronous response: the oil whirl and oil whip frequencies and amplitudes are also well predicted by the model. Whirl frequencies related to the inner film as well as to the outer film were both observed, but never simultaneously.

Based on our numerical simulations, we observed that the internal oil flow within the oil connecting channels in the floating ring is responsible for 4-7% of the eventually occuring ring speed. Due to convergence issues, this influence has however not been implemented in time-transient run-up simulations. Nevertheless, the ring speed ratios predicted by our model were reasonably in line with our measurement results up to 150krpm, where our model made a sudden overestimation in ring speed ratio. It remains unclear if this discrepancy was due to the simplification of the oil connecting channel or due to another effect.

Furthermore, we noted that both in our measurements as in our simulations that hysteresis occurs due to the non-linear properties of the bearing: the run-up response is different to the run-down response. We also identified that hydrostatic pressure at the oil inlet may push the ring to the bearing housing, preventing it to float and rotate at low rotation speeds.

Lastly, we observed that friction losses do not depend quadratically on the rotation speed, but are instead highly dependent on the whirling amplitudes. Furthermore, the friction losses are similar for various bearing clearances as the minimum film thickness, which largely determines the friction losses, remains similar. The ring rotation speed remains constant in the range where severe oil whirl/whip occurs, which indicates that the ring speed in this condition is a consequence of the oil whip conditions rather than a cause. Our friction loss predictions and the trends with various oil supply conditions are considered to be reasonable up to 150krpm, where the aforementioned overestimation of ring speed ratio also caused an overestimation of friction losses.

5

DYNAMIC BEHAVIOR OF A TURBOCHARGER ROTOR-BEARING SYSTEM

In this chapter, we will analyze the dynamic behavior of a turbocharger rotor suspended by floating ring bearings. We will use the bearing model described in the previous chapter and adapt the Laval rotor model to a turbocharger rotor model: instead of one center mounted disk, the rotor has an overhang disk at each end of the shaft. We will validate the model by shaft displacement measurements on a real turbocharger. Furthermore, the rotor-bearing model will be used to analyze the effect of unbalance on the compressor wheel and the turbine wheel. Lastly, the effect of the oil supply conditions and the presence of a thrust bearing is analyzed.

5.1. INTRODUCTION

As introduced in Section 1.2, turbocharger rotors are commonly supported by floating ring bearings mounted in the middle section of the rotor. The rotor has a compressor wheel at one end and a turbine wheel at the other end, see Figure 5.1. Typical length scales for automotive turbochargers are 100mm rotor length and 50mm wheel diameter.

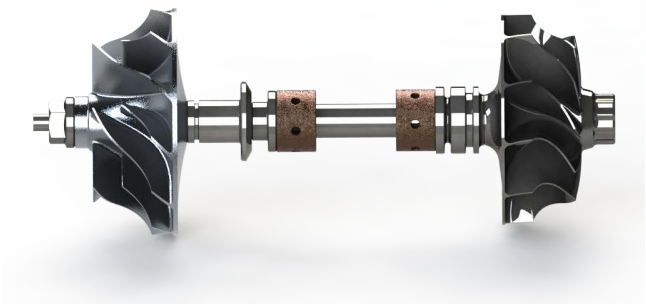

Figure 5.1: Turbocharger rotor with a compressor wheel (left hand side) and a turbine wheel (right hand side). The two bronze colored sections are the floating ring bearings. The thrust bearing is located in between the collars adjacent to the left hand floating ring bearing. This specific turbocharger rotor is for a small size gasoline engine and has a length of just over 100mm.

5.2. MODELING THE TURBOCHARGER ROTOR ON FLOATING RING BEARINGS

5.2.1. ROTOR

A cross-section of the rotor considered in this chapter is depicted in Figure 5.2.

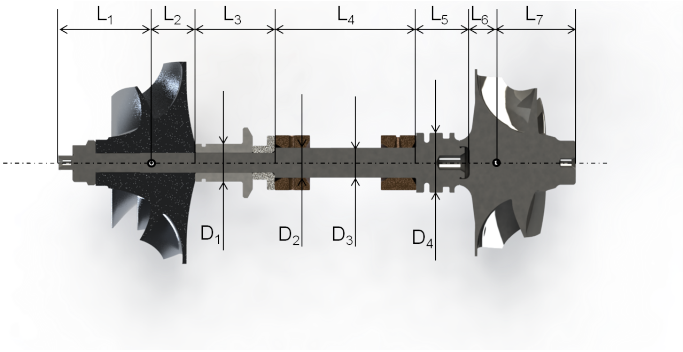

Figure 5.2: Cross-sectional view of the turbocharger rotor with the main rotor dimensions.

Table 5.1: Properties of the rotor depicted in Figure 5.2.

Name	Value	Unit	Name	Value	Unit	Name	Value	Unit
L_1	17	mm	L_7	14	mm	I_{XX_c}	$7.3{\cdot}10^{-7}$	kgm^2
L_2	10	mm	D_1	7	mm	I_{ZZ_c}	$1.6{\cdot}10^{-6}$	kgm^2
L_3	15.6	mm	D_2	6	mm	m_t	48.2	g
L_4	28	mm	D_3	6	mm	I_{XX_t}	$2.8{\cdot}10^{-6}$	kgm^2
L_5	8.8	mm	D_4	8	mm	I_{ZZ_t}	$3.9{\cdot}10^{-6}$	kgm^2
L_6	9	mm	m_c	15.5	g			

The compressor wheel is made of aluminium, the floating ring bearings are made of a bronze alloy and all other rotor components are made of steel. The material properties assumed for the model are given in Table 5.2. Linear, isotropic material properties are assumed. In addition, Rayleigh damping is assumed as described by Equation 3.16.

Table 5.2: Material properties of the rotor

Symbol	Value	Unit	Description
ρ_s	7850	$kg\,m^{-3}$	Density steel
E_s	210	GPa	Young's modulus steel
ρ_{alu}	2700	$kg\,m^{-3}$	Density aluminium
E_{alu}	69	GPa	Young's modulus aluminium
ρ_{bronze}	8780	$kg\,m^{-3}$	Density bronze
c_M	5.5	s^{-1}	Rayleigh damping coefficient
c_K	3e-7	s	Rayleigh damping coefficient

The geometry of the turbocharger rotor is more complex than the Laval rotor analyzed previously in Chapters 3 and 4. Particularly the bladed wheel geometries can not be straightforwardly modeled as a simple disk. Moreover, the compressor wheel is mounted to the rotor by a bolted connection which introduces interface damping between the components. Depending on the axial pre-stress caused by torquing up the nut, the modal damping ratios of a rotor may change [208]. In case of an automotive scale turbocharger rotor, however, the effect of the axial pre-stress from the nut on the modal response is negligibly small [209] and can therefore be ignored.

As a first step in building a turbocharger rotor model, a FEM model is created, consisting of $5 \cdot 10^5$ volume elements. A modal analysis is performed in free conditions, resulting in the eigenmodes depicted in Figure 5.3.

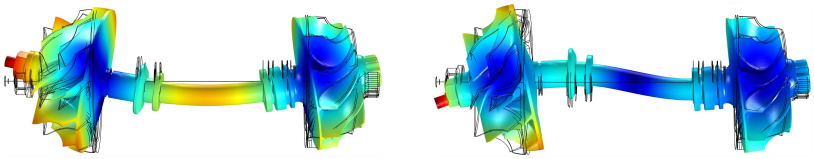

(a) First mode shape. (b) Second mode shape.

Figure 5.3: Modal analysis of the turbocharger rotor based on a FEM model using volume elements.

In addition to these radial eigenmodes, the first torsion mode is predicted at 2325 Hz. The rotor has no other eigenfrequencies in the range (0-10kHz).

For time-transient analysis, this FEM model would be too computationally expensive. Therefore, the model is reduced to a model incorporating only beam and disk elements following the methods presented in Section 3.2. A schematic representation of the beam-disk model is displayed in Figure 5.4. Note that the thrust bearing is excluded from this analysis: it is initially assumed that the radial and axial dynamics are decoupled. The influence of the thrust bearing on the radial dynamics will be separately investigated in Section 5.4.5.

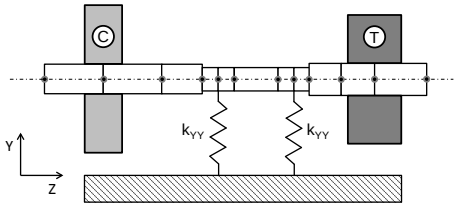

Figure 5.4: Schematic representation of the beam-disk model. *C* marks the compressor wheel and *T* marks the turbine wheel.

Concentrating on the rotor only, we initially do not take into account any stiffness or damping forces from the bearings and perform a modal analysis of the rotor in free conditions. The contributions of bending stiffnesses of the wheels to the shaft were chosen so that a good match was found between the volume element FEM model and the beam-disk element FEM model: the results in Figure 5.5 are similar to the results in Figure 5.3.

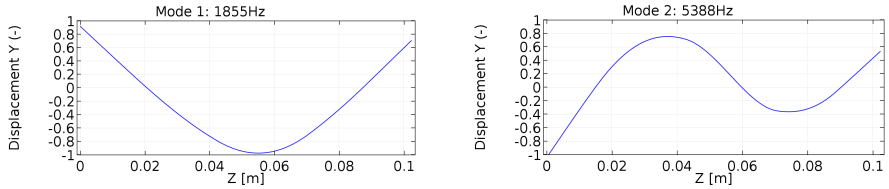

(a) First mode shape.

(b) Second mode shape.

Figure 5.5: Modal analysis of the turbocharger rotor based on a FEM model using beam and disk elements. The compressor wheel is mounted to the left hand side of the rotor, the turbine wheel to the right hand side.

To validate this *uncoupled* rotor model, i.e. without bearings, we performed hammer impact measurements on the rotor suspended in elastic rubber bands, see Figure 5.6.

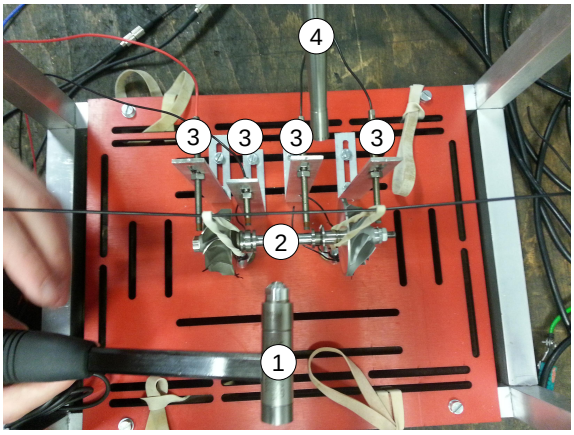

Figure 5.6: Experimental modal analysis: an impact hammer (1) strikes the turbocharger rotor (2). The resulting response is recorded using eddy current displacement sensors (3) and a microphone (4) [209].

Table 5.3 presents the results of the hammer impact measurements as well as the results of both FEM models. The experimental modal results are 5% lower than the FEM results, most likely due to the interface damping between the rotor components which is not included in the FEM models. Nevertheless, resemblance within 5% is considered to be acceptable here, so the rotor model is suitable to describe the structural dynamics.

Table 5.3: Modal analysis of the rotor: results

	FEM model: volume elements	FEM model: beam and disk elements	Experimental modal analysis
Mode 1 [Hz]	1855	1855	1770
Mode 2 [Hz]	5390	5388	5120

5.2.2. BEARINGS

As can be observed in Figure 5.1, the turbocharger under consideration features two floating ring bearings. The floating ring bearing model as presented in Section 4.2.1 is incorporated in the rotor-bearing model. To recapitulate, the following lumped variables are predicted by the floating ring bearing model:

- the ring rotation speed,
- the ring position,
- the fluid film friction loss,
- the shaft displacement at the bearing.

Furthermore, for each fluid film, the following distributed variables are predicted:

- the fluid film pressure distribution,
- the fluid film viscosity distribution,
- the fluid film mass fraction distribution,
- the fluid film temperature distrubution.

5.3. TEST SETUP

In order to validate the predictions of the rotor-bearing model, measurements have been performed. The response of a turbocharger rotor-bearing system over a run-up was measured using a modified turbocharger, depicted in Figure 5.7.

(a) Modified turbocharger rotor-bearing system: top view. The rotor features an additional cylindrical section in front of the compressor wheel (left hand side).

(b) Modified turbocharger rotor-bearing system: front view. Grub screws can be inserted in the holes indicated by the arrows.

Figure 5.7: Turbocharger rotor-bearing system used for measurements in this chapter.

On this turbocharger, a cylindrical section was added to the compressor side of the rotor, so that the amount of unbalance can be adjusted by inserting grub screws in the holes. The cylindrical section also serves as a measurement surface to measure the shaft displacement of the rotor.

For the measurements in this chapter, the turbocharger was driven by compressed air at ambient temperature. This excludes the considerable input of heat from the turbine which would normally strongly influence the temperature distribution of the oil films [168]. The oil is supplied to the bearing housing at a controlled temperature and pressure. Furthermore, during the measurements, the turbocharger was suspended in compliant rubber fixings to minimize the effect of structural dynamics of the support structure, i.e. steel manifolds, boost piping etc. We ascertained that the turbocharger support structure was free of any resonances in its operating range, 30krpm-200krpm by means of hammer impact testing.
The rotor model of Section 5.2.1 was updated by including the mass of the cylindrical section in front of the compressor wheel, which lowered the eigenfrequencies by roughly ten percent compared to the original turbocharger.

5.4. RESULTS

5.4.1. MODAL ANALYSIS OF THE LINEARIZED ROTOR-BEARING SYSTEM

The beam-disk model of the rotor as presented in Section 5.2.1 was used to perform a linear eigenvalue analysis at various rotation speeds in the operating range, resulting in the Campbell plot in Figure 5.8.

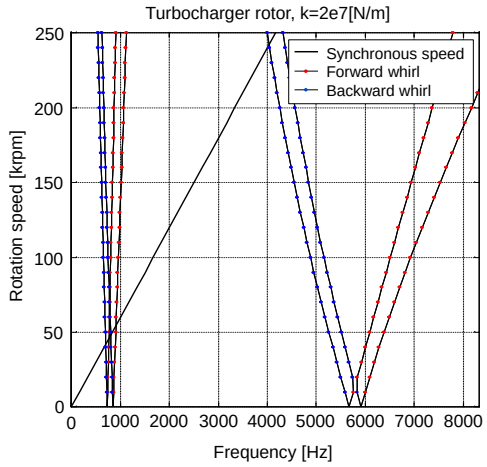

(a) Campbell plot.

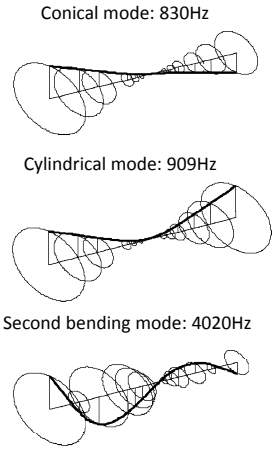

(b) Orbits at critical speeds. Left side is compressor side.

Figure 5.8: Campbell plot of the beam-disk FEM model of the turbocharger rotor. A linear bearing stiffness of $2{\cdot}10^7$N/m and no damping is assumed.

For this analysis, the bearings were assumed to be linear isotropic springs with a constant stiffness. Based on the results of Chapter 4, a stiffness of $2{\cdot}10^7$N/m seems a reasonable estimate. Although in Chapter 4, we clearly observed that floating ring bearings have non-linear dynamic properties, performing an analysis on the linearized turbocharger rotor-bearing system can give insight in the modes which can be encountered, as demonstrated by Tian [136].

As can be seen in Figure 5.8, the turbocharger rotor-bearing system traverses two critical speeds around 50krpm and one at 240krpm. Around 50krpm, the rotor has a *conical mode* which is mostly a rigid body mode. The second mode, near 900Hz, has a mode shape combining the *first bending mode* with in-phase rigid body translation. This mode is commonly referred to as the *cylindrical mode* [11, 164].

Note that the conical mode is excited by unbalance configurations where the unbalance vector on the compressor wheel is in counterphase with that of the turbine wheel, whereas the cylindrical mode is excited by in-phase unbalance configurations. The mode at 240krpm may be triggered by counterphase unbalance, although it is a backward mode which –in case of linear dynamics– may not be excited by unbalance excitation [20]. This rotor-bearing system, however, is highly non-linear, so an increased response may well be expected at this rotation speed.

Once again, it should be realized that in this analysis linear isotropic bearing stiffness were assumed, which may therefore not reveal the more complex sub-synchronous whirling modes caused by the (sometimes negative) anisotropic non-linear spring stiffness properties of a real floating ring bearing [136]. These properties will be considered in the next sections.

5.4.2. RUN-UP AT STANDARD OPERATING CONDITIONS

The turbocharger was operated in a run-up from 30krpm to 200krpm by controlling the turbine inlet pressure. During this run, the standard operating conditions were as follows:

- The oil inlet pressure p_i is set at 4 bar, and a temperature T_i of 303K.
- The rotor unbalance on the compressor side is set at 150mg·mm and 0mg·mm on the turbine side .

The shaft displacement of the turbocharger rotor-bearing system was measured on the compressor side, as depicted in Figure 5.7. Figure 5.9a presents the waterfall plot of this measurement data and adjacent to it, Figure 5.9b, a waterfall plot of the simulation data, based on the non-linear rotor-bearing model as presented in Section 5.2.

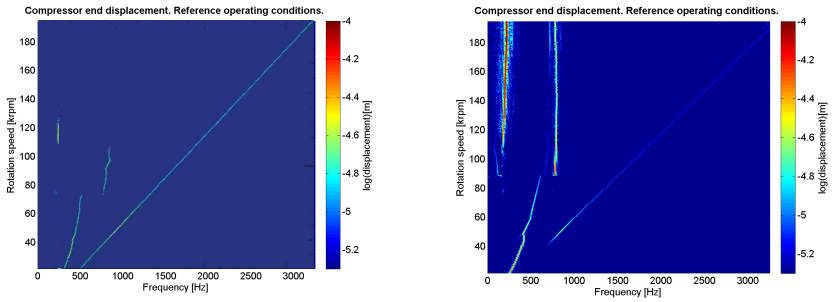

(a) Measurement data.

(b) Simulation data.

Figure 5.9: Waterfall plots of shaft displacement measured on the compressor side during a run-up at standard operating conditions.

The synchronous trace shows the traversal of a critical speed at 50krpm. In the sub-synchronous domain of the waterfall plots, three traces can be distinguished. Based on the simulation results, the operational deflection shapes of the synchronous response and the three sub-synchronous responses have been visualized in Figures 5.10a- 5.10d:

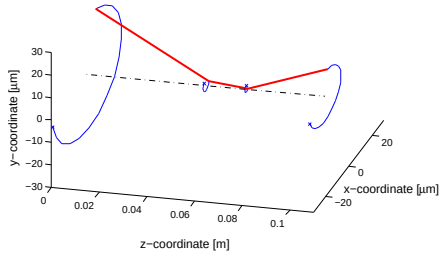

(a) Synchronous operational deflection shape, Ω =50krpm, ω=830Hz.

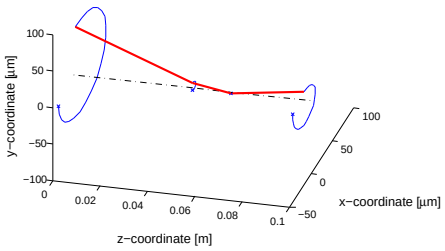

(b) Sub-synchronous operational deflection shape 1: cylindrical forward mode, range 30krpm-80krpm, ω =350Hz-450Hz.

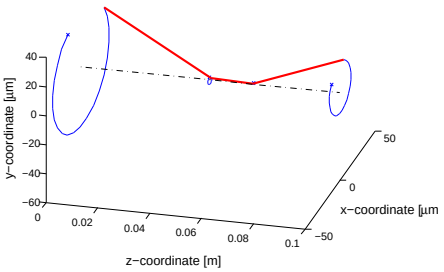

(c) Sub-synchronous operational deflection shape 2: cylindrical forward mode, range 80krpm-125krpm, ω =750Hz-800Hz.

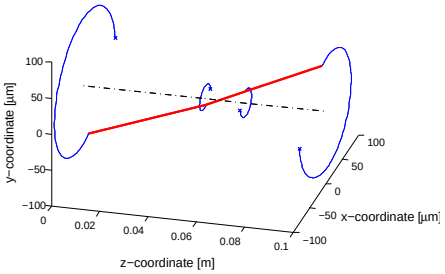

(d) Sub-synchronous operational deflection shape 3: conical forward mode, range 115krpm-145krpm ω =250Hz.

Figure 5.10: Simulation data: orbits of the rotor. The left hand side is the compressor side.

The critical speed is correctly predicted by the non-linear rotor-bearing model as well as the frequencies of the sub-synchronous modes. However, the predictions of the onset speeds and end speeds of the sub-sychronous traces are different to the measurement results: the jump to the second sub-synchronous mode is overpredicted and the third sub-synchronous mode is predicted to remain over the entire speed range whereas in the measurement results, it disappears above 130krpm.

The data of Figure 5.9 was also processed using band-pass filters to obtain the amplitude of the synchronous and sub-synchronous response as a function of rotation speed, as presented in Figure 5.11. As can be seen in Figure 5.11a, the sub-synchronous displacement amplitude of the model differs from the measurement results, particularly at higher speeds where the model predicts sub-synchronous vibration whereas none was measured. Possible causes of this discrepancy are expected to come from the measured turbocharger:

- the floating ring bearings were not perfectly circular,
- the unbalance distribution was different than assumed,
- the thrust bearing influenced the sub-synchronous vibrations,

- the seals influenced the sub-synchronous vibrations.

The synchronous response in Figure 5.11b shows that the measured turbocharger has an offset in displacement amplitude, most likely caused by either unroundness or a concentricity error of the measurement surface. Besides this, the predicted peak amplitude is slightly higher, meaning that the assumed unbalance of 150mg·mm on the compressor wheel is overestimated.

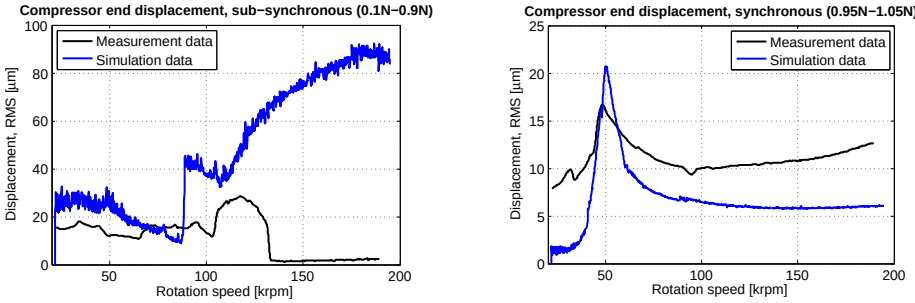

(a) Sub-synchronous response.

(b) Synchronous response.

Figure 5.11: Order filtered data of shaft displacement measured on the compressor side under standard operating conditions.

Comparing the results of Section 5.4.1 with these results, we see that the linearized model correctly predicted the critical speed, but failed to hint at the sub-synchronous modes. This shows that the linearized model can be used to predict the synchronous response, but not to predict the sub-synchronous response.

Based on the definition in Equation 4.32, the simulated shaft and ring displacements are transformed to bearing eccentricities, as depicted in Figure 5.12.

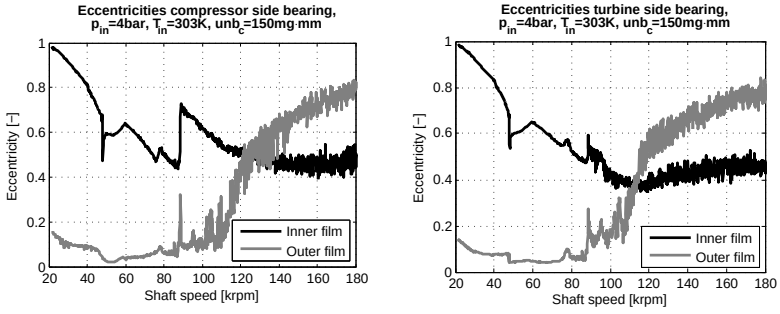

(a) Compressor side bearing.

(b) Turbine side bearing.

Figure 5.12: Simulation results: bearing eccentricities during a run-up at reference operating conditions.

At low rotation speed, the inner oil film runs at a high eccentricity and the outer oil film runs at a low eccentricity. With increasing rotation speed, the eccentricity of the inner oil film decreases whereas the eccentricity of the outer oil film increases. More specifically: the sub-synchronous modes 1 and 2 as shown in Figures 5.10b and 5.10c are mostly in the inner oil film whereas the third sub-synchronous mode leads to a high eccentricity in the outer oil film.

At the onset speed of the second oil whirl, above 85krpm, the compressor side bearing shows a larger eccentricity than the turbine side bearing. For the rest of the rotation speed range, the eccentricities of both bearings have a similar magnitude.

As can be seen in Figure 5.13, the friction loss increases approximately quadratically with rotation speed. A small jump in friction loss can be seen at the onset speed of oil whirl. Furthermore, the friction loss profile is similar to the friction loss profile of the Laval rotor analyzed in Chapter 4.

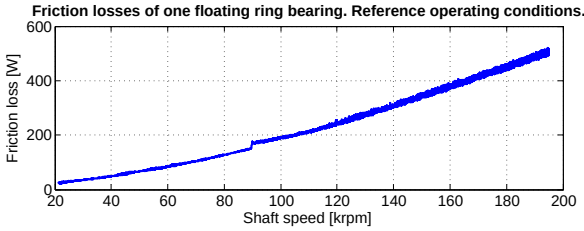

Figure 5.13: Simulation results: friction loss of the compressor side floating ring bearing at reference operating conditions.

5.4.3. INFLUENCE OF UNBALANCE ORIENTATION

The unbalance in the previous Section was set at 150mg·mm at the compressor side and 0mg·mm at the turbine side. In this Section, four different unbalance configurations are simulated, as depicted in Figure 5.14, where each vector represents 150mg·mm of unbalance:

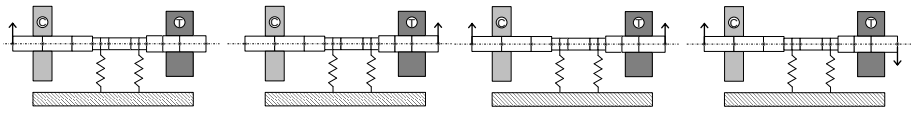

Figure 5.14: Unbalance configurations analyzed in this Section. Each vector represents 150mg·mm of unbalance.

A similar study was performed by Tian [164], but his study only focused on the influence of the unbalance configuration on the sub-synchronous vibrations. Both our study as well as Tian's study contain only simulation data: no measurement data of these various configurations is currently available. Figure 5.15 depicts the unbalance responses of the various unbalance configurations.

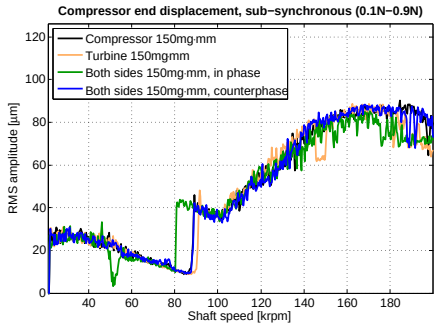

(a) Sub-synchronous response.

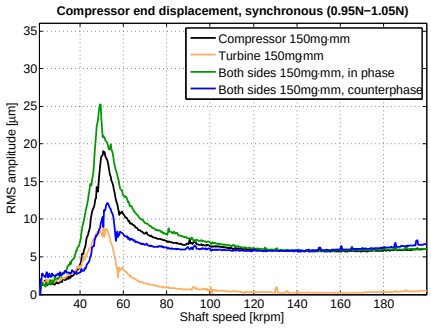

(b) Synchronous response.

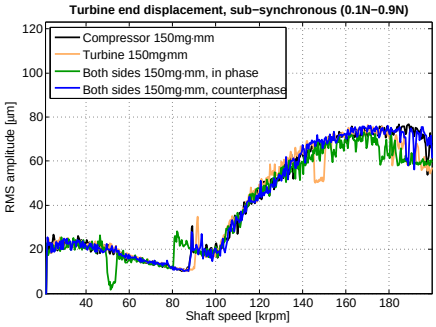

(c) Sub-synchronous response.

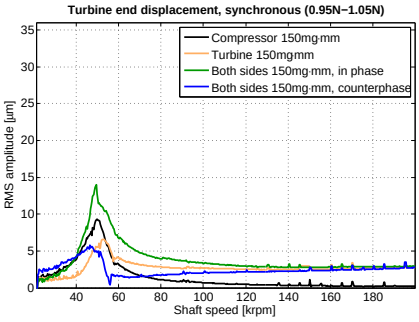

(d) Synchronous response.

Figure 5.15: Simulation data: shaft displacement as a function of unbalance configuration.

The unbalance configuration influences the onset speed of oil whirl between 80krpm and 90krpm, but does not have a major effect on its eventual amplitude. The sub−synchronous whirling frequencies (not depicted here) also did not change with the unbalance configuration. In the study of Tian [164], the sub-synchronous response did change as a function of the unbalance configuration, most likely due to the larger amount of unbalance imposed by Tian.

The synchronous response is clearly affected by the unbalance configuration: the amplitude at the critical speed of 50krpm increases with increasing unbalance. Unbalance located on the compressor has the largest effect on the compressor displacement, and, remarkably also on the turbine side displacement. Furthermore, the compressor side is typically twice as sensitive for unbalance induced vibrations as the turbine side, most likely due to its larger overhang from the bearing span, as can also be seen in the mode shape at the critical speed, Figure 5.10a.

When the unbalance vectors are in phase, the displacement amplitude at the critical speed is larger than when placed in counterphase, which can be understood by the mode shape at the critical speed, see Figure 5.10a. On the contrary, at the maximum rotation speed, the unbalance configuration with the unbalance vectors in counterphase shows the largest amplitudes, which is most likely caused by the second bending mode, see

Figure 5.8b, being excited at speeds above 200krpm.

Figure 5.16 presents the bearing reaction forces of both bearings as a function of the unbalance configuration. These forces are important to evaluate as they are transferred from the turbocharger to the surrounding parts and can cause audible noise issues when mounted in a vehicle [210]. As can be seen in Figure 5.16, the sub-synchronous bearing load amplitudes are generally similar for both bearings. In the range 90krpm-140krpm, the turbine side bearing loads are considerably higher than the compressor side bearing loads while –as can be seen in Figure 5.15– the turbine side displacements are actually smaller than the compressor side displacements. Furthermore, at the jump near 90krpm, the load on the compressor-side bearing decreases whereas the load on the turbine-side bearing increases. This is caused by the jump from a (mostly) conical mode to a (mostly) cylindrical mode, see Figure 5.10.

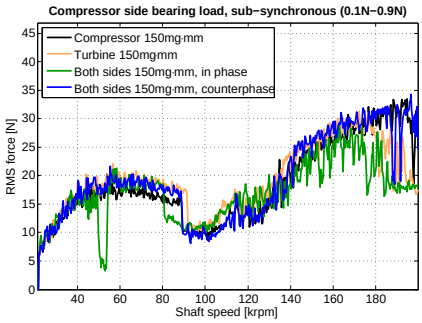

(a) Sub-synchronous load on compressor side bearing.

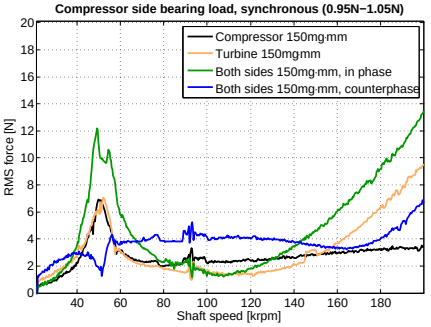

(b) Synchronous load on compressor side bearing.

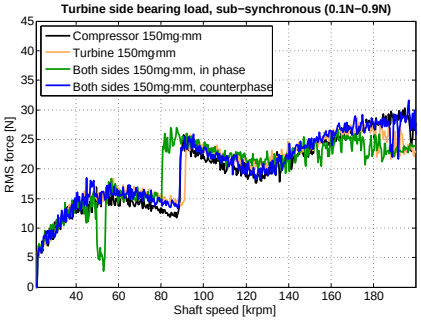

(c) Sub-synchronous load on turbine side bearing.

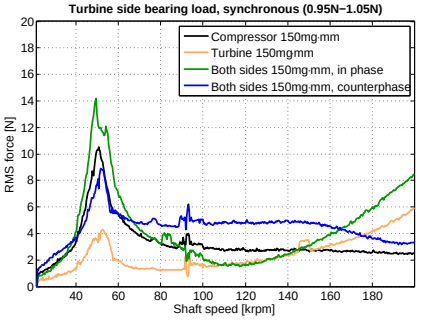

(d) Synchronous load on turbine side bearing.

Figure 5.16: Simulation data: bearing loads as a function of unbalance configuration.

As for the synchronous bearing loads, as depicted in Figure 5.16b and 5.16d, a clear dependence on the unbalance configuration is observed. The traversal of the critical speed at 50krpm shows a peak response in the bearing load. Note that the synchronous

response is caused by unbalance excitation, which by nature increases quadratically with rotation speed. This explains the increase in bearing load at speeds above 120krpm without the rotor displacements showing a clear increase above 120krpm, as depicted in Figure 5.15: when the displacement remains constant, but the (synchronous) oscillation frequency increases, the reaction force on the bearing system will increase quadratically with oscillation frequency.

5.4.4. INFLUENCE OF OIL SUPPLY TEMPERATURE

For the Laval rotor, the influence of the oil supply temperature was staightforward: the higher the supply temperature, the lower the displacement amplitudes on the rotor, see Section 4.4.3. For the turbocharger rotor in this chapter, the temperature dependency is less straightforward as will be shown in this section.

As presented in Figure 5.17, the sub-synchronous displacement amplitude at the compressor side generally increases with increasing oil feed temperatures. The contrary is true for the synchronous displacement amplitudes: the higher the supply temperature, the lower the response when traversing the critical speed.

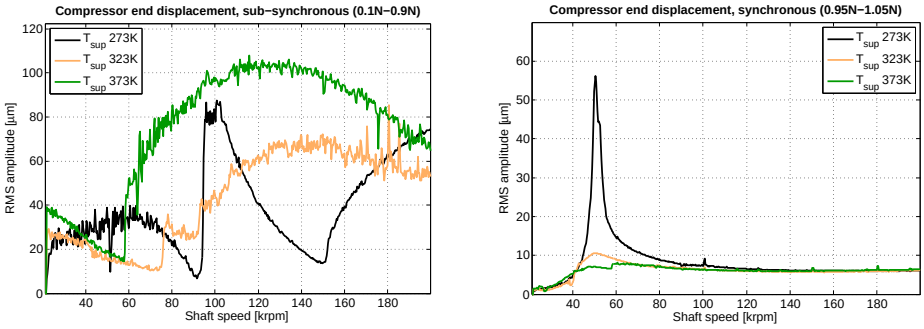

(a) Sub-synchronous response.

(b) Synchronous response.

Figure 5.17: Simulation data: shaft displacement as a function of oil supply temperature.

As can be seen in the waterfall plots in Figure 5.18, the sub-sychronous response in terms of whirl frequencies is clearly a function of oil feed temperature. For the low oil feed temperature condition, most of the sub-synchronous response consists of a single oil whirl mode whereas for the other two oil feed conditions, two seperate oil whirl modes are present over a large rotation speed range.

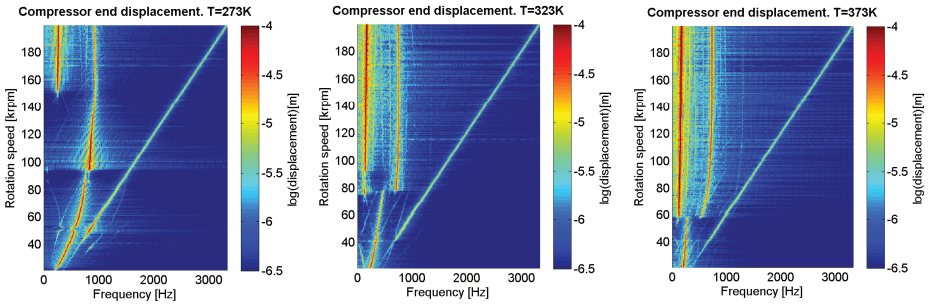

(a) $T_i 273K$. (b) $T_i 323K$. (c) $T_i 373K$.

Figure 5.18: Simulation data: waterfall plots of shaft displacement as a function of oil supply temperature.

5

Considering the bearing loads, as presented in Figure 5.19, it is clear that these are generally higher when the oil feed temperature is lower. At low oil feed temperature, the viscosity of the oil is high and therefore the bearing stiffness and damping properties will also be high, leading to relatively high bearing loads.

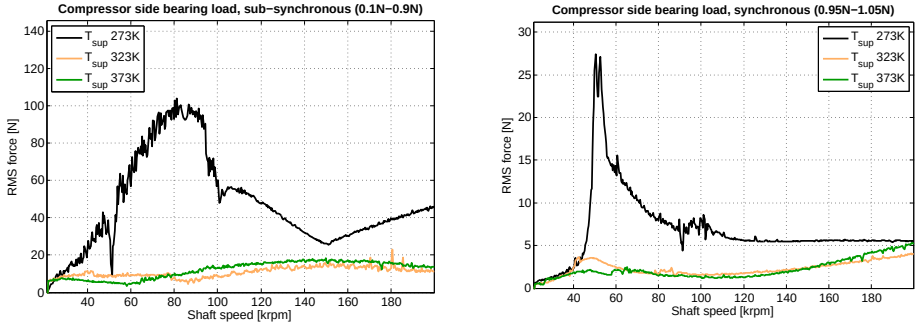

(a) Sub-synchronous load on compressor side bearing.

(b) Synchronous load on compressor side bearing.

Figure 5.19: Simulation data: bearing loads as a function of oil supply temperature.

The influence of the oil feed temperature is also clearly notable on the friction loss, as depicted in Figure 5.20. The friction loss profile seems to follow the exponential decay of the viscosity with increasing temperature.

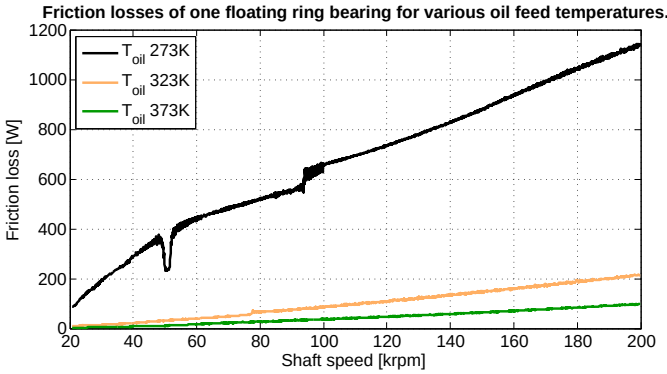

Figure 5.20: Friction loss of the compressor side bearing for various oil feed temperatures.

5.4.5. INFLUENCE OF THE THRUST BEARING

Up to this moment, the rotordynamic reponse in radial direction has been assumed to be independent of the thrust bearing. In reality, turbochargers with floating ring bearings always have a separate thrust bearing to carry the axial load on the compressor wheel and the turbine wheel. In case of the turbocharger considered here, a two-sided taper-land bearing supports the rotor, see Figure 5.21.
In order to study the effect of the thrust bearing on the radial dynamics, a thrust bearing model was developed. The details of this thrust bearing model are described in Appendix F. This thrust bearing model produced stiffness and damping terms in tilting direction of the rotor. These stiffness and damping terms, as given in Figures F.8a and F.8b were determined by applying a perturbation on respectively the position and velocity around the thrust bearing equilibrium position. In this analysis, three thrust load conditions are compared:

- no thrust load, resulting in zero tilting stiffness and damping and thus equal to the model used to analyze the reference operating conditions in Section 5.4.2,
- mild thrust load, where the engine is assumed to load the rotor at one third of its maximum thrust load profile as depicted in Figure F.2,
- full thrust load, as depicted in Figure F.2 with a maximum axial force of approximately 58N at 200krpm.

The rotordynamic model was updated by adding these tilting stiffness and damping terms as a polynomial expression depending on thrust load and rotation speed at the node where the thrust bearing is located, as schematically depicted in Figure 5.21. All other details of the model were kept identical to the model as presented in Section 5.4.2.

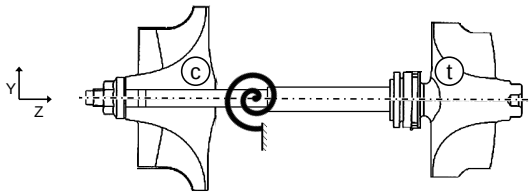

Figure 5.21: Schematic representation of the addition of tilting stiffness and damping to the rotor-bearing model. *c* represents the compressor wheel and *t* represents the turbine wheel.

The shaft displacement as depicted in Figures 5.22 and 5.23 clearly shows the influence of the thrust bearing: it suppresses sub-synchronous vibrations.

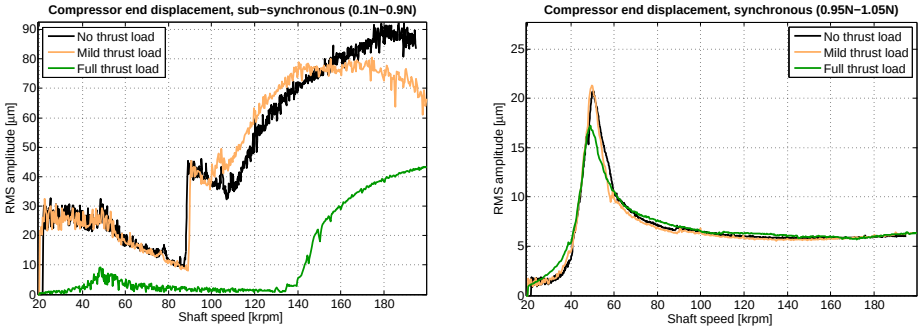

(a) Sub-synchronous response.

(b) Synchronous response.

Figure 5.22: Simulation data: shaft displacement as a function of thrust load.

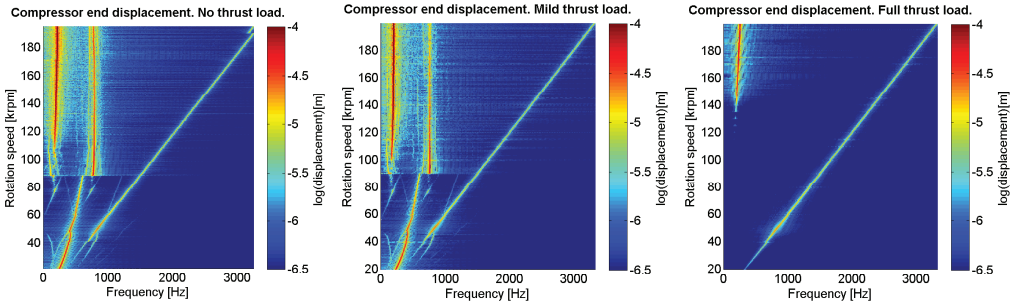

(a) No thrust load.

(b) Mild thrust load.

(c) Full thrust load.

Figure 5.23: Simulation data: waterfall plots of shaft displacement as a function of thrust load.

Especially at high thrust load, the suppression of sub-synchronous vibrations is evident. Also the amplitude of the displacement of the compressor disk becomes smaller

when there is a higher contribution of the thrust bearing. Hence, the thrust bearing adds stability to the rotor and can reduce peak vibrations, but only when a significant amount of thrust load is applied to the rotor.

5.4.6. INFLUENCE OF MULTILOBE RING FEATURE: LOBE CONFIGURATION

Plain journal bearings which have non-cylindrical features, such as the lemon bore or offset bearing, can have reduced self-excited sub-synchronous vibrations compared to plain journal bearings [51]. Analogous to this, floating ring bearings with multilobe features show a significantly lower sub-synchronous response compared to conventional, cylindrical floating ring bearings. This was shown by simulations and measurements by Eling [185] and later also by simulations of Bernhauser [211].
In this section, we will compare the response of a turbocharger with standard floating ring bearings with a turbocharger featuring various multilobe configurations as depicted in Figure 5.24.

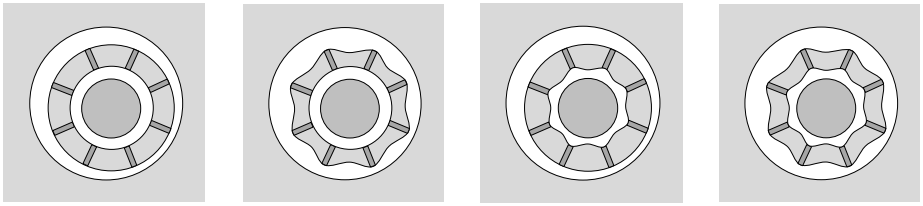

(a) Standard, circular floating ring.

(b) Multilobe on the outside.

(c) Multilobe on the inside.

(d) Multilobe on both sides.

Figure 5.24: Floating ring bearing configurations.

The multilobe feature is incorporated in the rotor-bearing model by adapting the film height function. As explained in Section 4.2.1 the film height function for a standard, circular floating ring bearing expressed in a co-rotating reference frame is:

$$\begin{aligned} h_{\text{out}} &= C_{\text{out}} - e_{\text{r\_}x}\cos\left(\frac{\theta}{R_{\text{r}}}\right) - e_{\text{r\_}y}\sin\left(\frac{\theta}{R_{\text{r}}}\right) \\ h_{\text{in}} &= C_{\text{in}} - \left(e_{\text{s\_x}} - e_{\text{r\_x}}\right)\cos\left(\frac{\theta}{R_{\text{s}}}\right) - \left(e_{\text{s\_y}} - e_{\text{r\_y}}\right)\sin\left(\frac{\theta}{R_{\text{s}}}\right) \end{aligned} \tag{5.1}$$

For a multilobe floating ring bearing, the film height function is extended with a multilobe feature:

$$\begin{aligned} h_{\text{out}} &= C_{\text{out}} - e_{\text{r\_}x}\cos\left(\frac{\theta}{R_{\text{r}}}\right) - e_{\text{r\_}y}\sin\left(\frac{\theta}{R_{\text{r}}}\right) - C_{\text{lobe\_out}}\cos\left(\frac{n\theta}{R_{\text{r}}} + \pi\right) \\ h_{\text{in}} &= C_{\text{in}} - \left(e_{\text{s\_x}} - e_{\text{r\_x}}\right)\cos\left(\frac{\theta}{R_{\text{s}}}\right) - \left(e_{\text{s\_y}} - e_{\text{r\_y}}\right)\sin\left(\frac{\theta}{R_{\text{s}}}\right) - C_{\text{lobe\_in}}\cos\left(\frac{n\theta}{R_{\text{s}}}\right) \end{aligned} \tag{5.2}$$

where the number of lobes n is set to six in all cases and the lobe amplitudes $C_{\text{lobe\_in}}$ and $C_{\text{lobe\_out}}$ are both set to 2μm.

Figure 5.25 shows the resulting waterfall plots of the four configurations and Figure 5.26 shows the same data, filtered by order filters.

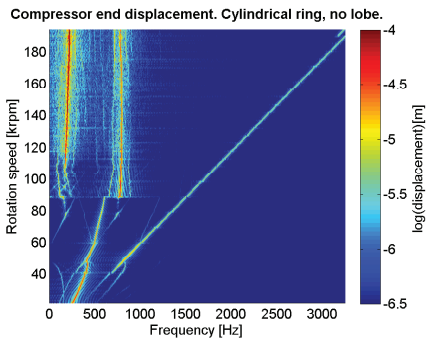

(a) No lobe feature.

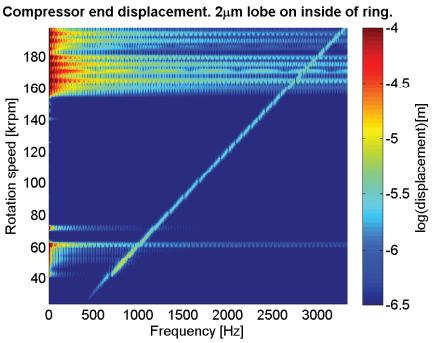

(b) Lobe on inside of ring.

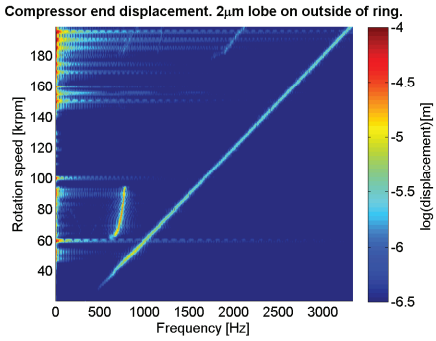

(c) Lobe on outside of ring.

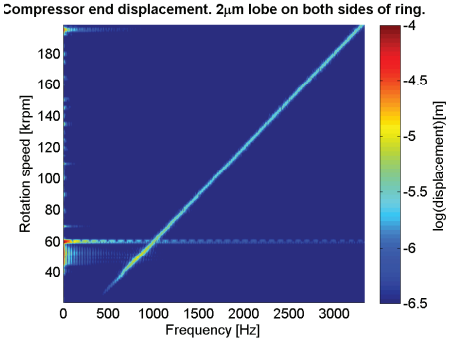

(d) Lobe on both sides of ring.

Figure 5.25: Simulation data: waterfall plots of shaft displacement for various multilobe configurations. The horizontal lines are due to numerical computation issues, and are not related to physical occurence of vibration.

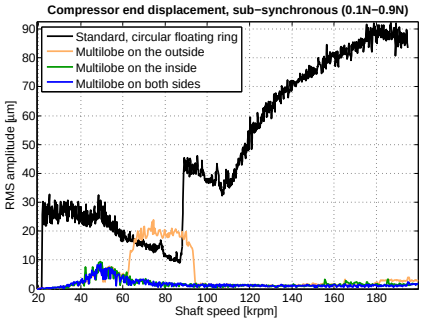

(a) Sub-synchronous response.

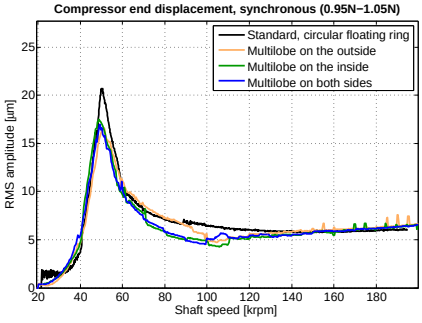

(b) Synchronous response.

Figure 5.26: Simulation data: shaft displacement as a function of multilobe configuration.

The multilobe feature, particularly when applied to both sides of the ring, can reduce the sub-synchronous vibrations significantly. The synchronous vibration level at the critical speed is also reduced by 25%.

Figure 5.27 shows that the friction loss profile of bearings with and without multilobe features. In case of the multilobe on both sides of the ring, the friction loss is typically 5% higher than the circular floating ring bearing. The multilobe feature however improves the stability of the bearing. Therefore, in future research, larger clearances may be studied which –together with the multilobe feature– offer a stable and low friction bearing solution.

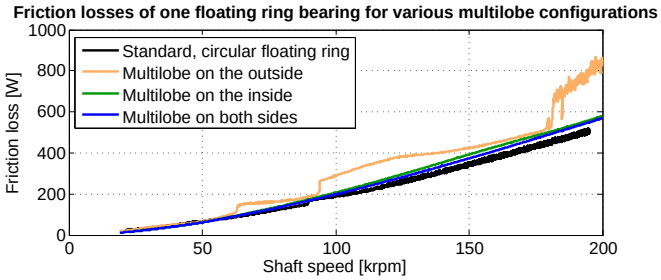

Figure 5.27: Friction loss for various multilobe configurations.

5.5. CONCLUSION

The dynamic behavior of a turbocharger rotor-bearing system was analyzed in this chapter. A rotor model was created and validated by hammer impact testing. This rotor model was coupled to the bearing model as presented in Section 4 and used to perform run-up simulations. The run-up simulations have been compared with measurement results: the synchronous response shows a fair quantative agreement whereas the sub-synchronous response in terms of whirl frequencies and jump speeds also shows fair agreement. The response is characterized by traversal of a critical speed at 50krpm and three sub-synchronous modes in the range 200Hz-800Hz.

The turbocharger rotor-bearing model has been used to demonstrate the effect of the unbalance configuration, which was shown to have a significant impact on the synchronous response. Unbalance on the compressor has the highest impact on the response at the critical speed whereas unbalance on the turbine side has the highest impact on the response at maximum rotation speeds.
Increase in oil supply temperature was shown to reduce the synchronous response at the critical speed. In addition, the thrust bearing seems to have an effect in suppressing sub-synchronous vibrations, particularly at high thrust load conditions. Also the multi-lobe ring feature showed to be able to suppress sub-synchronous vibrations.

The correlation between measurement results and simulation results was clearly not as good as in case of the Laval rotor of the previous Chapter. Possibly, some effects were not included in the model, but may have been relevant in the test setup:

- the influence of the aerodynamic load on the turbine wheel and compressor wheel
- the influence of the seals at each side of the bearing housing

In addition, the bearings or bearing housing bore may also have been slightly unround. Possibly, the amount of out-of-plane unbalance on the rotor may have been more pronounced than in case of the Laval rotor, triggering different sub-synchronous vibration patterns than expected from our simulations.

6

ROBUST DESIGN OPTIMIZATION OF A LAVAL ROTOR SUPPORTED BY PLAIN JOURNAL BEARINGS

In the previous chapters, we developed experimentally validated rotor-bearing models. The next step is to use these parametric models to optimize the design of the rotor-bearing system. In this chapter, a Laval rotor supported by plain journal bearings will be optimized. First, the optimization objectives and constraints will be introduced. Subsequently, a sensitivity study is performed to select the most sensitive design parameters. In a first step, the rotor is optimized without taking into account uncertainties in the design and the operating conditions: a deterministic optimization. In a second step, the optimization is extended to include uncertainties in the design and operating conditions: a robust optimization. The added value of the robust optimization will become clear, as the deterministic optimum results in violation of the constraints under the influence of uncertanties in the rotor-bearing design and its operating conditions.

This chapter is based on a collaborative study of Frank Immerzeel and Rob Eling (see also [38]).

6.1. INTRODUCTION

As stated in the Introduction, Section 1.4, the ultimate goal of our research is:

To develop a method for optimizing the mass-produced automotive turbocharger rotor-bearing system, based on a validated model and resulting in a realistic optimal design which takes into account production and environmental variations.

The turbocharger rotor-bearing model presented in Chapter 5 is considered to be too computationally expensive for use in a parametric optimization: depending on the level of multiphysical detail, the time-transient simulation requires several hours to several days to run. Instead, the optimization in this chapter will be performed on the Laval rotor supported by plain journal bearings, as described in Chapter 3. However, it should be noted that the optimization method presented in this chapter can be applied to any rotor-bearing system. The specific objectives and constraints in this chapter are chosen with the demands of automotive turbochargers in mind, as stated in Section 1.3.

6.2. ROTOR-BEARING MODEL

The optimization is peformed on the Laval rotor depicted in Figure 6.1. Our goal is to optimize the design variables of the rotor-bearing system with respect to the objectives which will be stated in Section 6.3. We focus on the design variables describing the shaft and bearing geometries while keeping the design of the disk unchanged. The reason is that in a turbocharger rotor-bearing system, the dimensions of the wheels are primarily determined by aerodynamic performance and hence should be considered as a given rotordynamic *payload*.

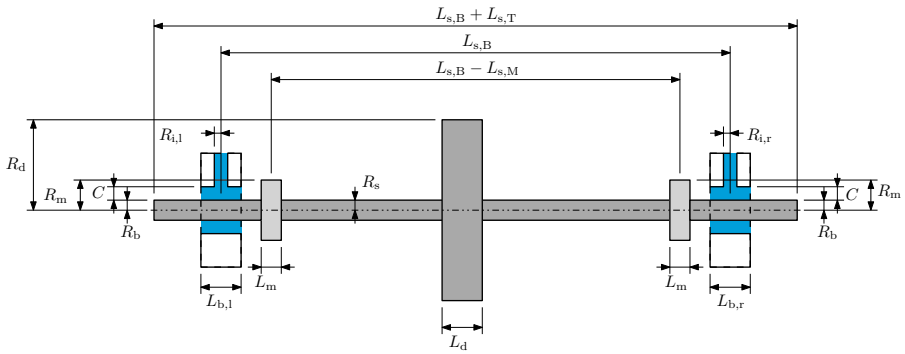

Figure 6.1: Schematic representation of the Laval rotor supported by plain journal bearings. The values of the design variables can be found in Table 6.1.

The design of the rotor-bearing system is identical to the one described in Chapter 3. For our optimization, we identified 9 control variables which govern the design of the rotor-bearing system, as presented in Table 6.1. Note that the main shaft radius R_s and the radius of the shaft at the bearing sections R_b can be configured independently. The

bearing clearance is identical for both bearings. The length, however, may be different for each of the two bearings.

Table 6.1: Design variables for this optimization study. The values in the column labeled as *Ref.* are the nominal design values as originally used in Chapter 3. The values under *Min.* and *Max.* are the upper and lower bounds of the design variable.

Name	Ref.	Min.	Max.	Unit	Description
$L_{s,B}$	120	80	160	mm	Bearing span
$L_{s,T}$	46.6	30	60	mm	Shaft overhang
R_s	3.0	1.8	6.0	mm	Shaft radius between meas. disks
R_b	3.0	1.0	6.0	mm	Shaft radius in bearings
$L_{b,l}$	3.6	2.4	7.2	mm	Length left bearing
$L_{b,r}$	3.6	2.4	7.2	mm	Length right bearing
C	15	10	30	μm	Clearance bearings
$R_{i,l}$	1.0	0.5	1.1	mm	Radius left oil inlet
$R_{i,r}$	1.0	0.5	1.1	mm	Radius right oil inlet

Our goal is to optimize the behavior of the rotor-bearing system over the entire operating range. This means that within the optimization process, a time-transient run-up simulation is performed for each design configuration, which is very time-consuming. In order to keep calculation times within accaptable limits, the model described in Chapter 3 was simplified in two ways:

- the mass-conservative cavitation condition was replaced by a Gümbel cavitation condition [69, 97]
- the distributed thermal model was replaced by a lumped thermal model [154].

A study on the differences for these modeling assumptions is presented in reference [69], where we observed that the synchronous response did not change significantly due to these simplifications. The sub-synchronous response did change: the simplified model underpredicts the onset speed of oil whirl by roughly 10%, as shown in Figure 6.2.

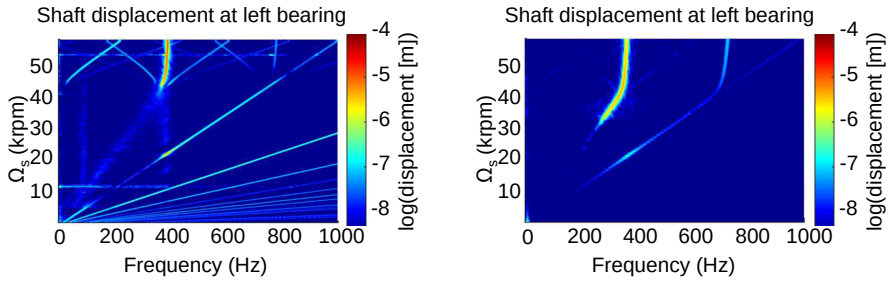

(a) Measurement result.

(b) Simulation result.

Figure 6.2: Comparison of the response of the simplified rotor-bearing model with measurement results.

This difference was considered to be acceptable for this optimization study.

We also replaced the rotation speed profile during a run-up. In the previous chapters, a linear run-up profile was assumed:

$$\Omega(t) = \Omega_{\text{min}} + (\Omega_{\text{max}} - \Omega_{\text{min}}) \frac{t}{t_{\text{end}}} \tag{6.1}$$

In this chapter, we use an exponential rotation speed profile, so that an equal number of oscillations is simulated for each rotation speed:

$$\Omega(t) = \Omega_{\text{min}} \tau (e^{\frac{t}{\tau}} - 1) \tag{6.2}$$

In addition, the virtual time span $(t_{\text{min}}, t_{\text{max}})$ which is simulated for each design configuration, was reduced from 20 seconds to 10 seconds. Lastly, the numerical integration solver settings were further optimized. All in all, this led to a reduction of computation time from 100 hours in Chapter 3 to 20 minutes for our simplified model.

We evaluated the repeatability of the model to quantify the influence of numerical noise on model evaluations in the optimization. Based on 10 evaluation runs of the model with exactly the same input, a variation of the weighted objective value of ±3% was observed. This appeared to be mostly due to the onset speed of oil whirl, which varies from one simulation to another [38].

6.3. OPTIMIZATION OBJECTIVES

The goal of this optimization study is to minimize:

- synchronous vibrations,
- sub-synchronous vibrations,
- bearing force amplitudes,
- bearing friction losses

over a run-up. In this section, we will clarify how we translated these demands to a set of numerical performance indicators.

6.3.1. SYNCHRONOUS AND SUB-SYNCHRONOUS VIBRATIONS

The typical turbocharger whining noise sometimes experienced when driving a vehicle originates from the turbocharger vibration level [210]. Turbocharger whining noise is a very tonal kind of noise. When we want to set up a rating for turbocharger noise originating from vibration intensity, we must take into account the frequency-dependent sensitivity of human hearing: vibrations occuring outside the critical band of human hearing are unlikely to cause unacceptably high turbocharger whining noise. Therefore, we weight the vibration intensity by a frequency-dependent equal-loudness contour, as defined in ISO standard 226:2003 [212].

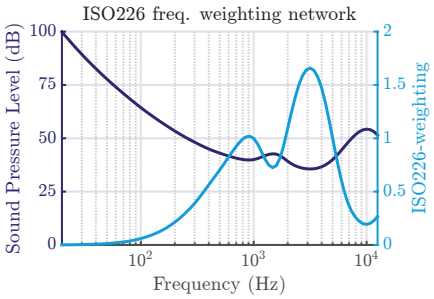

Figure 6.3: Equal loudness contour based on ISO standard 226:2003 [212] and its inverse function which is used to weigh the RMS-values of synchronous and sub-synchronous vibration. The weighting function is normalized to be 1 at 1kHz.

In order to evaluate the intensity of the forced vibrations and the self-excited vibrations of the center disk in our Laval rotor, we filtered the center disk displacement output of our simulations with bandpass filters with bands $0.9\Omega_s < \omega < 1.1\Omega_s$ and $0.1\Omega_s < \omega < 0.9\Omega_s$ respectively. We then calculated the root-mean-square values of the vibration as a function of rotation speed. Subsequently, we applied the frequency-dependent weighting as depicted in Figure 6.3 and integrated the resulting value over the rotation speed range. This way, we obtained a single value expressing the vibration intensity for a specific design.

6.3.2. BEARING FORCE AMPLITUDES

Although the turbocharger rotor is the main source of turbocharger whining noise, it is often not the main radiator of noise. Instead, the turbocharger rotor vibrations are transferred to adjacent components such as heat shields and the exhaust system [11]. When we want to limit the noise at the source, a first option would be to minimize the reaction forces from the bearings to the rotor.

In order to express the bearing force intensity as a single value, we started with calculating the vector sum of the bearing forces F_X,F_Y, as a function of rotation speed Ω_s. We then integrated this over the rotation speed range.

6.3.3. FRICTION LOSS

Minimization of friction loss in a turbocharger is beneficial for two reasons:

- it increases the efficiency of the turbocharger [171],
- it reduces the transient response time of a turbocharger [161].

For an automotive turbocharger, friction loss reduction at low rotation speed is particularly of interest, as the turbine input power is relatively low here, so the influence of friction is relatively large. We therefore applied a penalty function for the bearing friction losses at low speeds. The penalty function is set to a linearly decreasing value with rotation speed, being 2 at the minimum rotation speed and 1 at the maximum rpm. The

friction losses of both bearings are multiplied by the penalty function, integrated over the rotation speed range and added up, resulting in one scalar value.

6.3.4. WEIGHTING MULTIPLE OBJECTIVES

In total, we thus defined four individual objectives for our optimization study. As it is not likely that one particular design will perform optimally with regard to all four objectives, and it is therefore important to weight how important each objective is. We therefore applied a *weighted sum multi-objective optimization*, where the overall objective function is the sum of the individual objectives, each scaled by a weighting parameter. These weighting parameters depend on how much improvement is possible for each individual objective within the design space as set in Table 6.1. This means that if for a single objective, much improvement can be expected, its weighting function is relatively low. Further details on the weighting method used in this multi-objective optimization can be found in [38].

6.4. OPTIMIZATION CONSTRAINTS

Our optimization should result in a design which fulfills the objectives as stated in Section 6.3 in an optimal way, by varying the design variables as presented in Table 6.1. Under no conditions, however, the rotor-bearing system is allowed to fail during its operation. To prevent any wear or failure to the rotor-bearing system, we imposed three constraints:

- the oil film thickness should always be high enough to prevent wear,
- the stress in the rotor should always be safe to prevent fatigue issues,
- the displacement of the center disk should not exceed its clearance towards its surroundings.

These three constraints may not be violated at any point during a run-up. Specific details for each constraint will now be described.

6.4.1. OIL FILM THICKNESS

The oil film in the plain journal bearing is basically a layer of lubricant which separates the moving shaft from the stationary housing, preventing metal-to-metal contact. In case of automotive turbochargers, the oil used to lubricate the turbocharger is also used to lubricate the combustion engine, meaning that particles from the combustion process may contaminate the oil. These particles may cause wear to the turbocharger bearings [8, 213]. In order to limit the chances of wear, a minimum film thickness of 2µm was imposed, allowing particles smaller than this to always flow out of the bearings without causing damage.

6.4.2. ROTOR STRESS

The second constraint imposed to prevent failure is to limit the stress in the rotor. In our model, we made use of Rayleigh beam elements to describe the rotor, as described in Section 3.2.1, allowing the stress distribution along the elements to be evaluated. Note

that this does not include the effect of a sudden step in rotor diameter, for which corrections are necessary to include local notch effects. For simplicity, however, we only considered the bending stresses along the rotor under the assumption that local notch effects can eventually be alleviated by the inclusion of chamfers.
The yield strength (tensile) of the rotor material, (*Steel 1.2379*), is σ_y = 827 MPa [38]. The rotor is under repetitive cyclic loading, and hence the maximum stress needs to be considerably lower than the yield stress to avoid fatigue issues [214]. Therefore, the maximum stress allowed for long-term use is set at 650 MPa.

6.4.3. DISK DISPLACEMENT

In a turbocharger, the disks (wheels) are enclosed in housings: the compressor housing and the turbine housing. The clearance between the disks and the housings strongly affects its aerodynamic performance: the smaller the air gap in between both, the higher their efficiencies in compression and expansion [5]. Contact between the stationary housing and the rotating disk can cause severe turbocharger failures [8]. Therefore, the maximum displacement of the disk needs to be limited at any time during a run-up. For the Laval rotor, the maximum displacement of the center disk was set to 150μm.

6.5. SENSITIVITY STUDY

A well-known challenge within the field of optimization is the *curse of dimensionality* [215]: the computational effort required to find an optimum grows rapidly with the number of design variables. Performing an optimization with 9 design variables and a model which requires 20 minutes to run is already challenging; the extra computational burden when considering uncertainties for a robust optimization will make it even more challenging. Therefore, the number of design variables was reduced by performing a sensitivity analysis, which resulted in a ranking of importance of all design variables. Particularly, we performed a *global sensitivity analysis*, which considers the global sensitivity of a control variable on the objective over the entire design space.

Our global sensitivity analysis was performed using the *Elementary Effects Method*, which is a sensitivity analysis method which is effective in identifying the most important factors in a model that contains many factors, with a relatively small number of model evaluations [216]. In our case, we required 1200 model evaluations, which we ran in parallel on a computer cluster [38]. The results are expressed as estimated means of the absolute elementary effects, and are displayed in Figure 6.4. The graph shows the upper four design variables are dominant, and therefore we limit our design space for both the deterministic and the robust optimization to these four variables.
Furthermore, the resulting means of the absolute elementary effects were observed to be constant already after 600 model evaluations for all 9 design variables, indicating that they are well converged and so the 1200 model evaluations are sufficient to obtain consistent values for the sentivities.

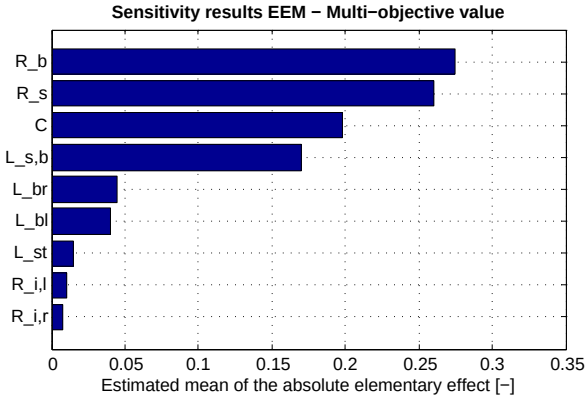

Figure 6.4: Results of the global sensitivity analysis. The higher the value, the higher the sensitivity of the design variable on the multi-objective value of the design.

Figure 6.5 presents the sensitivity of the four dominant design variables (R_b, R_s, C, $L_{s,b}$) on the individual objective functions.

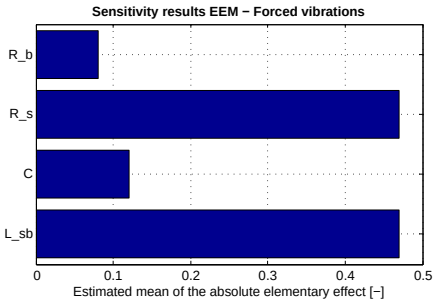

(a) Forced excitation.

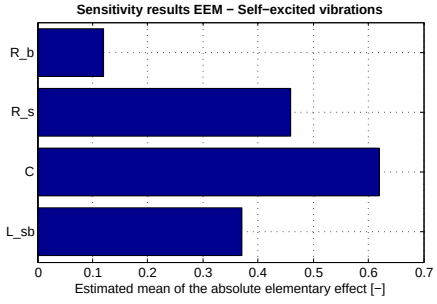

(b) Self-excitation.

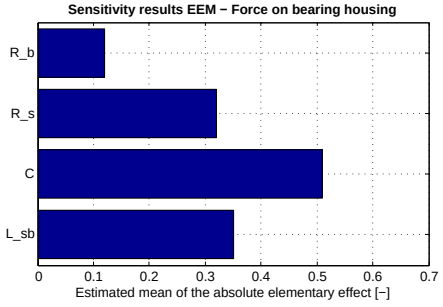

(c) Bearing housing forces.

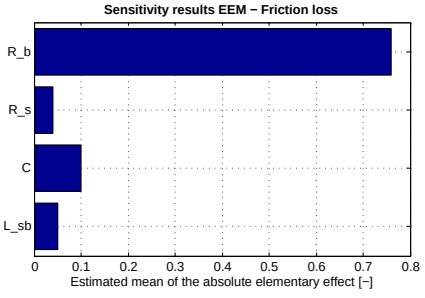

(d) Friction losses.

Figure 6.5: Sensitivity results for the individual objectives.

As a reminder, Figure 6.6 highlights the four dominant design variables.

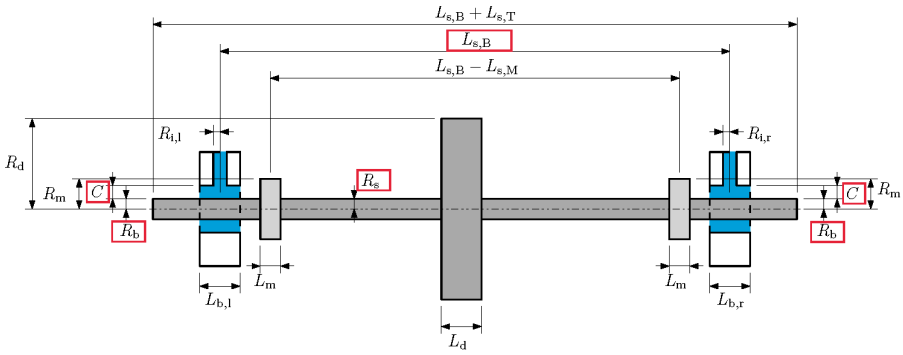

Figure 6.6: Schematic representation of the Laval rotor supported by plain journal bearings. The values of the design variables can be found in Table 6.1.

The following observations were made for the four dominant design variables:

- **Radius** R_b
  The radius of the shaft at the bearing location, R_b, is the most influential design variable for our optimization. The multi-objective function increases monotonically with increasing R_b; in other words: the smaller radius R_b, the better. As can be observed in Figure 6.5d, the influence of R_b on the multi-objective function originates mostly from the friction loss, which in itself is dominated by shear loss as demonstrated in Chapters 3. When isoviscous conditions and zero shaft load would be assumed, the shear loss would reduce with the third power of R_b [51]. The other three objectives actually decrease with increasing R_b, but these effects are minor compared to the influence of R_b on the friction loss.

- **Radius** R_s
  The radius of the shaft in between the bearings, R_s, is almost as influential as R_b, which is mostly due to its influence on its rotordynamic behavior, as can be observed in Figures 6.5a and 6.5b. A monotonic decrease in multi-objective value is observed with an increase in R_s, in other words: the larger radius R_s, the better. We observed that the vibrations of the disk generally decrease with an increase of shaft radius R_s which is related to the increase of bending stiffness of the shaft. Furthermore, an increase of R_s also pushes the onset speed of oil whip to a higher value, meaning that these self-excited vibrations occur in a smaller part of the rotation speed range. The opposite trend is observed for the forces to the bearing housing: these increase with an increase in shaft radius R_s.

- **Bearing clearance** C
  The multi-objective function increases non-monotonically with increasing bearing clearance C. Furthermore, it is observed that the bearing clearance shows a strong interaction with the other design parameters. This means that a rotor-bearing system which is optimized as a system should be able to outperform a system composed of an individually optimized rotor and bearings. The bearing clearance C is the dominant variable for the amount of self-excited vibrations, as

can be seen in Figure 6.5b. The higher the clearance, the more self-excited vibrations. The bearing clearance C is also the dominant variable for the forces transferred to the bearing housing, see Figure 6.5c. As C gets larger, the ability of the bearing to act as a squeeze damper increases, and hence the forces transferred to the bearing housings decrease. Lastly, the friction loss increases with the inverse of the clearance C, but this influence is much smaller than the influence of radius R_{b}.

- **Bearing span** $L_{\mathrm{s,b}}$
  The bearing span $L_{\mathrm{s,b}}$ has the inverse effect to R_{s}: increasing $L_{\mathrm{s,b}}$ will decrease the bending stiffness and hence increase the vibration amplitudes. This relation was observed to be non-monotonically over the design space. The influence of the bearing span $L_{\mathrm{s,b}}$ on the multi-objective function is generally smaller than the influence of R_{s}, probably because the bending stiffness of the rotor scales with the fourth power of R_{s} and the third power of $L_{\mathrm{s,b}}$.

6.6. DETERMINISTIC OPTIMIZATION

6.6.1. METHOD

Our optimization can be characterized by the following features:

- the optimization is multi-objective,
- it is subject to multiple constraints,
- the objective and constraint functions are non-linear,
- model evaluations only give values at the design point, it does not give gradient information,
- and each model evaluation is computationally expensive.

Therefore, this optimization can be considered to be quite challenging, even with considerable computational resources available. One way of making the optimization more time-efficient, is to make use of *metamodels* for the objective and constraint functions [217]. The metamodel mimics the true function based on a limited amount of initial sampling points. The functions, in this case, are the objective functions and the constraint functions, both as a function of the design variables.
Particularly because from the sensitivity analysis we learned that our four design variables mostly show monotonic behavior, the metamodels need relatively few model evaluations to capture the behavior correctly. In this way, with a relatively small initial number of model evaluations, we can already quickly see how the design variables affect the performance of the rotor-bearing system.

Our metamodels are based on *kriging*, which is an interpolating estimation technique based on stochastics. Kriging predicts the values of the function between the known sample points and also gives an estimate on the error of its prediction. Ordinary kriging creates an approximate function which always contains the exact points as

obtained by the model evaluations. As the output of our rotor-bearing model contains a repeatability error of up to ±3%, applying ordinary kriging may result in large errors in the estimated function: a ±3% error together with a small step within the design space will cause spikes in the estimated function. In order to reduce the influence of the repeatability error, we make use of *regression kriging*, which allows the estimated function to deviate from the values actually predicted by the model evaluations [38].

The metamodel is created on the basis of an initial dataset of 64 model evaluations, evenly spread over the four-dimensional design space (R_b, R_s, C, $L_{s,b}$) by a *Latin hypercube* experimental design. We found that 64 initial model evaluations was a good starting point; Latin hypercubes with more than 64 model evaluations did not make the optimization faster or result in a better optimum [38].

Based on the initial sample set, the metamodels for the objective functions and the constraint functions were created. With these metamodels, we predicted the global constrained optimum. The optimum predicted by the metamodel, however, may still deviate from the real optimum as the fidelity of the metamodel is still limited [218]. To improve the fidelity of the metamodel in the areas of interest, more model evaluations are required. The *Expected Improvement* critrerion used by the EGO method makes it possible to select the points on which the predicted objective function is most promising [219], and was thus applied in an iterative fashion, see Figure 6.7. For improving the fidelity of the estimated constraint functions, we made use of the *Probability of Feasibility* criterion [220]. By combining the Expected Improvement outcome with the Probability of Feasibility outcome, a new location can be found which improves the predicition fidelity of both the objective functions and the constraint functions. In this way, the optimum can be found by a minimum number of computationally expensive model evaluations.

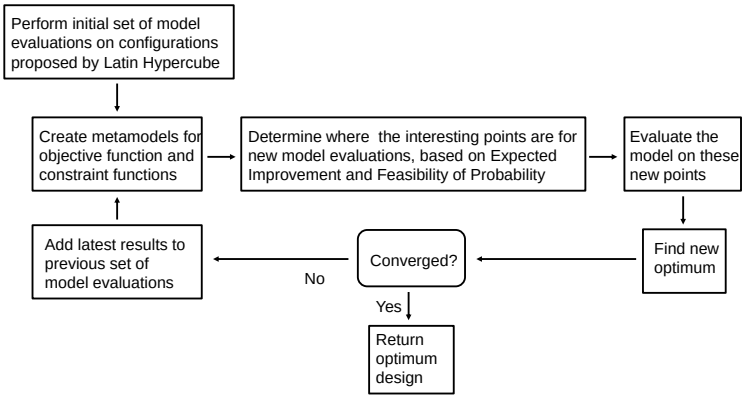

Figure 6.7: Flowchart of the deterministic optimization.

6.6.2. RESULTS

The optimum based on the initial dataset of 64 samples already provided a clear improvement in the multi-objective value over the reference design of the rotor-bearing system. Nevertheless, the iterative process based on Expected Improvement and Probability of Feasibility criteria was started. It appeared that after 100 iterations, the optimization process was well converged, as can be seen in Figure 6.8a. Figure 6.8b shows the evolution of the design variabes during the optimization. As can be seen, most of the improvements were found in the first 20 iterations. The lack of improvement in steps 20-80 is due to convergence issues of the model, one of the aspects which made this optimization study particularly challenging [38]. Nevertheless, at iteration 79, some further improvement in the design was found. In total, the optimization with 64 initial samples and 100 optimization iterations took 36 hours on an 8-core Intel Xeon E5-2630v3, 2.4 GHz with 128GB RAM, of which 94% was spent on running the model itself and 6% on creating metamodels and using them to find interesting new design configurations to evaluate[38].

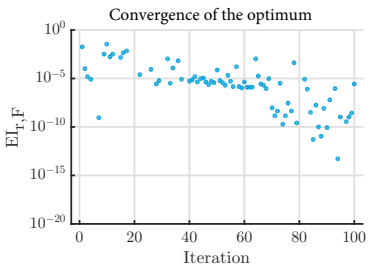

(a) Expected improvement value combined with Probability of feasibility: the decreasing value means that the optimization converges.

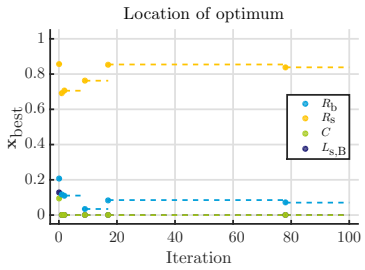

(b) Evolution of the design variables (normalized) during the iterative optimization process.

Figure 6.8: Key parameters during the iterative deterministic optimization.

Table 6.2 summarizes the results of the deterministic optimization. As could already be expected from the results of the sensistivity analysis:

- bearing radius R_{b} becomes smaller, mainly to reduce the friction losses. However, it is not bounded by the limits of the design space.
- shaft radius R_{s} becomes larger to reduce the vibration amplitude at the center disk. It is also not bounded by the limits of the design space.
- bearing clearance C is minimized to reduce sub-synchronous vibrations.
- bearing span $L_{\mathrm{s,B}}$ is minimized to reduce synchronous vibrations.

Table 6.2: Comparison of deterministic optimum with reference design for the objective and constraint values.

Design variable	*Reference*	*Det. optimum*
R_b (mm)	3.0	1.35
R_s (mm)	3.0	5.32
C (µm)	15	10.0
$L_{s,B}$ (mm)	120	80.0
Objectives	*Reference*	*Det. optimum*
Multi-objective	0.2887	$3.099 \cdot 10^{-2}$
Forced vibrations	0.1259	$1.570 \cdot 10^{-2}$
Self-excited vibrations	0.4318	$6.323 \cdot 10^{-3}$
Force	$6.614 \cdot 10^{4}$	$3.004 \cdot 10^{4}$
Friction	$3.465 \cdot 10^{5}$	$8.129 \cdot 10^{4}$
Constraints	*Reference*	*Det. optimum*
Min. oil-film thickness (µm)	4.451	4.504
Max. stress shaft (MPa)	52.74	2.860
Max. displacement disk (µm)	89.11	5.512

The run-up simulation results of the optimized design are compared with the result of the reference design –as presented in Section 6.2– in Figure 6.9. As can be seen in Figure 6.9b, the optimized design shows considerably less unbalance-induced vibration due to the higher shaft radius R_s which pushes the first bending frequency out of the operating range. Together with the small bearing clearance C, this also results in absence of oil whirl and oil whip, as shown in Figure 6.9a. Note that the dashed lines represent the values weighed by the ISO226 weighing, as given in Figure 6.3. Furthermore, the reaction forces on the bearing housing are reduced as well as the friction loss, see Figures 6.9c and 6.9d respectively.

Overall, the multi-objective value of the optimized design is almost ten times better than the reference design, indicating that the optimziation has been very useful. None of the constraints were violated. In fact, the minimum oil film thickness, the stresses in the shaft and the maximum displacements of the disk even improved in the optimized design.

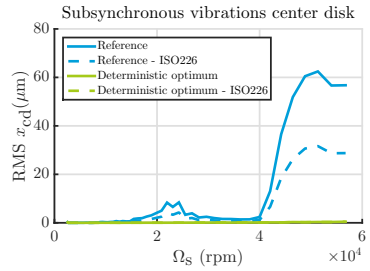

(a) Sub-synchronous vibration on disk.

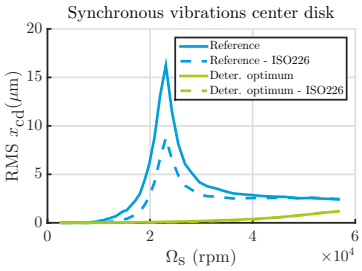

(b) Synchronous vibration on disk.

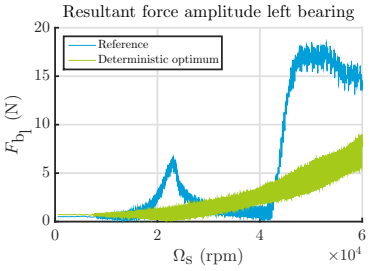

(c) Bearing reaction forces.

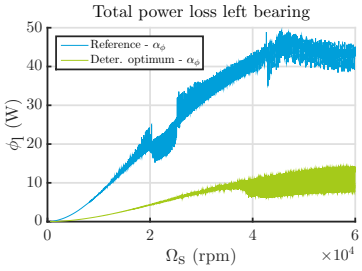

(d) Friction losses.

Figure 6.9: Comparison of the performance of the reference rotor-bearing system with the optimized rotor-bearing system. The center disk design, the amount of unbalance and the oil feed conditions are kept constant.

6.7. ROBUST OPTIMIZATION

The deterministic optimization study in Section 6.6 focused on optimizing the performance of the rotor-bearing system at a defined oil supply condition and a defined amount of rotor unbalance. This is not a representative scenario for automotive turbochargers: the oil supply temperature may vary between -30°C up to +150°C and the unbalance on the compressor wheel and turbine wheel may vary in amplitude and orientation [164]. Moreover, although the individual parts of a turbocharger rotor-bearing system are usually created by high-precision machining steps [5], micrometer-range variations in the dimensions are inevitable. These variations can lead to a deterioration in the performance of the rotor-bearing system or causing one of the constraints to be violated.

As we want to make sure that our rotor-bearing system performs optimally

- for different oil supply conditions,
- for various unbalance configurations,
- even when the actual dimensions of the rotor-bearing system are affected by production errors,

a *robust optimization* needs to be performed. In our robust optimization, we look for the *best worst case design*, meaning that the resulting design achieves the best multi-objective value even when all uncertainties have the least favorable value.

6.7.1. METHOD

Our robust optimization method is based on the work of Ur Rehman [221], making use of the Expected Improvement and Probability of Feasibility criteria similar to Section 6.6. This method is suitable for optimization of cases in which the uncertainty bands are known, but the distribution of the uncertainty is unknown. In case of mass-produced turbocharger parts, the geometries are specified by tolerance bands and, as such, the uncertainty bands for the geometries are known. Furthermore, the method of Ur Rehman [221] ensures that the robust optimum is always compatible with the constraints. Further details of the robust optimization method can be found in [38].

Our robust optimization is performed with the model described in Section 6.2 as a parametric base model. The objectives and the constraints are equal to those of the deterministic optimization, see Sections 6.3 and 6.4.

6.7.2. SENSITIVITY STUDY INCLUDING UNCERTAINTIES

The sensitivity study described in Section 6.5 was limited to one specific operating condition. In this robust optimization study, we need to include the influence of the unbalance configuration and oil supply conditions. Therefore, the sensitivity study of Section 6.5 is extended with the variables listed in Table 6.3.

Table 6.3: Additional uncertainty parameters to Table 6.1 for the sensitivity analysis for robust optimization.

Name	Range	Unit	Description
O_{cd}	-1 – +1	mm	Axial offset of unbalance on center disk
mr_{unb}	75 – 400	mg mm	Unbalance magnitude on center disk
p_i	0.15 – 0.35	MPa	Pressure oil supply
T_i	16 – 40	°C	Inlet temperature of oil

The result of the sensitivity study is presented in Figure 6.10.

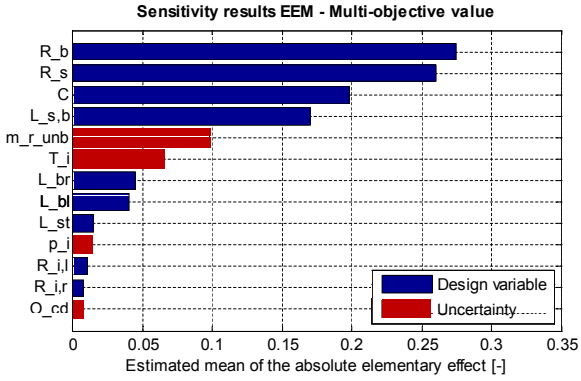

Figure 6.10: Result of the sensitivity analysis including uncertainty parameters listed in Table 6.3.

As can be seen, mr_{unb} and T_{i} have a significant influence on the multi-objective value. Particularly:

- **Unbalance amount** mr_{unb} The multi-objective value is observed to increase monotonically with the unbalance amount mr_{unb}. Clearly, this is because the forced vibration amplitude and the bearing reaction force both increase with increasing unbalance amount. The self-excited vibrations and the friction losses did not change significantly with unbalance amount.
- **Oil supply temperature** T_{i} The oil inlet temperature mostly affects the friction losses, which decreases with increasing oil temperature. Furthermore, the self-excited vibrations increase with decreasing oil temperature, but this effect is less pronounced than the effect of the oil inlet temperature on the friction losses. Hence, the multi-objective value generally decreases over the design space.

Based on the results of the sensitivity study, the robust optimization was performed with the four most sensitive design variables as well as the two most sensitive enviromental uncertainties. In addition, the uncertainty in the bearing clearance is incorporated in the optimization, because small variations in clearance can result in a change of rotor-bearing behavior, as shown in Section 3.4.8. So in this robust optimization, uncertainties in environmental conditions as well as on the design variables are included. An overview of the design variables and their range considered in this robust optimization is presented in Table 6.4.

Table 6.4: Design variables and uncertainty parameters for the robust optimization.

Design variables					
Name	Ref.	Min.	Max.	Unit	Description
R_{b}	3.0	1.0	6.0	mm	Shaft radius in bearings
R_{s}	3.0	1.8	6.0	mm	Shaft radius between meas. disks
C	15	15	25	µm	Clearance bearings
$L_{\text{s,B}}$	120	80	160	mm	Bearing span
Uncertainty parameters					
Name	Ref.	Min.	Max.	Unit	Description
mr_{unb}	250	75	400	mg·mm	Unbalance at center disk
T_{i}	26	16	40	°C	Inlet temperature oil
δ_{Cl}	0	-5	5	µm	Uncer. clearance left bearing
δ_{Cr}	0	-5	5	µm	Uncer. clearance right bearing

6.7.3. RESULTS

Similar to the deterministic optimization, the robust optimization is initiated with an initial sample set based on a Latin hypercube experimental design. In this case, 480 initial model evaluations have been performed to obtain a metamodel description for the 8-dimensional optimization problem. Out of the 480 initial model evaluations, 127 designs violated the minimum oil film thickness constraint. Another 21 designs violated the maximum shaft displacement constraint. This shows that, when uncertainties are

taken into account, the feasible design space of the rotor-bearing system is much smaller than in case of the deterministic optimization.

Following the evaluation of the intitial 480 model configurations, the iterative scheme as depicted in Figure 6.7 was started. The optimizer iteratively finds an optimum, where the main improvements were found during the first 25 iterations. The subsequent iterations did not result in further improvements of the design, but rather improved the fidelity of the metamodel.

We found that the optimum predicted by the initial metamodel –based on the sample set of 480 model evaluations– was already close to the global robust optimum: only a relatively small improvement was obtained by the iterative optimization sequence [38]. The complete optimization with 480 initial model evaluations and 200 optimization iterations took 343 hours on an octacore Intel Xeon E5-2630v3, 2.4 GHz with 128GB RAM: almost 10 times as much as the deterministic optimization study. Approximately 2/3 of the computation time was spent on running the rotor-bearing model whereas 1/3 is spent on creating and updating the metamodels and using it to determine the optimum compatible with the constraints.

Figure 6.11 visualizes the reference rotor design, the deterministic optimum design and the robust optimum design. The numerical values for the four design variables which were optimized can be found in Table 6.5.

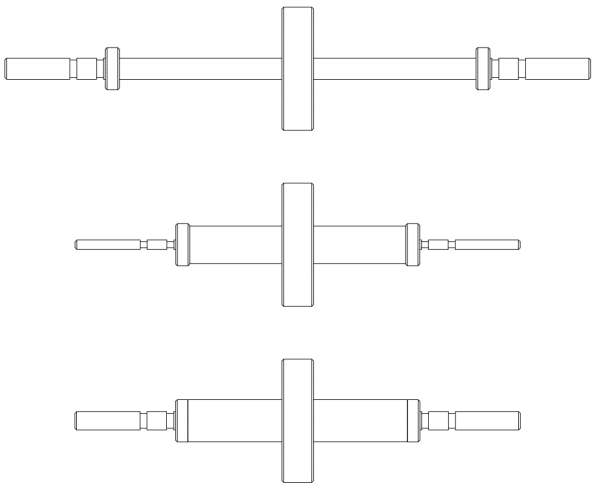

Figure 6.11: Reference design, deterministic optimum design and robust optimum design.

Table 6.5: Comparison of the robust optimum design with the reference design and the deterministic optimum design.

Control variable	Ref. design	Det. optimum	Rob. optimum
R_b (mm)	3.0	1.35	2.62
R_s (mm)	3.0	5.32	5.98
C (μm)	15.0	10.0	15.0
$L_{s,B}$ (mm)	120	80.0	80.1

Both the deterministic and the robust optimum designs feature a short bearing span $L_{s,B}$ and a large shaft radius R_s. As a result, the first eigenfrequency of the rotor-bearing system is pushed out of the operating range (0-60krpm), to 1262Hz. Therefore, the vibration amplitudes at the shaft and the bearing reaction forces remain relatively low.
The bearing clearance C also appeared to be optimum at its lowest value for both optimizations. For this small clearance, the bearing remains stable over the entire operating range and does not show any sub-synchronous vibrations. A smaller clearance generally results in higher friction losses, however, the reduction of R_b will result in a decrease of friction loss and was shown to be more influential than the clearance, see Figure 6.5.
The main difference between the deterministic design and the robust design was found in the radius at the bearings, R_b. In order to minimize the friction losses, this value has to be as low as possible. The optimum found by the deterministic optimization, however, violates the minimum oil film thickness constraint when parametric uncertainties are imposed to the rotor-bearing design and its operating conditions.

The worst-case conditions for the multi-objective value were found to be: maximum unbalance, minimum oil temperature and a clearance error leading to minimum clearance. From this result, it may seem as if it would have been sufficient to perform a deterministic optimization while assuming these worst-case condition. This is found to be not true: the worst-case condition for the oil film thickness constraint is actually at high oil supply temperature and low unbalance values. So therefore, in order to ascertain that the optimum is compatible with all constraints, it is important to perform a robust optimization for these kind of rotor-bearing systems.

The results of a run-up with the reference design, the deterministic optimum and the robust optimum are presented in Figure 6.12. It is evident that the robust optimum performs better than the reference design, but not as good as the deterministic optimum. Expressed in numbers: the multi-objective value of the deterministic optimum is 10 times better than the reference design whereas the multi-objective value of the robust optimum is 2 to 5 times better, depending on the values of the parametric uncertainties. The deterministic optimum, however, violates the minimum oil film thickness constraint under the influence of the uncertainties.

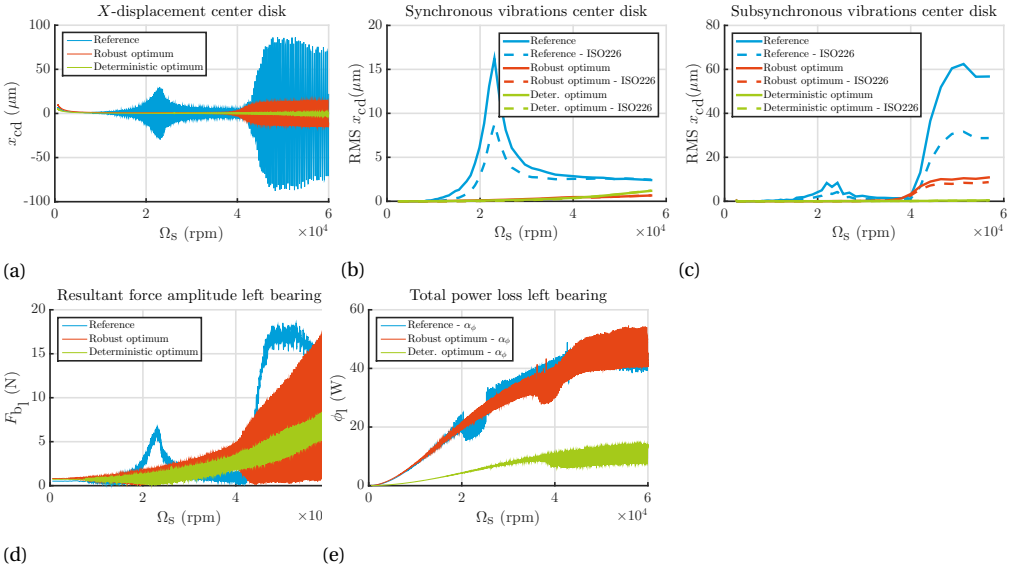

Figure 6.12: Comparison of the robust optimum with the reference design and the deterministic optimum. Figure (a) shows the displacement of the disk during the run-up, (b) and (c) the filtered signals for respectively the synchronous and subsynchronous vibration, (d) the resultant force on the bearing housing and (e) the friction loss in the bearing.

6.8. CONCLUSION

In this chapter, we optimized the design of the Laval rotor supported by plain journal bearings, as presented initially in Chapter 3. By performing a global sensitivity study based on the Elementary Effects method, it became clear that only half of the initially considered design variables and uncertainties are actually important. The sensitivity study also showed that the bearing clearance has considerable interaction with the other design variables. This demonstrates that rotor-bearing systems incorporating fluid film bearings should best be optimized as a coupled system.

The numerical model for describing a run-up of the rotor-bearing system as presented in Chapter 3 is computationally expensive. Therefore, we constructed a metamodel to describe the multi-objective function and the constraint functions, so that the numerical model needs to be evaluated as few times as possible. We made use of an efficient way of iteratively determining new sample points to feed to the metamodel, based on the Expected Improvement criterium for the objective and the Probability of Feasibility criterium for the constraint function. Therefore, the optimization generally tends to converge already after 25 iterations. Nevertheless, getting the optimization to run efficiently proved to be very time-consuming. Therefore, in practice, performing a large set of model evaluations using parallel computing on a cluster and using this data to build a metamodel seems a more effective way to obtain an optimum instead of iteratively looking for new sample points to improve the metamodel.

The added value of robust optimization compared to deterministic optimzation is shown in this chapter: the deterministic optimum violated one of the constraints. Imposing the worst-case uncertainty values in order not to avoid the constraint would have resulted in an inferior optimum compared to the true robust optimum. Hence, robust optimization ensures the best worst-case design without violating the constraints.

The resulting optimum design features a short, stiff shaft with minimum bearing clearances. As a result, the eigenfrequency is pushed out of the operating range and the bearing remains stable under all conditions. For an automotive turbocharger, this design philosophy would probably not be feasible, as the operating speed range is much larger than evaluated in this optimization. When the turbocharger shaft would be stiffened so that its eigenfrequency would be above its operating range, probably the shaft radius will be so large that excessive friction loss can be expected.

In future research, the optimization methods, as used in this chapter, can be applied to find the global robust optimum design of a turbocharger rotor-bearing system. The most important changes to the current optimization will be that both the inner and the outer oil film clearances need to be included as design variables. Furthermore, the unbalance configurations may vary, as depicted in Figure 5.14, and the temperature range which needs to be considered may be larger. Lastly, the rotation speed range will be larger, so multiple eigenmodes may play a role in the run-up and therefore the metamodels are unlikely to be as monotonic as in this study.

7

CONCLUSION

When developing a competitive turbocharger for the automotive market, the requirements for the rotor-bearing system should be fulfilled in an optimal way, at any operating condition and even if the turbocharger is manufactured with the geometric imperfections that are inevitable in high-volume, low-cost manufacturing. Therefore, the goal of this research was stated as:

To develop a method for optimizing the mass-produced automotive turbocharger rotor-bearing system, based on a validated model and resulting in a realistic optimal design which takes into account production and environmental variations.

The dynamic behavior of a turbocharger rotor-bearing system depends on numerous factors, many of which are not straightforwardly controllable when running a turbocharger on a hot gas test stand, diminishing quantitative correspondence between measurement results and simulation results. Therefore, we took a step-by-step approach in building a model, as shown in Figure 7.1.

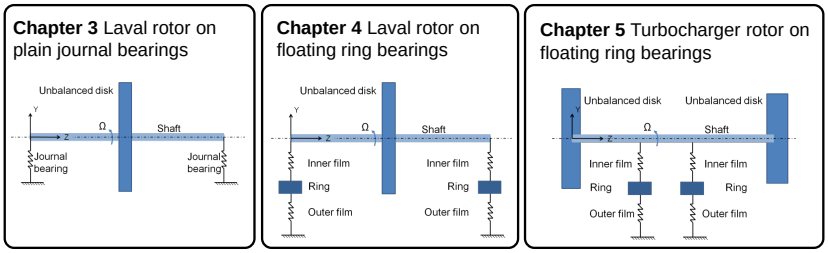

Figure 7.1: Step-by-step model development process to describe the complex multiphysical behavior of a turbocharger rotor-bearing system.

This approach, starting with a simple but well-controlled rotor-bearing system, has proven to be of great value in this study.

7.1. MODELING TURBOCHARGER ROTOR-BEARING SYSTEMS

Several methods exist to model the dynamic behavior of a turbocharger rotor-bearing system. Analytical methods are limited to only very simple rotor-bearing systems [34], therefore numerical discretization methods are more suitable to describe the complex multi-physical behavior of turbocharger rotor-bearing systems. In our study, we observed that simplified rotor-bearing models based on linearized bearing coefficients provide reasonable predictions of the synchronous response of the system. However, when oil whirl and/or oil whip occur, performing multiphysical time-transient simulations – as done in this study– is a more reliable method for capturing the non-linear behavior and for providing visualization of all relevant variables to help understand the complex behavior of the system.

The models developed in this study generally consist of a combination of coupled models: bearing models, rotor models and thermal models. The models are used for time-transient simulation of run-up profiles, so that the response over the entire rotation speed range can be predicted. The bearing models include a realistic fluid rheology description, a mass-conservative cavitation algorithm, oil feeding channel features, oil connecting channel features and a distributed thermal model. High rotation speeds cause friction losses in the bearing and therefore cause considerable temperature changes –and thus viscosity changes– in the lubricant. The addition of a thermal network model for predicting the temperatures of the shaft and the bearing housing was a key element in obtaining good correspondence between simulation results and measurement results. The resulting model may be considered to be one of the most detailed turbocharger rotor-bearing models currently found in literature.

One major limitation of our model is the enormous computation time necessary to perform run-up simulations. As the rotation speed varies from zero to thousands of rpm, many small time steps are needed to provide predictions of the behavior at any operating speed. For each time step, the equations governing the rotordynamics, fluid flow and temperature distribution need to be solved. As these are all coupled and show non-linear behavior, each time step is a computational burden, resulting in long computation times. However, when some of the numerical accuracy may be sacrificed, the model can be simplified. As an example: for our optimization in Chapter 6, we reduced the computation time of the initially fully detailed model from 100 hours to 20 minutes. Although the simplified model showed less correspondence with our measurement results, it was still able to predict the relevant input-output trends correctly and thus was an acceptable base for optimization studies.

An interesting by-product of this research is the discovery of the stabilizing effect of the lobe geometry on a floating ring bearing. By employing lobes on the inside and outside of the ring, sub-synchronous vibrations –responsible for *turbocharger constant tone noise* – can be significantly reduced, as demonstrated by the succesful implementation in series production turbochargers.

7.2. OPTIMIZATION OF HIGH SPEED ROTOR-BEARING SYSTEMS INCORPORATING FLUID FILM BEARINGS

The response of a turbocharger rotor-bearing system strongly depends on its design parameters. Statements on what the influence is of each individual design parameter are therefore only valid for a particular rotor-bearing system, which explains many contradicting claims on this topic in literature. The creation of a fully parametric rotor-bearing model –as done in this study– enables prediction of any desired design configuration. As some of the bearing parameters, such as the clearance, strongly influence the rotor behavior, the rotor-bearing system should always be analyzed as a coupled system: optimization of only the bearing without including the dynamics of the rotor (or vice versa) renders an inferior optimum compared to optimization of the coupled rotor-bearing system.

Furthermore, we demonstrated an optimization of a Laval rotor supported by plain journal bearings. We found that the uncertainties in rotor unbalance and in oil supply temperature are clearly factors to take into account when optimizing the rotor-bearing design. As a result, the deterministic optimum violated some of the constraints when these uncertainties were imposed. The robust optimum ensured operation without violating the constraints at any combination of uncertainties. The optimization method employed required a minimum amount of run-up simulations by making use of metamodels for the objective functions and the constraint functions, combined with a sophisticated method of determining new sampling points for iteratively improving the metamodels.

7.3. RECOMMENDATIONS

Although a validated turbocharger rotor-bearing model has been developed and an efficient global robust optimization method has been demonstrated, both ingredients have not been combined in this research. The computation time of the turbocharger rotor-bearing model was considered to be excessive for use as a base for (robust) optimization. Therefore, the model should be simplified while keeping the correct input-output trends.

A number of possibilities on simplifying the model can be mentioned:

- As turbochargers in practice operate at either ambient temperature (during start-up of the engine) or at warm temperatures (i.e. steady oil temperature above 100 degrees Celsius), it would make sense to simplify the model to isoviscous conditions: the spatial temperature variations in one operating condition are much smaller than the temperature variations between operating conditions [168].

- The cavitation algorithm may be simplified to a non-mass conservative approach such as Gümbel conditions without great loss of accuracy [69].

- Instead of using time-transient solvers, continuation techniques may be employed to decrease the computation times [222].

The methods developed in this study are considered to form a basis for future optimization of turbocharger rotor-bearing systems. Before actually starting such work, the following modeling items deserve further attention:

- The viscosity of the lubricant in this study was described as a function of shear rate and temperature. The coefficients for these relations were partly based on measurements, partly based on literature values, see Appendix A. The shear-rate dependence was taken from literature values due to lack of measurement equipment with sufficient range of shear rates. The currently assumed values may therefore not be reliable and should be verified experimentally.
- The bearing housing has been considered to be rigid throughout this study. In reality, the turbocharger bearing housing will have resonance frequencies within the operating range of the rotor. Therefore, the dynamics of the bearing housing (and its support structure) should be investigated in future studies.
- The outlet boundaries of the bearings have been considered to be non-submerged. In reality, a bubbly mixture is more likely to be present at the sides of the bearing. Further investigations should be performed on the effect of the boundary condition of the oil outlet of the bearings on the rotor-bearing behavior.

A

VISCOSITY MEASUREMENTS

This Appendix contains the viscosity description of the lubricant which is used throughout this Thesis.

A.1. VISCOSITY-TEMPERATURE RELATION

The lubricant, *Mobil 1 ESP Formula 5W30*, is a common multi-grade automotive engine oil consisting of petroleum-based and non-petroleum-based synthetic chemical compounds. Its viscosity is a function of temperature T, shear rate $\dot{\gamma}$ and pressure p. The viscosity-temperature dependency is measured using a Brookfield CAP 2000 cone-on-plate viscometer with a 0.45^o cone angle. The measurement device features a temperature controlled plate and cone as well as a controlled rotation speed.
Based on 30 repetitive measurements at $T = 318K$ and $\dot{\gamma} = 333.33s^{-1}$, the standard deviation of the measurement is determined to be $\sigma = 0.00219Pa \cdot s$. Figure A.2 gives the viscosity-temperature measurement based on 5 repetitive measurements on 7 different temperatures, as well as a fit using the Vogel equation, Equation 4.31.

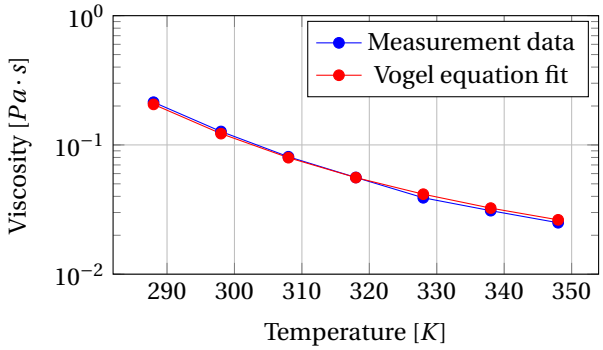

Figure A.1: Viscosity-temperature relation of Mobil 1 ESP Formula 5W30, T = 318K and $\dot{\gamma}$ = 333.33s^{-1}. Vogel coefficients a = 4.44e-4 Pa·s, b = 633.26^{o}C and c = 88.56^{o}C .

A

A.2. VISCOSITY-SHEAR RATE RELATION

The Brookfield CAP 2000 cone-on-plate viscometer which was used for determining the viscosity-temperature relation can also be used for measuring the viscosity-shear rate dependency of oil. However, the shear rate of engine oil in automotive turbochargers is commonly in the range of $1e4s^{-1}$ up to $1e6s^{-1}$. The CAP 2000 viscometer at our disposal was only capable of measuring up to $\dot{\gamma} = 5e3s^{-1}$ and hence values from literature are used instead: Knauder et al [198] published the shear-rate dependent parameters of a similar 5W30 engine oil based on measurements as well as information from the oil manufacturer.

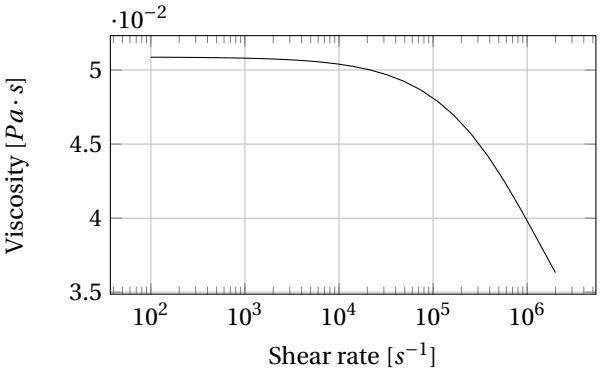

Figure A.2: Viscosity vs shear rate of Mobil 1 ESP Formula 5W30, $T = 318K$, $p = p_{amb}$.

A.3. VISCOSITY-PRESSURE RELATION

As we expect only moderate pressures in our bearings, the viscosity is assumed to be independent of pressure.

Table A.1 summarizes the parameters of the Vogel equation, Equation 4.31.

Table A.1: Viscosity parameters of Mobil 1 ESP Formula 5W30.

a	4.44e-4	Pa · s
b	633.26	^oC
c	88.56	^oC
d	0.8	-
r	0.5	-
K	7.2e-7	s

B

THERMAL MODEL LAVAL ROTOR ON PLAIN JOURNAL BEARINGS

This Appendix describes the thermal network model of a Laval rotor on plain journal bearings, as described in Chapter 3. First, a conjugate heat transfer analysis is performed to get insight in the temperature distribution within the rotor-bearing system. Then, the model is converted into a thermal network model. As will be shown in this Appendix, by carefully simplifying the heat flow through bodies, a simple yet effective model can be developed to predict the relevant temperatures of the rotor-bearing system.

B.1. TEMPERATURE DISTRIBUTION BASED ON CONJUGATE HEAT TRANSFER.

In order to gain insight in the temperature distribution in the rotor-bearing system, a 3D conjugate heat transfer analysis is performed to obtain the steady state temperatures. The geometry of the model as well as its boundary conditions are displayed in figure B.1. The conjugate heat model uses a segregated solver to solve the Navier-Stokes equation and the energy equation on a finite element basis [199] and takes several hours to converge. The numerical values applicable to this rotor-bearing system are included in Table xx.

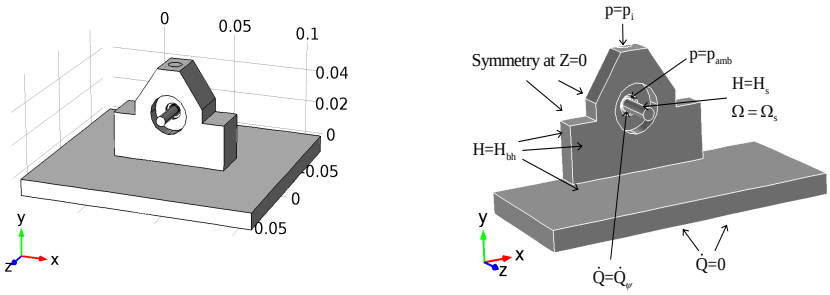

Figure B.1: Geometry and boundary conditions of the conjugate heat transfer model. The rotor rotates at rotation speed Ω_s in centered position. Oil is fed through the top of the bearing housing at pressure $p = p_i$ and can flow out at ambient pressure $p = p_{amb}$ at the side of the bearing. The oil has a viscosity described by equation 4.31 and generates heat by viscous friction $\dot{Q}_\psi$. Heat is transferred to ambient air via the shaft (forced convection H_s, Equation B.2) and via the bearing housing (natural convection H_{bh}). The underside of the base plate is isolated: zero heat transfer $\dot{Q} = 0$ is imposed here.

B.1.1. CONJUGATE HEAT TRANSFER: RESULTS AT COLD OIL SUPPLY CONDITIONS.

Figure B.2 gives the resulting temperature distribution at Ω_s=60.000rpm, which is the maximum operating speed of the rotor-bearing system. The oil temperature at the inlet was set at T_i=293K, which is also the ambient temperature T_{amb}.

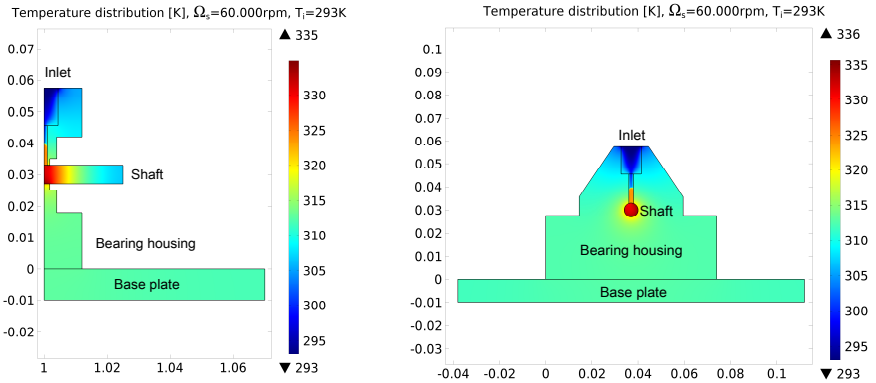

(a) Cross-sectional view in the YZ-plane.

(b) Cross-sectional view in the XY-plane.

Figure B.2: Temperature distribution based on conjugate heat transfer analysis at Ω_s=60.000rpm, T_i=293K.

At these conditions:

- the friction heat $\dot{Q}_\psi$ causes the bearing to heat up to a maximum temperature of 334K. The maximum is reached in the fluid film, close to the wall of the shaft.
- the temperature difference over the height of the fluid film is approximately 10K,

where the shaft is clearly warmer than the bearing housing. This causes a difference in thermal expansion between the shaft and the bearing housing of 0.3μ m, which can considered to be negligible.

- the shaft temperature shows a considerable temperature gradient along the shaft (in axial direction) caused by strong forced convection due to its rotation in air.

Furthermore, clearly noticeable in Figure B.2 is the heating of the oil in the inlet channel. The temperature of the oil when it enters the bearing is increased from 293K to 325K. Hence, most of the temperature increase of the oil occurs in the inlet channel, and not in the fluid film itself. This is due to:

- the convection of heat from the warm bearing housing to the oil,
- mixing of hot oil and cold oil near the inlet of the bearing,
- conduction of heat within the oil.

The friction loss in the bearing at T_i=293K, Ω_s=60.000rpm is predicted to be 45W, of which:

- 50% is convected to ambient temperature by the shaft
- 30% is convected to ambient temperature by the bearing housing
- 20% is transported by the oil leaving the bearing.

This shows that the friction heat is mostly dissipated by the shaft and the bearing housing, and not so much by the lubricant itself. This is mainly due to the small clearance which limits the oil flow rate through the bearing. Clearly, adiabatic conditions can not be assumed in this case.

Figure B.3 gives the temperature distribution in the fluid film, halfway the clearance. Clearly noticeable is the influence of the oil inlet channel, which supplies relatively cold oil to the fluid film.

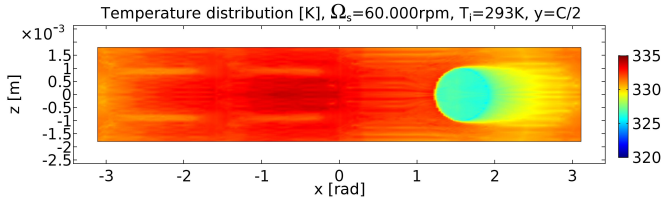

Figure B.3: Temperature distribution in the fluid film.

The thermal time constants are obtained by a transient thermal analysis, resulting in a time constant of approximately 5 seconds for the bearing housing and the shaft. As the thermal time constant of the system is much larger than the time constant of motion of the rotor-bearing system, we only need to take into account the steady state components in the thermal model.

B.1.2. CONJUGATE HEAT TRANSFER: RESULTS AT HOT OIL SUPPLY CONDITIONS.

In case the temperature of the oil at the inlet is increased from T_i=293K to T_i=348K, similar observations can be made:

- the friction heat $\dot{Q}_\psi$ causes the bearing to heat up to a maximum temperature of 357K. The maximum is reached in the fluid film, close to the wall of the shaft.
- the temperature difference over the height of the fluid film is only 3K, where the shaft is warmer than the bearing housing. The difference in thermal expansion between the shaft and the bearing housing is negligibly small: 0.1µm.
- the shaft temperature again shows a considerable temperature gradient along the shaft (in axial direction) caused by strong forced convection due to its rotation in air.
- most of the temperature increase of the oil occurs in the inlet channel and not in the film domain.

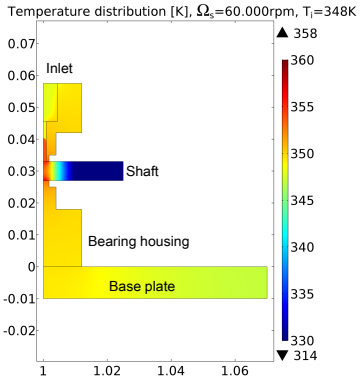

(a) Cross-sectional view in the YZ-plane.

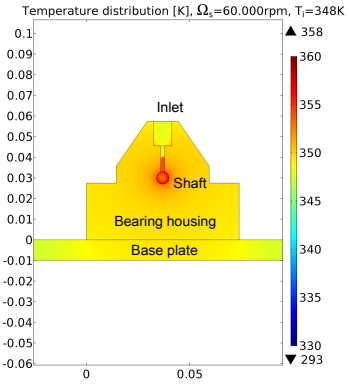

(b) Cross-sectional view in the XY-plane.

Figure B.4: Temperature distribution based on conjugate heat transfer analysis at Ω_s=60.000rpm, T_i=348K.

The friction loss in the bearing at T_i=348K, Ω_s=60.000rpm is predicted to be 23W, of which:

- 25% is convected to ambient temperature by the shaft
- 60% is convected to ambient temperature by the bearing housing
- 15% is transported by the oil leaving the bearing.

Again, the transport of heat by oil flow is the least significant heat path, but in this case the bearing housing carries away most of the heat.

Figure B.5 gives the temperature distribution in the fluid film, halfway the clearance. The cooling effect of the oil inlet channel is less pronounced as in the case T_i=293K.

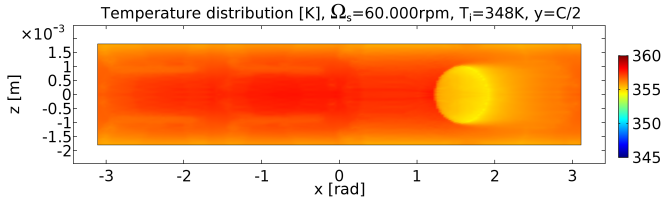

Figure B.5: Temperature distribution in the fluid film.

B.2. TEMPERATURE DISTRIBUTION BASED ON A THERMAL NETWORK MODEL.

The conjugate heat transfer described in Section B.1 requires a large number of elements —in the order of 10^6— and is therefore, computationally heavy. It is therefore not suitable for time-transient calculations as required in our studies. Instead, we can make use of simplified relations between thermal nodes, strategically placed at positions where we want to know the temperature and locations between where there is a significant thermal gradient. Based on the results of the conjugate heat transfer analysis, the thermal nodes are chosen at the locations depicted in Figure B.6.

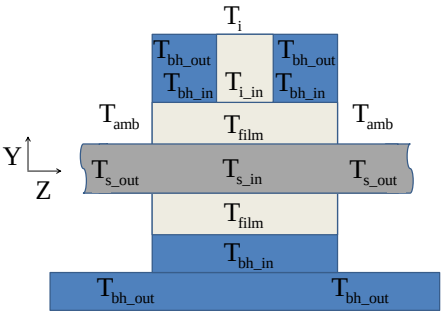

Figure B.6: Cross-sectional schematic view of the rotor-bearing system indicating the thermal nodes used in the thermal network model. $T_{\text{bh\_in}}$ denotes the temperature of the bearing housing adjacent to the fluid film and $T_{\text{bh\_out}}$ represents the temperature of the outside of the bearing housing.

The friction heat from the bearing $\dot{Q}_\psi$ exits the rotor-bearing system via three heat flow paths: via the bearing housing, via the shaft and via the oil flowing out of the bearing housing. Based on these three heat flow paths, the thermal network model depicted in Figure B.7 is composed.

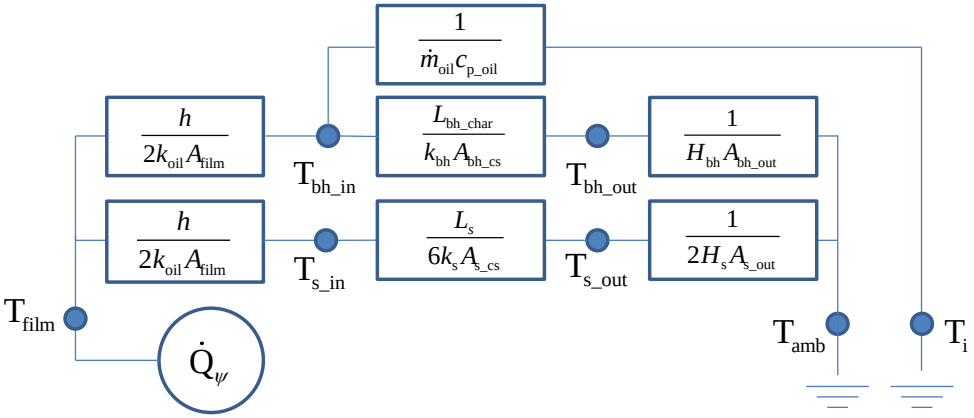

Figure B.7: The thermal network model of the rotor-bearing system including the bearing housings.

The thermal network can be understood as follows:

- the friction heat from the bearing $\dot{Q}_\psi$ is conducted from halfway the fluid film to the bearing housing at temperature $T_{\text{bh\_in}}$ and the shaft at temperature $T_{\text{s\_in}}$. An average temperature at the center of the height of the fluid film is assumed here, as proposed by San Andres [154].

- the heat in the bearing housing is conducted to the outer surface of the bearing housing at temperature $T_{\text{bh\_out}}$, where it is transferred to the ambient air by natural convection H_{bh}. The characteristic length of conduction is characterized as[196]:

$$L_{\text{char\_bh}} = \frac{V_{\text{bh}}}{2A_{\text{bh\_o}}} \tag{B.1}$$

- the heat in the shaft is conducted to the outer surface of the shaft at temperature $T_{\text{s\_out}}$, where it is transferred to the ambient air by forced convection H_{s}. The thermal node on the shaft is positioned at a length of $L/3$ at each side of the bearing. This is chosen because the temperature decay in the shaft in axial direction is dominated by forced convection, and hence can be approximated by an exponentially decaying profile which has its average temperature at $L/3$. The convection from this node to ambient air depends on the shaft outer area $\text{A}_{\text{s\_o}}$ and on the convection coefficient of the rotating shaft [196]:

$$H_{\text{s}} = \frac{k_{\text{air}}}{15R_{\text{s}}}\text{Re}_{\text{air}}{}^{2/3}\text{Pr}_{\text{air}}{}^{1/3} \tag{B.2}$$

where:

$$\text{Re}_{\text{air}} = \frac{4\Omega_s {R_s}^2}{\nu_{\text{air}}} \tag{B.3}$$

The kinematic viscosity of air ν_{air} is assumed to be constant.

- the heat that leaves the bearing by the oil flow is not straightforward to simplify. In the oil inlet channel, heat flows from the bearing housing into the oil. Also, mixing of warm and cold oil occurs at the oil inlet, followed again by a heat flow towards the bearing housing. A simplification is made here: we assume that the heat which leaves the bearing by the oil flow originates from the bearing housing. Then, this heat path depends on the temperature difference $T_{\text{bh\_in}} - T_{\text{i}}$, the specific heat capacity of oil $c_{\text{p\_oil}}$ and the instantaneous mass flow $\dot{m}_{\text{oil}}$.

In order to verify if we could lump the temperatures of the bearing housing and the shaft, the ratio of inner-to-outer thermal resistance was calculated. This ratio is expressed by the Biot number [196] and was found to be sufficiently low, so lumping these two bodies was found to be acceptable.

B.3. VERIFICATION OF THE THERMAL NETWORK MODEL.

Temperature predictions of the thermal network model are compared with results from the conjugate heat transfer model at three different rotation speeds, see Figure B.8.

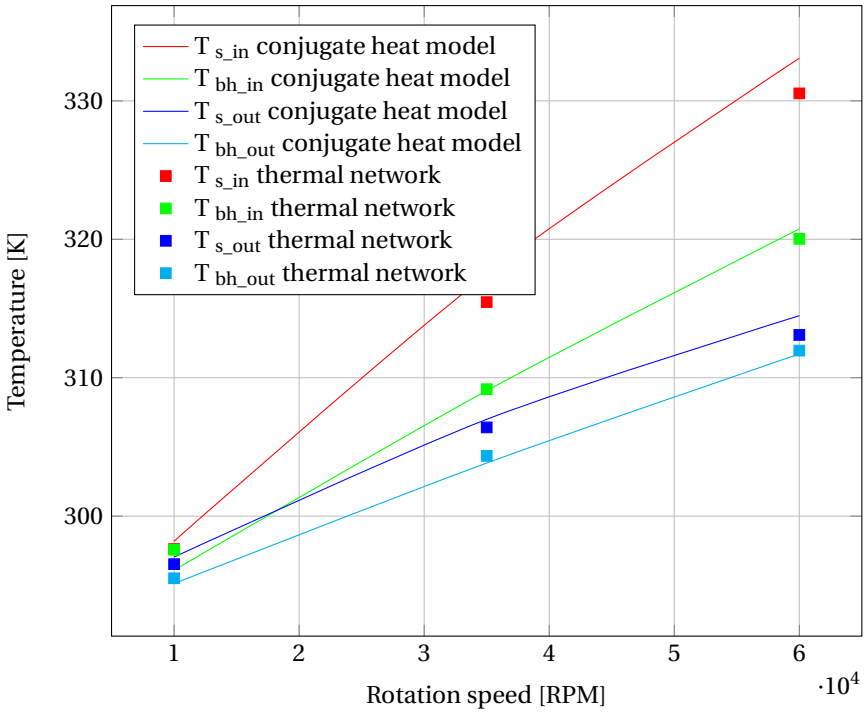

Figure B.8: Comparison of results from the conjugate heat model (Section B.1) with the thermal network model (Section B.2) at p_{i}=3bar, T_{i}=293K. The lines represent the prediction of the conjugate heat transfer model and the markers represent the results of the thermal network model.

The thermal network model underestimates the temperatures by a maximum of $3K$,

which is considered to be acceptable. To get this correlation, the variables $L_{\text{char\_bh}}$ and L_{s} were tuned. Adjustments of less than 20% for each of these two variables were needed.

C

SHAFT MASS, STIFFNESS AND GYROSCOPIC MATRICES

This Appendix contains the mass, stiffness and gyroscopic matrices of a shaft section as described in Section 3.2.1.

C

C.1. STIFFNESS MATRICES

The local elementary stiffness sub-matrices $\boldsymbol{K}^{\text{el}}$ can be written as [188]:

$$\mathbf{K}_{11}^{\text{el}} = \begin{bmatrix} \frac{12EI_{yy}}{L_{\text{el}}^3} & 0 & 0 & 0 & \frac{6EI_{yy}}{L_{\text{el}}^2} & 0 \\ \cdots & \frac{12EI_{xx}}{AL_{\text{el}}^3} & 0 & -\frac{6EI_{xx}}{L_{\text{el}}^2} & 0 & 0 \\ \cdots & \cdots & \frac{EA}{L_{\text{el}}} & 0 & 0 & 0 \\ \cdots & \cdots & \cdots & \frac{4EI_{yy}}{L_{\text{el}}} & 0 & 0 \\ \cdots & symm. & \cdots & \cdots & \frac{4EI_{xx}}{L_{\text{el}}} & 0 \\ \cdots & \cdots & \cdots & \cdots & \cdots & \frac{GI_{zz}}{L_{\text{el}}} \end{bmatrix}$$

$$\mathbf{K}_{12}^{\text{el}} = \begin{bmatrix} -\frac{12EI_{yy}}{L_{\text{el}}^3} & 0 & 0 & 0 & \frac{6EI_{yy}}{L_{\text{el}}^2} & 0 \\ 0 & -\frac{12EI_{xx}}{AL_{\text{el}}^3} & 0 & -\frac{6EI_{xx}}{L_{\text{el}}^2} & 0 & 0 \\ 0 & 0 & -\frac{EA}{L_{\text{el}}} & 0 & 0 & 0 \\ 0 & \frac{6EI_{yy}}{L_{\text{el}}^2} & 0 & \frac{2EI_{yy}}{L_{\text{el}}} & 0 & 0 \\ -\frac{6EI_{xx}}{L_{\text{el}}^2} & 0 & 0 & 0 & \frac{2EI_{xx}}{L_{\text{el}}} & 0 \\ 0 & 0 & 0 & 0 & 0 & \frac{GI_{zz}}{L_{\text{el}}} \end{bmatrix} = \mathbf{K}_{21}^{\text{el}\ T} \tag{C.1}$$

$$\mathbf{K}_{22}^{\text{el}} = \begin{bmatrix} \frac{12EI_{yy}}{L_{\text{el}}^3} & 0 & 0 & 0 & -\frac{6EI_{yy}}{L_{\text{el}}^2} & 0 \\ \cdots & \frac{12EI_{xx}}{AL_{\text{el}}^3} & 0 & \frac{6EI_{xx}}{L_{\text{el}}^2} & 0 & 0 \\ \cdots & \cdots & \frac{EA}{L_{\text{el}}} & 0 & 0 & 0 \\ \cdots & \cdots & \cdots & \frac{4EI_{yy}}{L_{\text{el}}} & 0 & 0 \\ \cdots & symm. & \cdots & \cdots & \frac{4EI_{xx}}{L_{\text{el}}} & 0 \\ \cdots & \cdots & \cdots & \cdots & \cdots & \frac{GI_{zz}}{L_{\text{el}}} \end{bmatrix}$$

where for a circular shaft with radius R_s:

$$I_{xx} = I_{yy} = \frac{\pi {R_s}^4}{4} I_{zz} = \frac{\pi {R_s}^4}{2} \tag{C.2}$$

C.2. MASS MATRICES

The local mass matrices of the shaft elements can be written as [188]:

$$
\mathbf{M}_{11}^{\text{el}} = \rho A L_{\text{el}} \begin{bmatrix} \frac{13}{35} & 0 & 0 & 0 & \frac{11L_{\text{el}}}{210} & 0 \\ \dots & \frac{13}{35} & 0 & -\frac{11L_e}{210} & 0 & 0 \\ \dots & \dots & \frac{1}{3} & 0 & 0 & 0 \\ \dots & \dots & \dots & \frac{L_{\text{el}}^2}{105} & 0 & 0 \\ \dots & symm. & \dots & \dots & \frac{L_{\text{el}}^2}{105} & 0 \\ \dots & \dots & \dots & \dots & \dots & \frac{L_{\text{el}}}{3} \end{bmatrix}
$$

$$
\mathbf{M}_{12}^{\text{el}} = \rho A L_{\text{el}} \begin{bmatrix} \frac{9}{70} & 0 & 0 & 0 & \frac{13L_{\text{el}}}{420} & 0 \\ 0 & \frac{9}{70} & 0 & \frac{-13L_{\text{el}}}{420} & 0 & 0 \\ 0 & 0 & \frac{1}{6} & 0 & 0 & 0 \\ 0 & \frac{13L_{\text{el}}}{420} & 0 & -\frac{L_{\text{el}}^2}{140} & 0 & 0 \\ -\frac{13L_{\text{el}}}{420} & 0 & 0 & 0 & -\frac{L_{\text{el}}^2}{140} & 0 \\ 0 & 0 & 0 & 0 & 0 & \frac{L_{\text{el}}}{6} \end{bmatrix} = \mathbf{M}_{12}^{\text{el}\,T} \tag{C.3}
$$

$$
\mathbf{M}_{22}^{\text{el}} = \rho A L_{\text{el}} \begin{bmatrix} \frac{13}{35} & 0 & 0 & 0 & -\frac{11L_{\text{el}}}{210} & 0 \\ \dots & \frac{13}{35} & 0 & \frac{11L_e}{210} & 0 & 0 \\ \dots & \dots & \frac{1}{3} & 0 & 0 & 0 \\ \dots & \dots & \dots & \frac{L_{\text{el}}^2}{105} & 0 & 0 \\ \dots & symm. & \dots & \dots & \frac{L_{\text{el}}^2}{105} & 0 \\ \dots & \dots & \dots & \dots & \dots & \frac{L_{\text{el}}}{3} \end{bmatrix}
$$

C.3. GYROSCOPIC MATRICES

The shaft element experiences a gyroscopic torque when the shaft center line is not aligned with the rotation speed vector. The gyroscopic sub-matrices $\boldsymbol{G}_{\text{el}}$ for a slender shaft are given by [20]:

$$
\mathbf{G}_{11}^{\text{el}} = \Phi \begin{bmatrix} 0 & 36 & (15\Phi_{\text{el}}-3)L_{\text{el}} & 0 \\ -36 & 0 & 0 & (15\Phi_{\text{el}}-3)L_{\text{el}} \\ (3-15\Phi_{\text{el}})L_{\text{el}} & 0 & 0 & (4+5\Phi_{\text{el}}+10{\Phi_{\text{el}}}^2){L_{\text{el}}}^2 \\ 0 & (3-15\Phi_{\text{el}})L_{\text{el}} & -(4+5\Phi_{\text{el}}+10{\Phi_{\text{el}}}^2){L_{\text{el}}}^2 & 0 \end{bmatrix}
$$

$$
\mathbf{G}_{12}^{\text{el}} = \Phi \begin{bmatrix} 0 & -36 & (15\Phi_{\text{el}}-3)L_{\text{el}} & 0 \\ 36 & 0 & 0 & (15\Phi_{\text{el}}-3)L_{\text{el}} \\ (15\Phi_{\text{el}}-3)L_{\text{el}} & 0 & 0 & (-1-5\Phi_{\text{el}}+5{\Phi_{\text{el}}}^2){L_{\text{el}}}^2 \\ 0 & (15\Phi_{\text{el}}-3)L_{\text{el}} & (1+5\Phi_{\text{el}}-5{\Phi_{\text{el}}}^2){L_{\text{el}}}^2 & 0 \end{bmatrix}
$$

$$
\mathbf{G}_{21}^{\text{el}} = \Phi \begin{bmatrix} 0 & -36 & (3-15\Phi_{\text{el}})L_{\text{el}} & 0 \\ 36 & 0 & 0 & (3-15\Phi_{\text{el}})L_{\text{el}} \\ (3-15\Phi_{\text{el}})L_{\text{el}} & 0 & 0 & (-1-5\Phi_{\text{el}}+5{\Phi_{\text{el}}}^2){L_{\text{el}}}^2 \\ 0 & (3-15\Phi_{\text{el}})L_{\text{el}} & (1+5\Phi_{\text{el}}-5{\Phi_{\text{el}}}^2){L_{\text{el}}}^2 & 0 \end{bmatrix}
$$

$$
\mathbf{G}_{22}^{\text{el}} = \Phi \begin{bmatrix} 0 & 36 & (3-15\Phi_{\text{el}})L_{\text{el}} & 0 \\ -36 & 0 & 0 & (3-15\Phi_{\text{el}})L_{\text{el}} \\ (15\Phi_{\text{el}}-3)L_{\text{el}} & 0 & 0 & (4+5\Phi_{\text{el}}+10{\Phi_{\text{el}}}^2){L_{\text{el}}}^2 \\ 0 & (15\Phi_{\text{el}}-3)L_{\text{el}} & -(4+5\Phi_{\text{el}}+10{\Phi_{\text{el}}}^2){L_{\text{el}}}^2 & 0 \end{bmatrix} \tag{C.4}
$$

where [20]:

$$\Phi = \frac{\rho_s I_s}{15 L_{el}(1 + \frac{12 E_{el} I_s}{\kappa_s G_s A_{el} L_{el}^2})^2} \tag{C.5}$$

D

Oil Flow in Connecting Channels of Floating Ring Bearings

The purpose of this study is to investigate the influence of the oil connecting channels on the pressure distribution of a floating ring bearing.

D.1. FRB pressure distribution based on a 3D CFD model

D.1.1. 3D CFD model details

The oil flow through the FRB fluid domain is modeled using a steady state 3D CFD model, using a commercial FEM-package [199]. Figure D.1 shows the fluid domain and its boundary conditions. Here, shaft speed Ω_s is imposed as a tangential velocity along the inner wall of the fluid domain and ring speed Ω_r is imposed along all walls of the ring, including the walls of the oil connecting channels. The fluid is modeled as an incompressible and isoviscous fluid. Numerical values of a typical automotive turbocharger FRB are used, summarized in Table D.1.

In this model, the shaft and ring displacements e_s and e_r are prescribed. Thus, the film thicknesses in terms of the eccentricity are given by:

$$\begin{aligned} h_{\text{out}}(\theta) &= C_{\text{out}}(1 - \varepsilon_{\text{out,x}}\cos(\theta) - \varepsilon_{\text{out,y}}\sin(\theta)) \\ h_{\text{in}}(\theta) &= C_{\text{in}}(1 - \varepsilon_{\text{in,x}}\cos(\theta) - \varepsilon_{\text{in,y}}\sin(\theta)) \end{aligned} \tag{D.1}$$

Parts of this Appendix are published in: Eling, R.; van Ostayen, R.A.J.; Rixen, D. *Proceedings of SIRM 2015 – 11th International Conference on Vibrations in Rotating Machines*, **2015**; ID50.

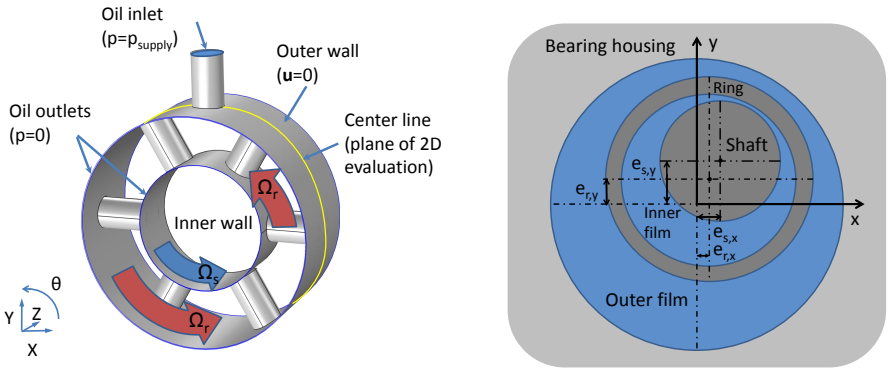

(a) Fluid domain

(b) Kinematics

Figure D.1: Details of the 3D CFD model of the floating ring bearing.

where the eccentricities ε are defined as:

$$\begin{aligned} \varepsilon_{\text{in,x}} &= \frac{e_{\text{s,x}} - e_{\text{r,x}}}{C_{\text{in}}} \\ \varepsilon_{\text{in,y}} &= \frac{e_{\text{s,y}} - e_{\text{r,y}}}{C_{\text{in}}} \\ \varepsilon_{\text{out,x}} &= \frac{e_{\text{r,x}}}{C_{\text{out}}} \\ \varepsilon_{\text{out,y}} &= \frac{e_{\text{r,y}}}{C_{\text{out}}} \end{aligned} \tag{D.2}$$

Outer ring radius $[m]$	$5 \cdot 10^{-3}$	Inner ring radius $[m]$	$3 \cdot 10^{-3}$
Outer ring width $[m]$	$5 \cdot 10^{-3}$	Inner ring width $[m]$	$3 \cdot 10^{-3}$
Outer clearance $[m]$	$50 \cdot 10^{-6}$	Inner clearance $[m]$	$20 \cdot 10^{-6}$
Oil inlet pressure $[Pa]$	$4 \cdot 10^{5}$	Oil channel radius $[m]$	$0.75 \cdot 10^{-3}$
Oil viscosity $[Pa \cdot s]$	0.1		

Table D.1: Properties of the floating ring bearing considered in this Appendix.

The CFD model needs a large number of elements to obtain a reasonable element aspect ratio in the thin film sections. A mesh convergence study has been performed, which showed that a mesh of minimally $1 \cdot 10^6$ elements is suitable for this analysis. The Reynolds numbers for the films in this study are always lower than 100, hence, the fluid flow can be considered to be fully laminar. The Reynolds number for the oil connecting channels are typically between 100 and 2500, depending on the rotation speed, the channel geometry and the oil viscosity. In this study, cavitation is treated by setting negative pressures to zero.

D.1.2. 3D CFD MODEL: PRESSURE DISTRIBUTION

Figure D.2 shows the pressure distribution on the center line (see Figure D.1) when the FRB is in center position (zero eccentricity) at medium rotation speed. As can be seen, sharp pressure gradients occur at the transition from thin film section to the oil connecting channel section: the pressure decreases when entering the channel and increases

when exiting the channel. This effect is mostly seen in the inner film, as the inner film thickness is smaller. Moreover, the relative wall velocity of the inner film is higher than of the outer film.

It is observed that the pressure increase at the transition boundary out of the connecting channel is larger than the pressure decrease at the transition boundary into the oil connecting channel. This means that the oil connecting channel locally increases the reaction forces acting on the shaft and the ring.

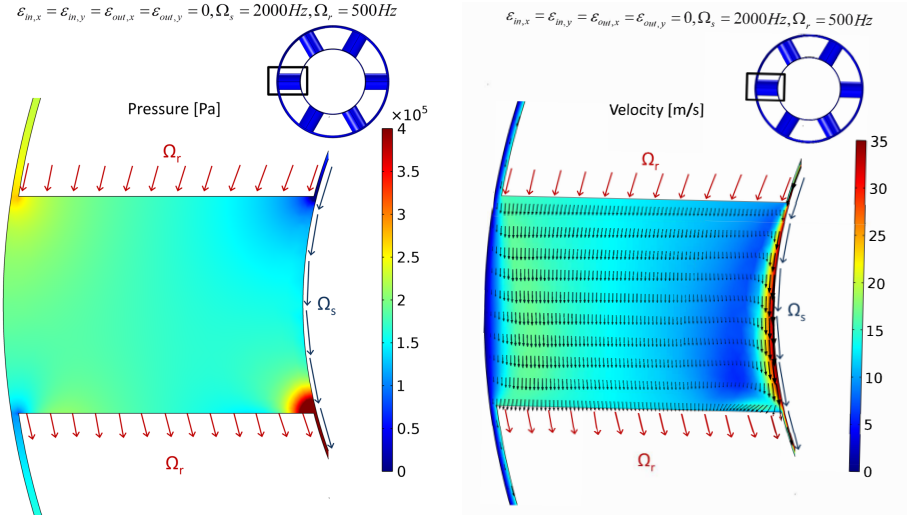

(a) Pressure

(b) Flow velocity

Figure D.2: Oil flow through an oil connecting channel showing sharp pressure gradients at the transition from thin film section to the channel domain. The arrows in the shaft and ring domain represent the imposed velocity of the shaft and the ring.

Figure D.3 shows the circumferential pressure profiles at the center line of the oil films of the FRB in centric operation, where the supply pressure is situated around $\theta = \pi/2$.

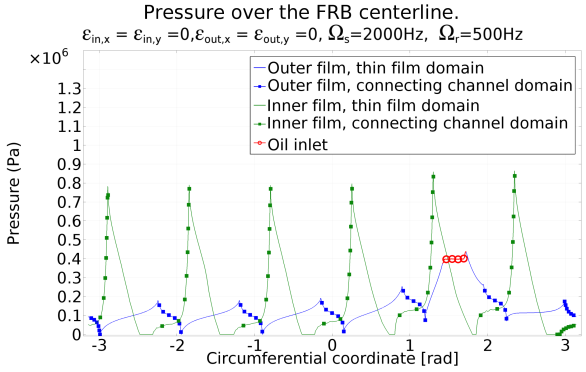

Figure D.3: Center line pressure around the circumference of the oil films of the FRB at centric operation clearly showing the influence of the oil connecting channels on the pressure distribution.

The influence of the oil connecting channels is clearly noticeable in sharp pressure gradients at the edges of the channel. In centric operation, peak pressures of several bar in the inner film are observed. The peak pressures in the outer film are smaller. Furthermore, it can be seen that the overall pressure in the inner fluid film is lower than the outer fluid film pressure due to the centrifugal forces on the fluid.
At small eccentricities, the effect of the oil connecting channels dominates the center line pressure distribution. It was found that at higher eccentricities, *i.e. typically* $\varepsilon > 0.3$, the pressure distribution in the FRB is dominated by the hydrodynamic pressure from the converging-diverging film. In addition, the influence of the oil connecting channels on the pressure distribution was found to decrease for lower viscosity or by the addition of chamfered edges neer the transition zones.

D.1.3. 3D CFD MODEL: RING SPEED

During operation, the ring will rotate with a rotation speed of typically 0.2-0.4 Ω_s, depending on the shaft speed, the oil viscosity and the specific FRB geometry[11]. The inner film drives the ring while the outer film restrains the rotation of the ring. The simulation results in the previous section were obtained by imposing $\Omega_s = 2000 Hz$ and $\Omega_r = 500 Hz$. The ring speed can also be obtained by iteratively balancing the torque on the ring [11, 144, 168]:

$$I_r \ddot{\theta}_r = T_{in} + T_{out} \tag{D.3}$$

where the drag torques of the films are determined by integrating the shear stress of the fluid over the inner and outer bearing areas.

As can be seen in Figure D.2, the fluid exerts a pressure on the side walls of the oil connecting channels, causing an additional torque which can drive the ring: $T_{channel}$. Figure D.5 presents the resulting ring speed ratios when this extra torque term is included. The extra torque term $T_{channel}$ appears to have a significant influence in determining the ring speed ratio: it delivers extra driving torque to the ring. As a result, the ring speed ratio is underestimated by up to 10% when the effect of the pressure inside the oil connecting channels is neglected. Under lower viscosity conditions, $\eta = 0.01[Pa \cdot s]$, the underestimation of ring speed ratio was smaller: $4-7\%$. This result was also found in the experi-

ments of Trippett and Li [147], where the number of oil connecting channels was found to influence the ring speed ratio.

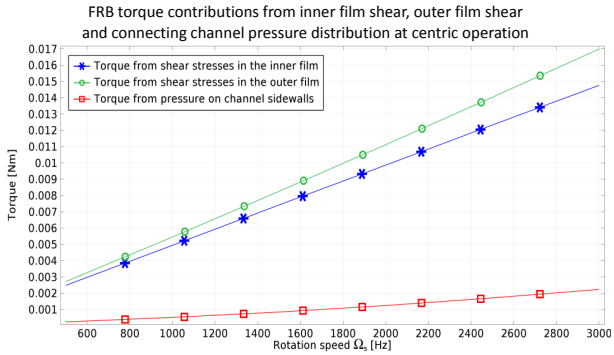

Figure D.4: Torque contribution of the oil connecting channels.

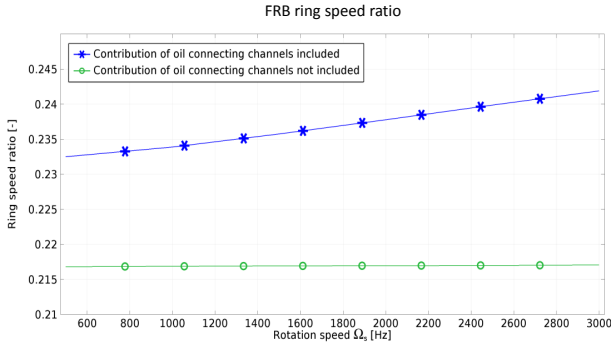

Figure D.5: Effect of the connecting channel flow on the ring speed ratio: although the torque contribution from the oil connecting channels is an order of magnitude smaller than the torques generated by the shear stresses in the thin films; the ring speed ratio is significantly increased by the torque generated in the oil connecting channels.

D.2. OIL CONNECTING CHANNEL METAMODEL

The results from the steady state 3D CFD model show that the internal flow in the connecting channels influences the FRB pressure distribution and the ring speed ratio, and can therefore not be neglected. One way to include the effect of the internal flow of the oil connecting channels is to use a 3D CFD model, but this is considered to be too computationally expensive for time-transient simulations. Therefore, the 3D CFD model will be replaced by a model which uses the Reynolds equations to model the flow in the thin film sections. For the oil connecting channel domains depicted in Figure D.6, a metamodel will now be introduced.

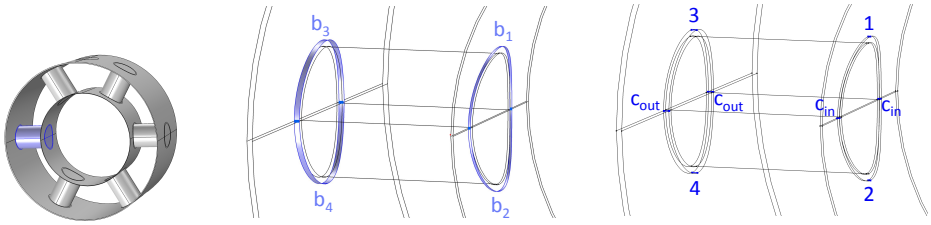

(a) A connecting channel in the FRB model

(b) Boundaries b1-b4

(c) Points 1-4 and c_{in}, c_{out}

Figure D.6: Computation domain of the oil connecting channel which will be replaced by a metamodel.

D

In order to include the inlet and exit effects, the domain that we study consists of an isolated channel plus a section of the film domain having a radius of 4 times the nominal film clearance, which was found to be a sufficient value as the ram pressure effects are very local near the transition between the film domain and the channel domain, as can also be seen in figure D.3.
In a previous study [180], we found that the flow through the boundaries of the oil connecting channel can be described as a linear function of pressures surrounding the channel as well as rotation speeds and eccentricties of the shaft and the ring. Similar relations were also found for the pressure at the center of the oil channel and the ring torque. These relations were determined using multivariate regression analysis based on data of a CFD model of the connecting channel, which will also be applied here. The metamodel which describes the pressure distribution due to the presence of the oil connecting channel will be constructed in four steps:

1. Find relationships $\mathbf{Q}(\mathbf{p},\Omega,\varepsilon)$ based on a multivariate regression analysis of simulation results of a FRB CFD model, with ε being the eccentricity vector as described in Equation 4.32.

2. Find relationships $p_{c\_in}(\mathbf{p},\Omega,\varepsilon)$ and $p_{c\_out}(\mathbf{p},\Omega,\varepsilon)$ based on a multivariate regression analysis of simulation results of a FRB CFD model.

3. Assume a pressure distribution $p(z)$ over boundary b1...b4.

4. Couple the metamodel with the thin film domains so that the pressures over boundaries b1...b4 are continuous and conservation of mass over the channel holds.

An additional regression analysis will be done to determine the influence of the oil connecting channel on the torque on the ring: $T_{\text{channel}}(\mathbf{p},\Omega,\varepsilon)$.

D.2.1. FLOW THROUGH BOUNDARIES B1...B4

The first step of constructing the metamodel is to find a linear relation for the flow Q through boundaries b1...b4, based on a linearization around a reference operating point:

$$\mathbf{Q} = \mathbf{Q}_0 + \mathbf{A}(\mathbf{p}-\mathbf{p}_0) + \mathbf{B}(\Omega-\Omega_0) + \mathbf{C}\mathrm{E} \tag{D.4}$$

where: $\mathbf{p} = \begin{bmatrix} p_1 & p_2 & p_3 & p_4 \end{bmatrix}^T$, $\Omega = \begin{bmatrix} \Omega_s & \Omega_r \end{bmatrix}^T$ and $\mathrm{E} = \begin{bmatrix} \varepsilon_{\mathrm{in,X}} & \varepsilon_{\mathrm{in,Y}} & \varepsilon_{\mathrm{out,X}} & \varepsilon_{\mathrm{out,Y}} \end{bmatrix}^T$.

Matrices **A**, **B** and **C** are the coefficient matrices which need to be determined by running the 3D CFD model over a range of operating conditions around a reference operating condition, see Table D.2.

Parameter	Reference value	Perturbation range
$\Omega_s[Hz]$	2000	± 250
$\Omega_r[Hz]$	$0.25\Omega_s$	$\pm 0.05\Omega_s$
$\varepsilon_{\mathrm{in,x}}$	0	± 0.1
$\varepsilon_{\mathrm{in,y}}$	0	± 0.1
$\varepsilon_{\mathrm{out,x}}$	0	± 0.1
$\varepsilon_{\mathrm{out,y}}$	0	± 0.1

Table D.2: Reference operating point and perturbation range for creating the metamodel

A number of CFD evaluations was subsequently performed over the entire design space. The sampling scheme was created using a 6-factor 5-level D-optimal design. In total, 30 evaluations of the CFD model were performed to gather the necessary data. The CFD results were then fitted using multivariate regression analysis based on Equation D.4. As can be seen in Figure D.7, a fit could be constructed.

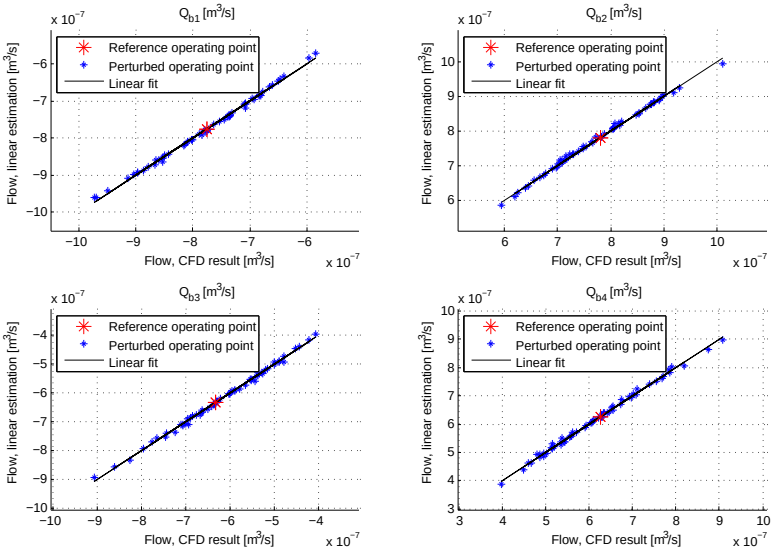

Figure D.7: Experimental dataset used for establishing the flow functions.

D.2.2. CENTER PRESSURE p_{c_in} AND p_{c_out}

The second step in constructing the metamodel is to find a linear relation between the pressure at points p_{c_in} and p_{c_out} and the operation variables:

$$\mathbf{p}_c = \mathbf{D}(\mathbf{p} - \mathbf{p}_0) + \mathbf{E}(\Omega - \Omega_0) + \mathbf{F}\mathrm{E} + \mathbf{p}_{c\_0} \tag{D.5}$$

where $\mathbf{p_c} = \begin{bmatrix} p_{c\_in} & p_{c\_out} \end{bmatrix}^T$. The results of the previously described 30 CFD evaluations were also used to establish the pressure function. The results are shown in figure D.8.

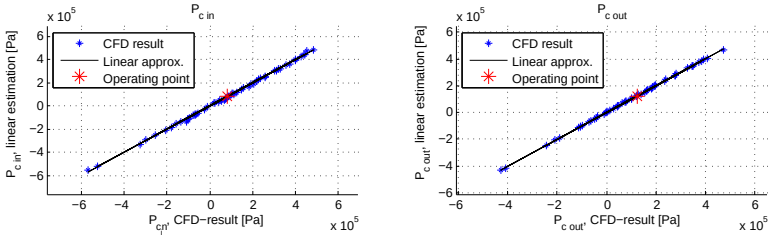

Figure D.8: Experimental dataset used for establishing the pressure functions.

D.2.3. PRESSURE DISTRIBUTION OVER THE CHANNEL BOUNDARIES AND COUPLING THE METAMODEL TO THE THIN FILM SECTIONS

In order to couple the metamodel to the thin film domain, a pressure distribution over the boundaries b1...b4 needs to be assumed. Based on evaluation of data from the 30 CFD evaluations, a symmetric quadratic function of the axial coordinate z corresponds very well:

$$\begin{aligned} &p_{b\_i}(z) = c_{1\_i} z^2 + c_{2\_i} \\ &with\ i = 1..4 \end{aligned} \tag{D.6}$$

so that for each of the boundaries, the pressure distribution can be described by two coefficients c_{1_i}, c_{2_i}. We assume that the shaft and the ring do not tilt, so that:

$$\begin{aligned} p_{b\_1}(L/2) = p_{b\_2}(L/2) = p_{b\_1}(-L/2) = p_{b\_2}(-L/2) = p_{c\_in} \\ p_{b\_3}(L/2) = p_{b\_4}(L/2) = p_{b\_3}(-L/2) = p_{b\_4}(-L/2) = p_{c\_cout} \end{aligned} \tag{D.7}$$

Thus coefficient c_{2_i} is equal to the pressures estimated by Equation D.5. Another relation is now still needed to determine coefficient c_{1_i}. This is done by the principle of conservation of mass: a weak coupling between the pressure in the thin film section and the pressure at the boundaries b1...b4 of the metamodel is used. This allows for obtaining the flow going in and out of the thin film domain, which can then be set equal to the flow estimation given in Equation D.4. Thus, an iterative scheme solves the system of equations by providing c_{1_i} and c_{2_i} by minimizing $Q_{est} - Q_{reyn}$.

D.3. REYNOLDS-BASED FRB INCLUDING OIL CONNECTING CHANNEL METAMODEL

In the previous section, the concept of the oil connecting channel metamodel was explained. This will now be applied to a FRB model which uses the Reynolds equation for the thin film section, again using the numerical values of Table D.1. For comparison, another Reynolds-based FRB model is constructed which uses a 'passive' pressure coupling for the oil connecting channels, i.e. ignoring the internal flow phenomena. Figure D.9 shows the resulting pressure distribution in the FRB during centric operation. It can be seen that a 'passive'pressure coupling does not take into account the local pressure gradients due to the transition between the film domain and the channel domain.

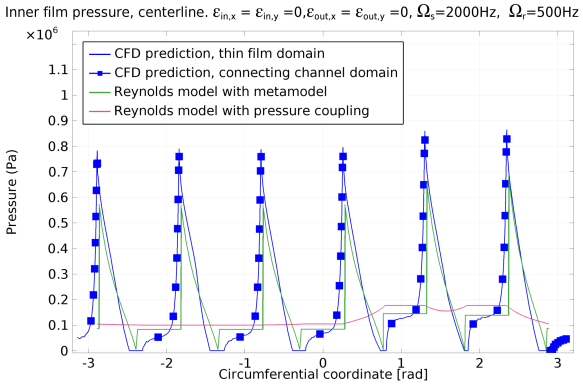

(a) Inner film pressure

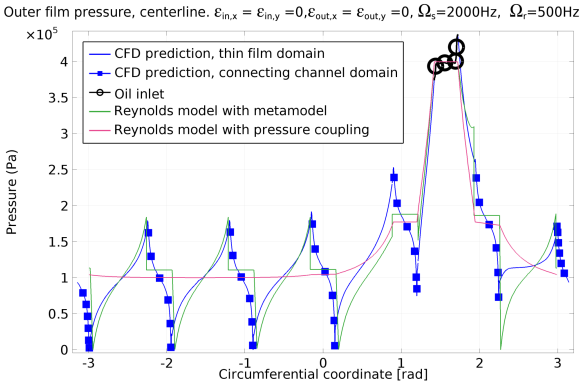

(b) Outer film pressure

Figure D.9: Comparison of predictions of centerline film pressures using three different models. The Reynolds-based model with pressure coupling does not show the pressure increase at the transition boundaries whereas the Reynolds model with the metamodel does take this effect into account.

Figure D.10 shows the same plot, but then when a shaft and ring eccentricity is imposed.

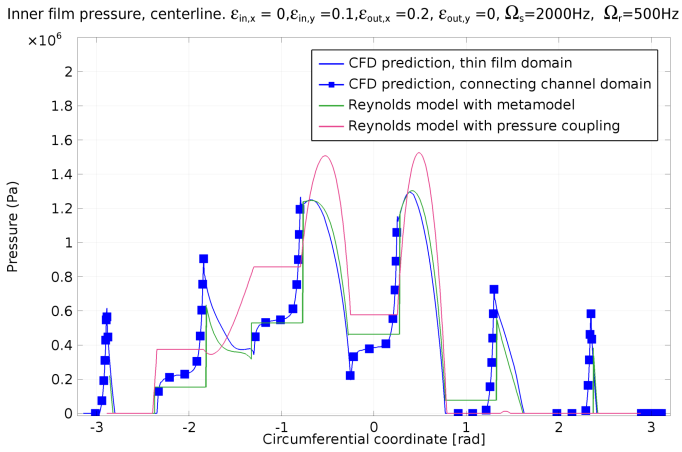

(a) Inner film pressure

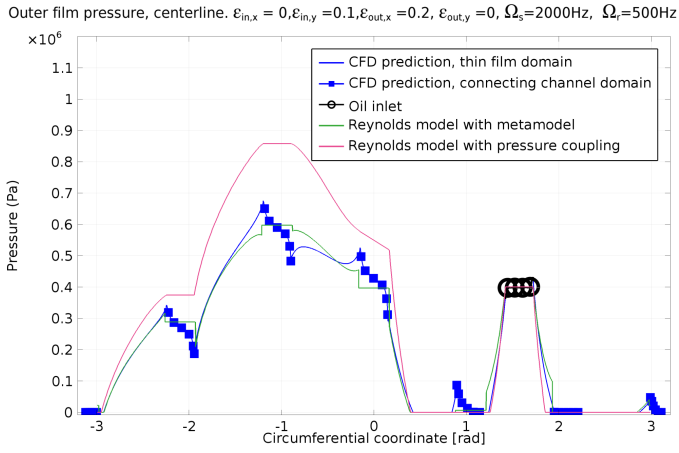

(b) Outer film pressure

Figure D.10: Comparison of predictions of centerline film pressures using three different models. The Reynolds-based model with pressure coupling does not show the pressure increase at the transition boundaries whereas the Reynolds model with the metamodel does take this effect into account.

D.4. CONCLUSION

The internal flow in the oil connecting channel of a FRB is influenced by inertia and shear flow terms, causing vortices in the oil connecting channels. The shear-driven flow in the thin film sections experiences a pressure decrease when entering the channel and a pressure increase when exiting the channel, caused by both the fluid inertia as well as by the channel vortices. As the inner and outer film velocities and film thicknesses are generally not equal, there is a net difference in pressure on the side walls of the oil connecting channel, which acts as a driving torque on the ring. If this effect is neglected, the ring speed would be underestimated by 4% – 10%.

A computationally inexpensive metamodel was presented, in which the channel flow is modeled as a linear combination of pressures and wall velocities surrounding the channel. Using this flow model, the effect of the connecting channels on the pressure distribution of the FRB can be included in a Reynolds-based model. In this way, the flow in the oil connecting channels -which was shown to have an important influence on the FRB pressure distribution- can be taken into account when performing time-transient analysis of FRBs.
Further work should focus on the influence of the oil connecting channel flow on the time-transient behavior of the rotor-bearing system.

E

SQUEEZE MOTION DESCRIPTION IN A CO-ROTATING REFERENCE FRAME

This Appendix contains the derivation of the fluid film squeeze motion in time.

E.1. OUTER FILM

As can be observed in Figure E.1a, the film thickness of the outer film depends on the displacement of the ring and can be described in the global reference frame as:

$$h_{\text{out}} = C_{\text{out}} - e_{\text{r\_X}} \cos(\Theta) - e_{\text{r\_Y}} \sin(\Theta) \tag{E.1}$$

where C_{out} represents the nominal outer clearance, $e_{\text{r\_X}}$ and $e_{\text{r\_Y}}$ are the ring displacements in global X and Y direction and Θ is the global angle:

$$\Theta = \tan^{-1}\left(\frac{Y}{X}\right) \tag{E.2}$$

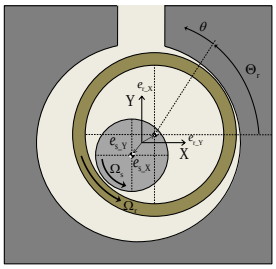

(a) Floating Ring Bearing kinematic description. Clearances are magnified for visualization.

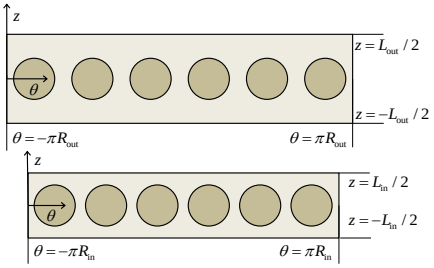

(b) Film domain of the floating ring bearing in the co-rotating reference frame $\{\theta, z\}$. The dark circles represent the oil connecting channels between the inner and outer oil films.

Figure E.1: Floating ring bearings. The fluid domain consists of the outer oil film and the inner oil film.

The instantaneous angle of the ring Θ_r in the global reference frame can be found by integrating its rotation speed over time with a reference position at time $t = 0$ aligned in the X-axis direction:

$$\Theta_r = \int_0^t \Omega_r \, dt \tag{E.3}$$

We can write the outer film thickness in the co-rotating reference frame as:

$$h_{\text{out}} = C_{\text{out}} - e_{r\_x}\cos(\theta) - e_{r\_y}\sin(\theta) \tag{E.4}$$

Resulting in the following time-derivative:

$$\begin{aligned}
&\tfrac{\partial h_{out}}{\partial t} = \Omega_r \sin(\Theta_r) e_{r_X} \cos(\theta) - \cos(\Theta_r)\dot{e}_{r_X}\cos(\theta) + \cos(\Theta_r) e_{r_X}\sin(\theta) \\
&-\Omega_r \cos(\Theta_r) e_{r_Y} \cos(\theta) - \sin(\Theta_r)\dot{e}_{r_Y}\cos(\theta) + \sin(\Theta_r) e_{r_Y}\sin(\theta) \\
&+\Omega_r \cos(\Theta_r) e_{r_X} \sin(\theta) + \sin(\Theta_r)\dot{e}_{r_X}\sin(\theta) + \sin(\Theta_r) e_{r_X}\cos(\theta) \\
&-\Omega_r \sin(\Theta_r) e_{r_X} \sin(\theta) - \cos(\Theta_r)\dot{e}_{r_Y}\sin(\theta) - \cos(\Theta_r) e_{r_Y}\cos(\theta)
\end{aligned} \tag{E.5}$$

E

E.2. INNER FILM

The film thickness of the inner film in the global reference frame is given by:

$$h_{\text{in}} = C_{\text{in}} - \left(e_{\text{s\_X}} - e_{\text{r\_X}}\right)\cos(\Theta) - \left(e_{\text{s\_Y}} - e_{\text{r\_Y}}\right)\sin(\Theta) \tag{E.6}$$

which in the co-rotating reference frame becomes:

$$h_{\text{in}} = C_{\text{in}} - \left(e_{\text{s\_x}} - e_{\text{r\_x}}\right)\cos(\theta) - \left(e_{\text{s\_y}} - e_{\text{r\_y}}\right)\sin(\theta) \tag{E.7}$$

with the following time-derivative:

$$\begin{aligned}
&\rightarrow \tfrac{\partial h_{in}}{\partial t} = \\
&\Omega_r \sin(\Theta_r) e_{s_X} \cos(\theta) - \cos(\Theta_r)\dot{e}_{s_X}\cos(\theta) + \cos(\Theta_r) e_{s_X}\sin(\theta) \\
&-\Omega_r \cos(\Theta_r) e_{s_Y} \cos(\theta) - \sin(\Theta_r)\dot{e}_{s_Y}\cos(\theta) + \sin(\Theta_r) e_{s_Y}\sin(\theta) \\
&-\Omega_r \sin(\Theta_r) e_{r_X} \cos(\theta) + \cos(\Theta_r)\dot{e}_{r_X}\cos(\theta) - \cos(\Theta_r) e_{r_X}\sin(\theta) \\
&+\Omega_r \cos(\Theta_r) e_{r_Y} \cos(\theta) + \sin(\Theta_r)\dot{e}_{r_Y}\cos(\theta) - \sin(\Theta_r) e_{r_Y}\sin(\theta) \\
&+\Omega_r \cos(\Theta_r) e_{s_X} \sin(\theta) + \sin(\Theta_r)\dot{e}_{s_X}\sin(\theta) + \sin(\Theta_r) e_{s_X}\cos(\theta) \\
&+\Omega_r \sin(\Theta_r) e_{s_Y} \sin(\theta) - \cos(\Theta_r)\dot{e}_{s_Y}\sin(\theta) - \cos(\Theta_r) e_{s_Y}\cos(\theta) \\
&-\Omega_r \cos(\Theta_r) e_{r_X} \sin(\theta) - \sin(\Theta_r)\dot{e}_{r_X}\sin(\theta) - \sin(\Theta_r) e_{r_X}\cos(\theta) \\
&-\Omega_r \sin(\Theta_r) e_{r_Y} \sin(\theta) + \cos(\Theta_r)\dot{e}_{r_Y}\sin(\theta) + \cos(\Theta_r) e_{r_Y}\cos(\theta)
\end{aligned} \tag{E.8}$$

F

THRUST BEARING MODEL.

This Appendix describes an isothermal thrust bearing model.

F.1. THRUST BEARING MODEL

The thrust bearing of a turbocharger carries the axial forces acting on the rotor, commonly referred to as the *thrust load*. In an automotive turbocharger, typically four different axial forces can be distinguished:

- the aerostatic forces acting on the (projected) front and back surface of both wheels,
- as well as the forces resulting from changing the momentum of the air flow from axial to radial direction at the compressor and vice versa at the turbine.

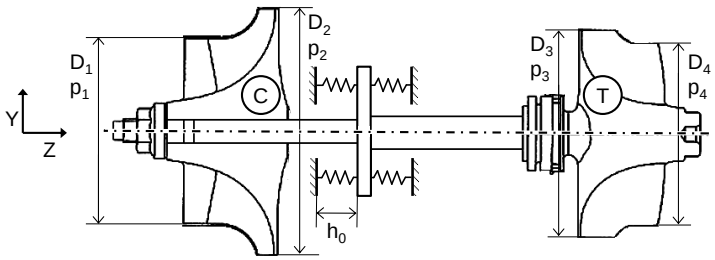

Figure F.1: Turbocharger rotor with a compressor wheel (left hand side) and a turbine wheel (right hand side) and a thrust bearing in between. The thrust bearing carries the aerostatic loads from both sides of the two wheels as well as the impulse load of the air entering and exiting the turbocharger in axial direction.

In equation form, the net thrust load of a turbocharger with diameters D_1-D_4 as depicted in Figure F.1 can be expressed as:

$$F_{\text{thrust}} = F_{\text{aerostatic\_C}} + F_{\text{impulse\_C}} + F_{\text{aerostatic\_T}} + F_{\text{impulse\_T}} \tag{F.1}$$

where:

$$
\begin{aligned}
F_{\text{aerostatic\_C}} &= \frac{\pi {D_1}^2}{4} p_1 - \frac{\pi {D_2}^2}{4} p_2 \\
F_{\text{impulse\_C}} &= -\dot{m}_{\text{air}} v_1 \\
F_{\text{aerostatic\_T}} &= \frac{\pi {D_3}^2}{4} p_3 - \frac{\pi {D_4}^2}{4} p_4 \\
F_{\text{impulse\_T}} &= -\dot{m}_{\text{air}} v_2
\end{aligned}
\tag{F.2}
$$

In this equation, the pressures p_1-p_4, the mass flow $\dot{m}_{\text{air}}$ and the corresponding air velocities v_1, v_4 depend on the instantaneous operating conditions of the combustion engine attached to the turbocharger. Automotive turbochargers are usually operated under transient conditions due to vehicle accelerations and decelerations. Furthermore, it is known that the exhaust gas flow which drives the turbine is a pulsating flow so that the rotor experiences axial oscillations , especially when the combustion engine is operated under part load conditions [223]. At full engine load conditions, the axial oscillations are relatively small. For this analysis, we will consider full engine load operating conditions and therefore we only take into account the steady state load on the thrust bearing. Based on the projected surface areas of the compressor and the turbine wheels, the pressures p_1-p_4 as well as the mass flow through the turbocharger $\dot{m}_{\text{air}}$, the thrust load profile depicted in Figure F.2 is predicted.

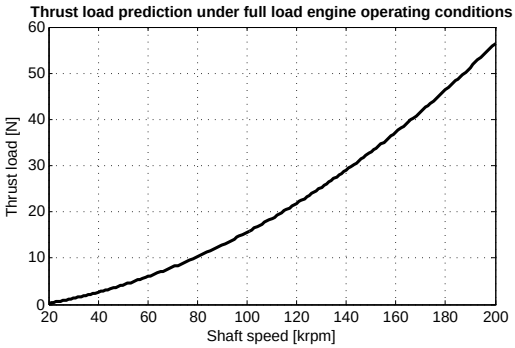

Figure F.2: Thrust load profile of a typical small size passenger vehicle turbocharger.

The thrust bearing considered in this Appendix is a taper-land bearing, featuring converging tapers machined into the bearing surface to create hydrodynamic carrying capacity. Figure F.3a gives a schematic representation of the thrust bearing fluid domain.

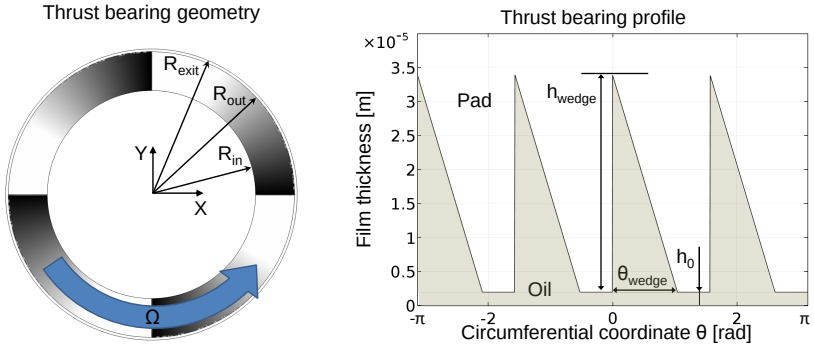

(a) Thrust bearing geometry. (b) Film height.

Figure F.3: Thrust bearing : the bearing contains four wedges and four lands (white surfaces in Figure **a**). The bearing is fed from the inside at $r = R_{\text{in}}$. Oil can exit the bearing by flowing outwards at $r = R_{\text{exit}}$.

When the rotor is perfectly perpendicular to the bearing surface (i.e. no rotor tilting), the film height h_{aligned} can be written as the following piecewise function:

$$\begin{aligned}
&h_{\text{aligned}}(R_{\text{in}} \leq r < R_{\text{out}}, (n-1)\tfrac{\pi}{2} \leq \theta < \theta_{\text{wedge}} + (n-1)\tfrac{\pi}{2}) = h_0 + h_{\text{wedge}}\left(1 - \frac{\theta-(n-1)\frac{\pi}{2}}{\theta_{\text{wedge}}}\right)\\
&h_{\text{aligned}}\left(R_{\text{in}} \leq r < R_{\text{out}}, \theta_{\text{wedge}} + (n-1)\tfrac{\pi}{2} \leq \theta < \tfrac{\pi}{2} + (n-1)\tfrac{\pi}{2}\right) = h_0\\
&h_{\text{aligned}}\left(R_{\text{out}} \leq r \leq R_{\text{exit}}\right) = h_0\\
&\text{for}\\
&n = 1..4
\end{aligned} \tag{F.3}$$

where the geometry of the bearing is given by R_{in}, R_{out}, R_{exit}, h_{wedge}, and θ_{wedge}, see Table F.1. The film height above the land, h_0 follows from the axial load which is applied to the bearing: the higher the load on the bearing, the smaller the film height h_0. When the shaft is tilted, for example when the rotor is orbiting in a conical mode, the film height can be expressed as:

$$h = h_{\text{aligned}} + h_{\text{tilt}} \tag{F.4}$$

which for small tilting angles $\alpha, \beta \ll 1$ can be written as [183]:

$$h_{\text{tilt}} = r\left(\alpha\cos(\theta) + \beta\sin(\theta)\right) \tag{F.5}$$

Table F.1: Design parameters of the thrust bearing.

Name	Value	Unit	Name	Value	Unit
R_{in}	3.75	mm	h_{wedge}	32	μm
R_{out}	5.15	mm	θ_{wedge}	$\pi/3$	rad
R_{exit}	5.25	mm			

Fluid inertia terms can generally be discarded when analyzing fluid flow in automotive turbocharger thrust bearings [224] and hence the Reynolds equation can be used,

which can be written in cylindrical coordinates as:

$$\frac{\partial}{\partial r}\left(\frac{h^3}{12}\frac{\partial p}{\partial r}\right)+\frac{1}{r^2}\frac{\partial}{\partial \theta}\left(\frac{h^3}{12}\frac{\partial p}{\partial \theta}\right)=\frac{\mu\Omega}{2}\frac{\partial h}{\partial \theta}+\mu\frac{\partial h}{\partial t} \tag{F.6}$$

This equation can be solved over the fluid domain depicted in Figure F.3a using the following boundary conditions:

$$\begin{cases} p(r=R_{\text{in}})=p_{\text{sup}} \\ p(r=R_{\text{exit}})=0 \end{cases} \tag{F.7}$$

Oil is supplied to the bearing at the inner radius at supply pressure p_{sup}, therefore, negative pressures are unlikely to occur in this type of bearing and so the need for a mass-conservative cavitation description is limited. Hence, we chose to apply Gümbel cavitation conditions, where pressures predictions below zero are truncated to zero.

Although it is well known that temperature variations greatly affect the thrust bearing operation [101], developing a thermal model for the thrust bearing and its surroundings is out of the scope of this research. Instead, we will consider an isothermal model where $T=T_{\text{sup}}$. The viscosity in this case is assumed to be a function of the local shear rate only:

$$\mu_{\text{oil}}(\dot{\gamma})=A\left(r+\frac{1-r}{1+(K\dot{\gamma})^d}\right) \tag{F.8}$$

where:

$$A=ae^{\frac{b}{(T_{\text{sup}}+c)}} \tag{F.9}$$

using the constants a, b, c, d and r corresponding to the specific type of oil, see Appendix A.

F.2. THRUST BEARING FORCES

Figure F.4 gives the resulting pressure distribution at $\Omega = 100.000$rpm with the rotor being perfectly perpendicular to the bearing surface, i.e. no rotor tilting.

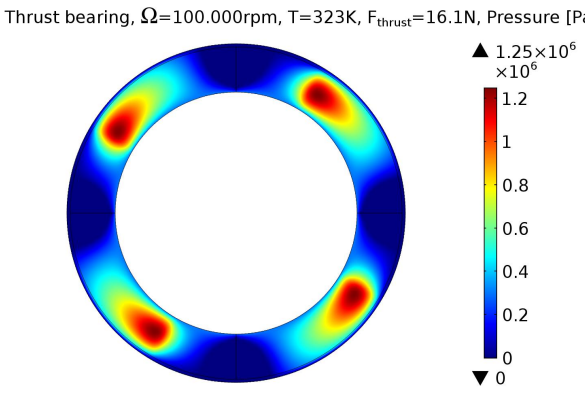

Figure F.4: Thrust bearing pressure distribution under perfect shaft-to-bearing perpendicularity.

The shaft experiences tilting angles in the order of $1 \cdot 10^{-3}$ rad as visualized in Figure 5.10. This results in an asymmetric pressure distribution and thus a torque on the X-axis or -as in this case- the Y-axis.

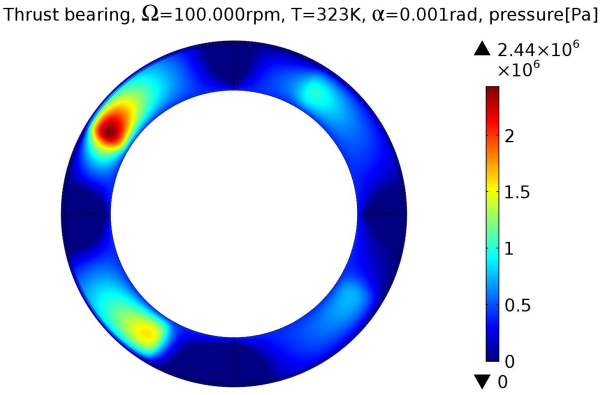

Figure F.5: Thrust bearing pressure distribution under tilted shaft-to-bearing orientation.

Integration of the pressure over the area of the thrust bearing gives the bearing reaction force and torque:

$$\begin{aligned} F_{\text{thrust}} &= \int_0^{2\pi} \int_{R_{\text{in}}}^{R_{\text{exit}}} p r dr d\theta \\ M_{\text{thrust}_X} &= \int_0^{2\pi} \int_{R_{\text{in}}}^{R_{\text{exit}}} r p \cos(\theta) r dr d\theta \\ M_{\text{thrust}_Z} &= \int_0^{2\pi} \int_{R_{\text{in}}}^{R_{\text{exit}}} r p \sin(\theta) r dr d\theta \end{aligned} \tag{F.10}$$

The thrust load profile under full engine load conditions as depicted in Figure F.2 results in the following film height h_0, (h_0 is visualized in Figure F.1):

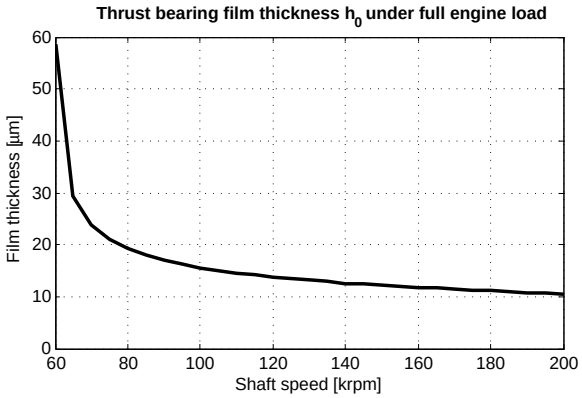

Figure F.6: Thrust bearing film thickness under full load engine operating conditions.

F.3. THRUST BEARING STIFFNESS AND DAMPING TERMS

Having found the equilibrium position h_0 of the thrust bearing under full load engine operating conditions, we can now apply small perturbations in displacement and velocity around the equilibrium position to obtain the linearized thrust bearing stiffness and damping:

$$\begin{aligned} k_{\text{thrust}} &= \frac{dF_{\text{thrust}}}{dh_0} \\ c_{\text{thrust}} &= \frac{dF_{\text{thrust}}}{d\dot{h}_0} \end{aligned} \tag{F.11}$$

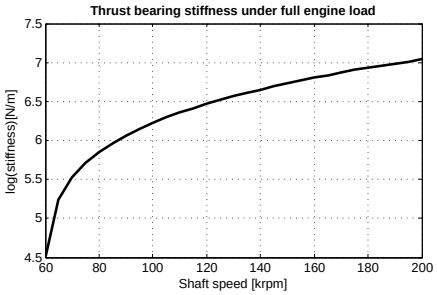

(a) Thrust bearing stiffness.

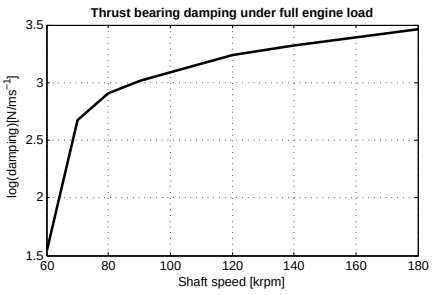

(b) Thrust bearing damping.

Figure F.7: Thrust bearing stiffness (**a**) and damping (**b**) around its equilibrium position under full load.

A similar perturbation around the equilibrium can be made in case the rotor experiences tilting:

$$\begin{aligned} k_{\text{thrust}_X} &= \frac{dM_{\text{thrust}_X}}{d\alpha} \\ c_{\text{thrust}_X} &= \frac{dM_{\text{thrust}_X}}{d\dot{\alpha}} \end{aligned} \tag{F.12}$$

resulting in the the tilting stiffness and damping profiles depicted in Figure F.8.

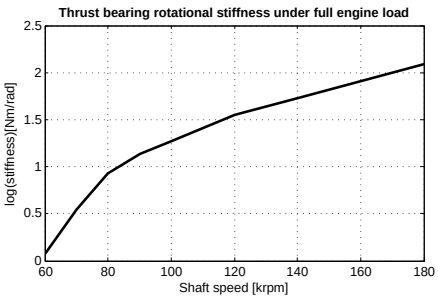

(a) Thrust bearing tilting stiffness.

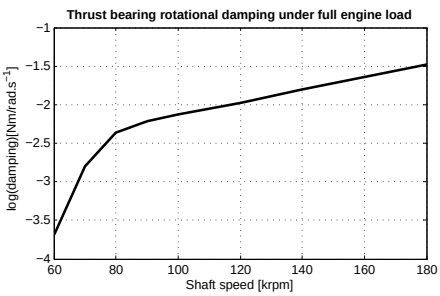

(b) Thrust bearing tilting damping.

Figure F.8: Thrust bearing rotational stiffness (**a**) and damping (**b**) around its equilibrium position under full load.

CURRICULUM VITÆ

Rob ELING

17-10-1984	Born in Boxmeer, The Netherlands.
1996–2002	High School, VWO Elzendaal College, Boxmeer
2003–2006	BSc Mechanical Engineering. Cum laude Fontys Hogeschool Eindhoven
2006–2009	MSc Mechanical Engineering. Specialization: Mechatronics Delft University of Technology
2009–2012	Simulation Engineer Mitsubishi Turbocharger and Engine Europe
2012–2017	PhD Mechanical Engineering Delft University of Technology
2017 – current	Project leader R&D. Topic: electrically assisted turbochargers Mitsubishi Turbocharger and Engine Europe

List of Publications

Journal Publications

8. **R. Eling**, M. te Wierik, R. van Ostayen, D. Rixen, *Rotordynamic and Friction Loss Measurements on a High Speed Laval Rotor Supported by Floating Ring Bearings*, Lubricants (2017).

7. A. Charitopoulos, R. Visser, **R. Eling**, C. Papadopoulos, *Design optimization of an automotive turbocharger thrust bearing using a CFD-based THD computational approach*, Lubricants (In review).

6. **R. Eling** M. te Wierik, R. van Ostayen, D. Rixen, *Towards Accurate Prediction of Unbalance Response , Oil Whirl and Oil Whip of Flexible Rotors Supported by Hydrodynamic Bearings*, Lubricants (2016).

5. S. Alakhramsing, R. van Ostayen, **R. Eling** *Thermo-Hydrodynamic Analysis of a Plain Journal Bearing on the Basis of a New Mass Conserving Cavitation Algorithm*, Lubricants (2015).

Conference Proceedings

4. **R. Eling**, R. van Ostayen, D. Rixen, *Multilobe Floating Ring Bearings for Automotive Turbochargers*, Proceedings of the 9th IFToMM International Conference on Rotor Dynamics, Milan (2015).

3. **R. Eling** R. van Ostayen, D. Rixen, *Oil Flow in Connecting Channels of Floating Ring Bearings*, Proceedings of the SIRM conference, Magdeburg (2015).

2. **R. Eling**, M. te Wierik, R. van Ostayen, D. Rixen, *Multiphysical modeling comprehensiveness to model a high speed Laval rotor on journal bearings*, Proceedings of the 14th Pprime conference, Poitiers (2015).

1. **R. Eling**, M. te Wierik, R. van Ostayen, D. Rixen, *Dynamics of rotors on hydrodynamic bearings*, Proceedings of the Comsol Conference, Rotterdam (2015).

REFERENCES

[1] A. Bandivadekar, K. Bodek, L. Cheah, C. Evans, T. Groode, J.B. Heywood, E. Kasseris, M.A., and M. Weiss. *On the Road in 2035 - Reducing transportation's petroleum consumption and GHG emissions*. Number July. 2008.

[2] Volker Korte, Neil Fraser, James Taylor, and Rene Dingelstadt. Efficient Downsizing for Future Gasoline Engines. *Motortechnische Zeitung*, 72(5):42–49, 2011.

[3] Achim Königstein, Uwe Dieter Grebe, Ko-Jen Wu, and Per-Inge Larsson. Differentiated Analysis of Downsizing Concepts. *Motortechnische Zeitung*, 69(6):4–11, 2008.

[4] Wikipedia. Wikipedia: Turbocharger, 2015.

[5] Hermann Hiereth and Peter Prenninger. Charging the internal combustion engine, Chapter 11: Mechanics of superchargers. In *Charging the internal combustion engine*, pages 194–207. 2007.

[6] Larry Ronan and William. Abernathy. The development and introduction of the automotive turbocharger : a case of innovation in response to fuel economy regulation. Technical report, Lexington Technology Associates, Washington, 1979.

[7] Peter Langen, Wolfgang Hall, Peter Nefischer, and Detlef Hiemesch. The New Two-stage Turbocharged Six-cylinder Diesel Engine of the BMW 740d. *Autotechnische Zeitung*, (2), 2010.

[8] Dellis Polichronis, Retzios Evaggelos, Geralis Alcibiades, Gasparakis Elias, and Pesiridis Apostolos. Turbocharger Lubrication - Lubricant Behavior and Factors That Cause Turbocharger Failure. *International Journal of Automotive Engineering and Technologies*, 2(1):40–54, 2013.

[9] Karl-Heinz Bauer, Craig Balis, David Paja, Peter Davies, and Damien Marsal. High Volume Series Production of Ball Bearing Turbochargers. *Motortechnische Zeitung*, 72(4):48–51, 2011.

[10] Dieter Zeppei, Silvio Koch, and Amir Rohi. Ball Bearing Technology for Passenger Car Turbochargers. *MTZ*, pages 26–31.

[11] Hung Nguyen-Schäfer. *Rotordynamics of Automotive Turbochargers*. Springer Berlin Heidelberg, 2012.

[12] Kostandin Gjika, Pradeep Mahadevan, and Antoine Costeux. Turbocharger Synchronous Vibration Control on High Speed Balancer: Test and Prediction. *Journal of Engineering for Gas Turbines and Power*, 136(7):071603, 2014.

[13] Fanghui Shi and Dinfeng Deng. An Analysis for Floating Bearings in a Turbocharger. In *SAE World congress*, 2011.

[14] Matthijs Mansveld. A field study on turbocharger wear, damage and failure. Technical report, HTS Autotechniek Rotterdam, Rotterdam.

[15] B Rémy, T Lamquin, and B Bou-Saïd. The Modified Phan-Thien and Tanner model applied to turbochargers thrust bearing. pages 449–458. 2014.

[16] IHS. IHS 2000-2020 Turbocharged Engine database. Technical report, IHS, 2015.

[17] Wikipedia. Wikipedia: automotive industry.

[18] Robert R. Inman, Dennis E. Blumenfeld, Ningjian Huang, and Jingshan Li. Designing production systems for quality: Research opportunities from an automotive industry perspective. *International Journal of Production Research*, 41(9):1953–1971, 2003.

[19] Rob Eling. *The structural dynamics of a turbocharger rotor-bearing system*. Msc. thesis, TU Delft, 2009.

[20] Michael I. Friswell, John E. T. Penny, Seamus D. Garvey, and Arthur W. Lees. *Dynamics of rotating machines*. Cambridge University Press, Cambridge, 2010.

[21] Michel Lalanne and Guy Ferraris. *Rotordynamics Prediction in Engineering*. Wiley, 1997.

[22] B. O. Al-Bedoor. Transient torsional and lateral vibrations of unbalanced rotors. *Journal of Sound and Vibration*, 229:627–645, 2000.

[23] M. Li and L. Yu. Analysis of the coupled lateral torsional vibration of a rotor-bearing system with a misaligned gear coupling. *Journal of Sound and Vibrationibration*, 243(2):283–300, 2001.

[24] Giancarlo Genta. *Dynamics of Rotating System*. 2005.

[25] F C Nelson. Rotor dynamics without equations. *International Journal of COMADEM*, 10(3):2–10, 2007.

[26] P. T. Pedersen. On forward and backward precession of rotors. *Ingenieur-Archiv*, 42(1):26–41, 1972.

[27] Fabrizio Stefani. FEM Applied to Hydrodynamic Bearing Design. *New tribological ways*, pages 451–477, 1011.

[28] Matthew B Wagner, Amir Younan, Paul Allaire, and Randy Cogill. Model reduction methods for rotor dynamic analysis: A survey and review, 2010.

[29] M Friswell, J E T Penny, and S D Garvey. Model reduction for structures with damping and gyroscopic effects. *Proceedings of the International Seminar on Modal Analysis*, 3:1151–1158, 2001.

[30] Luis San Andrés. Kinematics of Journal Bearings. *Modern Lubrication Theory*, pages 1–10, 2012.

[31] D. Fuller. *Theory and Practice of Lubrication for Engineers*. 1984.

[32] A. El-Shafei, S. H. Tawfick, M. S. Raafat, and G. M. Aziz. Some Experiments on Oil Whirl and Oil Whip. *Journal of Engineering for Gas Turbines and Power*, 129(1):144, 2007.

[33] Helio Fiori de Castro, Katia Lucchesi Cavalca, and Rainer Nordmann. Whirl and whip instabilities in rotor-bearing system considering a nonlinear force model. *Journal of Sound and Vibration*, 317(1-2):273–293, 2008.

[34] F C Van Breemen. *Stability Analysis of a Laval Rotor on Hydrodynamic Bearings by Numerical Continuation*. Msc. thesis, TU Delft, 2016.

[35] Yukio Hori. *Hydrodynamic lubrication*. Springer Japan, 2006.

[36] Agnieszka Muszynska. Experimental and analytical study on fluid whirl and fluid whip modes. *Rotordynamic Instability Problems in High- . . .* , pages 277–292, 1994.

[37] A Muszynska. Whirl and whip-Rotor/bearing stability problems. *Journal of Sound and Vibration*, 110(3):443–462, 1986.

[38] Frank Immerzeel. *Global Robust Optimization of Computationally Expensive Systems*. Msc. thesis, TU Delft, 2016.

[39] B L Newkirk and H D Taylor. Shaft whipping due to oil action in journal bearings. Technical Report 8, 1925.

[40] Oscar Pinkus. Reynolds Centennial: A Brief History of the Theory of Hydrodynamic Lubrication. *Journal of Tribology*, 109(1):2–20, 1987.

[41] a. Stodola. Kritische Wellenstörung infolge der Nachgiebigkeit des Oelpolsters im Lager. *Schweizerische Bauzeitung*, 85(21):265–266, 1925.

[42] Hummel. Kritische drehzahlen als folge der nachgiebigkeit des schmiermittels im lager. *AW Zickfeldt*, 287, 1926.

[43] J. W. Lund. Review of the Concept of Dynamic Coefficients for Fluid Film Journal bearings. *Journal of Tribology*, 109(January):37–41, 1987.

[44] J. W. Lund and B Sternlicht. Rotor-Bearing Dynamics With Emphasis on Attenuation. *Journal of Basic Engineering*, December:491–498, 1962.

[45] J W Lund and E Saibel. Oil Whip Whirl Orbits of a Rotor in Sleeve Bearings. *Journal of Engineering for Industry*, (11):813–823, 1967.

[46] C. J. Myers. *Linear and Nonlinear Vibrational Characteristics of Oil Lubricated Journal Bearings*. PhD thesis, University of Leeds, 1981.

[47] M. T. Gardner, C. J. Myers, M. D. Savage, and C. M. Taylor. Analysis of Limit-Cycle Response in Fluid-Film Journal Bearings Using the Method of Multiple Scales. *The Quarterly Journal of Mechanics and Applied Mathematics*, 38(1):27–45, 1985.

[48] C. J. Myers. Bifurcation Theory Applied to Oil Whirl in Plain Cylindrical Journal Bearings. *Journal of Applied Mechanics*, 51(June 1984):244, 1984.

[49] Cheng-Chi Wang, Ming-Jyi Jang, and Yen-Liang Yeh. Bifurcation and nonlinear dynamic analysis of a flexible rotor supported by relative short gas journal bearings. *Chaos, Solitons & Fractals*, 32(2):566–582, apr 2007.

[50] Mark Thomas Gardner. *Dynamic behaviour of oil lubricated journal bearings*. PhD thesis, 1983.

[51] Gwidon Stachowiak and Andrew W Batchelor. *Engineering Tribology*. Butterworth-Heinemann, 4th edition, 2014.

[52] M. T. M. Crooijmans, H. J. H. Brouwers, D. H. Van Campen, and Alex De Kraker. Limit Cycle Predictions of a Nonlinear Journal-Bearing System. *Journal of Engineering for Industry*, 112(May 1990):168–171, 1990.

[53] Philip Bonello and Pham Minh Hai. Computational Studies of the Unbalance Response of a Whole Aero-Engine Model With Squeeze-Film Bearings. *Journal of Engineering for Gas Turbines and Power*, 132(March 2010):032504, 2009.

[54] Frank Schilder, Jan Rübel, Jens Starke, Hinke M. Osinga, Bernd Krauskopf, and Mizuho Inagaki. Efficient computation of quasiperiodic oscillations in nonlinear systems with fast rotating parts. *Nonlinear Dynamics*, 51(4):529–539, mar 2007.

[55] K. Avramov, M. Shulzhenko, O. Borysiuk, and C. Pierre. Influence of periodic excitation on self-sustained vibrations of one disk rotors in arbitrary length journals bearings. *International Journal of Non-Linear Mechanics*, 77:274–280, 2015.

[56] P. Sundararajan and S. T. Noah. Dynamics of Forced Nonlinear Systems Using Shooting/Arc-Length Continuation Method—Application to Rotor Systems. *Journal of Vibration and Acoustics*, 119(1):9, 1997.

[57] Jocelyn Rebufa, Fabrice Thouverez, Erick Le Guyadec, and Denis Mazuyer. Nonlinear Effects of Surface Texturing on the Performance of Journal Bearings in Flexible Rotordynamic Systems. *Journal of Tribology*, 139(5):051705, 2017.

[58] R Sghir and M. Chouchane. Nonlinear stability analysis of a flexible rotor-bearing system by numerical continuation. *Journal of Vibration and Control*, (March), 2014.

[59] J C Deepak and S T Noah. Experimental Verification of Subcritical Whirl Bifurcation of aRotor Supported on a Fluid Film Bearing. *Journal of Tribology*, 120(July):605–609, 1998.

[60] B L Newkirk. Oil film whirl—An investigation of disturbances due to oil films in journal bearings. *Trans. ASME*, 78:985–988, 1956.

[61] Oscar Pinkus. Experimental investigation of resonant whip. *Trans. ASME*, 1956.

[62] T Someya. Negative pressure in the oil-film of journal bearing. *Annals*, (September), 2003.

[63] J. R. Mitchell, R. Holmes, and J. Byrne. Oil Whirl of a Rigid Rotor in 360 Journal Bearings: Further Characteristics. *Proceedings of the Institution of Mechanical Engineers*, 180(25):pp. 593–610, 1965.

[64] G. Capone. The Influence of Oil Supply Pressure on the Behavior of a w. *Trans. ASME*, 114(October), 1992.

[65] Zenglin Guo, Toshio Hirano, and R. Gordon Kirk. Application of CFD Analysis for Rotating Machinery—Part I: Hydrodynamic, Hydrostatic Bearings and Squeeze Film Damper. *Journal of Engineering for Gas Turbines and Power*, 127(2):445, 2005.

[66] Jan Rubel. *Vibrations in Nonlinear rotordynamics*. Phd thesis, Heidelberg, 2009.

[67] Amira Amamou and Mnaouar Chouchane. Non-linear stability analysis of floating ring bearings using Hopf bifurcation theory. *Proceedings of the Institution of Mechanical Engineers, Part C: Journal of Mechanical Engineering Science*, 225(12):2804–2818, jul 2011.

[68] Aydin Boyaci, H. Hetzler, Wolfgang Seemann, Carsten Proppe, and J. Wauer. Analytical bifurcation analysis of a rotor supported byfloating ring bearings. *Nonlinear Dynamics*, 57(4):497–507, aug 2008.

[69] Rob Eling, Mathys Wierik, Ron Van Ostayen, and Daniel Rixen. Towards Accurate Prediction of Unbalance Response , Oil Whirl and Oil Whip of Flexible Rotors Supported by Hydrodynamic Bearings. pages 1–18, 2016.

[70] D Souchet and D Bonneau. S. Piffeteau D. Souchet D. Bonneau. 122(January), 2000.

[71] S Messé and A. Lubrecht. Transient elastohydrodynamic analysis of an overhead cam/tappet contact. *Proceedings of the Institution of Mechanical Engineers, Part J: Journal of Engineering Tribology*, 214(5):415–425, 2000.

[72] Matthias Schleer, Seung Jin Song, and Reza S. Abhari. Clearance Effects on the Onset of Instability in a Centrifugal Compressor. *Journal of Turbomachinery*, 130(3):031002, 2008.

[73] Anders Angantyr. *Rotordynamic Optimization of Large Turbo Systems using Genetic Algorithms*. Phd thesis, Lulea University, 2006.

[74] Antonija Duvnjak. Derivation of the Reynolds equation for lubrication of a rotating shaft. *Archivum Mathematicum*, 43(4), 2007.

[75] A Z Szeri. Some Extensions of the Lubrication Theory of Osborne. *Journal of Tribology*, 109(86):21–36, 1987.

[76] Luis San Andres. Lectures notes 4: Static load performance of plain journal bearings, 2010.

[77] Francisco Carrusca Pimenta de Brito. *Thermohydrodynamic performance of twin groove journal bearings considering realistic lubricant*. Phd thesis, Universidade do Minho, Braga, 2009.

[78] F. W. Ocvirk. Short-Bearing Approximation for Full Journal Bearings. *National Advisory Committee for Aeronautics*, NACA TN 28, 1952.

[79] a. Cameron and W. L. Wood. The Full Journal Bearing. *Proceedings of the Institution of Mechanical Engineers*, 161(1):59–72, 1949.

[80] Gustavo G Vignolo, Daniel O Barilá, and Lidia M Quinzani. Approximate Analytical Solution to Reynolds Equation for Finite Length Journal Bearings. *Tribology International*, 44(10):1089–1099, 2011.

[81] T. V. V. L. N. Rao, S. Biswas, H. Hirani, and K. Athre. An Analytical Approach to Evaluate Dynamic Coefficients and Nonlinear Transient Analysis of a Hydrodynamic Journal Bearing. *Tribology Transactions*, 43(1):109–115, jan 2000.

[82] T. V. V. L. N. Rao, S. Biswas, and K. Athre. A Methodology for Dynamic Coefficients and Nonlinear Response of Multi-Lobe Journal Bearings. *Tribology Transactions*, 44(1):111–117, jan 2001.

[83] B. R. Reason and I. P. Narang. Rapid Design and Performance Evaluation of Steady-State Journal Bearings—A Technique Amenable to Programmable Hand Calculators. *A S L E Transactions*, 25(4):429–444, 1982.

[84] K.P. Gertzos, P.G. Nikolakopoulos, and C.a. Papadopoulos. CFD analysis of journal bearing hydrodynamic lubrication by Bingham lubricant. *Tribology International*, 41(12):1190–1204, dec 2008.

[85] M J Braun and W M Hannon. Cavitation formation and modelling for fluid film bearings: a review. *Proceedings of the Institution of Mechanical Engineers, Part J: Journal of Engineering Tribology*, 224(9):839–863, jan 2010.

[86] D Dowson, CM M Taylor, Cavitation I N Bearings, D Dowson, and CM M Taylor. Cavitation in bearings. *Annual Review of Fluid Mechanics*, pages 35–66, 1979.

[87] Jean-Louis Ligier and Bruno Noel. Friction Reduction and Reliability for Engines Bearings. *Lubricants*, 3(3):569–596, 2015.

[88] Shivam Alakhramsing, Ron van Ostayen, and Rob Eling. Thermo-Hydrodynamic Analysis of a Plain Journal Bearing on the Basis of a New Mass Conserving Cavitation Algorithm. *Lubricants*, 3(2):256–280, 2015.

[89] Biao Yu and JT Sawicki. Comparison of Mobility Method and Mass Conservation Method in a Study of Dynamically Loaded Journal Bearings. *International Journal of Rotating Machinery*, 8(1):71–79, 2002.

[90] Rohit S. Paranjpe. Transient thermohydrodynamic analysis including mass conserving cavitation for dynamically loaded journal bearings. *American Society of Mechanical Engineers (Paper)*, (94):1 – 10, 1994.

[91] K Mistry, S Biswas, and K Athre. A new theoretical model for analysis of the fluid film in the cavitation zone of a journal bearing. *Journal of tribology*, 119(4):741–746, 1997.

[92] D. G. Christopherson. New Mathematical Method for the Solution. *Proceedings of the Institution of Mechanical Engineers*, (l):126–135, 1940.

[93] G. Bayada, M. Chambat, and M. El Alaoui. Variational Formulations and Finite Element Algorithms for Cavitation Problems. *Journal of Tribology*, 112(April):398, 1990.

[94] Hooshang Heshmat. The Mechanism of Cavitation in Hydrodynamic Lubrication. *Tribology Transactions*, 34(2):177–186, 1991.

[95] H G Elrod. A Cawitation Algorithm. *Transactions of the ASME*, 103(July 1981):350–354, 1981.

[96] David E Brewe. Theoretical Modeling of the Vapor Cavitation in Dynamically Loaded Journal Bearings. *Transactions of the ASME, Journal of Tribology*, 108(41):628–638, 1986.

[97] Steffen Nitzschke, Elmar Woschke, Christian Daniel, and Jens Strackeljan. Einfluss der masseerhaltenden Kavitation auf gleitgelagerte Rotoren unter instationärer Belastung. In *SIRM 2013*, pages 1–11, 2013.

[98] G Bayada, Insa De Lyon, and L Chupin. Compressible fluid model for hydrodynamic lubrication cavitation. pages 1–38, 2013.

[99] H. Allmaier, C. Priestner, F. M. Reich, H. H. Priebsch, C. Forstner, and F. Novotny-Farkas. Predicting friction reliably and accurately in journal bearings the importance of extensive oil-models. *Tribology International*, 48:93–101, 2012.

[100] Christopher J Seeton. Viscosity-temperature correlation for liquids. *Tribology Letters*, 22(1):67–78, 2006.

[101] Oscar Pinkus. *Thermal aspects of fluid film tribology*. 1990.

[102] Scott Bair and Peter Kottke. Pressure-Viscosity Relationships for Elastohydrodynamics. *Tribology Transactions*, 46(June 2015):289–295, 2003.

[103] Lowrie B. Sargent. Pressure-Viscosity Coefficients of Liquid Lubricants. *A S L E Transactions*, 26(1):1–10, 1983.

[104] Burak a. Gecim. Non-Newtonian Effects of Multigrade Oils on Journal Bearing Performance. *Tribology Transactions*, 33(3):384–394, jan 1990.

[105] B. Wright, N. van Os, and J. Lyons. The Effects of Shear Rate and Temperature on the Viscosity of Multigrade Oils. *SAE International*, 1983.

[106] R I Taylor. The inclusion of lubricant shear thinning in the short bearing approximation. *Proceedings of the Institution of Mechanical Engineers, Part J: Journal of Engineering Tribology*, 213(1):35–46, jan 1999.

[107] R.P. Chhabra and J.F. Richardson. *Non-Newtonian Flow and Applied Rheology*. 2008.

[108] Shivam Alakhramsing. *A thermo-hydrodynamic analysis of full oating ring bearings including realistic fluid rheology and cavitation*. Msc. thesis, TU Delft, 2014.

[109] D. E. Sander, H. Allmaier, H. H. Priebsch, F. M. Reich, M. Witt, T. Fullenbach, A. Skiadas, L. Brouwer, and H. Schwarze. Impact of high pressure and shear thinning on journal bearing friction. *Tribology International*, 81:29–37, 2015.

[110] H.W. Swift. Theory and experiment applied to journal bearing design. *Proc. IMechE of the General Discussion on Lubrication*, 1937.

[111] J Bouyer and M Fillon. Relevance of the Thermoelastohydrodynamic Model in the Analysis of a Plain Journal Bearing Subjected to Severe Operating Conditions. *Proceedings of the Institution of Mechanical Engineers, Part J: Journal of Engineering Tribology*, 218(5):365–376, 2004.

[112] W. F. Cope. The Hydrodynamical Theory of Film Lubrication. In *Proc. R. Soc. Lond*, pages 201–217, 1949.

[113] Dowson. A generalized Reynolds equation for fluid-film lubrication. *International Journal of Mechanical Sciences*, 4:159 – 170, 1962.

[114] D Dowson, Jd Hudson, B Hunter, and Cn March. An experimental investigation of the thermal equilibrium of steadily loaded journal bearings. *Proc. Inst. Mech. Eng*, 181:70–80, 1966.

[115] R Boncompain. Analysis of Thermal Effects in Hydrodynamic Bearings. *Journal of Tribology-Transactions of the Asme*, 108(2):219 – 224, 1986.

[116] M. M. Khonsari and J J Beaman. Thermohydrodynamic Analysis of Laminar Incompressible Journal Bearings. *Tribology Transactions*, 8197(July 2013):37–41, 2008.

[117] M. T. Ma and C. M. Taylor. An experimental investigation of thermal effects in a cavitating inducer. *Tribiology International*, 29(Figure 1):19–26, 1996.

[118] L Costa, a S Miranda, M Fillon, and J C P Claro. An analysis of the influence of oil supply conditions on the thermohydrodynamic performance of a single-groove journal bearing. *Proceedings of the Institution of Mechanical Engineers, Part J: Journal of Engineering Tribology*, 217(2):133–144, 2003.

[119] Isabelle Pierre, Electricite de France, Jean Bouyer, and Michel Fillon. Thermohydrodynamic Behavior of Misaligned Plain Journal Bearings: Theoretical and Experimental Approaches. *Tribology Transactions*, 47(4):594–604, 2004.

[120] C. Rajalingham. Influence of Thermal Conduction Across the Fluid Film on the THD Characteristics of a Plain Journal Bearing. *Journal of Tribology*, 116(April 1994):397–399, 1994.

[121] Marcel Mahner, Andreas Lehn, and Bernhard Schweizer. Thermogas- and thermohydrodynamic simulation of thrust and slider bearings : Convergence and efficiency of different reduction approaches. *Tribology International*, 93:539–554, 2016.

[122] Donghyun Lee and Daejong Kim. Thermohydrodynamic Analyses of Bump Air Foil Bearings With Detailed Thermal Model of Foil Structures and Rotor. *Journal of Tribology*, 132(April):021704, 2010.

[123] HG Elrod. Efficient numerical method for computation of the thermohydrodynamics of laminar lubricating films. Technical report, 1989.

[124] Mechanical Engineering. A Thermohydrodynamic Analysis of a Twin Axial Groove Bearing Under Different Loading Directions. 114(April), 1992.

[125] D Dowson and AV Ruddy. An analysis of the circumferentially grooved journal bearing with consideration of lubricant film reformation. *Proceedings of the ...*, 1985.

[126] D. Vijayaraghavan. An Efficient Numerical Procedure for Thermo- hydrodynamic Analysis of. *Journal of Tribology*, 1(July), 1996.

[127] Jang Jiin-Yuh and Chang Chong-Ching. Adiabatic analysis of finite width journal bearings with non-newtonian lubricants. *Wear*, 122(1):63–75, feb 1988.

[128] Gunhee H. Jang, K. S. Kim, Ho Seong Lee, and C. S. Kim. Analysis of a hydrodynamic bearing of a HDD spindle motor at elevated temperature. *ASME Journal of Tribology*, 126(2):353–359, 2004.

[129] MK Fitzgerald and PB Neal. Temperature distributions and heat transfer in journal bearings. *Journal of tribology*, 114(January):122–130, 1992.

[130] S.S. Banwait and H.N. Chandrawat. Study of thermal boundary conditions for a plain journal bearing. *Tribology International*, 31(6):289–296, 1998.

[131] Robert J Raymond. Crankpin Bearings in High Output Aircraft Piston Engines The Evolution of their Design and Loading, 2014.

[132] M.C. C. Shaw, TJ J Nussdorfer Jr, T. J. Nussdorfer Jr., and TJ J Nussdorfer Jr. An analysis of the full-floating journal bearing. *National Advisory Committee for Aeronautics*, 866, 1947.

[133] B Garre. Schwimmende Lagerbuechse Floating Lagerbuechse, 1944.

[134] H.V. Shebat. Bearing patent US2076254 A, 1937.

[135] P. I. Orloff. National Advisory Committee for Aeronautics. *Aeronautical Engineering (Moscow)*, 9(January 1935):pp. 25–56, 1935.

[136] L. Tian. *Investigation into Nonlinear Dynamics of Rotor-Floating Ring Bearing Systems in Automotive Turbochargers*. PhD thesis, University of Sussex, 2012.

[137] A Tatara. An experimental study of the stabilizing effect of floating-bush journal bearings. *Bulletin of JSME*, 13:858–863, 1970.

[138] Masato Tanaka and Y. Hori. Stability Characteristics of Floating Bush Bearings. *Journal of Lubrication Technology*, 94(3):248, 1972.

[139] a. Tondl. Experimental Investigation of Self-Excited Vibrations of Rotors due to the Action of Lubricating Oil Film in Journal Bearings. *Wear*, 5(1):136–147, 1962.

[140] Juraj Dworski. High-Speed Rotor Suspension Formed by Fully Floating Hydrodynamic Radial and Thrust Bearings. *... of Engineering for Gas Turbines and ...*, (63):1–16, 1964.

[141] F.K. Orcutt and C.W. Ng. Steady-state and dynamic properties of the floating-ring journal bearing. *Journal of Tribology*, 1968.

[142] Chin-hsiu Li and SM Steve M Rohde. On the steady state and dynamic performance characteristics of floating ring bearings. *Journal of Tribology*, 103(80):2–10, 1981.

[143] Chris Holt, Luis San Andres, Sunil Sahay, Peter Tang, Gerry LaRue, Kostandin Gjika, Gerry La Rue, and Kostandin Gjika. Test Response and Nonlinear Analysis of a Turbocharger Supported on Floating Ring Bearings. *Journal of Vibration and Acoustics*, 127(2):107, 2005.

[144] Bernhard Schweizer. Dynamics and stability of turbocharger rotors. *Archive of Applied Mechanics*, 80(9):1017–1043, aug 2009.

[145] L. Tian, W.J. J Wang, and Z.J. J Peng. Effects of bearing outer clearance on the dynamic behaviours of the full floating ring bearing supported turbocharger rotor. *Mechanical Systems and Signal Processing*, 31:155–175, aug 2012.

[146] Luis San Andres, Juan Carlos Rivadeneira, Kostandin Gjika, Christopher Groves, and Gerry LaRue. Rotordynamics of Small Turbochargers Supported on Floating Ring Bearings—Highlights in Bearing Analysis and Experimental Validation. *Journal of Tribology*, 129(2):391, 2007.

[147] Richard J. Trippett and Dennis F. Li. High-speed Floating-Ring Bearing Test and Analysis. *A S L E Transactions*, 27(27):73–81, 1984.

[148] D.M. Clarke, C Fall, and C I Itjiul. A steady-state model of a floating ring bearing, including thermal effects. *Journal of ...*, 114(January 1992), 1992.

[149] H. R. Born. Analytical & Experimental Investigation of the Stability of the Rotor-Bearing System of a New Small Turbocharger. In *Gas Turbine Conference and Exhibition*, 1987.

[150] Stefan Pischinger, Stoffels Harald, Christoph Steffens, Richard Aymanns, Remi Stohr, and Martin Atzler. Acoustic Development for Exhaust Gas Turbochargers.pdf. *MTZ*, 69(03 2008):42–49, 2008.

[151] JA A Calvo, V Diaz, and JL San L San Roman. Controlling the turbocharger whistling noise in diesel engines. *International Journal of Vehicle Noise and vibration*, 2(1):17–28, 2006.

[152] Luis San Andres, Vince Barbarie, Avijit Bhattacharya, and Kostandin Gjika. On the Effect of Thermal Energy Transport to the Performance of (Semi) Floating Ring Bearing Systems for Automotive Turbochargers. *Journal of Engineering for Gas Turbines and Power*, 134(10):102507, 2012.

[153] Bernhard Schweizer. Total instability of turbocharger rotors - Physical explanation of the dynamic failure of rotors with full-floating ring bearings. *Journal of Sound and Vibration*, 328(1-2):156–190, nov 2009.

[154] Luis San Andres, J Kerth, L San Andrés, J Kerth, L San Andres, J Kerth, Luis San Andres, J Kerth, L San Andrés, and J Kerth. Thermal effects on the performance of floating ring bearings for turbochargers. *Proceedings of the Institution of Mechanical Engineers, Part J: Journal of Engineering Tribology*, 218(5):437–450, jan 2004.

[155] Juan Carlos Rivadeneira. *Predictions versus Measurements of Turbocharger Nonlinear Dynamic Response*. PhD thesis, 2006.

[156] Kostandin Gjika, Luis San Andres, and Gerry D. LaRue. Nonlinear Dynamic Behavior of Turbocharger Rotor-Bearing Systems With Hydrodynamic Oil Film and Squeeze Film Damper in Series: Prediction and Experiment. *Journal of Computational and Nonlinear Dynamics*, 5(4):041006, 2010.

[157] J Kerth. *Prediction and measurement of the rotordynamic response of an automotive turbocharger with floating ring bearings*. PhD thesis, 2003.

[158] Bernhard Schweizer. Oil whirl, oil whip and whirl/whip synchronization occurring in rotor systems with full-floating ring bearings. *Nonlinear Dynamics*, 57(4):509–532, 2009.

[159] Bernhard Schweizer and Mario Sievert. Nonlinear oscillations of automotive turbocharger turbines. *Journal of Sound and Vibration*, 321(3-5):955–975, 2009.

[160] U Tomm, Aydin Boyaci, Carsten Proppe, and Wolfgang Seemann. Rotor dynamic analysis of a passenger car turbocharger using run-up simulation and bifurcation theory. *IMechE 9th International Conference on Turbochargers and Turbocharging*, pages 335–346, 2010.

[161] Hung Nguyen-Schäfer. *Aero and Vibroacoustics of Automotive Turbochargers*. Springer-Verlag, Stuttgart, 2013.

[162] Elmar Woschke and Christian Daniel. Numerical run-up simulation of a turbocharger with full floating ring bearings. *ICOVP 2011*, pages 1–6, 2011.

[163] Christian Daniel, Elmar Woschke, Steffen Nitzschke, Jens Strackeljan, Nicolas Driot, Karl-ludwig Braun, and Panagiotis Koutsovasilis. Validierung der Hochlaufsimulation für automotive Abgasturbolader. In *SIRM2015 – 11. Internationale Tagung Schwingungen in rotierendenMaschinen*, pages 1–9, Magdeburg, 2015.

[164] L. Tian, W.J. J Wang, and Z.J. J Peng. Nonlinear effects of unbalance in the rotor-floating ring bearing system of turbochargers. *Mechanical Systems and Signal Processing*, 34(1-2):298–320, jan 2013.

[165] José Ramón Serrano, Pablo Olmeda, Andrés Tiseira, Luis Miguel García-Cuevas, and Alain Lefebvre. Theoretical and experimental study of mechanical losses in automotive turbochargers. In *Energy*, volume 55, pages 888–898. Elsevier Ltd, jun 2013.

[166] Nick Baines, Karl D. Wygant, and Antonis Dris. The Analysis of Heat Transfer in Automotive Turbochargers. *Journal of Engineering for Gas Turbines and Power*, 132(4):042301, 2010.

[167] D. Bohn, T. Heuer, and K. Kusterer. Conjugate Flow and Heat Transfer Investigation of a Turbo Charger. *Journal of Engineering for Gas Turbines and Power*, 127(July 2005):663, 2005.

[168] D Porzig, H Raetz, H Schwarze, and J R Seume. Thermal analysis of small high-speed floating-ring journal bearings. In *11th International Conference on Turbochargers and Turbocharging*, number Figure 1, pages 421–436, 2014.

[169] D Vetter, T Hagemann, and H Schwarze. *Predictions for run-up procedures of automotive turbochargers with full- floating ring bearings including thermal effects and different bearing setups*. 2014.

[170] Yajing Li, Feng Liang, Yu Zhou, Shuiting Ding, Farong Du, Ming Zhou, Jinguang Bi, and Yi Cai. Numerical and experimental investigation on thermohydrodynamic performance of turbocharger rotor-bearing system. *Applied Thermal Engineering*, 121:27–38, 2017.

[171] M. Deligant, P. Podevin, and G. Descombes. Experimental identification of turbocharger mechanical friction losses. *Energy*, 39(1):388–394, mar 2012.

[172] L Tian, M Wakelin, C Lancaster, and M Lindsay. The effect of oil film instability on power losses prediction of a turbocharger rotor-fully floating ring bearing system. In *IMechE 12th International Conference on turbochargers and turbocharging*, 2016.

[173] E Sjöberg. *Friction Characterization of Turbocharger Bearings*. Msc. thesis, KTH, 2013.

[174] Bjoern Hoepke, Tolga Uhlmann, Stefan Pischinger, Bernhardt Lueddecke, and Dietmar Filsinger. Analysis of Thrust Bearing Impact on Friction Losses in Automotive Turbochargers. *Journal of Engineering for Gas Turbines and Power*, 137(8):82507, 2015.

[175] Ashley Maruyama. *Prediction of automotive turbocharger nonlinear dynamic forced response with engine-induced housing excitations*. Msc. thesis, Texas A&M university, 2007.

[176] Luis San Andres, Ashley Maruyama, Kostandin Gjika, and Sherry Xia. Turbocharger Nonlinear Response With Engine-Induced Excitations: Predictions and Test Data. *Journal of Engineering for Gas Turbines and Power*, 132(3):032502, 2010.

[177] Shiyuan Pei, Hua Xu, Meng Yun, Fanghui Shi, and Jun Hong. Effects of surface texture on the lubrication performance of the floating ring bearing. *Tribology International*, 102:143–153, 2016.

[178] D Arumuga Perumal. Simulation of Flow in Two-Sided Lid-Driven Deep Cavities. *Journal of applied science in the thermodynamics and fluid mechanics Vol. 6, No. 1/2012, ISSN 1802-9388*, 6(1):1–6, 2012.

[179] Donald D. Heckelman and C. M. McC. Ettles. Viscous and Inertial Pressure Effects at the Inlet to a Bearing Film. *Tribology Transactions*, 31(1):1–5, mar 2008.

[180] Rob Eling, Ron a. J. Van Ostayen, and Daniel J. Rixen. Oil Flow in Connecting Channels of Floating Ring Bearings. (February):1–9, 2015.

[181] Chang-Jian. Nonlinear Simulation of Rotor Dynamics Coupled with Journal and Thrust Bearing Dynamics under Nonlinear Nonlinear Simulation of Rotor Dynamics Coupled with Journal and Thrust Bearing Dynamics under Nonlinear. *Tribology Transactions*, 53(September 2014):37–41, 2010.

[182] Shuo Li, Sedat Tuzcu, Michael Klaus, Prof Adrian Rienäcker, and Prof Hubert Schwarze. Analyse der Einfluesse der hydrodynamischen Axiallagerung auf das. pages 1–10, 2015.

[183] Ioannis Chatzisavvas, Aydin Boyaci, Panagiotis Koutsovasilis, and Bernhard Schweizer. Influence of hydrodynamic thrust bearings on the nonlinear oscillations of high-speed rotors. *Journal of Sound and Vibration*, 380:224–241, 2016.

[184] Daniel Tamunodukobipi, Chang Ho Kim, and Yong-Bok Lee. Dynamic Performance Characteristics of Floating-Ring Bearings With Varied Oil-Injection Swirl-Control Angles. *Journal of Dynamic Systems, Measurement, and Control*, 137(2):021002, sep 2014.

[185] Rob Eling, Ron a.J. van Ostayen, and Daniel Rixen. Multilobe Floating Ring Bearings for Automotive Turbochargers. In *Proceedings of the 9th IFToMM International Conference on Rotor Dynamics*, 2015.

[186] Gerrit Nowald, Aydin Boyaci, Robert Schmoll, Panagiotis Koutsovasilis, Nicolas Driot, and Bernhard Schweizer. Influence of axial grooves in full-floating-ring bearings on the nonlinear oscillations of turbocharger rotors. (February):1–8, 2015.

[187] Elmar Woschke, G Stefan, Steffen Nitzschke, Christian Daniel, and Jens Strackeljan. Proceedings of the 9th IFToMM International Conference on Rotor Dynamics. 21:1081–1090, 2015.

[188] Robert D. Cook, David S. Malkus, Michael E. Plesha, and Robert J. Witt. *Concepts and Applications of Finite Element Analysis*. Wiley, 4 edition, 2001.

[189] M. Deligant, P. Podevin, and G. Descombes. CFD model for turbocharger journal bearing performances. *Applied Thermal Engineering*, 31(5):811–819, apr 2011.

[190] Praneetha Boppa and Gerald L. Morrison. A numerical study of squeeze film dampers. In *Proceedings of ASME Turbo Expo 2013*, pages 1–10, 2013.

[191] Luis San Andres. Lecture notes 2: Derivation of the classical Reynolds equation for thin film flows, 2010.

[192] Luis San Andres. Lectures notes 1: The fundamental assumptions of hydrodynamic lubrication, 2010.

[193] P G Nikolakopoulos and C A Papadopoulos. Non-linearities in misaligned journal bearings. *Tribology International*, 27(4):243–257, 1994.

[194] S Nitzschke, E Woschke, D Schmicker, and J. Strackeljan. Regularised cavitation algorithm for use in transient rotordynamic analysis. *International Journal of Mechanical Sciences*, 113:175–183, 2016.

[195] Juha Saari. *Thermal analysis of High speed Induction Machines*. Number 100. 1998.

[196] A.F. Mills. *Basic heat and mass transfer*. Pearson Education, 2nd revise edition, 1998.

[197] O Aglen and A Andersson. Thermal analysis of a high-speed generator. In *Industry Applications Conference, 2003*, pages 547–554, 2003.

[198] Christoph Knauder, Hannes Allmaier, David Emanual Sander, Stefan Salhofer, Franz Markus Reich, and Theodor Sams. Analysis of the Journal Bearing Friction Losses in a Heavy-Duty Diesel Engine. *Lubricants*, 3:142–154, 2015.

[199] A B Comsol. COMSOL multiphysics users guide. *Version: September*, 2005.

[200] M. Wierik. *The Behavior of High Speed Rotors on Fluid Film Bearings*. Msc. thesis, TU Delft, 2016.

[201] Bernard J. Hamrock, Steven R. Schmid, and Bo O. Jacobson. *Fundamentals of Fluid Film Lubrication*. CRC Press, 2004.

[202] J D Knight and A J Niewiarowski. Effects of Two Film Rupture Models on the Thermal Analysis of a Journal Bearing. *Journal of Tribology*, 112(2):183–188, 1990.

[203] Wolfgang Köhl, Martin Kreschel, and Dietmar Filsinger. Modellabgleich eines Turboladerrotors in Schwimmbuchsenlagerung an- hand gemessener Schwimmbuchsendrehzahlen. 5(1):1–10, 2015.

[204] Gerrit Nowald, Robert Schmoll, and Bernhard Schweizer. Transient Run-Up Simulations of Rotors in Journal Bearings Considering Mass-Conserving Cavitation Approaches. In *SIRM 2017*, number March, 2017.

[205] Luis San Andres and Arian Vistamehr. Nonlinear rotordynamics of vehicle turbochargers: parameters affecting sub harmonic whirl frequencies and their jump. In *The 8th IFToMM International Conference on Rotor Dynamics*, pages 1077–1086, 2010.

[206] E. Woschke, C. Daniel, and S. Nitzschke. Excitation mechanisms of non-linear rotor systems with floating ring bearings - simulation and validation. *International Journal of Mechanical Sciences*, 134(October):15–27, 2017.

[207] Matthew D. Brouwer, Farshid Sadeghi, Craig Lancaster, Jamie Archer, and James Donaldson. Whirl and Friction Characteristics of High Speed Floating Ring and Ball Bearing Turbochargers. *Journal of Tribology*, 135(4):041102, jun 2013.

[208] D. Sun and R. Liao. Damping prediction technique of the bolted joint structure considering pretension force. *Open Civil Engineering Journal*, 9(1):622–626, 2015.

[209] D. van. Schuur, M. Fransen, M. te Wierik, and L. Lobert. Non-rotational behaviour of a turbocharger shaft. Technical report, 3mE, Delft, 2013.

[210] Lukas Bernhauser, Lorenz Steinwender, and Hans Irschik. Designing a Metric for the Customer Relevance of Synchronous Turbocharger Whistling in the Driver ' s Cabin. (4):5369–5376, 2016.

[211] Lukas Bernhauser, Martin Heinisch, Markus Schörgenhumer, and Manfred Nader. The effect of non-circular bearing shapes in hydrodynamic journal bearings onto the vibration behavior of turbocharger structures. *Lubricants*, 2016.

[212] Din Iso. *Akustik - Normalkurven gleicher Lautstärkepegel (ISO 226:2003)*. 2006.

[213] D Deng, Fanghui Shi, Lou Begin, I Du, and General Motors. The Effect of Oil Debris in Turbocharger Journal Bearings on SubSynchronous NVH. *SAE International*, 2015-01-12(April), 2015.

[214] Bruce Boardman. Fatigue resistance of Steels. *Properties and Selection: Irons, Steels, and High Performance Alloys*, 1:673–688, 1990.

[215] G. Gary Wang and S. Shan. Review of Metamodeling Techniques in Support of Engineering Design Optimization. *Journal of Mechanical Design*, 129(4):370, 2007.

[216] Terry Andres, Stefano Tarantola, Jessica Cariboni, Marco Ratto, Debora Gatelli, Andrea Saltelli, Michaela Saisana, and Francesca Campolongo. *Global Sensitivity Analysis. The Primer.* 2008.

[217] R. Jin, X. Du, and W. Chen. The use of metamodeling techniques for optimization under uncertainty. *Structural and Multidisciplinary Optimization*, 25(2):99–116, 2003.

[218] D Apley, J Liu, G Student, and W Chen. Understanding the Effects of Model Uncertainty in Robust Design With Computer Experiments. *Journal of Mechanical Design*, 2006.

[219] Donald R Jones, Matthias Schonlau, and William J Welch. Efficient Global Optimization of Expensive Black-Box Functions. *Journal of Global Optimization*, 13:455–492, 1998.

[220] J M Parr, A J Keane, A I J Forrester, and C M E Holden. Infill sampling criteria for surrogate-based optimization with constraint handling Infill sampling criteria for surrogate-based optimization with constraint handling. *Engineering Optimization*, 44(10):1147–1166, 2012.

[221] Samee ur Rehman and Matthijs Langelaar. Expected improvement based infill sampling for global robust optimization of constrained problems. *Structural and Multidisciplinary Optimization*, 2017.

[222] Sitae Kim and Alan B. Palazzolo. Effects of thermo hydrodynamic (THD) floating ring bearing model on rotordynamic bifurcation. *International Journal of Non-Linear Mechanics*, 95(May):30–41, 2017.

[223] Bernhardt Lüddecke, Philipp Nitschke, Michael Dietrich, Dietmar Filsinger, and Michael Bargende. Unsteady Thrust Force Loading of a Turbocharger Rotor During Engine Operation. *Journal of Engineering for Gas Turbines and Power*, 138(1):012301, 2015.

[224] B Remy, B. Bou-Saïd, and T Lamquin. Fluid inertia and energy dissipation in turbocharger thrust bearings. *Tribology International*, 95:139–146, 2016.